PETROGENESIS OF THE NEW AMALFI SHEET :

A highly differentiated Karoo intrusion.

by

CRAIG MILTON WILLIAMS

B.Sc.(Hons.)

Thesis submitted in fulfilment of the
requirements for the Degree of

Master of Science

in the Department of Geology
Rhodes University
Grahamstown
February 1995

DECLARATION

All work in this thesis is the original work of the author, except where specific acknowledgement is made to the work of others.

SIGNED 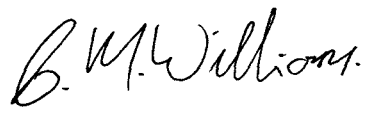

C.M.WILLIAMS
February 1995

CONTENTS

ACKNOWLEDGEMENTS

ABSTRACT

ACKNOWLEDGEMENTS.

I would like to thank my supervisor, Prof. H.V. Eales, for introducing me to what has been a stimulating project and for his continual support and advice. Grateful acknowledgement is made to the FRD for funding this project. I would also like to thank Patrick and Jan Rawlings, on whose previous farm the central portion of the intrusion is situated, for their instant and unwavering hospitality.

My colleagues at Anglo American Research Laboratories are thanked for their support and encouragement, as well as for allowing me the time to finally complete the thesis. Staff at the Bernard Price Institute of Geophysics, especially Dr. F.J. Kruger and Dr. Craig Smith, are thanked for help with the isotope analysis.

Members of staff and students within the Geology Department at Rhodes University are thanked for invaluable input and support during the completion of this thesis. In particular I would like to thank Dr. Rob Harris for help in producing the maps. Prof. J.S. Marsh for advice on the isotope section. Rob Skae, Billy Morgan, Abel Roman, John Hepple and Phoenix Hoyle for help on the technical side. Andrew Cook is thanked for proof reading the thesis. Lastly I would like to thank my friends Sue Frost, Paulo Kerber, Wolfgang Maier, Ralph Elias and Ayeshé Toombs for their invaluable help and support.

ABSTRACT.

The New Amalfi Sheet is a highly differentiated tholeiitic intrusion which is situated between the towns of Matatiele and Swartberg in East Griqualand. It lies within of the Central area of the Karoo Igneous Province. Rock types range from dolerites at the base and top through to a highly differentiated granophyre which is found as a 'sandwich horizon' within the top half of the sheet. The most evolved granophyre represents 15.86% of the initial liquid, which was found to be very similar in composition to the average Lesotho-type magma of Marsh and Eales (1984). The paragenetic sequence was found to be chromite → olivine → plagioclase → pigeonite and augite. Cumulus magnetite and ilmenite enter the paragenetic sequence together with immiscible sulphide droplets after 35% crystallization. In the late stages of crystallization, augite changes composition towards ferrohedenbergite. The reappearance of iron-rich olivine coincides with the disappearance of pigeonite and apatite appears as a cumulus phase for the first time after 70% crystallization. Granophyric intergrowth, which contains coarse perthitic K-feldspar, becomes the most abundant modal entity within the most evolved granophyres. Differentiation was dominated by fractionation of plagioclase and pyroxene, with subordinate olivine and opaque-oxide fractionation. A minor amount of assimilation of country rock occurred within the topmost granophyres. The intrusion has been dated, using the Rb-Sr isochron method, at 178.37 ± 5.52 Ma.

Extensive subsolidus deuteric alteration has resulted in the formation of a complete series of hydrothermally altered clinopyroxenes which are enriched in CaO but depleted in TiO_2 compared to the unaltered magmatic clinopyroxenes. It has also resulted in the formation of abundant vermiform ilmenite in the most evolved rocks, recognized by the fact that this phase is enriched in MnO compared to magmatic ilmenites. The very iron-rich orthopyroxene, ferrohypersthene, was found to have crystallized, during cooling of the sheet from the intercumulus liquid. Olivine in the dolerite re-equilibrated with the intercumulus liquid, becoming more iron-rich in composition.

1. INTRODUCTION.

The New Amalfi Sheet is a tholeiitic intrusion which forms part of the Karoo Igneous Province. It is intruded into the Beaufort Group sediments which belong to the Karoo Supergroup. From Figure 1.1a it can be seen that the New Amalfi Sheet is situated between Matatiele and Swartberg, in East Griqualand and, from Figure 1.1b, that it therefore falls within the limits of the Central area of the Karoo Igneous Province, as defined by Marsh and Eales (1984).

1.1 AIMS AND OBJECTIVES.

The first aim of this project is to provide a detailed account of the field relations, petrography, whole-rock geochemistry and mineral chemistry of the New Amalfi Sheet, and thereby produce a model for its formation. This will add to the model for the low-pressure fractionation of Karoo Central area tholeiitic magma, already presented by Eales (1990) for the Birds River Intrusion, and extend the presently small data base of mineral compositions for Karoo rocks. This study also has relevance to the study of the differentiation of tholeiitic intrusions in general, as the New Amalfi Sheet has many similarities with some better known differentiated tholeiitic intrusions in other parts of the world, namely the Red Hill Dike (McDougall, 1962), the Palisades Sill in New Jersey (Walker, 1969 and Walker et al., 1973), the Dufek Intrusion (Ford, 1970 and Himmelberg and Ford, 1976) and the Skaergaard Intrusion (Wager and Brown, 1968).

The second aim of this project is to study the origin of the granophyric rocks associated with the mafic rocks belonging to the New Amalfi Sheet. A Rb-Sr isotope study of the New Amalfi Sheet has been undertaken to attempt to solve this problem and to use the isotopic data to extract an isochron age for the New Amalfi Sheet. This has already been attempted for the Birds River Intrusion (Allsopp et al, 1984); however, because of problems arising from the possibility of contamination from sedimentary xenoliths and the susceptibility to alteration of glassy ferrotholeiites, no clearly defined isochron could be obtained.

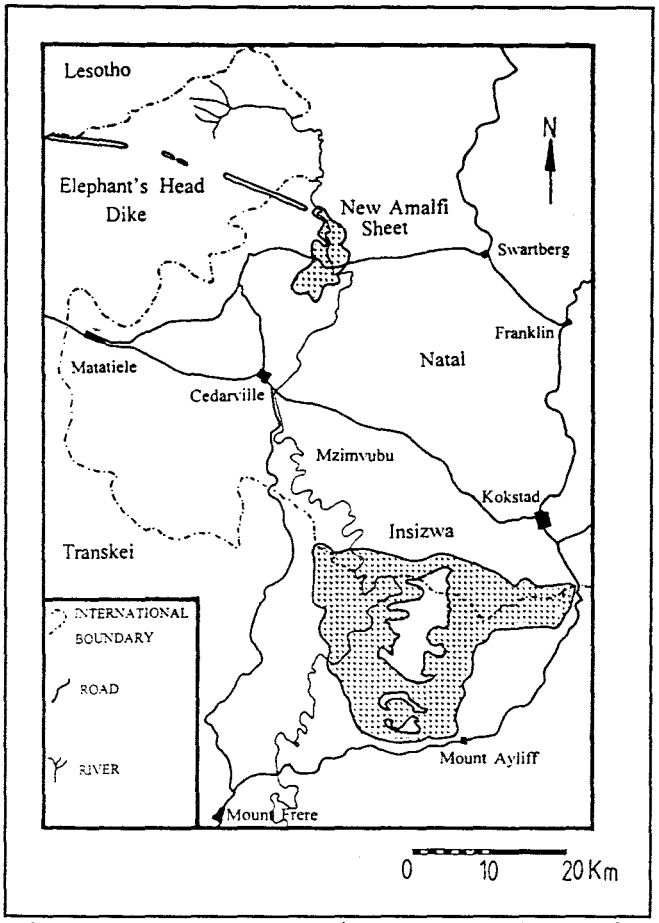

Figure 1.1 Locality map for the New Amalfi Sheet

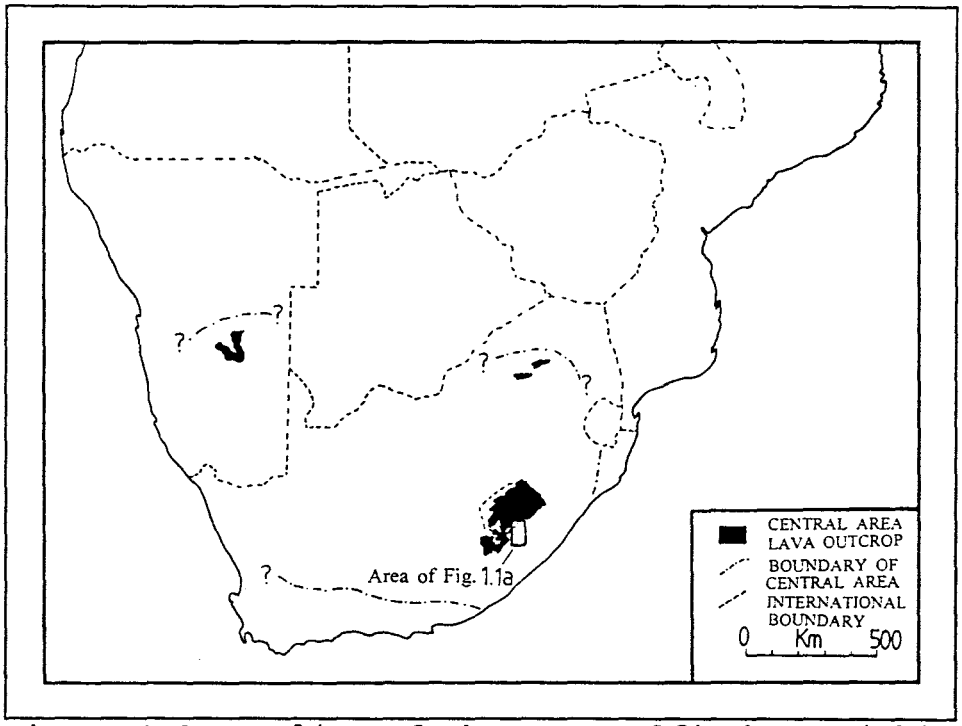

Figure 1.2 Locality of the New Amalfi Sheet within the confines of the Karoo Central area

1.2 DEFINITION OF TERMS.

In this thesis the term *'metasomatism'* is used extensively when discussing the possible origins of the New Amalfi Sheet granophyres. It is therefore important that the exact meaning that has been applied to this term in the text be established at the outset.

Lindgren (1928) defines metasomatism as "The process of practically simultaneous capillary solution and deposition by which a new mineral of partly or wholly differing chemical composition may grow in the body of an old mineral or mineral aggregate." Because metasomatism results in the growth of new mineral species, it is often confused with metamorphism. Best (1982) sees metasomatism as a 'type of metamorphism'. Korzhinsky (1970) states that "If the chemical composition of a rock is altered when its minerals are replaced by others, the processes involved are said to be metasomatic". This, therefore, is the fundamental distinction between metasomatism and metamorphism. Metasomatism always results in a change in the bulk chemical composition of the rock, whereas this is not necessarily the case during metamorphism.

It is also important to understand the process whereby metasomatism may act on a rock. Korzhinsky (1970) states that "Replacement is usually accomplished by pore solutions dissolving some minerals and immediately depositing others, so that the rock as a whole preserves its solid state in the course of replacement." With specific reference to the metasomatism of Karoo sediments by magmatic emanations, Walker and Poldervaart (1941) state that "The magmatic addition was relatively slight and magnesia and iron oxide are among the most readily diffusible constituents." Walker and Poldervaart (op cit.) state that these two elements combined with silica in the sediment to form the conspicuous prisms of pyroxene which characterize the coarser granophyres.

The term *'hydrothermal alteration'* is also used in the text and this term too may be confused with metasomatism. Hydrothermal

alteration can be defined as any mineralogic change in a rock brought about by the action of hydrothermal solutions. It is considered to be a much milder and more localized process than metasomatism in that it does not involve the complete replacement of the rock, or major changes in the bulk chemical composition of the rock.

In this thesis the terms '*cumulus*' and '*primary*', when used to describe a certain mineral or phase, are used as synonyms and are meant to describe the fact that the particular mineral precipitated directly from the cooling magma as a liquidus phase. The terms '*intercumulus*' and '*late-stage*' are also used as synonyms and imply the opposite in that the particular mineral or phase did not precipitate directly from the cooling magma but crystallized later from a trapped intercumulus liquid after the magma had essentially formed a rigid framework (i.e. after it had reached 60% crystallinity).

The term '*secondary*' when applied to a mineral or phase is meant to convey the fact that the particular mineral formed as a replacement of an earlier formed mineral, normally under the action of hydrothermal alteration.

1.3 GENERAL GEOLOGICAL SETTING.

1.3.1 The Karoo Igneous Province.

The Karoo Igneous Province is a tholeiitic Continental Flood Basalt (CFB) province of vast extent and is considered to be related to the break-up of Gondwanaland (Eales et. al., 1984). The sparsely scattered eroded remnants of extensive basaltic volcanism stretch from the south eastern Cape Province and Lesotho to southern Zambia and to the northern coasts of Namibia and Mozambique, a total outcrop area of 140 000 km^2 (Eales et. al., 1984). A much greater area is underlain by a vast network of sub-volcanic intrusive dykes, sills and ring complexes, which stretch from Angola, Zambia, Malawi and Mozambique in the north, down to a latitude of 33° in the south. Similar intrusive and extrusive rocks, also thought to be related to the break-up of

Gondwanaland, are found in Antarctica and Tasmania, as well as the Paraná basin of South America.

1.3.2 The Central area of the Karoo Igneous Province.

The Karoo Igneous Province has been subdivided into a number of different regions. The largest of these is the intracratonic Central area. Marsh and Eales (1984) identified eleven different magma types in the Central area. These eleven magma types, together with averaged compositional data, are listed in Table 1.1. Of these eleven, only three are not of basaltic composition, but have andesitic or dacitic affinities. These latter three magma types are insignificant in terms of volume compared to the enormous volumes of lavas and intrusives of basaltic composition in the Karoo Central area. Indeed, compared to the enormous volumes of the Lesotho magma type, which makes up most of the Lesotho Drakensberg and to which most of the Central area intrusives belong, all of the other ten magma types are insignificant in terms of volume. These other magma types are nevertheless important as they are found at the base of the lava pile and therefore provide insight into the initial stages of volcanicity in the Central area.

Walker and Poldervaart (1949) identified a number of dolerite types in the Karoo on a basis of petrography. Robey (1976) showed that there was no correlation between the dolerite types of Walker and Poldervaart (op cit.) and the magma types of Marsh and Eales (1984), except in the case of the Hangnest type which has an unusual abundance of orthopyroxene for Karoo rocks, and forms a discrete magma type. In terms of geochemistry, the magma types can be arranged in a sequence of increasing SiO_2 and minor decrease in MgO (Marsh & Eales, 1984). The Lesotho and Omega types exhibit the lowest SiO_2 and the highest MgO. SiO_2 increases through the Moshesh's Ford, Vaalkop, Pronksberg High-K, Hangnest and Kraai River types, accompanied by a moderate decrease in MgO. Therefore, the Lesotho type can be thought of as the most primitive of all the magma types of the Central area. The differences between different basaltic magma types are thought to be due to chemical heterogeneities in the mantle source-rock,

and the three acid magma types are thought to be the product of partial melting of crustal material (Marsh & Eales, 1984).

1.3.3 The Intrusive rocks of the Karoo Central area.

The Central area intrusives belong predominantly to the Lesotho magma type, but they show a much wider range in composition than

Table 1.1 Magma Types for the Central area with some average compositions (from Marsh and Eales, 1984).

Basaltic Magma Type	SiO_2	MgO	Zr ppm	Intermediate Magma Type	SiO_2	MgO	Zr ppm
Lesotho	51.5	7.0	94	Belmore Andesite	63.2	3.2	203
Omega	50.9	7.1	80	Pronksberg Dacite	65.4	2.4	203
Moshesh's Ford	52.5	5.9	146	Roedehoek Dacite	66.4	2.5	227
Vaalkop	52.9	6.4	117				
Pronksberg High-K	53.7	6.5	139				
Hangnest	53.9	6.5	150				
Kraai River	54.2	6.6	118				
Springbok Flats	51.1	6.3	117				

the extrusive rocks. This is due to the effects of *in situ* low-pressure differentiation (Marsh & Eales, 1984). Eales et al. (1984) state that differentiation is most commonly achieved by gravity settling or flow-concentration of phenocrysts. Normally, differentiation effects are subtle but in some cases they have led to the formation of cumulus picrites at Elephants Head (Eales, 1979a and 1979b), Ingeli (Maske, 1966) and at Insizwa (Scholtz, 1936 and Bruynzeel, 1957). At Birds River, highly fractionated liquids which exhibit up to seven-fold enrichment in some incompatible elements have been emplaced along ring

fractures and cooled quickly to form what have been termed glassy ferrotholeiites by Eales and Booth (1974).

The iron-enrichment trend, followed by combined silica, sodium and potassium enrichment in the late stages of differentiation of Karoo magma, has been noted by many workers including Poldervaart (1944) on the New Amalfi Sheet, Walker and Poldervaart (1949) for Karoo rocks in general, and Eales and Booth (1974) for the Birds River Intrusion. Walker and Poldervaart (1949) state that differentiation is achieved by gravity settling of olivine, pyroxene and plagioclase as well as the upward migration of acid residues. However, Eales (1990) in a recent paper on the Birds River Intrusion, states that the decoupling of cryptic variation in plagioclase and ferromagnesian phases is an indication that plagioclase primocrysts do not separate from the melt as effectively as the ferromagnesian phases.

Marsh and Eales (1984) state that the paragenesis of the intrusive rocks of the Central area is fairly consistent. Chromite nucleates first, and is followed by olivine which is in turn followed by plagioclase. Orthopyroxene is not common, except in the case of the Hangnest magma type, and it is preceded by plagioclase when it is present. The cotectic crystallization of calcium-rich clinopyroxene and pigeonite follows next. Late-stage phases which may be present are micropegmatite, biotite, apatite, amphibole, magnetite and various deuteric alteration products.

Limited microprobe data indicate a compositional range for olivine in the Karoo from Fo_{85} in Insizwa picrites to Fo_{11} in Birds River ferrotholeiites. Data on pyroxene compositions are even more sparse. The most magnesian clinopyroxene recorded to date comes from Insizwa ($Ca_{42}Mg_{50}Fe_{8}$) and the most iron-rich from Birds River ($Ca_{42}Mg_{6}Fe_{52}$), which is close to that determined optically by Poldervaart (1944) in the New Amalfi Sheet ($Ca_{30}Mg_{19}Fe_{51}$). Poldervaart (1944) also reported the presence of the very iron-rich orthopyroxene, eulite, in the iron-rich dolerites from the New Amalfi Sheet. Despite this report being widely quoted in the literature, the presence of this mineral has

not yet been confirmed with the use of modern analytical techniques.

1.4 PREVIOUS WORK ON THE NEW AMALFI SHEET AND OTHER SIMILAR DIFFERENTIATED THOLEIITIC INTRUSIONS.

In this section, previous work on the New Amalfi Sheet, and other differentiated tholeiitic intrusions which share similarities with the New Amalfi Sheet, is briefly summarized.

1.4.1 The New Amalfi Sheet.

Apart from a preliminary geochemical study of the New Amalfi Sheet by the author (Williams, 1991), no work using modern geochemical techniques has been done on the New Amalfi Sheet to date. Eales and Snowden (1979), Eales and Marsh (1979) and Eales (1979a & b) presented data on cumulus picrites from the adjacent Elephant's Head Dike, which is considered to have acted as a feeder for the New Amalfi Sheet (Poldervaart, 1944). The original study done on the New Amalfi Sheet (Poldervaart, op. cit.), was based on petrography, wet chemical analysis and optically-determined mineral chemistry. Poldervaart (1944) described the intrusion as a sheet that transgresses towards the northwest, having an irregular outcrop pattern, and a number of lateral extensions emanating from the main body.

A band of granophyric rocks occurs along the western margin of the sheet. Poldervaart (op. cit.) stated that the granophyre consists of quartz, micropegmatite, plagioclase and hedenbergite which is partially altered to hastingsite or brown serpentine. A large range in grain sizes was observed within these granophyres, with a marked increase near vertical joints, where a grid-iron pattern of interlocking ferromagnesian mineral laths was seen. Several small, rounded sandstone xenoliths were also noted within these granophyres. These xenoliths commonly consist of a core of yellow sandstone surrounded by one or more transitional zones, which are bounded by sharp contacts. Changes in the concentrations of various oxides, between the cores of these sandstone xenoliths and the surrounding granophyre, were

noted by Poldervaart (op. cit.). Notably, the granophyres showed a gain in Fe_2O_3, MgO, CaO and K_2O compared to the xenoliths. This evidence, combined with the fact that the granophyres occur in a well defined zone with sharp contacts, was seen to indicate that the granophyres were the product of a metasomatic conversion of Beaufort Group sediments, into which the sheet was emplaced.

In addition to the granophyres, a number of other rock types were noted. Picrites are found at the base of the Elephant's Head Dike. Eales (1979a) states that gravitative settling of olivine in the "dike" was responsible for the concentration of olivine within local depressions at the base of the "dike", resulting in the formation of the picrites. The picrites consist of 61 to 22 % olivine (Poldervaart, 1944) of composition Fo_{83} to Fo_{80} with Mg content increasing downwards (Eales & Snowden, 1979). Other phases include plagioclase, ortho- and clinopyroxenes, and minor amounts of biotite, ilmenite, chrome spinel and sulphides. A layered gabbro with alternating light-coloured feldspar-rich layers and dark feldspar-poor layers is found above the picrites (Eales and Snowden, 1979). Within the New Amalfi Sheet itself, Poldervaart (op. cit.) found that olivine dolerites occur in the lower and central portion of the sheet. These dolerites become poorer in olivine towards the middle of the sheet, with the olivine becoming more iron-rich. Plagioclase composition was noted to be fairly constant at An_{66}. Poldervaart noted that the dolerites contain subophitic clinopyroxene, often exhibiting twinning of the 'butterfly type'. Orthopyroxene of composition Of_{20} was noted to often show 'graphic' exsolution of calcium-rich pyroxene. Rare ophitic plates of orthopyroxene of composition Of_{42} were observed.

The olivine dolerites were described as being separated from the granophyres by a narrow zone of iron-rich dolerites. The contact between the olivine dolerites and the iron-rich dolerites was taken at the level where olivine disappears from the mineral assemblage. The iron-rich dolerites were described as changing upwards from quartz dolerites to fayalite-quartz dolerites, and then to fayalite-hedenbergite granophyres. The plagioclase composition was noted to change from An_{60} to An_{31} and the

clinopyroxenes from pale greenish-brown augite at the base of the quartz dolerites, to both a purple and a green hedenbergite in the fayalite-hedenbergite granophyres. The purple colour was considered to be due to the presence of Ti. Orthopyroxene was noted in the iron-rich dolerites and was described as showing a range in composition from Of_{67} to Of_{79} (eulite) with increasing differentiation. Fayalitic olivine was noted to reappear in the fayalite-quartz dolerites (Poldervaart, op. cit.).

Thus, Poldervaart concluded that the olivine-dolerite magma became differentiated as the result of the settling of olivine "followed by pronounced crystal fractionation in the rest-magma". During the middle stages of crystallization, differentiation proceeded towards iron enrichment, which, after reaching a maximum, was superseded by enrichment in soda, potash, alumina and silica. A block of Beaufort Group sandstone was invaded by magmatic emanations from the top of the sheet, thereby converting it into metasomatic granophyre.

1.4.2 The Birds River Intrusion.

The Birds River Intrusion and the New Amalfi Sheet have both undergone a high degree of fractionation of Central area tholeiitic magma. Eales and Booth (1974) and Eales and Robey (1976) presented petrographic and geochemical data on the differentiated mafic suite at Birds River, while Kenyon (1976) studied the metamorphic effects of the dolerite magma on the pyroclastic and sedimentary rocks which form two large, sheet-like xenoliths. Eales (1990) used data from Birds River to present a detailed model for the fractionation of Karoo Central area magma.

At Birds River, highly differentiated ferrotholeiites were emplaced first, as the result of cauldron subsidence of a plug of Stormberg Group Sediments which caused this differentiated magma to be forced upwards along arcuate fractures and emplaced at higher levels. A later injection of less fractionated magma gave rise to a large body of olivine gabbro, which now forms the bulk of the intrusion and completely surrounds the

ferrotholeiite. This gabbro fractionated *in situ* to form ferrogabbros which are now seen to form a rim along the outer contact with the ferrotholeiites. The intrusion has a shape that can be likened to that of a bell-jar, but breaks out as a sheet in the east (Eales and Booth, 1974).

The ferrotholeiites contain up to 66.5% silica and have a porphyritic texture with a glassy to variolitic groundmass. The groundmass contains phenocrysts of pyroxene, olivine, plagioclase and iron oxides. Eales and Booth (1974) state that the composition of the ferrotholeiites is very similar to that of the iron-rich dolerites at New Amalfi, described by Poldervaart (1944). The variation in the major-element chemistry of the gabbro-ferrotholeiite series shows a moderate iron-enrichment trend followed by strong silica enrichment. Eales and Booth (op. cit.) noted tolerably continuous trends in oxide concentrations if data from Birds River and New Amalfi were plotted together on the same diagram.

Reaction between the sedimentary xenoliths and the olivine gabbro magma by means of a combined process of metamorphism and metasomatism has produced rocks of varying metamorphic grade, culminating in a rock that has been almost totally recrystallized to form a homogeneous metasomatic granophyre (Kenyon, 1976). Kenyon rejected the idea that the granophyres may be differentiates of the gabbros, on four main criteria:

- There was found to be a definite gradation in the field from pyroclastic rocks to granophyre.
- The granophyres contain plagioclase that is more calcic than in the adjacent dolerites.
- The presence of tridymite, garnet, mullite and sillimanite in the granophyres points to a high-temperature metamorphic derivative of aluminous sediments.
- The contaminated dolerites and granophyres do not plot along the gabbro-ferrogabbro fractionation trend for the Birds River Intrusion.

These four main points can be used as useful criteria for

distinguishing truly metasomatic granophyres from granophyres that may be the result of igneous differentiation.

The model of Eales (1990) showed that the most differentiated ferrotholeiite represented a residuum 16% of the original liquid (i.e. 84% fractional crystallization). A least squares mixing program was used to model the fractional crystallization path up to 70% crystallization. From this it was shown that magnesian augite was initially the dominant fractionating phase, but that plagioclase became dominant in the later stages. At no stage was olivine a significant fractionating phase. Magnetite began to fractionate in significant amount (5%) only after 50% fractional crystallization.

1.4.3 The Red Hill Dike, Tasmania.

The Red Hill Dike forms part of the Jurassic Tasmanian tholeiitic dolerite suite. The dike is one mile wide and extends 1000 ft (300m) upwards from a flat-lying sheet at its base. Quartz dolerite, which makes up the bulk of the dike, grades upwards into a fayalite granophyre which in turn grades into a silicic granophyre (McDougall, 1962). This complete gradation from dolerite to granophyre is seen by McDougall to indicate that the granophyres are magmatic differentiates of the dolerites. He states that in most granophyres two varieties of the iron-rich pyroxene, ferrohedenbergite, are commonly intergrown. One is pale purple in colour, and the other pale green, and the similarity between this and the New Amalfi Sheet was noted by McDougall (op. cit.). He also noted that the Red Hill granophyre and the fayalite-hedenbergite granophyre from the New Amalfi Sheet, analyzed by Poldervaart (1944), are chemically very similar.

1.4.4 The Palisades Sill, New Jersey.

The Palisades Sill is a highly differentiated tholeiitic intrusion, with rock-types ranging from bronzite dolerite through to fayalite granophyre, and back into dolerite at the top (Walker et al., 1973). The Palisades Sill is perhaps best known for its olivine-rich layer, which has been seen by many

researchers as evidence for differentiation being achieved by gravity-induced settling of this phase from the magma. Husch (1990) argues against this and considers the olivine-rich layer to have originated from a separate intrusion of an olivine-normative magma that underwent olivine accumulation prior to its emplacement into the composite Palisades Sill. Husch (op. cit.) states that differentiation of the Palisades sill was achieved by the dominant fractionation of calcium-poor and calcium-rich pyroxene, and that olivine was not a significant fractionating phase.

A significant similarity between the Palisades Sill and the New Amalfi Sheet lies in the late-stage pyroxene chemistry. As has been described already for the New Amalfi Sheet and the Red Hill Dike, two coexisting clinopyroxenes are present in the Palisades Sill. Walker et al. (1973) described a mauve-brown and a pale-green ferroaugite, characterizing the middle-to-late stages of differentiation. Walker et al. (op. cit.) considered the pale-green ferroaugite to be the result of alteration of the mauve-brown ferroaugite. Numerous inclusions of hornblende, biotite and opaque ore in the pale-green ferroaugite were described as being the by-products of this alteration. The pale-green ferroaugite was noted to be richer in CaO and to contain less MgO and TiO_2 than the mauve-brown ferroaugite, thereby causing the pale-green ferroaugite to plot closer to the diopside-hedenbergite join in the pyroxene quadrilateral. The lower concentration of TiO_2 in the pale-green ferroaugite was seen to indicate that the pale-green ferroaugite was a later- crystallizing phase than the mauve-brown ferroaugite.

The very iron-rich orthopyroxene, ferrohypersthene, was also noted by Walker et al. (op cit.) to be present in the late-stage differentiates of the Palisades Sill. Ferrohypersthene was seen to occur initially as the result of the subsolidus inversion of ferropigeonite, but with continuing differentiation ferropigeonite disappeared from the assemblage, leaving only primary ferrohypersthene. With increasing differentiation, ferrohypersthene also disappeared from the assemblage, leaving the mauve-brown and the pale-green clinopyroxenes as the only

pyroxene phases present. Iron-rich olivine was noted to reappear prior to the disappearance of ferrohypersthene (Walker et al., 1973).

1.4.5 The Dufek Intrusion, Antarctica.

The Dufek Intrusion is 8 - 9 km thick, forming a layered mafic intrusion in the Pensacola Mountains of Antarctica. There are two exposed sections, each approximately 2 km thick. One is near the base, and the other close to the roof (Ford, 1970). The bulk of the intrusion is made up of layered gabbro, and the top-most exposed section is capped by granophyre. Smooth chemical trends through the layered mafic series into the granophyres point to a close genetic tie between the granophyres and the layered series (Ford, 1970).

Once again, apart from the presence of granophyres, the importance of this intrusion lies in the similarity of its pyroxene chemistry to that of the New Amalfi Sheet. Apart from the normal cumulus Ca-poor and Ca-rich pyroxene series, which are similar to those of the Bushveld Complex and the Skaergaard Intrusion, two other pyroxene series were noted by Himmelberg and Ford (1976) in the gabbros and granophyres of the uppermost exposed section. They are a pale-green augite-ferroaugite series and a hypersthene-ferrohypersthene series. The pale-green augites occur as patches within host brown augites belonging to the main Ca-rich series, with both being in optical continuity. The pale-green augites also contain inclusions of hornblende, biotite, iron-titanium oxides and relict brown augite. The pale-green augites are richer in Ca and Si and poorer in Al, Ti and Mn, compared to the brown augites (Himmelberg & Ford, op cit.).

Ferrohypersthene is found in minor amounts and shows no sign of having inverted from pigeonite. Both pale-green augite and ferrohypersthene show no exsolution features (Himmelberg & Ford, op cit.). These authors argued that the pale-green augites and the ferrohypersthene represented a lower-temperature assemblage than the two main pyroxene series, and were therefore of late-stage, post-cumulus origin.

1.4.6 The Skaergaard Intrusion.

The Skaergaard Intrusion is probably one of the most extensively studied mafic intrusive bodies in the world. As such, the general features of this intrusion, as outlined in Wager and Brown (1968), need not be repeated here. It is thus possible to move directly to the discussion of certain features of the Skaergaard Intrusion which are of direct relevance to the study of the New Amalfi Sheet, namely, the occurrence and origin of the various types of granophyres at Skaergaard and the late-stage pyroxene chemistry.

The origin of the granophyres associated with the Skaergaard intrusion has been the subject of a considerable amount of debate in the past. Wager and Brown (1968) described various different granophyre types based on their mode of occurrence and their petrography/chemistry. Firstly, the granophyres of the Tinden Sill, which is 30m thick at its thickest part but which tapers laterally, are emplaced within the lower part of the UBG_{α}. They are the most silicic of all the granophyres and consist of 10% albite phenocrysts in a groundmass of quartz and potassium feldspar with small amounts of accessory phases such as chlorite and zircon. Patches of granophyre containing strongly zoned plagioclase, potassium feldspar, ferrohedenbergite and iron-rich olivine are found scattered within the UBG, and were termed melanogranophyres by Wager and Brown (1968). The Sydtoppen transitional granophyres are exposed just below the Tinden Sill. These granophyres were termed 'transitional' by Wager and Brown (op. cit.) because they are of composition intermediate between that of the melanogranophyres and the Tinden Sill granophyres. Lastly, Wager and Brown (op. cit.) described the presence of cross-cutting granophyre veins similar in composition to that of the Tinden Sill, which they termed the Transgressive granophyres.

None of the above-mentioned granophyre occurrences shows any sign of chilled margins, and on this basis Wager and Brown (op. cit.) considered them to be differentiates of the layered series that had segregated due to filter-pressing. However, in the light of the high $^{87}Sr/^{86}Sr$ values determined by Hamilton (1963) for the

Tinden Sill granophyres, Wager and Brown (1968) conceded that these acid granophyres may have originated by the melting of country rock gneisses.

McBirney (1975) put forward the idea that the residual Skaergaard liquids were in fact much richer in iron than had previously been estimated. In the light of new experimental evidence that showed that there is an immiscible relationship between silica-rich and iron-rich liquids, and a density contrast between these two liquids, McBirney postulated that the melanogranophyres could have originated by the gravity separation of an immiscible, silica-rich residual melt.

Leeman and Dasch (1978) have shown that the Sr and Pb isotopic compositions of the melanogranophyres are equivalent to those of the layered series, and that they are therefore probably differentiates of the layered series. All of the other granophyres had much higher $^{87}Sr/^{86}Sr$ ratios, and therefore Leeman and Dasch concluded that crustal material was involved in their formation.

Brown and Vincent (1963) reported the existence of two clinopyroxene series in the Upper Zone of the Skaergaard Intrusion. The first is a brown variety which forms part of the main augite-to-ferrohedenbergite series. The second is a green ferrohedenbergite which was believed to be the product of a sub-solidus inversion of ferriferous ß-Wollastonite which crystallized as a temporary phase. The evidence for this was that some green ferrohedenbergite grains are made up of a mosaic of much smaller, optically discontinuous grains. Nwe and Copely (1975) studied the compositions of these green ferrohedenbergites using an electron microprobe, and discovered that they are richer in SiO_2 and depleted in Al and Ti, relative to the brown ferrohedenbergite.

1.5 SUMMARY.

a) Differentiated tholeiitic intrusions from other parts of the world often bear associated granophyres, which are

normally interpreted as being igneous differentiates. Of the six differentiated intrusions discussed, only the granophyres of the New Amalfi Sheet and Birds River Intrusion have been described by previous workers as being due to metasomatism of country rock.

b) The study of the Skaergaard granophyres has shown the usefulness of radiogenic isotopes in helping to distinguish between granophyres that are igneous differentiates and those that are of crustal origin.

c) Better known tholeiitic intrusions from other parts of the world often have two coexisting clinopyroxenes in the late-stage differentiates. One is often brown in colour and forms part of the main augite-ferrohedenbergite differentiation trend. The other has been described as a pale-green or green ferroaugite/ferrohedenbergite which is often richer in Ca than the brown variety, and therefore plots closer to the diopside-hedenbergite join.

d) Although the late-stage 'green' ferrohedenbergites are common to the six intrusions, the explanations as to their origin differ, namely:
- Alteration of brown clinopyroxene (Walker et al., 1973; Palisades Sill),
- Post-cumulus crystallization from intercumulus liquid (Himmelberg and Ford, 1976; Dufek Intrusion)
- Inversion of β-Wollastonite (Brown & Vincent, 1963; Skaergaard Intrusion)

There may be a common explanation for the origin of these late-stage pyroxenes and it is hoped that the detailed study of their occurrence in the New Amalfi Sheet will give greater insight into their origin

e) Out of the six intrusions described, iron-rich orthopyroxene is only seen in the Palisades Sill, Dufek Intrusion and the New Amalfi Sheet. Poldervaart (1944) offers no explanation for the occurrence in the New Amalfi Sheet, and in the case of the Palisades Sill it is seen by

Walker et al. (1973) to be both a primary crystallizing and a subsolidus phase, thereby extending the two-pyroxene field up to the point where ferrohypersthene ceases to exist as a primary phase. Himmelberg and Ford (1976) proposed that it crystallized from a late-stage intercumulus liquid in the case of the Dufek Intrusion.

2. FIELD WORK.

2.1 INTRODUCTION.

The New Amalfi Sheet is situated in East Griqualand within the foothills of the Drakensberg. The topography of the area is that of rolling grassy hills dissected by a number of rivers, the largest of which is the Umzimvubu river. The Umzimvubu river dissects the New Amalfi Sheet in a general north-south direction and is fairly straight and fast flowing where it cuts through the sheet. It changes to a slower moving, meandering river in the more flat-lying terrain to the south of the sheet.

The New Amalfi Sheet was mapped with the use of aerial photographs and a map was then compiled with the use of the MIPS (Map and Image Processing System) software (Figure 2.1). During the course of the mapping exercise, extensive sampling of various parts of the sheet was carried out and these sample positions are shown in Figure 2.2. A major problem encountered during the course of the mapping and sampling was the lack of sufficient outcrop. Very few actual contacts were ever seen in the field and the map is thus largely interpretive in nature, with most contacts having to be inferred between the available outcrop. Where outcrop was found, largely along river valleys and at the tops of rounded hills, the rock is badly altered in places, and this further hampered sampling.

2.2 FIELD DESCRIPTION OF THE DIFFERENT ROCK TYPES

The New Amalfi Sheet has been subdivided into three mappable units namely:

a) dolerite
b) gabbro
c) granophyre

The dolerite is found at the base and top of the sheet. The dolerite has been further subdivided into a western and eastern dolerite to distinguish between those dolerites sampled to the

Geological Map of the New Amalfi Sheet

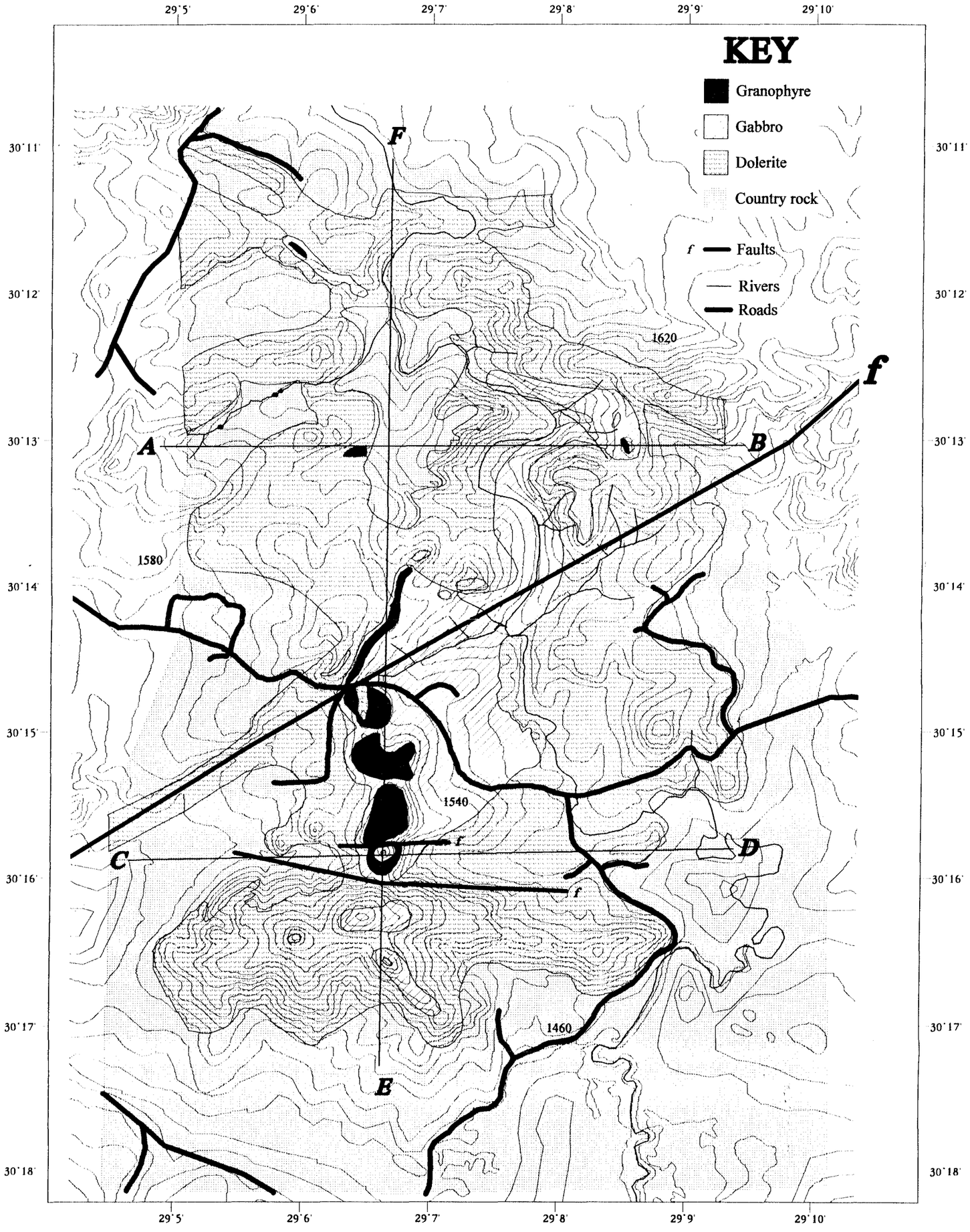

Contour interval: 20 meters

0 1250 2500 3750 5000 meters

Figure 2.1

Geological Map of the central portion of the New Amalfi Sheet showing sample positions

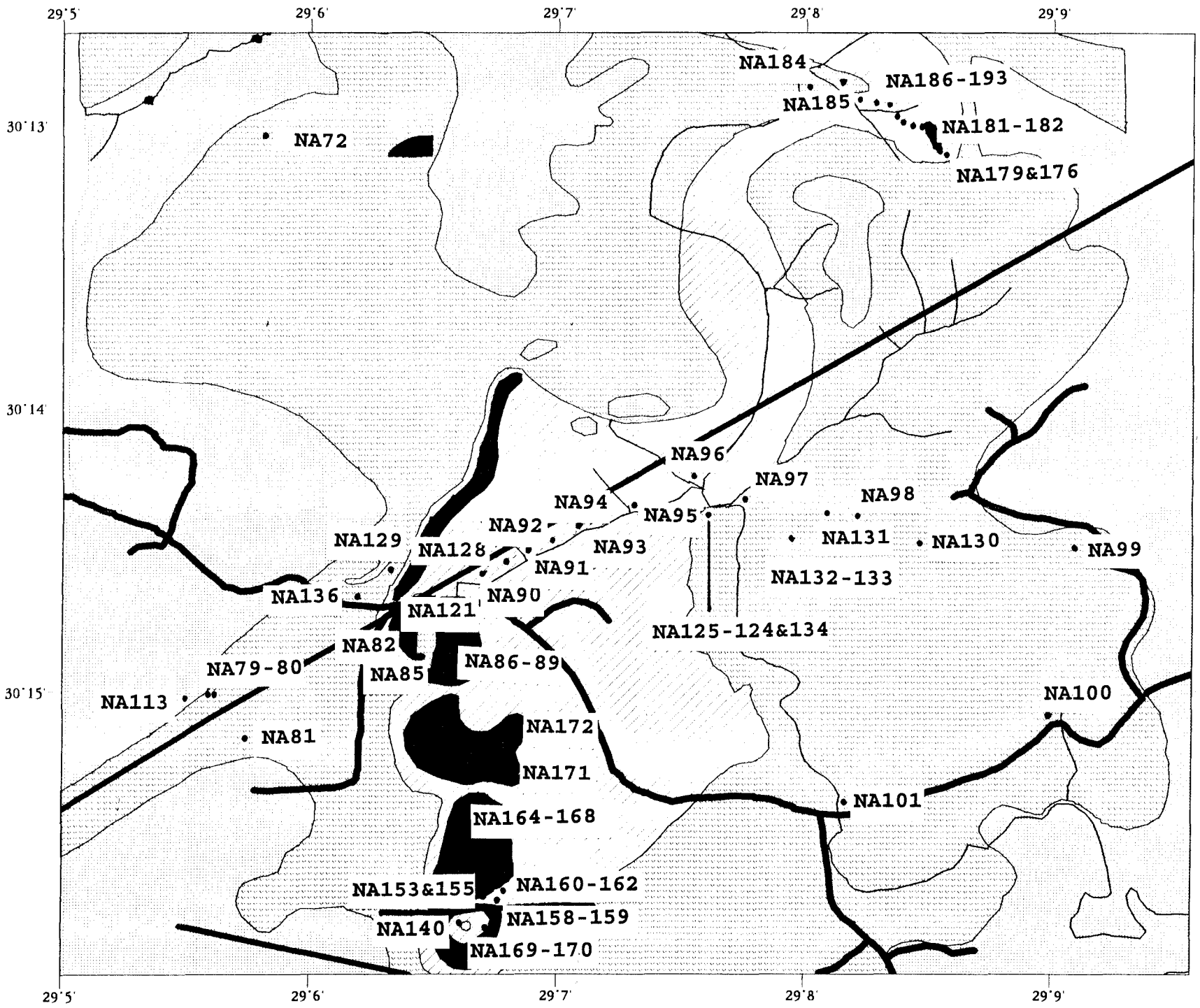

Figure 2.2

west and east of the gabbro-granophyre package, respectively.

2.2.1 Country Rock Sediments.

The New Amalfi Sheet is intruded into sandy-brown, fine to medium grained quartz-wackes which are interbedded with brown and green horizontally laminated mudstones. Poldervaart (1944) identified the country rock sediments as belonging to the Burghersdorp Beds of the Upper Beaufort Group. According to the present day classification these sediments belong to the Burgersdorp Formation of the Tarkastad subgroup, which forms part of the Beaufort Group of the Karoo Supergroup. In a number of places the remnants of the eroded country rock roof to the New Amalfi Sheet can be seen on the top of a number of rounded hills. The sediment has, however, been metamorphosed to a black lydianite that shows columnar jointing in places.

2.2.2 The Granophyres.

Although poorly exposed, there appears to be a gradational contact between the granophyres and the underlying gabbros. This is in contrast to the observations of Poldervaart (1944) who claimed that there was a sharp contact between the granophyres and the gabbros below. In hand specimen the granophyre can be seen to be coarse to very coarse grained, containing long laths of ferrohedenbergite within a matrix of feldspar and quartz. On weathered surfaces the rock has a light rusty-brown colour, whereas the rock has a creamier colour on fresh surfaces.

Near to the top of the granophyre unit, very coarse pegmatoidal ferrohedenbergite needles are seen, some reaching up to 20cm in length. A variety of textures is seen, including parallel alignment, smaller laths branching at 90° from a long central lath and smaller laths branching at an acute angle from a long central lath. A spectacular example of these different textures is shown in Plate 2.1.3 in which the staff is marked in divisions of 10cm. A close-up of the 90° branching pattern is shown in Plate 2.1.4.

PLATE 2.1

2.1.1 A view of the conical hill looking towards the north.

2.1.2 A view looking towards the south of three rounded hills capped by granophyre.

2.1.3 Coarse ferrohedenbergite laths seen in a granophyre boulder.

2.1.4 A close-up of a ferrohedenbergite crystal showing the 90° branching pattern. Scale demarcated in centimetres.

2.1.5 A band of drusy cavities surrounded by aplitic vein material.

2.1.6 A sandstone xenolith enclosed by granophyre.

2.1.7 A 10cm thick zone found at the base of the granophyres which shows parallel alignment of plagioclase laths and the development of thin anorthositic lenses.

2.1.8 Parallel alignment of plagioclase laths within the gabbro.

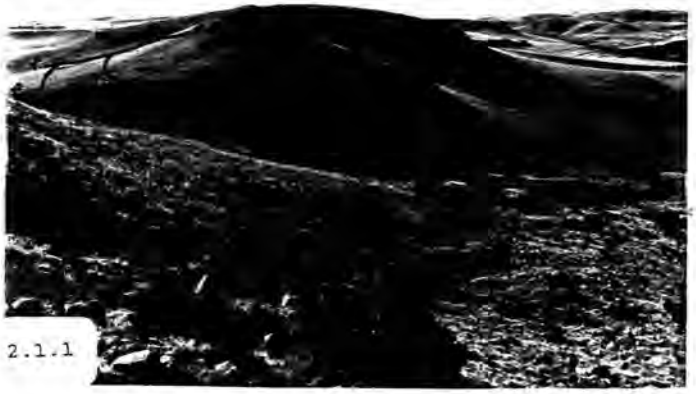

2.1.1

2.1.2

2.1.3

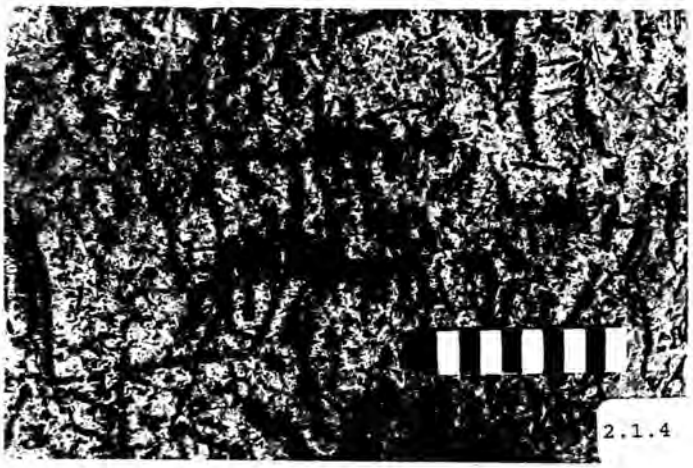

2.1.4

2.1.5

2.1.6

2.1.7

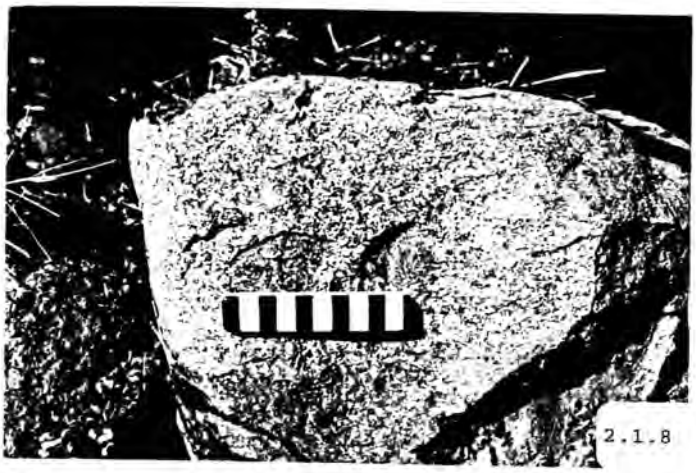

2.1.8

The granophyres often contain aplitic veins which are usually a few centimetres thick but which may reach up to 10cm in thickness. They consist essentially of feldspar and quartz and are notably poorer in ferromagnesian minerals than the surrounding granophyre. Another important feature of the granophyres is the presence of drusy cavities, often filled with euhedral quartz protruding from the edges of the cavities. These cavities can reach up to a few centimetres in diameter and are occasionally arranged in bands of around a metre in length, as is seen on Plate 2.1.5. Plate 2.1.5 also shows that the band of drusy cavities is surrounded by a zone of aplitic material which is lighter in colour than the sandy-coloured surrounding granophyre. These bands of drusy cavities and aplite appear to have been zones along which fluids moved through the granophyres. The granophyres also show an increase in grain size immediately next to joint planes, as was previously noted by Poldervaart (op. cit.). This probably also points to fluid movement along these planes, most probably after the rest of the granophyre was partially consolidated.

A number of small, rounded sandstone xenoliths, around 20cm in diameter, were found within the top 2m of granophyre exposed at the top of a rounded hill on the north-eastern edge of the intrusion (Plate 2.1.6). These sandstone xenoliths exhibit sharp contacts with the surrounding granophyre and this is in contrast to the findings of Poldervaart (1944) who described the country rock xenoliths as being separated from the surrounding granophyre by a number of concentric transitional zones. Poldervaart (op. cit.) considered these zones to be strong evidence for the metasomatic origin of the New Amalfi Sheet granophyres. One xenolith of more pelitic material was found to be surrounded by a leucocratic or aplitic halo, which is in turn surrounded by a zone of granophyre with a higher density of ferrohedenbergite laths than normal. These two zones surrounding the xenolith may be similar to the metasomatic transitional zones, described by Poldervaart (op. cit.). However these zones may merely represent progressive stages of reaction between the xenolith and the melt. The pelitic xenolith would have been reactive towards the granophyre magma because of its composition,

which is further removed from the composition of the granophyres than is the case with the sandstone xenoliths. This may also explain why no reaction took place between the sandstone xenoliths and the granophyre.

Plate 2.1.7 shows a 10 cm zone found near the base of the same granophyres that contain the xenoliths. Within this zone feldspar laths clearly show parallel alignment and in places form thin anorthositic lenses. Cox et al. (1979) state that the parallel alignment of mineral grains is evidence of the effects of magmatic movement on the orientation of grains. This magmatic movement is likely to be due to convective overturn, within the magma chamber. The parallel alignment of mineral grains could also be the result of compaction (H.V. Eales, pers. comm.).

2.2.3 The Gabbros.

The gabbros are coarse grained and contain easily identifiable equant laths of plagioclase and pyroxene. Small amounts of iron oxide and sulphides may be seen with the aid of a hand lens. Fresh surfaces have a mottled grey colour, whilst weathered surfaces have a rusty reddish-brown colour attesting to the richness in iron of these rocks. Weathered samples are very friable and are easily broken by hand. Parallel alignment of plagioclase laths, similar to that seen near to the base of the granophyres, is also seen in places within the gabbros, as shown in Plate 3.1.8.

2.2.4 The Dolerites.

The dolerites are medium grained and fresh surfaces have a bluish grey colour. Weathered surfaces are reddish brown in colour. Plagioclase and pyroxene can be seen in hand specimen with olivine occasionally discernible. Fine-grained glomeroporphyritic dolerite was found exposed in places near to the margins of the intrusion although the actual contact was seen on only one occasion. A fine-grained glomeroporhyritic dolerite also intrudes the granophyres in a number of places, but this represents a slightly later intrusive event.

2.3 GENERAL FORM OF THE INTRUSION.

From the outcrop pattern of the New Amalfi Sheet shown in Figure 2.1, it can be seen that the granophyres are surrounded by gabbro. The gabbro-granophyre package is in turn surrounded by dolerite and narrows towards the top of the New Amalfi Sheet. The Elephant's Head Dike joins the New Amalfi Sheet at its northern end. Poldervaart (1944) considered the Elephant's Head Dike to have acted as the feeder to the New Amalfi Sheet. Two peripheral sheets, each of around 80m thick, dipping at 5° to the north-west and north-east respectively, join the New Amalfi Sheet on its western and north-eastern sides. The lower contacts of these sheets steepen sharply where they merge with the edge of the New Amalfi Sheet. The steep lower contact of the western peripheral sheet, where it joins the New Amalfi Sheet, is exposed in a small quarry and was found to have a dip and dip direction of 048°/65°. Most of the dolerite shown to be exposed on the north-western side of the New Amalfi Sheet appears to belong to this shallow-dipping western peripheral sheet.

On the eastern side of the New Amalfi Sheet, the contact between the sheet and country rock, although not exposed and thus inferred, generally follows the topographic contours. This suggests that in this area the contact has a fairly shallow dip. The dip of the country rock sediments was measured in a quarry next to the eastern margin of the New Amalfi Sheet and was found to be 5° towards the west. It is assumed that the contact between the New Amalfi Sheet and the country rock in this area has the same orientation. The shallow dip of this contact indicates that it probably represents the bottom contact of the New Amalfi Sheet, and not the steeply dipping side contact.

The dip of the inferred contact between the New Amalfi Sheet and the country rock suddenly cuts sharply up through a number of contours in a valley on the north-eastern side of the New Amalfi Sheet, where it is joined by the eastern peripheral sheet. This suggests a sudden increase in the dip of the contact between the New Amalfi Sheet and the country rock. The steep dip of this contact probably indicates that it now represents the steeply

dipping edge of the New Amalfi Sheet, similar to that seen on the western side of the New Amalfi Sheet where it is joined by the western peripheral sheet.

In this same area a remnant of granophyre is exposed at the top of a rounded hill. A zone 10 cm thick in which feldspar laths show parallel alignment, forming thin anorthositic lenses in places, is found within the lowest granophyres (Plate 2.1.7). This thin zone dips at 5° towards the west and probably reflects the orientation of the granophyre in this area.

Vertical displacement of the granophyres was noted in the field by the juxtaposition of the granophyre with underlying units, in certain areas. This displacement has been attributed to the existence of four faults, two of which cut the New Amalfi Sheet in a north-south direction and two in a south west-north east direction. A small graben is found between each of these sets of faults. Although no actual faulted contacts were ever seen in the field, the orientation of the faults corresponds to that of lineaments seen on the aerial photograph of the area. Three cross-sections of the New Amalfi Sheet are shown in Figure 2.3a.

Within the southern-most graben, the top of the granophyres is exposed and can be seen to pass vertically back into gabbro. This graben is now seen as a conical hill bounded by two faults passing through saddles on its northern and southern sides. A view of this conical hill looking towards the north, is shown in Plate 2.1.1. In this plate, granophyres are exposed from the bottom of the conical hill to just above the change in slope half-way up the hill. Gabbro is present from this point to just below the top of the hill. The gabbro is capped by a thin veneer of dolerite, which probably represents a chilled margin, and hornfelsed sediment is found at the very top of the hill. The granophyres therefore appear to represent a 'sandwich horizon' similar to that documented for the Skaergaard intrusion by Wager and Brown (1968).

Granophyres are exposed at the top of the next hill behind the conical hill and thus the minimum displacement along the northern

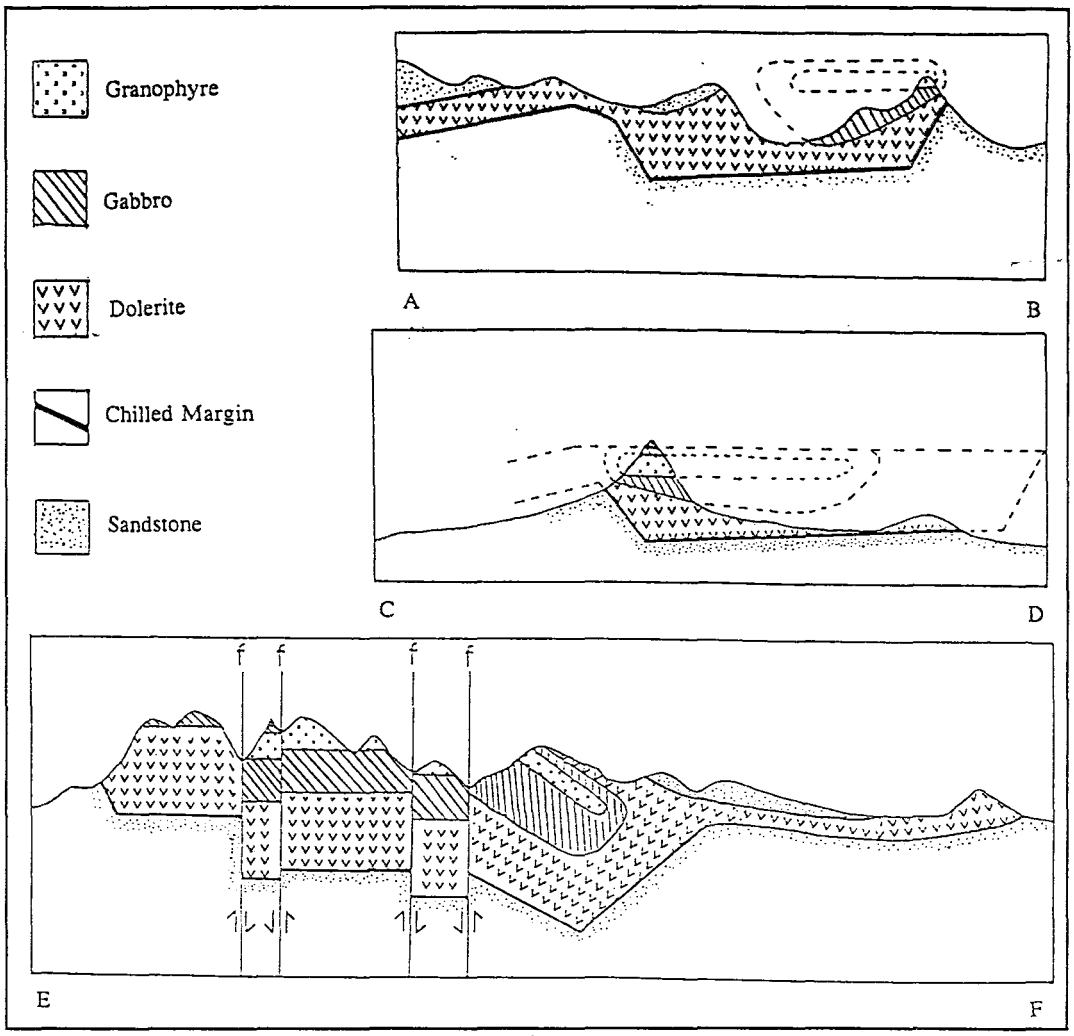

Figure 2.3 (a) Cross-sections across the New Amalfi Sheet. Scale 1 : 17000.

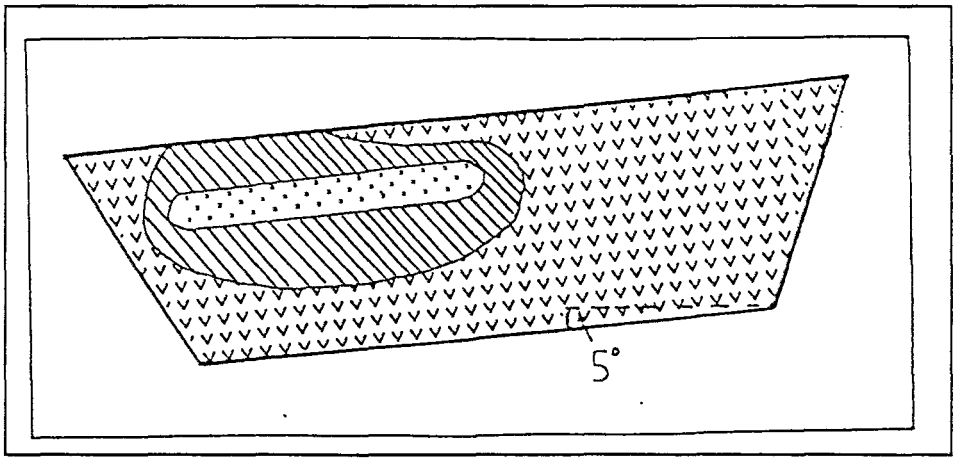

Figure 2.3 (b) Conceptual model for the structure of the New Amalfi Sheet.

graben fault is from the top of the granophyres on the conical hill to the top of the hill behind it, a vertical distance of 34m as measured from cross-section E-F in Figure 2.3a. Along the southern graben fault the displacement is much greater as dolerite, seen in the foreground of Plate 2.1.2, outcrops at the same level as the granophyre. The minimum displacement along this fault is 170m as measured from cross-section E-F in Figure 2.3a.

Plate 2.1.2 shows a view (looking towards the south) of three rounded hills capped by granophyre. It can be seen from Plate 2.1.2 that the granophyres outcropping in the hill in the foreground are downthrown relative to those outcropping in the hill behind it. The hill in the foreground in Plate 2.1.2 therefore represents the second small graben, with the two faults which bound it, found in the two saddles either side of the hill. The displacement along the southern graben fault was measured from cross-section E-F and found to be 51m. Displacement was combined with rotation along the northern graben fault, with the dip of the granophyres to the north of this fault greater than that on the south side of the fault. This can be seen from the map of the New Amalfi Sheet (Figure 2.1) by the sudden decrease in the outcrop width of the granophyres to the north of the northern-most fault.

The three generalized cross-sections in Figure 2.3a are based on a conceptual model of the basic structure of the New Amalfi Sheet shown in Figure 2.3b. This conceptual model is based on the limited structural information on the New Amalfi Sheet gained from the field, namely that:

- The sheet appears to have steeply dipping sides that transgress laterally into two more flatly dipping peripheral sheets.
- The base of the intrusion appears to be concordant with the surrounding country rock, and dips at 5° towards the west.
- The gabbro-granophyre package forms a 'sandwich horizon' within the top half of the intrusion, passing back up into dolerite.

The total vertical interval from the lowest to the highest point within the New Amalfi Sheet, as seen from Figure 2.1, is 250m. However, if allowance is made for the unexposed dolerites in the thickest part of the intrusion, then this vertical thickness becomes 440m.

2.4 SUMMARY.

a) Three main rock types were recognized within the field: dolerite, gabbro and granophyre.

b) Drusy cavities, aplitic veins and an increase in the grain size of the granophyres found immediately next to joint planes within the granophyres, together provide an indication that late stage fluid movement took place through the largely consolidated granophyres.

c) A number of small sedimentary xenoliths were found in one location within the topmost granophyres. These xenoliths have in all but one case sharp contacts with the surrounding granophyre.

d) One xenolith that is surrounded by progressive reaction haloes was probably more reactive towards the granophyre magma because it has a pelitic composition. The other xenoliths have felsic compositions and were therefore probably less reactive, hence the sharp contacts with the surrounding granophyre.

e) The basic form of the intrusion is that of a sheet, with steep sides which transgress laterally into two shallow-dipping peripheral sheets.

f) The granophyres are enclosed above and below by gabbro. The granophyre-gabbro package forms a 'sandwich horizon' within the top half of the main body of the New Amalfi Sheet, and is completely enclosed by dolerite.

g) Faulting subsequent to the emplacement of the sheet has caused the formation of two small grabens.

h) The calculated maximum vertical thickness of the sheet is 440m.

3 PETROGRAPHY.

3.1 INTRODUCTION.

This chapter deals with the petrographic variations that occur within the New Amalfi Sheet with differentiation, and will include both transmitted- and reflected-light studies. The field-based subdivision of the New Amalfi sheet has been expanded on the basis of petrography, as shown in Table 3.1. In the original description of the New Amalfi Sheet by Poldervaart (1944), the sheet was subdivided into the units shown in table 3.1. In the present study the rocks have been named according to the IUGS classification for plutonic rocks (Le Maitre, 1989). In this classification the modal proportions of plagioclase, quartz and potassium feldspar are recalculated to 100% and plotted within a ternary diagram which contains the fields of the various rock types. In this case all quartz and potassium feldspar are present as a granophyric intergrowth and, as the granophyric intergrowth is made up of approximately 50% quartz and 50% potassium feldspar, the modal amounts of quartz and potassium feldspar have each been taken to be half of the modal amount of the granophyric intergrowth.

The names olivine-dolerite and pigeonite-dolerite have been used to describe better the eastern and western dolerites, respectively; these are the same terms used originally by Poldervaart (1944). The quartz dolerite unit has been subdivided into the quartz gabbro and the quartz monzodiorite units, due to the coarse grain size of these rocks, and because the plagioclase composition falls below An_{50} midway through the unit. The term fayalite-quartz dolerite has been changed to granodiorite because these rocks plot within the granodiorite field of the IUGS scheme. The term fayalite-hedenbergite granophyre has been retained to describe those granophyres which contain iron-rich olivine. The granophyres which contain no olivine are simply called granophyres, and the term 'metasomatic granophyre' has been dropped because the alleged metasomatic origin of these rocks is disputed by the author.

Table 3.1) Classification of New Amalfi Sheet rocks.

FIELD CLASS.	PETROGRAPHIC CLASS.	POLDERVAART'S CLASS.	Mg #
granophyre	granophyre	metasomatic granophyre	< 6.5
	fayalite-hedenbergite granophyre	fayalite-hedenbergite granophyre	6.6 - 12.1
gabbro	granodiorite	fayalite dolerite	12.1 - 16
	quartz monzodiorite	quartz dolerite	16.1 - 32.6
	quartz gabbro		32.7 - 49
Western dolerite	pigeonite dolerite	pigeonite dolerite	50 - 62
Eastern dolerite	olivine dolerite	olivine dolerite	50 - 70

3.2 PETROGRAPHIC DESCRIPTION OF THE DIFFERENT ROCK TYPES.

3.2.1 Olivine dolerites.

These dolerites are found to the east of the granophyres and correspond thus to the eastern dolerites of the field-based classification. The general texture of these rocks is ophitic (Plate 3.1.1) with an average grain size of 1mm. Euhedral olivine is abundant (14%) at the base of this unit and this may indicate some degree of gravity-induced settling of this mineral. The olivine is sometimes partially altered to iddingsite or chlorophaeite. Individual olivine grains are 1mm in diameter and contain small inclusions of chromite (Plate 3.1.2) and dendritic exsolution of a spinel phase (Plate 3.1.3), identical to that described by Eales and Snowden (1979) and which was considered by these authors to be due to exsolution. In some cases olivine grains can be seen to enclose small plagioclase laths (Plate 3.1.2). The olivine itself is often partially to totally enclosed by pyroxene grains.

PLATE 3.1

(pl = plane light; xn = crossed nicols; FOV = field of view)

3.1.1 Ophitic texture of olivine dolerites (pl, FOV = 6.25mm).

3.1.2 Olivine grain enclosing plagioclase and chromite in lowest olivine dolerite (xn, FOV = 1.56mm).

3.1.3 Dendritic exsolution of spinel in olivine in lowest olivine dolerite (pl, FOV = 0.39mm).

3.1.4 Inverted pigeonite in olivine dolerite showing graphic exsolution and fine-scale planar exsolution parallel to (100) (xn, FOV = 1.56mm).

3.1.5 Inverted pigeonite herring-bone twin in olivine dolerite showing well developed exsolution of augite parallel to the relict monoclinic (001) plane (xn, FOV = 1.56mm).

3.1.6 Poorly developed fine-scale exsolution of pigeonite in augite parallel to (001) in olivine dolerite. Patch of altered bleached hydrothermal pyroxene with associated hornblende and specks of opaque oxide inclusions on bottom-left side of grain. Note that exsolution is not preserved where hydrothermal alteration has occurred (pl, FOV = 1.56mm).

3.1.7 Glomeroporphyritic texture in contact pigeonite dolerite (xn, FOV = 6.25mm).

3.1.8 Pigeonite core (bolder relict) to augite grain in pigeonite dolerite (xn, FOV = 1.56mm).

3.1.1

3.1.2

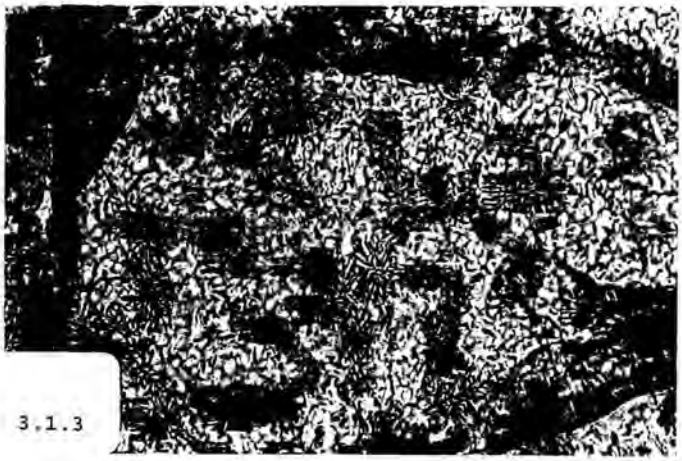

3.1.3

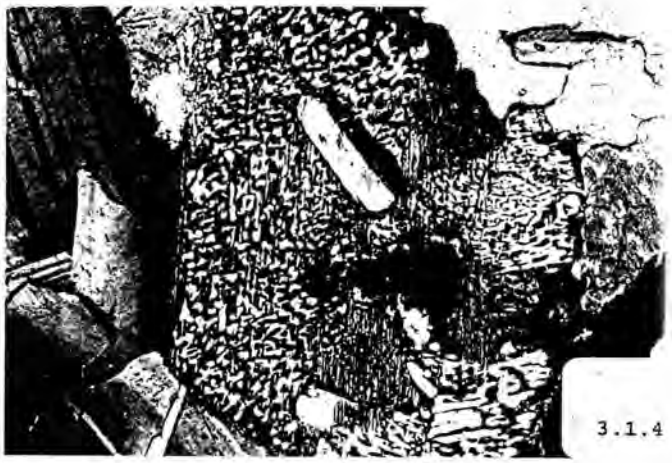

3.1.4

3.1.5

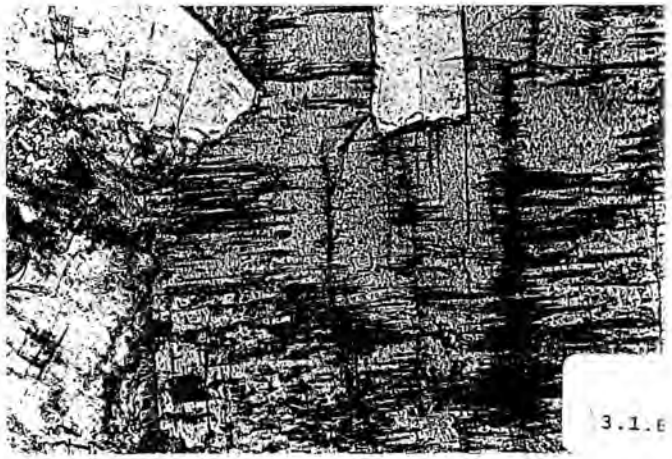

3.1.6

3.1.7

3.1.8

Augite and pigeonite form composite grains that have an average grain size of 1.5 mm, but can reach up to 3 mm and which ophitically enclose smaller plagioclase laths. The pigeonite is often inverted to hypersthene which shows graphic exsolution of augite and in some cases fine-scale exsolution of augite parallel to (100) (Plate 3.1.4). Plagioclase laths have an average grain size of 0.5 mm with larger grains showing compositional zoning. Minor amounts of opaque oxides are present as well as minor amounts of granophyric intergrowth, which is found in the interstices between plagioclase laths.

With increasing height above the base of this unit, the proportion of olivine drops to ca. 1%. The olivine no longer contains inclusions of chromite and plagioclase, or exsolved spinel. The texture of the olivine dolerites changes from ophitic to subophitic as they are now slightly coarser grained than the basal olivine dolerites and have an average grain size of 1.5mm. The graphic exsolution in the inverted pigeonite gives way to the development of more continuous, thick lamellae of augite parallel to the relict monoclinic (001) crystallographic plane, sometimes forming herringbone twins (Plate 3.1.5). Some grains of inverted pigeonite still show the fine-scale exsolution of augite parallel to (100), but as this occurred below the inversion temperature it is not as well developed as the (001) exsolution. In the augite, fine-scale exsolution of pigeonite parallel to (001) is now also seen (Plate 3.1.6).

The bleaching of the normally brown augite to a colourless phase, accompanied by the appearance of inclusions of opaque oxide and hornblende[1], is first seen in the topmost olivine dolerites (Plate 3.1.6). Opaque oxide, granophyric intergrowth and very small amounts of apatite, biotite, chlorite and actinolite appear in the interstices between plagioclase laths.

Chromite was the first mineral to form in the olivine dolerites, as it is found only as inclusions in olivine. The chromite was

---

[1]This bleaching of the normally brown augite is due to hydrothermal alteration and will be discussed at length in the next chapter.

followed by olivine, and some plagioclase may have nucleated at this time as well, judging from its presence as inclusions in olivine. This was followed by the precipitation of the bulk of the plagioclase and then clinopyroxene and pigeonite, giving rise to the ophitic texture. Post-cumulus apatite, biotite, granophyric intergrowth, opaque oxide, chlorite and actinolite were formed late in the paragenesis.

3.2.2 Pigeonite Dolerites.

The pigeonite dolerites are found to the west of the band of granophyre, and thus correspond to the western dolerites of the field-based classification. The difference between these dolerites and the olivine dolerites is that olivine is less abundant and the pigeonite shows none of the well-developed exsolution seen in the olivine dolerites. This indicates that these dolerites cooled faster than the olivine dolerites. This was because the pigeonite dolerites form part of the western peripheral sheet which is much thinner than the New Amalfi Sheet itself.

Fine grained contact dolerite has a glomeroporphyritic texture (Plate 3.1.7) and contains clusters of plagioclase and pyroxene phenocrysts within a groundmass of small plagioclase laths and interstitial pyroxene and opaque oxide. The glomeroporhyritic texture indicates that plagioclase and pyroxene were on the liquidus at the time of intrusion of the pigeonite dolerites. Further away from the contact the dolerites are medium-grained and contain a small amount of altered olivine, almost always enclosed in ophitic plates of augite and pigeonite up to 1mm in diameter. In some cases, pigeonite can be seen to form cores to augite grains (Plate 3.1.8). This may indicate that pigeonite initially preceded augite in the paragenetic sequence. Some ophitic plates of orthopyroxene were also noted, but because of the lack of exsolution, it is unclear whether this represents inverted pigeonite or primary orthopyroxene. Plagioclase laths are on average 0.2mm in diameter. Interstitial opaque oxide completes the mineral assemblage. Further away from the contact, olivine is absent and the grain size continues to increase, so

that ophitic plates of augite and pigeonite are now on average 1.5mm in diameter and plagioclase laths reach 1mm in diameter, often showing compositional zoning. Small amounts of granophyric intergrowth and biotite are now seen in the interstices between plagioclase laths.

Although there are slight differences in petrography between the olivine dolerite and the pigeonite dolerite, they both show the general petrographic characteristics of the Kokstad Dolerite Type, as defined by Walker and Poldervaart (1949). These general characteristics are that they contain an abundance of plagioclase (over 50%), they contain clinopyroxene together with orthopyroxene, or pigeonite, or both, and they contain highly variable amounts of olivine.

3.2.3 Dolerite Pegmatite.

In some places within the pigeonite dolerites, isolated patches of dolerite pegmatite were noted. These dolerite pegmatites or pegmatitic schlieren have previously been described in Karoo rocks, most notably by Walker and Poldervaart (1949) and Eales and Booth (1973). In all cases, they have been described as the result of the crystallization of a late-stage water-rich melt under conditions of reduced temperature and viscosity.

The dolerite pegmatite at New Amalfi is coarse-grained and has a sub-ophitic texture. Large equant plagioclase grains of 1.5mm diameter on average exhibit marked compositional zoning and are sometimes enclosed by abundant granophyric intergrowth. Ophitic plates of augite have an average grain size of 2mm. Augite is often altered to a colourless, bleached hydrothermal clinopyroxene. The augite shows exsolution parallel to (001), with occasional development of herringbone twins. Pigeonite is also present and in some cases is clearly seen to form cores to augite grains.

Orthopyroxene is present and shows either no exsolution or fine-scale exsolution parallel to (100). It is unclear whether this represents primary orthopyroxene or inverted pigeonite. Other

phases include opaque oxide and abundant late-stage phases such as biotite, hornblende and apatite, often found within the granophyric intergrowth.

3.2.4 Quartz Gabbros

On the eastern side of the intrusion, olivine dolerite passes upwards into quartz gabbro. The transition is marked by a number of significant petrographic changes, namely, the disappearance of olivine from the assemblage, an increase in grain size to an average of 2mm, and a change in the general texture of the rock from ophitic to intergranular. Other features of this transition are the decline in the proportion of pigeonite and inverted pigeonite, and the appearance of the iron-rich orthopyroxene, ferrohypersthene.

Plagioclase is the most abundant phase within the quartz gabbros. Individual grains are more equant than in the dolerites and exhibit marked compositional zoning. The proportion of plagioclase declines with height through the quartz gabbros from 57% to 49%, but it still remains the most abundant phase throughout the unit.

The proportion of augite increases in proportion to the decrease in pigeonite and orthopyroxene, and it is seen to form composite grains with pigeonite, inverted pigeonite and ferrohypersthene grains. As the intergranular texture suggests, the pyroxenes are found in the interstices between plagioclase laths, indicating that they crystallized after the plagioclase.

Augite often contains exsolution lamellae of pigeonite parallel to (001) and, as the augite is often twinned, this gives rise to the formation of herringbone twins (Plate 3.2.1). Cores of pigeonite can be seen in some augite grains. The presence of bleached hydrothermal pyroxene is widespread, often affecting more than half of any specific augite grain (Plate 3.2.2). The hydrothermal pyroxene is often not in optical continuity with the rest of the unaltered grain, and this, together with the presence of hornblende and opaque oxide inclusions, imparts a blotchy

PLATE 3.2

3.2.1 Augite herring-bone twin in quartz gabbro showing well developed fine-scale exsolution of pigeonite parallel to (001) (xn, FOV = 1.56mm).

3.2.2 Unaltered brown augite relict in quartz gabbro (middle of grain) showing exsolution of pigeonite parallel to (001) with incipient hydrothermal alteration at the top and bottom of grain now affecting approximately 50% of the grain and obliterating previous exsolution (pl, FOV = 1.56mm).

3.2.3 Parallel alignment of plagioclase and augite grains in quartz gabbro. Note blotchy nature of interference colours in top augite grain (xn, FOV = 6.25mm).

3.2.4 Inverted pigeonite grain (in quartz gabbro) which has inverted to two separate crystals with differently orientated crystallographic axes (one in extinction) because of the sluggish inversion of iron-rich pigeonite (xn, FOV = 1.56mm).

3.2.5 Ferrohypersthene in quartz gabbro showing (001) section (with characteristic blocky cleavage) found in interstices between plagioclase laths, together with quartz and stilpnomelane (xn, FOV = 1.56mm).

3.2.6 Ferrohypersthene in quartz gabbro found together with augite in composite pyroxene grain. Ferrohypersthene in (100) section thus exhibits only one set of cleavage traces (pl, FOV = 6.25mm).

3.2.7 Large lath of cumulus apatite in granodiorite. Note ferrohypersthene at top right and altered fayalite (bottom centre) (pl,FOV = 1.56mm).

3.2.8 Large amounts of granophyric intergrowth in granodiorites, enclosing smaller plagioclase laths. (xn, FOV = 6.25mm).

3.2.1

3.2.2

3.2.3

3.2.4

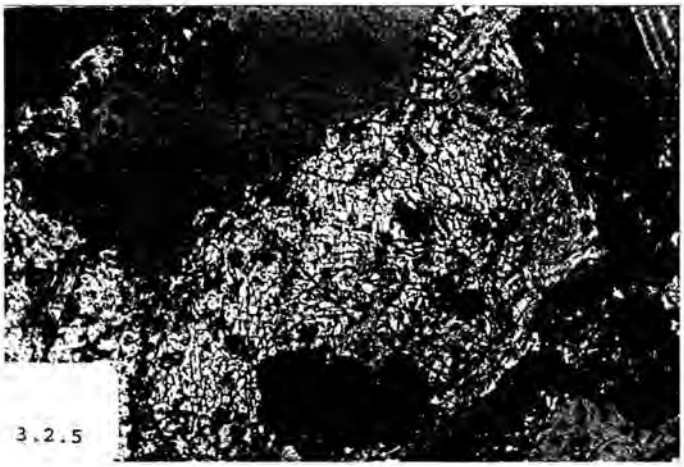

3.2.5

3.2.6

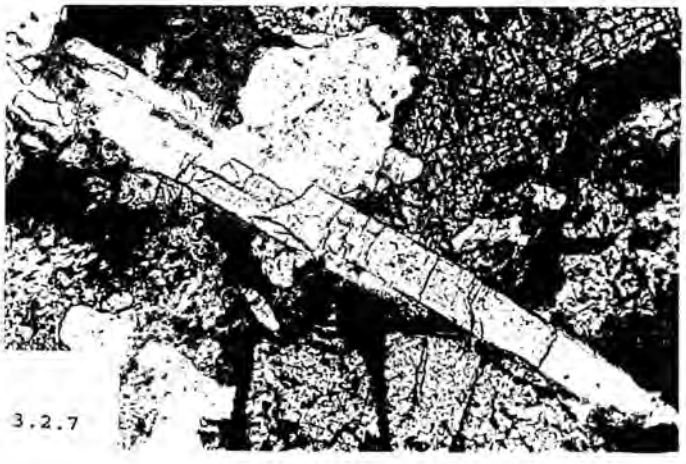

3.2.7

3.2.8

appearance to the pyroxene grain between crossed nicols (Plate 3.2.3). The hydrothermal alteration also has the effect of destroying any exsolution intergrowth that may have been present (Plate 3.2.2).

Pigeonite is often found as grains that have inverted to two or more hypersthene crystals with differently orientated crystallographic axes, due to the sluggish inversion of iron-rich pigeonite. This feature has also been reported for the Skaergaard Intrusion by Wager and Brown (1968). The inverted pigeonite always shows well developed exsolution of augite parallel to (001), sometimes also forming herringbone twins. The ferrohypersthene is commonly seen in sections parallel to (001) where it is characterized by two prominent cleavage planes almost at 90° to each another (Plate 3.2.5). Where grains exhibit sections parallel to (100), only one set of cleavage planes is seen (Plate 3.2.6). Other distinguishing features include a higher relief than the other pyroxenes, and the absence of exsolved phases. The ferrohypersthene first appears as an interstitial phase found in the interstices between plagioclase laths, together with late stage phases such as granophyric intergrowth (Plate 3.2.5). At the top of the quartz gabbros, the ferrohypersthene is seen forming cores to augite grains, or as separate grains.

The proportion of granophyric intergrowth increases from 6% to 10% towards the top of the unit. Other interstitial accessory phases present include apatite, stilpnomelane, opaque oxide, biotite and hornblende. At one specific level within this unit, strong parallel alignment of plagioclase and pyroxene grains imparts an igneous lamination to the rock (Plate 3.2.3).

3.2.5 Quartz Monzodiorites.

As mentioned above, these rocks were originally also termed quartz dolerites by Poldervaart (1944). They have here been termed quartz monzodiorites because they plot within the field of quartz monzodiorites as defined by the IUGS classification, and because the An content of the plagioclase in these rocks is

below 50%.

The rock has an intergranular texture and plagioclase is still the dominant phase in the rock, although the proportion of plagioclase declines with height from 49% to 43%. Ferroaugite is the main pyroxene phase, at around 30%.

The transition from quartz gabbro to quartz monzodiorite is marked by the appearance of opaque oxide as a cumulus phase (8%). The opaque oxide is often intergrown with pyroxene, with a rim of biotite or hornblende separating the two phases. This phenomenon will be discussed in the next section on reflected-light petrography. Granophyric intergrowth is present in proportions increasing from 11% to 19%, while apatite, although still an accessory phase, is often found within the granophyric intergrowth. In the topmost quartz monzodiorites, olivine re-appears as large, euhedral, yellow grains of fayalite which reach up to 2mm in diameter, and this coincides with the disappearance of pigeonite, although small amounts of iron-rich orthopyroxene are still present.

3.2.6 Granodiorites.

These rocks were originally termed fayalite dolerites by Poldervaart (op. cit.) but here they have been termed granodiorites because they plot within the field of granodiorites, according to the IUGS classification. The transition from quartz monzodiorite to granodiorite is marked by the appearance of apatite as a cumulus phase. It is seen as long colourless laths with high relief (Plate 3.2.7), or as numerous inclusions in olivine and ferroaugite grains.

Plagioclase remains the most abundant phase in the rock, despite declining in proportion with height from 43% to 39%. The intergranular texture of the quartz gabbros and quartz monzodiorites begins to give way to a granophyric texture in the granodiorites as increasingly large patches of granophyric intergrowth occasionally completely enclose some smaller plagioclase grains (Plate 3.2.8). Granophyric intergrowth is now

the second-most abundant modal component, increasing in proportion with height from 19% to 38% in the granodiorites.

Ferroaugite declines in proportion from 24% to 12% with stratigraphic height. The disappearance of pigeonite is associated with a textural change in the remaining clinopyroxene, as the ferroaugite is now found as single euhedral grains (on average 2mm in diameter) that are almost completely converted to the bleached hydrothermal clinopyroxene with ubiquitous associated hornblende and opaque oxide (Plate 3.3.1). Exsolution is no longer seen in the clinopyroxene and this is probably because of the effect of the hydrothermal alteration. Small amounts of ferrohypersthene are present in the rock (1%) as euhedral grains displaying a blocky 90° cleavage. Fayalite is also present in the granodiorites and the fact that olivine, orthopyroxene and quartz coexist within the granodiorites (Plate 3.2.7) may indicate that the forbidden zone of Lindsley and Munoz (1969), which is the limit of stability of calcium-poor pyroxene, was reached, (assuming that the orthopyroxene is primary). This will be debated in the next chapter. Opaque oxide declines rapidly in proportion through the granodiorites from the peak of 8% reached at the end of the quartz monzodiorites to around 3% in the topmost granodiorites.

3.2.7 Fayalite-Hedenbergite Granophyres.

The disappearance of ferrohypersthene and an increase in granophyric intergrowth to between 47% and 61% marks the transition from granodiorite to fayalite-hedenbergite granophyre. Granophyric intergrowth is now dominant and, as such, the rock has a generally granophyric texture. Some of the quartz in the granophyric intergrowth has a needle-like habit, which indicates that the quartz once existed as the polymorph, tridymite (Plate 3.3.2) as is also seen at Birds River (Eales and Booth, 1974).

Plagioclase continues to decline in proportion with height from 34% to 9% and is now seen almost exclusively as euhedral grains surrounded by granophyric intergrowth. Pyroxene, although now only constituting between 13% and 8% of the rock, occurs as

PLATE 3.3

3.3.1 Large, single clinopyroxene grain in granodiorite now almost completely altered to bleached hydrothermal clinopyroxene with large amounts of associated hornblende (pl, FOV = 6.25mm).

3.3.2 Granophyric intergrowth in fayalite-hedenbergite granophyre showing needle-like habit of the quartz (xn, FOV = 1.56mm).

3.3.3 Large euhedral fayalite crystal showing partial alteration to iddingsite, and inclusions of apatite in fayalite-hedenbergite granophyre (pl, FOV = 6.25mm).

3.3.4 Drusy cavity in granophyre filled with stilpnomelane and lined with euhedral quartz crystals. Note euhedral zircon grain grown on quartz grain (pl, FOV = 1.56mm).

3.3.5 Composite Ti-magnetite-ilmenite grain in quartz monzodiorite. Note faint exsolution of ilmenite and fine exsolution of ulvöspinel in Ti-magnetite which imparts a bad polish to the Ti-magnetite (ref, FOV = 0.98mm).

3.3.6 Composite sulphide globule (in quartz monzodiorite) containing darker (yellow) chalcopyrite and lighter pyrrhotite (ref, FOV = 0.98mm).

3.3.7 Ti-magnetite (in granodiorite) now with well developed exsolution of ilmenite parallel to (111) and better polish indicating absence of ulvöspinel exsolution (ref, FOV = 0.98mm).

3.3.8 Chalcopyrite globule (in fayalite-hedenbergite granophyre) showing secondary alteration to covellite (ref, FOV = 0.39mm).

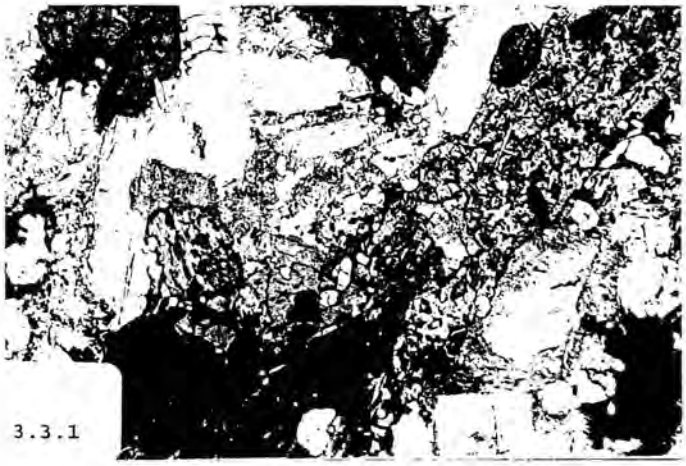

3.3.1

3.3.2

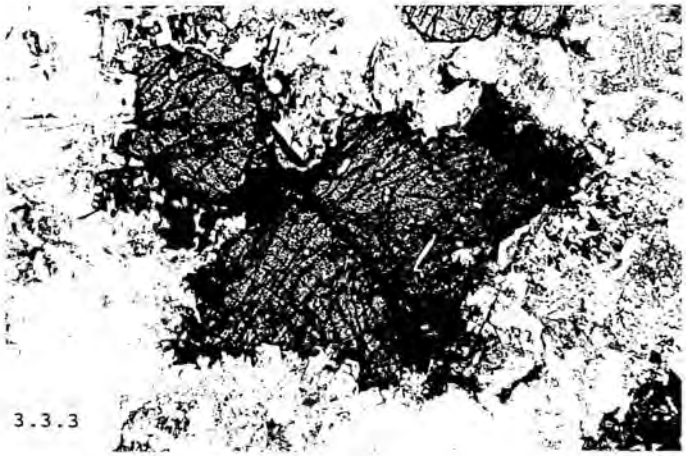

3.3.3

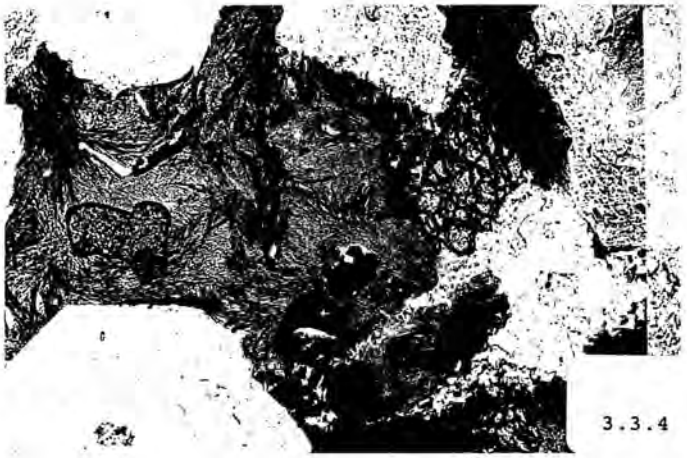

3.3.4

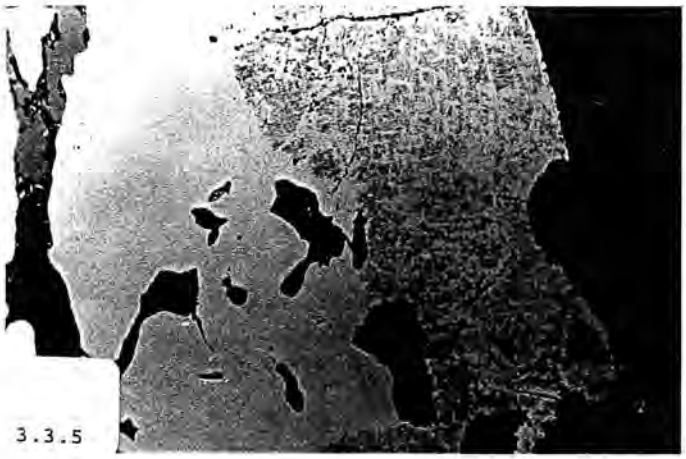

3.3.5

3.3.6

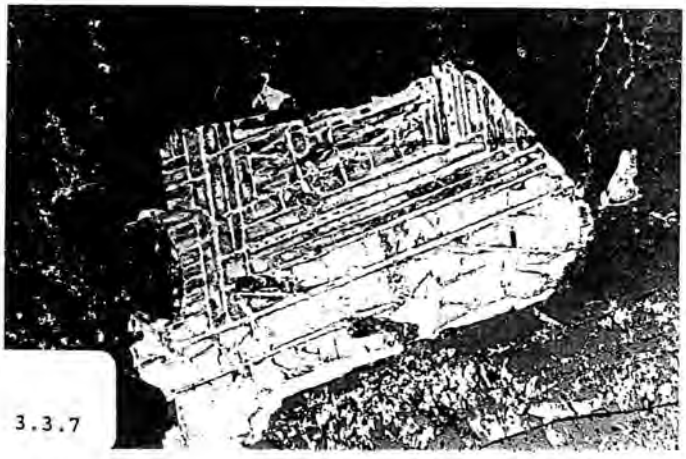

3.3.7

3.3.8

prisms up to 1mm in diameter and up to 5mm in length. Large, euhedral olivine grains up to 2mm in diameter are present, and contain inclusions of apatite (Plate 3.3.3). The olivine is now largely altered to iddingsite and chlorophaeite. Opaque oxide is present at around 3% of the rock, and apatite has declined in proportion from its peak of 3% in the granodiorites to around 1%. In the topmost fayalite-hedenbergite granophyres, occasional drusy cavities are lined by euhedral quartz and filled with stilpnomelane and biotite.

3.2.8 Granophyres.

The transition from fayalite-hedenbergite granophyre to granophyre is marked by the disappearance of olivine from the mineral assemblage. Granophyric intergrowth makes up the bulk of the rock at around 80%. Large patches of perthitic potassium feldspar and euhedral quartz are now seen within the granophyric intergrowth. A very small amount of plagioclase is also present, and both the plagioclase and potassium feldspar are extensively altered to sericite. Clinopyroxene forms only around 4% of the rock and is found as long prisms often over 7mm in length. It is completely altered to bleached hydrothermal pyroxene. Opaque oxide forms approximately 2% of the rock. Apatite is no longer seen.

An important feature of the granophyres is the abundance of drusy cavities filled with stilpnomelane, biotite, opaque oxide and the late-stage accessory phase, zircon. Sometimes the cavity fillings are dissected by cracks that appear to have formed from the drying-out of the cavity filling. The zircon is euhedral and is often seen to be growing out from the edge of quartz grains (Plate 3.3.4). This indicates that the zircon is not of detrital origin but that it grew in situ from late-stage deuteric fluids that circulated through the drusy cavities.

3.2.9 The Xenoliths.

As has been mentioned in the previous, chapter a number of small sedimentary xenoliths of around 20cm diameter are found within

the topmost granophyres. The mineralogy of the xenoliths is similar to that of the adjacent granophyres, but they are much finer grained and have a hypidiomorphic-granular texture. They are fine- to medium-grained and contain subhedral quartz, potassium feldspar, clinopyroxene, opaque oxide, biotite and hornblende. Plagioclase is present in very small amounts, but it is usually not possible to distinguish between it and the potassium feldspar because of the high degree of sericitization affecting both phases. There is a sharp contact between the xenoliths and the adjacent granophyre, marked by a sudden change in grain size and texture.

3.2.10 Aplitic Veins.

Cross-cutting aplitic veins are found within the granophyres and the underlying rocks down to the level of the quartz gabbros. The mineralogy of these veins is similar to that of the granophyres in that they contain quartz, potassium feldspar and a small amount of ferrohedenbergite and opaque oxide. The quartz is subhedral in habit and this imparts a hypidiomorphic-granular texture to the rock. The other difference between these veins and the granophyres is that they are fine-grained. These veins also contain drusy cavities which are filled with stilpnomelane and, occasionally, accessory calcite. These drusy cavities probably indicate that the aplitic veins were zones along which fluids moved through the sheet.

3.3 PETROGRAPHY OF THE OPAQUE PHASES.

In this section the petrography of the opaque phases within the rocks of the New Amalfi Sheet will be discussed with reference to changes that occur with progressive differentiation. In the olivine dolerites, small amounts of Ti-magnetite and ilmenite are present as euhedral to subhedral grains. It was possible to distinguish between the ilmenite and magnetite in most cases because the ilmenite exhibits slight anisotropism. It was found that the ilmenite is generally more euhedral than the magnetite, the latter filling the interstices between plagioclase laths. A similar pattern has also been described in Karoo dolerites by

Reynolds (1983) who suggested that the habit of the ilmenite in Karoo dolerites is related to the cooling rate of the rock, with more euhedral ilmenite grains found in rocks that cooled more quickly. In the New Amalfi Sheet dolerites, magnetite is often seen to surround more euhedral ilmenite grains. A similar feature was noted by Reynolds (op. cit.), who saw this to indicate that the ilmenite probably nucleated slightly earlier than the magnetite.

The presence of small, round inclusions of chromite in olivine was established by electron microprobe analysis. These chromite inclusions are seen only within the lowest olivine dolerite sample taken from the New Amalfi Sheet (NA99). Eales and Snowden (1979) reported a similar occurrence of chromite inclusions in olivine from the adjacent Elephant's Head Dike. In addition to these oxide phases, two sulphide phases (chalcopyrite and pyrrhotite) are found in trace amounts, forming intergrown sulphide globules within the olivine dolerites.

The habit of the oxide phases changes between the olivine dolerites and the overlying quartz gabbros. Ilmenite and magnetite now form large compound anhedral grains, 1 to 2 mm in diameter, within the interstices between plagioclase laths. The Ti-magnetite can now be easily distinguished from the ilmenite because it shows exsolution of sparse ilmenite lamellae and very fine exsolution of ulvöspinel in between the sparse ilmenite lamellae. This has resulted in a poor polish for the Ti-magnetite compared to the smooth ilmenite which exhibits no exsolution, so that these two phases are easily distinguished. The sulphide phases, chalcopyrite and pyrrhotite, are again present in the quartz gabbros, but still in trace amounts.

The exsolution of ulvöspinel in Ti-magnetite has previously been described in Karoo dolerites by Reynolds (1983) who states that this feature reflects low fO_2 conditions during cooling at temperatures below the magnetite-ulvöspinel solvus. Reynolds (op. cit.) also noted the tendency for ilmenite and Ti-magnetite to form large anhedral aggregates found interstitially between plagioclase and pyroxene grains in coarser-grained Karoo

dolerites. Reynolds attributes this form of intergrowth to granule oxidation-exsolution of ilmenite from adjacent Ti-magnetite. Buddington and Lindsley (1964) showed that granule oxidation exsolution of ilmenite from magnetite takes place under high fO_2 conditions. It is unlikely therefore that the composite grains of ilmenite and magnetite found within the quartz gabbros of the New Amalfi Sheet formed because of oxidation-exsolution of Ti-magnetite, since the presence of exsolved ulvöspinel within the magnetite indicates low fO_2 conditions. Therefore, the ilmenite within the composite oxide grains formed from direct crystallization together with magnetite. The interstitial habit of these two phases, however, indicates that they do not represent primary cumulus phases at this stage. Haggerty (1976) studied the changes in the petrography of oxide phases with progressive oxidation and is also of the opinion that most composite ilmenite and magnetite grains do not represent granule oxidation-exsolution of Ti-magnetite but primary simultaneous crystallization of both phases.

There is a marked increase in the proportion of the oxide phases at the base of the quartz monzodiorites, and this is seen to mark the entrance of Ti-magnetite and ilmenite as cumulus phases. Magnetite and ilmenite are still found to form composite anhedral grains with the Ti-magnetite exhibiting exsolution of ulvöspinel, which indicates that the fO_2 was still low (Plate 3.3.5). The ilmenite portion of each grain shows complex 'vermiform' intergrowths with pyroxene grains, with secondary biotite or hornblende separating the ilmenite from the host pyroxene. This has previously been documented in Karoo rocks by Reynolds (1983) who interpreted the phenomenon as being due to the reaction of Ti-magnetite with late-stage hydrous fluids to produce biotite or hornblende. The ilmenite component of composite grains is left unaffected and Fe and Ti ions liberated from the destruction of the Ti-magnetite combine to form new ilmenite which grows around the existing ilmenite, thus forming vermiform intergrowths of ilmenite surrounded by late-stage alteration products. Reynolds (op. cit.) states that this vermiform habit of the ilmenite is typical of late-stage differentiates or rocks that have undergone deuteric alteration. A few individual euhedral, lath-like grains

of ilmenite are also present, in addition to those seen to be intergrown with Ti-magnetite, and this may indicate an earlier stage of ilmenite nucleation. The sudden increase in the proportion of the oxide phases is mirrored by an equally sudden increase in the proportion of the sulphides chalcopyrite and pyrrhotite, although these phases still do not represent more than 1% of the rock. Once again, the chalcopyrite and pyrrhotite are seen to form composite sulphide globules (Plate 3.3.6).

There is a gradual decline in the proportion of the opaque oxide phases from the top of the quartz monzodiorites through the granodiorites to around 2%. In the granodiorites, Ti-magnetite and ilmenite still form composite anhedral grains. However, the exsolution of ilmenite in the magnetite is now well developed, with thick lamellae of ilmenite aligned parallel to the (111) crystallographic plane of the Ti-magnetite to produce the 'trellis network' exsolution pattern described previously in Karoo Ti-magnetites by Eales et al. (1980) and Reynolds (1983), (Plate 3.3.7). The host Ti-magnetites are now also free of the fine exsolved ulvöspinel, thereby allowing the host Ti-magnetites to take a better polish. The well developed ilmenite lamellae and the absence of ulvöspinel within the Ti-magnetite indicate the presence of higher fO_2 conditions than those that existed in the underlying rocks, during cooling of the granodiorites. This resulted in extensive oxidation of the magnetite-ulvöspinel solid solution thereby causing the exsolution of ilmenite lamellae within the Ti-magnetite parallel to the octahedral (111) plane, as described by Buddington and Lindsley (1964). Long, euhedral laths of ilmenite are also present within the granodiorites and once again this seems to indicate an earlier period of ilmenite nucleation. In the fayalite-hedenbergite granophyres and the granophyres, the occurrence of opaque phases is similar to that in the granodiorites. The main difference is that the vermiform intergrowths of ilmenite with late-stage hydrous phases, such as biotite and hornblende, are now common, indicating the increasing abundance of hydrous fluids reacting with Ti-magnetite to produce these intergrowths. The small amounts of chalcopyrite in the rock are also now seen to have undergone secondary alteration to covellite (Plate 3.3.8).

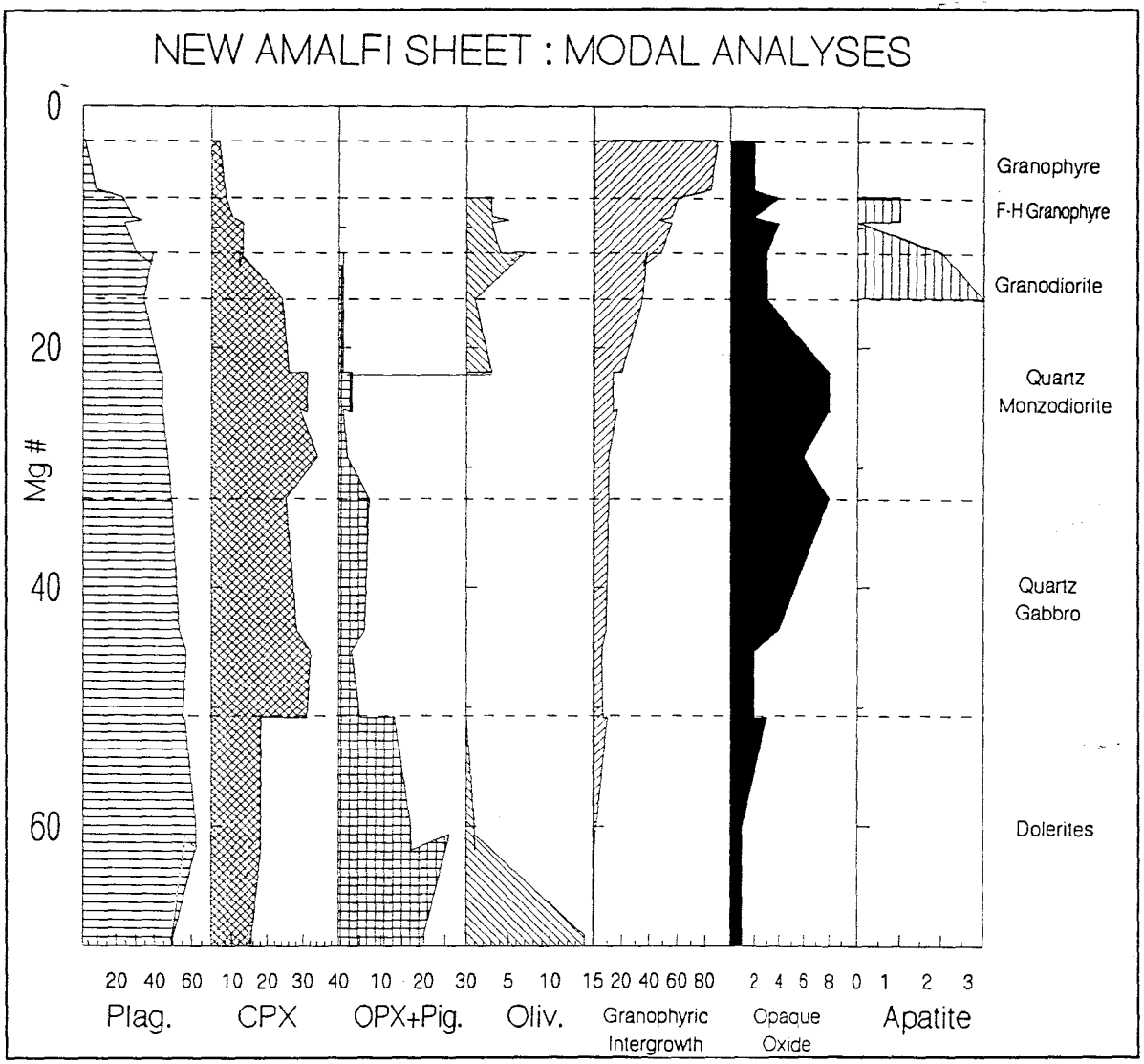

Figure 3.1 Modal analysis of selected samples plotted against Mg# so as to resemble a vertical section.

3.4 SUMMARY.

a) Modal analyses from a representative suite of samples are shown in Figure 3.1 which serves as a good graphical summary of the petrography of the New Amalfi Sheet. The modal analyses have been plotted against whole rock Mg# as this is the best way to separate the samples in order of increasing degree of differentiation with stratigraphic height. The continuous modal trends seen, especially in the case of the granophyric intergrowth, suggest that there is a genetic link between the mafic rocks of the sheet and the granophyres.

b) Olivine is abundant in the dolerites at the base of the sheet, and this may indicate some degree of gravity-induced settling of this mineral.

c) Pigeonite shows no sign of exsolution in the pigeonite dolerites and this indicates that these dolerites cooled faster than the olivine dolerites, probably because they form part of the thinner western peripheral sheet.

d) The glomeroporphyritic texture of the pigeonite dolerites, found close to the contact with surrounding country rock, indicates that plagioclase and pyroxene were on the liquidus at the time that the pigeonite dolerites were intruded.

e) The olivine dolerites and the pigeonite dolerites both show the general characteristics of the Kokstad Dolerite Type as defined by Walker and Poldervaart (1949).

f) The fact that olivine, iron-rich orthopyroxene and quartz coexist within the granodiorites indicates that the absolute limit of orthopyroxene stability, the forbidden zone of Lindsley and Munoz (1969), was reached within these rocks, if the orthopyroxene is a primary liquidus phase.

g) The presence of drusy cavities filled with stilpnomelane

and euhedral zircon indicates that these cavities were zones of fluid movement and that the zircon grew from these probably late-stage, water-rich fluids. The aplitic veins were also zones of late-stage fluid movement

h) The exsolution of ulvöspinel from Ti-magnetites within the quartz gabbros indicates low fO_2 conditions. The disappearance of this phenomenon in the Ti-magnetites found within the granodiorites, together with the development of 'trellis network' exsolution of ilmenite in the Ti-magnetites, indicates that the fO_2 had increased within these rocks.

i) The coarse intergrowths of Ti-magnetite and ilmenite in the quartz gabbros and quartz monzodiorites are unlikely to be because of oxidation exsolution (because of the prevailing low fO_2 conditions) but rather the result of simultaneous crystallization.

j) The increase in the proportion of bleached pyroxene and vermiform ilmenite with stratigraphic height within the intrusion indicates an increase in hydrothermal/deuteric activity with stratigraphic height in the intrusion.

3.4.1 The Paragenetic sequence of the primary phases of the New Amalfi Sheet.

DOLERITES

chromite → chromite+olivine → chromite+olivine+plag →
chromite+olivine+plag+pigeonite+augite

⇓

QUARTZ GABBROS

plag+pigeonite+augite+ferrohypersthene

⇓

QUARTZ MONZODIORITES

plag+pigeonite+ferroaugite+ferrohypersthene+ilm.+Timagnetite →
plag+ferroaugite+ferrohypersthene+ilmenite+Timagnetite+olivine

⇓

GRANODIORITES

plag+ferroaugite+ferrohypersthene+ilmenite+Timagnetite+olivine +apatite+granophyric intergrowth

⇓

FAYALITE-HEDENBERGITE GRANOPHYRES

plag+ferrohedenbergite+ilmenite+Timagnetite+olivine+apatite+ granophyric intergrowth

⇓

GRANOPHYRES

plag+ferrohedenbergite+ilmenite+Timagnetite+granophyric intergrowth

4. MINERAL CHEMISTRY.

4.1 INTRODUCTION.

The compositions of pyroxenes, olivines, feldspars, magnetite and ilmenite were determined by electron microprobe analysis of 41 representative samples taken from the New Amalfi Sheet. A summary of analytical techniques and conditions used is given in appendix I.

4.2 PYROXENES.

A total of 484 calcium-rich pyroxene analyses and 159 calcium-poor pyroxene analyses have been plotted within the pyroxene quadrilateral in Figure 4.1. The only analyses excluded from this group were those that contained between 5 and 15 wt% CaO, since these analyses fall within the miscibility gap between naturally occurring calcium-poor and calcium-rich pyroxenes and therefore represent mixtures of host and exsolution lamellae, and not liquidus compositions (Deer et al, 1978).

4.2.1 Calcium-Rich Pyroxenes.

4.2.1.1 Two varieties of calcium-rich pyroxene.

As can be seen from Figure 4.1, there is a wide range in the CaO concentration of the calcium-rich pyroxenes. Figure 4.2 shows a histogram of CaO distribution within the calcium-rich pyroxenes. It can be seen that there are three peaks in CaO distribution at between 18.4 and 18.6 wt%, 19.6 and 20 wt%, and 20.6 and 20.8 wt%. Figure 4.3 shows that there is a bimodal distribution of TiO_2 concentration within the calcium-rich pyroxenes, with one peak between 0.1 and 0.2 wt%, and the other peak between 0.7 and 0.8 wt%. During the study of the calcium rich pyroxenes from the New Amalfi Sheet, it was discovered that some normally brown augite grains had been partially 'bleached' to a dirty white colour (Plate 4.1). Electron microprobe analysis of these grains showed that the bleached portions of the augite grains had higher

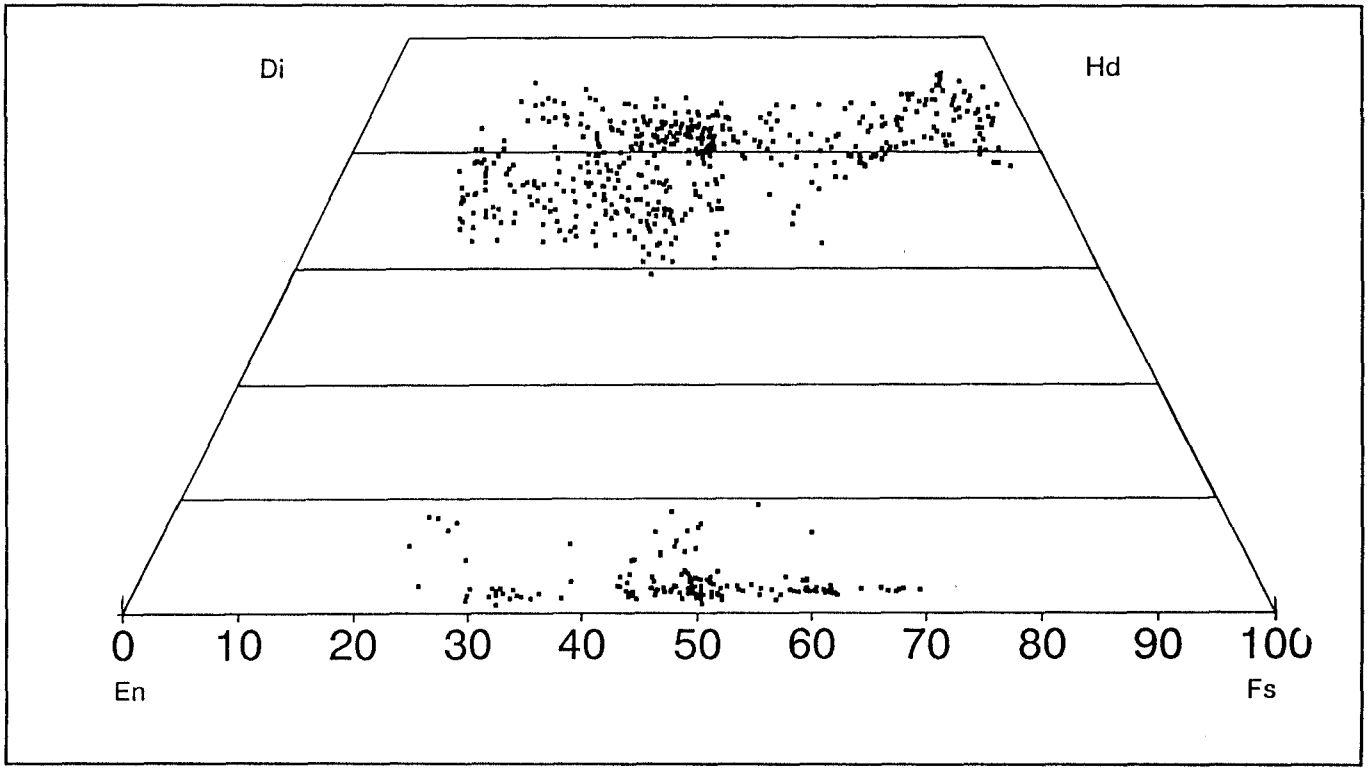

Figure 4.1 643 single pyroxene analyses from the New Amalfi Sheet plotted on the pyroxene quadrilateral.

Table 4.1 Comparison of analyses from a traverse of the augite grain in Plate 4.1, using a focused 1μ and a defocused 10μ electron beam.

POSITION	1		2		3		4		5	
BEAM WIDTH	1μ	10μ	1μ	10μ	1μ	10μ	1μ	10μ	1μ	10μ
SiO2	51.6	50.8	52.7	52.3	51.8	51.5	51.6	51.5	51.3	51.6
TiO2	0.11	0.07	0.09	0.14	0.61	0.57	0.57	0.57	0.64	0.7
Al2O3	0.46	0.44	0.75	1.06	1.59	1.44	1.57	1.49	1.35	1.4
Cr2O3	0	0	0	0	0	0	0	0	0	0
FeO	14.7	14.8	11.1	11.3	12.2	14.4	15.2	15.0	16.7	15.7
MnO	0.35	0.32	0.30	0.23	0.32	0.30	0.38	0.32	0.40	0.39
NiO	0.04	0	0.03	0	0.01	0	0.04	0	0.04	0.02
MgO	11.0	10.8	13.0	13.0	14.0	14.7	14.1	13.9	13.5	13.3
CaO	21.8	21.6	22.8	22.7	20	17.1	17.2	17.2	16.3	17.4
Na2O	0.20	0.2	0.13	0.15	0.26	0.17	0.21	0.19	0.23	0.22
Total	100	99.0	101	101	101	100	101	100	100	101

CaO and lower TiO_2 concentrations than the originally brown portions. A longitudinal traverse of one such grain, shown in Plate 4.1, clearly shows this. From Table 4.1 it can be seen that positions 1 and 2, found within the bleached portion of the grain, have high CaO and low TiO_2 concentrations, whereas positions 4 and 5, found within the brown portion of the grain, have comparatively lower CaO and higher TiO_2 concentrations. Apart from this, examination of Table 4.1 also shows that the bleached pyroxene has less Al2O3, FeO and MgO, compared to the brown calcium-rich pyroxene.

The composition of the pyroxene grain at position 3, is similar to that at positions 4 and 5, when analysed with a defocused 10μ beam. However position 3 has an intermediate CaO composition of 20 wt% and has retained a high TiO_2 concentration of 0.6 wt%, when analysed with a focused 1μ beam. This feature is discussed further in the next paragraph. Examination of Plate 4.1 also shows that the transition from brown to bleached augite is gradational, as seen from the gradational colour change from pure

Plate 4.1 Longitudinal traverse along a partially altered calcium-rich pyroxene grain.

Table 4.2

AVERAGE COMPOSITIONS OF BROWN CLINOPYROXENES

Sample	NA99	NA97	NA72	NA132	NA124&125	NA136	NA133
Wt.%							
SiO2	52.88	52.82	52.25	52.51	52.04	50.46	51.74
TiO2	0.65	0.56	0.49	0.51	0.57	0.78	0.56
Al2O3	2.06	1.79	1.78	1.72	1.89	3.82	1.71
Cr2O3	0.60	0.28	0.26	0.31	0.39	0.33	0.13
FeO	8.08	8.66	9.74	10.25	10.79	10.92	10.94
MnO	0.17	0.21	0.20	0.19	0.16	0.23	0.20
NiO	0.05	0.04	0.10	0.02	0.05	0.03	0.01
MgO	17.25	17.10	17.12	16.10	15.62	15.67	15.61
CaO	18.19	18.42	17.46	18.10	18.67	17.39	18.88
Na2O	0.15	0.24	0.13	0.15	0.18	0.28	0.21
Total	100.09	100.12	99.53	99.86	100.35	99.93	100.00
Cations (based on six oxygens)							
Si	1.9443	1.9455	1.9419	1.9512	1.9347	1.8821	1.9339
Ti	0.0181	0.0154	0.0138	0.0144	0.0159	0.0220	0.0158
Al	0.0894	0.0778	0.0779	0.0754	0.0828	0.1681	0.0753
Cr	0.0174	0.0083	0.0076	0.0090	0.0114	0.0098	0.0039
Fe2+	0.2492	0.2671	0.3041	0.3192	0.3362	0.3410	0.3426
Mn	0.0054	0.0065	0.0062	0.0059	0.0051	0.0073	0.0063
Ni	0.0015	0.0011	0.0030	0.0005	0.0014	0.0010	0.0003
Mg	0.9446	0.9384	0.9471	0.8913	0.8647	0.8708	0.8689
Ca	0.7170	0.7272	0.6951	0.7200	0.7437	0.6947	0.7562
Na	0.0111	0.0175	0.0095	0.0107	0.0127	0.0205	0.0150
Totals	3.9981	4.0048	4.0063	3.9976	4.0086	4.0172	4.0182
Charge	0.021	-0.010	-0.013	0.005	-0.017	-0.035	-0.036
Mg#	79.3	77.8	75.9	73.9	72.1	71.9	71.7
n	12	8	10	7	15	5	6

Sample	NA100	NA80	NA129	NA92	NA95	NA93	NA90
Wt.%							
SiO2	52.15	52.10	51.01	50.43	51.25	50.98	50.78
TiO2	0.76	0.45	0.69	0.59	0.79	0.55	0.67
Al2O3	1.55	1.61	1.93	1.32	1.45	1.08	1.22
Cr2O3	0.11	0.22	0.20	0.01	0.07	0.00	0.08
FeO	12.04	12.62	12.53	16.25	16.07	16.75	17.80
MnO	0.27	0.22	0.27	0.28	0.28	0.29	0.34
NiO	0.04	0.04	0.01	0.01	0.04	0.01	0.05
MgO	15.68	15.19	14.24	12.61	12.38	11.64	11.22
CaO	17.38	17.51	19.04	18.09	17.64	18.48	17.77
Na2O	0.14	0.12	0.27	0.18	0.26	0.20	0.20
Total	100.11	100.08	100.19	99.77	100.24	99.98	100.12
Cations (based on six oxygens)							
Si	1.9462	1.9504	1.9212	1.9363	1.9504	1.9571	1.9547
Ti	0.0215	0.0128	0.0195	0.0170	0.0227	0.0158	0.0194
Al	0.0681	0.0707	0.0859	0.0595	0.0652	0.0486	0.0551
Cr	0.0032	0.0065	0.0060	0.0002	0.0022	0.0001	0.0025
Fe2+	0.3769	0.3974	0.3946	0.5222	0.5116	0.5386	0.5734
Mn	0.0085	0.0071	0.0086	0.0092	0.0092	0.0094	0.0111
Ni	0.0011	0.0011	0.0003	0.0004	0.0012	0.0004	0.0014
Mg	0.8709	0.8451	0.7994	0.7207	0.7019	0.6649	0.6429
Ca	0.6951	0.7023	0.7682	0.7445	0.7193	0.7605	0.7327
Na	0.0104	0.0091	0.0195	0.0136	0.0192	0.0145	0.0146
Totals	4.0019	4.0027	4.0232	4.0236	4.0028	4.0099	4.0079
Charge	-0.004	-0.005	-0.046	-0.039	-0.006	-0.020	-0.009
Mg#	69.8	68.1	67.0	58.0	57.9	55.3	52.8
n	5	5	4	29	9	57	20

Table 4.2 (cont.)

Sample	NA91	NA190	NA192	NA153	NA179	NA164	NA89
Wt.%							
SiO2	50.19	49.41	48.92	49.03	48.43	47.89	48.60
TiO2	0.65	0.43	0.60	0.53	0.78	0.71	0.68
Al2O3	1.23	0.78	0.74	0.66	0.85	0.21	0.62
Cr2O3	0.07	0.02	0.00	0.06	0.07	0.00	0.06
FeO	18.00	22.86	24.86	24.81	26.31	27.71	27.60
MnO	0.33	0.33	0.35	0.33	0.42	0.37	0.43
NiO	0.02	0.02	0.01	0.02	0.04	0.03	0.03
MgO	11.22	7.56	6.35	5.12	4.42	3.37	2.50
CaO	17.89	18.63	17.91	18.91	18.97	19.24	19.11
Na2O	0.19	0.22	0.13	0.26	0.13	0.12	0.20
Total	99.79	100.26	99.87	99.75	100.42	99.64	99.82
Cations (based on six oxygens)							
Si	1.9425	1.9538	1.9577	1.9704	1.9495	1.9616	1.9804
Ti	0.0188	0.0128	0.0179	0.0162	0.0236	0.0220	0.0209
Al	0.0562	0.0365	0.0350	0.0315	0.0404	0.0100	0.0299
Cr	0.0022	0.0005	0.0002	0.0020	0.0021	0.0000	0.0020
Fe2+	0.5828	0.7558	0.8324	0.8340	0.8861	0.9495	0.9409
Mn	0.0108	0.0109	0.0119	0.0112	0.0142	0.0128	0.0149
Ni	0.0007	0.0006	0.0004	0.0007	0.0014	0.0011	0.0009
Mg	0.6465	0.4456	0.3781	0.3065	0.2649	0.2054	0.1511
Ca	0.7421	0.7895	0.7683	0.8142	0.8183	0.8444	0.8341
Na	0.0140	0.0171	0.0098	0.0203	0.0105	0.0097	0.0156
Totals	4.0165	4.0233	4.0117	4.0069	4.0109	4.0163	3.9906
Charge	-0.030	-0.027	-0.009	-0.014	-0.002	0.024	0.019
Mg#	52.5	37.1	31.1	26.9	23.0	17.8	13.8
n	15	5	10	15	13	4	10

Sample	NA86	NA82	NA134	NA87	NA88
Wt.%					
SiO2	47.31	47.06	47.27	47.57	47.17
TiO2	0.69	0.89	0.83	0.44	0.68
Al2O3	0.61	0.78	0.73	0.39	0.54
Cr2O3	0.06	0.09	0.06	0.08	0.08
FeO	28.85	29.66	30.86	29.77	30.46
MnO	0.43	0.51	0.44	0.45	0.47
NiO	0.03	0.02	0.01	0.04	0.07
MgO	1.76	1.51	1.23	0.93	0.91
CaO	19.65	18.63	17.77	19.51	19.62
Na2O	0.17	0.14	0.17	0.18	0.14
Total	99.57	99.29	99.39	99.35	100.13
Cations (based on six oxygens)					
Si	1.9554	1.9536	1.9641	1.9774	1.9540
Ti	0.0213	0.0277	0.0261	0.0137	0.0212
Al	0.0299	0.0383	0.0358	0.0190	0.0263
Cr	0.0020	0.0029	0.0021	0.0024	0.0025
Fe2+	0.9974	1.0296	1.0726	1.0348	1.0551
Mn	0.0151	0.0180	0.0156	0.0157	0.0164
Ni	0.0011	0.0008	0.0003	0.0013	0.0022
Mg	0.1085	0.0932	0.0764	0.0577	0.0565
Ca	0.8701	0.8286	0.7911	0.8691	0.8706
Na	0.0139	0.0111	0.0138	0.0143	0.0113
Totals	4.0145	4.0037	3.9979	4.0054	4.0161
Charge	0.001	0.009	0.005	-0.003	0.007
Mg#	9.8	8.3	6.6	5.3	5.1
n	4	4	5	1	3

Table 4.2 (cont.)

AVERAGE COMPOSITIONS OF BLEACHED CLINOPYROXENES

Sample	NA99	NA97	NA100	NA124&125	NA129	NA133	NA95
Wt.%							
SiO2	52.80	52.77	52.78	52.45	51.92	51.29	51.94
TiO2	0.44	0.40	0.40	0.42	0.37	0.25	0.29
Al2O3	1.33	1.11	1.50	1.64	1.21	0.86	0.74
Cr2O3	0.19	0.21	0.21	0.36	0.14	0.10	0.07
FeO	8.16	8.10	8.78	9.05	10.37	12.64	14.66
MnO	0.20	0.16	0.18	0.15	0.20	0.24	0.27
NiO	0.00	0.03	0.03	0.05	0.02	0.05	0.03
MgO	14.91	14.54	15.35	15.16	13.92	12.19	11.27
CaO	22.35	21.85	21.17	20.98	21.86	21.82	20.72
Na2O	0.19	0.23	0.15	0.16	0.23	0.18	0.22
Total	100.56	99.41	100.56	100.42	100.25	99.62	100.21
Cations (based on 6 oxygens) :							
Si	1.9534	1.9716	1.9514	1.9450	1.9474	1.9587	1.9796
Ti	0.0122	0.0112	0.0112	0.0116	0.0106	0.0071	0.0083
Al	0.0580	0.0488	0.0653	0.0715	0.0534	0.0386	0.0332
Cr	0.0054	0.0062	0.0061	0.0105	0.0042	0.0031	0.0021
Fe2+	0.2526	0.2531	0.2723	0.2814	0.3254	0.4061	0.4679
Mn	0.0062	0.0052	0.0057	0.0047	0.0063	0.0079	0.0088
Ni	0.0001	0.0010	0.0008	0.0015	0.0007	0.0016	0.0010
Mg	0.8220	0.8097	0.8446	0.8365	0.7784	0.6913	0.6396
Ca	0.8861	0.8747	0.8389	0.8338	0.8786	0.8926	0.8460
Na	0.0133	0.0166	0.0106	0.0117	0.0168	0.0130	0.0161
Total	4.0094	3.9980	4.0070	4.0082	4.0217	4.0200	4.0026
Charge	-0.019	0.004	-0.014	-0.017	-0.043	-0.034	-0.005
Mg#	76.5	76.2	75.5	74.8	70.5	63.1	57.8
n	3	3	5	13	5	4	9

Sample	NA92	NA80	NA90	NA176	NA91	NA160	NA190
Wt.%							
SiO2	51.04	51.67	51.93	51.55	51.01	50.26	50.03
TiO2	0.16	0.31	0.18	0.12	0.16	0.20	0.12
Al2O3	0.56	0.78	0.50	0.45	0.46	0.48	0.44
Cr2O3	0.01	0.05	0.07	0.08	0.07	0.00	0.04
FeO	15.67	15.76	16.05	16.85	17.76	19.47	20.37
MnO	0.27	0.24	0.32	0.32	0.29	0.27	0.30
NiO	0.01	0.04	0.05	0.03	0.05	0.01	0.04
MgO	10.97	10.47	10.23	9.34	9.25	8.50	7.71
CaO	20.95	21.04	21.00	21.08	20.87	20.93	20.97
Na2O	0.18	0.14	0.16	0.15	0.31	0.21	0.17
Total	99.81	100.49	100.49	99.98	100.22	100.32	100.19
Cations (based on 6 oxygens) :							
Si	1.9677	1.9756	1.9880	1.9924	1.9781	1.9649	1.9683
Ti	0.0047	0.0089	0.0052	0.0035	0.0047	0.0058	0.0035
Al	0.0254	0.0349	0.0225	0.0207	0.0210	0.0223	0.0202
Cr	0.0002	0.0015	0.0020	0.0025	0.0020	0.0000	0.0013
Fe2+	0.5055	0.5038	0.5143	0.5456	0.5760	0.6368	0.6711
Mn	0.0087	0.0078	0.0105	0.0105	0.0095	0.0090	0.0098
Ni	0.0004	0.0013	0.0014	0.0011	0.0014	0.0002	0.0011
Mg	0.6298	0.5967	0.5830	0.5374	0.5342	0.4949	0.4513
Ca	0.8656	0.8619	0.8614	0.8732	0.8673	0.8765	0.8844
Na	0.0134	0.0101	0.0122	0.0110	0.0232	0.0157	0.0132
Total	4.0215	4.0025	4.0005	3.9979	4.0174	4.0261	4.0240
Charge	-0.029	-0.005	-0.001	0.004	-0.033	-0.026	-0.025
Mg#	55.5	54.2	53.2	49.6	48.1	43.7	40.2
n	32	1	13	8	8	4	1

Table 4.2 (cont.)

Sample	NA191	NA192	NA164	NA128	NA179	NA89	NA86
Wt.%							
SiO2	50.40	49.28	48.55	48.60	48.58	49.37	48.41
TiO2	0.06	0.13	0.14	0.14	0.29	0.12	0.13
Al2O3	0.26	0.35	0.25	0.30	0.35	0.27	0.26
Cr2O3	0.00	0.00	0.00	0.06	0.05	0.07	0.06
FeO	20.16	24.62	26.42	26.60	26.84	26.56	27.09
MnO	0.35	0.33	0.42	0.37	0.45	0.35	0.41
NiO	0.01	0.01	0.01	0.03	0.02	0.03	0.03
MgO	7.58	4.68	3.33	2.84	2.55	2.28	2.28
CaO	20.88	20.75	20.64	20.44	20.38	20.60	21.16
Na2O	0.25	0.14	0.20	0.19	0.24	0.22	0.18
Total	99.95	100.29	99.94	99.58	99.75	99.88	100.02
Cations (based on 6 oxygens) :							
Si	1.9838	1.9766	1.9753	1.9846	1.9830	2.0056	1.9781
Ti	0.0019	0.0040	0.0042	0.0043	0.0090	0.0038	0.0042
Al	0.0120	0.0167	0.0119	0.0143	0.0169	0.0129	0.0128
Cr	0.0001	0.0000	0.0000	0.0020	0.0015	0.0021	0.0020
Fe2+	0.6640	0.8263	0.8992	0.9093	0.9161	0.9027	0.9258
Mn	0.0116	0.0111	0.0144	0.0127	0.0155	0.0121	0.0142
Ni	0.0002	0.0002	0.0002	0.0011	0.0008	0.0011	0.0011
Mg	0.4444	0.2791	0.2019	0.1723	0.1550	0.1379	0.1386
Ca	0.8807	0.8915	0.8998	0.8946	0.8914	0.8965	0.9265
Na	0.0189	0.0112	0.0154	0.0155	0.0193	0.0171	0.0145
Total	4.0177	4.0168	4.0223	4.0107	4.0085	3.9917	4.0177
Charge	-0.027	-0.020	-0.019	-0.019	-0.017	0.017	-0.017
Mg#	40.1	25.3	18.3	15.8	14.5	13.2	13.0
n	7	3	5	3	1	7	8

Sample	NA82	NA88
Wt.%		
SiO2	48.37	47.89
TiO2	0.26	0.43
Al2O3	0.29	0.45
Cr2O3	0.09	0.07
FeO	27.57	29.92
MnO	0.43	0.44
NiO	0.06	0.08
MgO	1.94	0.70
CaO	20.84	20.55
Na2O	0.18	0.19
Total	100.04	100.73
Cations (based on 6 oxygens) :		
Si	1.9792	1.9680
Ti	0.0080	0.0133
Al	0.0142	0.0217
Cr	0.0030	0.0023
Fe2+	0.9438	1.0283
Mn	0.0150	0.0153
Ni	0.0018	0.0025
Mg	0.1181	0.0427
Ca	0.9137	0.9048
Na	0.0144	0.0153
Total	4.0113	4.0144
Charge	-0.010	-0.008
Mg#	11.1	4.0
n	3	3

brown to totally bleached augite, and that analysis 3 is found on the edge of this gradational zone.

Figure 4.4 shows a traverse from the bleached portion to the brown portion of an augite grain, using a focused electron beam. Figure 4.4 can be divided into three zones. Firstly, there is a zone of brown augite with CaO concentrations below 19 wt% and TiO_2 concentrations above 0.6 wt%. Secondly, there is a zone of bleached pyroxene with CaO above 20.5 wt% and TiO_2 below 0.2 wt%. Between these two zones is a transitional zone with concentrations of CaO mainly between 19 and 20.5 wt% and with more erratic TiO_2 concentrations ranging between 0.1 and 0.6 wt%. This traverse therefore shows that there is a gradual transition zone between pure brown and totally bleached augite. Furthermore, examination of Figure 4.4 shows that a focused beam analysis taken at the edge of the transitional zone, next to the brown augite zone, would have a CaO concentration of between 19 and 20.5 wt%. However, a defocused beam analysis of this same spot would sample some of the brown augite as well, thereby imparting a lower CaO concentration to the analysis. This is probably what has caused the difference in CaO concentration between defocused and focused beam analyses seen for position 3 in Table 4.1. The transitional zone between the brown and bleached augite probably also causes the middle peak on the CaO histogram for calcium-rich pyroxenes in Figure 4.2. A middle peak is not seen in the TiO_2 histogram shown in Figure 4.3, probably because the TiO_2 distribution in the transitional zone is more erratic.

It was decided to use a focused instead of a defocused beam for all pyroxene analyses because of the greater detail this affords. It can be seen from Table 4.1 that there is essentially no difference between focused and defocused beam analyses, except for analysis 3, the reasons for which have already been discussed. The fact that the other analyses are essentially the same when analyzed with a focused or a defocused beam, indicates that the exsolution present in the brown augite is at a very fine scale. Buchanan (1979) states that the effective area analyzed by a focused electron beam is 3μ. From this he calculated that if the exsolution density of a pyroxene is greater than 90

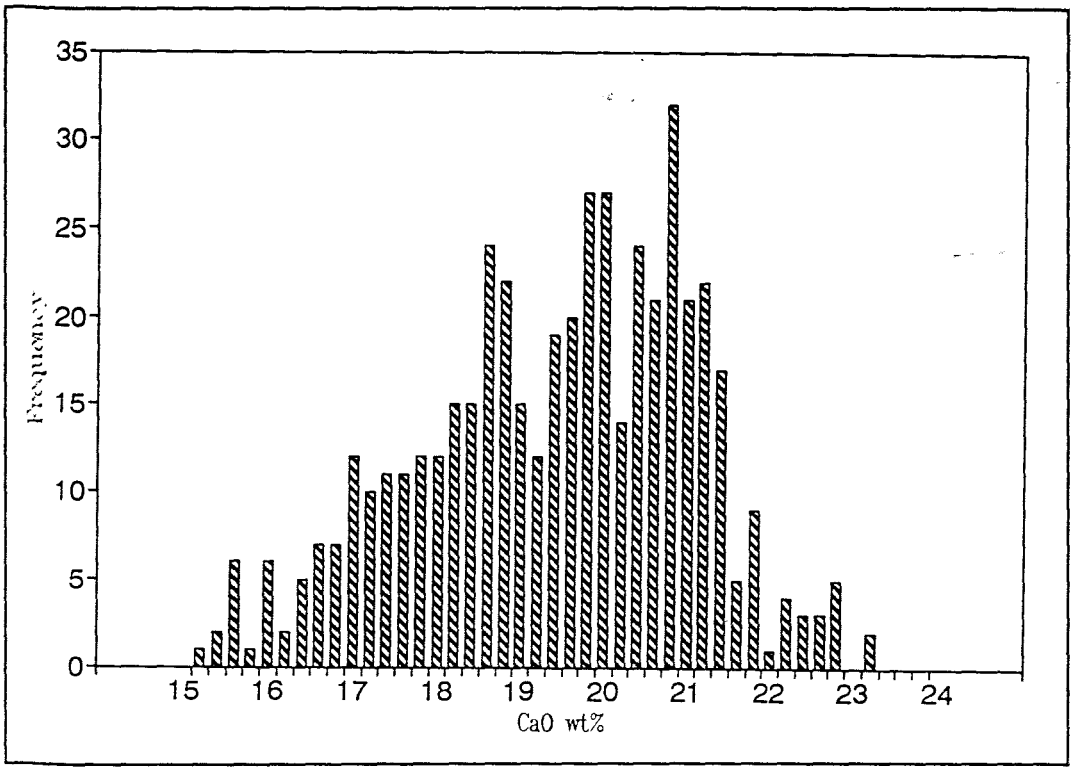

Figure 4.2 CaO histogram for 484 single New Amalfi Sheet calcium-rich pyroxene analyses.

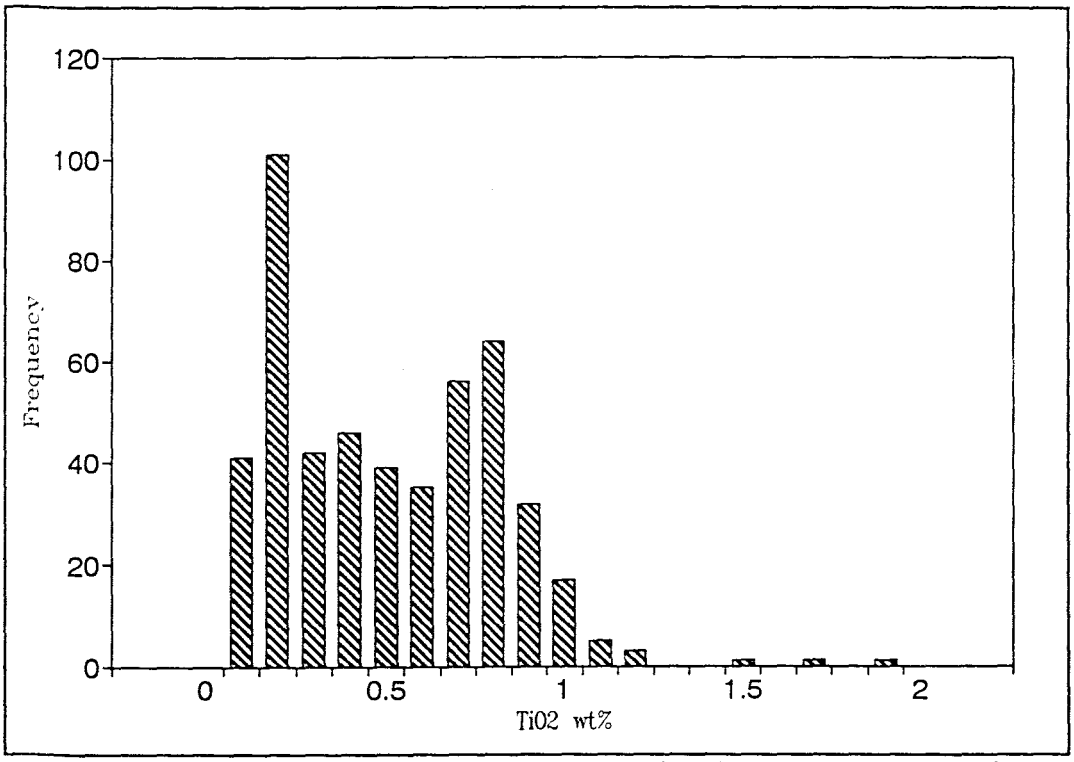

Figure 4.3 TiO_2 histogram for 484 single New Amalfi Sheet calcium-rich pyroxene analyses.

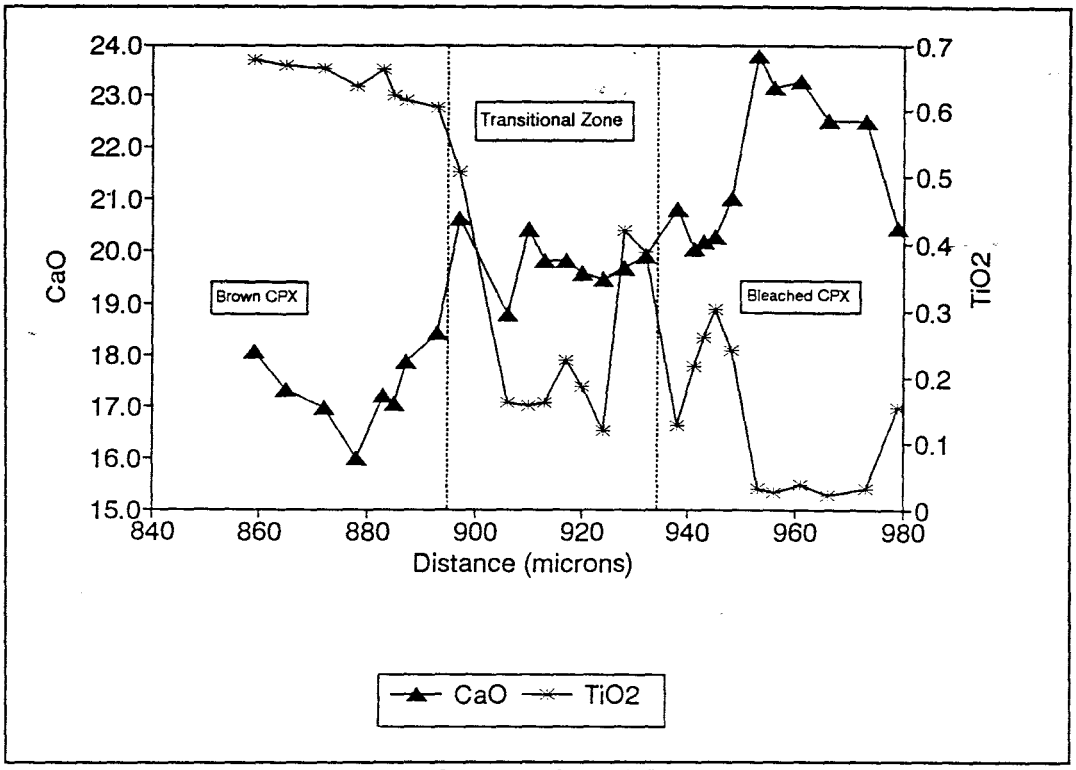

Figure 4.4 Traverse from the bleached to the brown portion of a partially altered pyroxene grain.

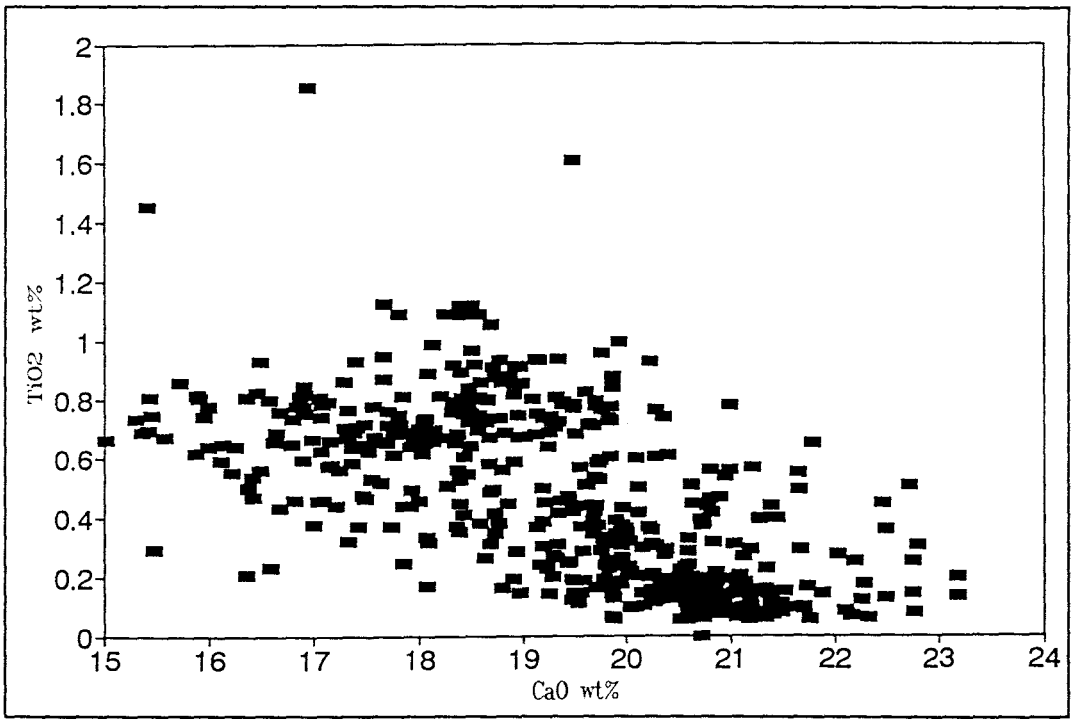

Figure 4.5 TiO_2 versus CaO for 484 single New Amalfi Sheet calcium-rich pyroxene analyses.

lamellae per millimetre, then the analysis will closely approach that of the bulk composition (obtained by analysis with a defocused beam). It was noted during the petrographic study of the New Amalfi Sheet that the augites exhibit very fine-scale exsolution (see Plate 3.2.1) and this is probably why focused and defocused beam analyses of brown augite are similar, except in the special case where an analysis is taken at the edge of the transition zone, between brown and bleached pyroxene.

A graph of TiO_2 versus CaO for all 484 single calcium-rich pyroxene analyses shows two populations, one with high TiO_2 and low CaO concentrations and the other with the opposite (Figure 4.5). These two populations correspond to the brown and bleached calcium-rich pyroxenes respectively. A transitional zone can again be seen between 19 and 20 wt% CaO, and 0.4 and 0.6 wt% TiO_2. Brown and bleached calcium-rich pyroxenes can also be distinguished by using a plot of CaO/TiO_2 versus CaO for all 484 focused beam analyses, shown in Figure 4.6. It can be seen from this plot that there are two trends. There is one tightly constrained trend of low CaO/TiO_2 values and another erratic trend of higher CaO/TiO_2 values which begins between 19 to 20 wt% CaO. These two trends therefore represent the brown and bleached calcium-rich pyroxene assemblages respectively. These two trends seem to intersect just below 20 wt% CaO, and 20 wt% CaO may therefore be a useful value to distinguish between brown and bleached pyroxene analyses.

It can therefore be seen that there are two varieties of calcium-rich pyroxene within the New Amalfi Sheet rocks, namely the brown variety and the bleached variety, so named because the latter seems to have formed from the original brown variety. The transition from brown to bleached calcium-rich pyroxene is gradational and therefore, as with all gradational features, a dividing line must be drawn to distinguish between the two varieties. Therefore, it was decided to draw the line at 20 wt% CaO and to call any pyroxene analysis with 20 wt% CaO or more, bleached pyroxene and any pyroxene analysis with less than 20 wt% CaO the brown variety. A mean and standard deviation were then calculated for all single brown and bleached pyroxene analyses.

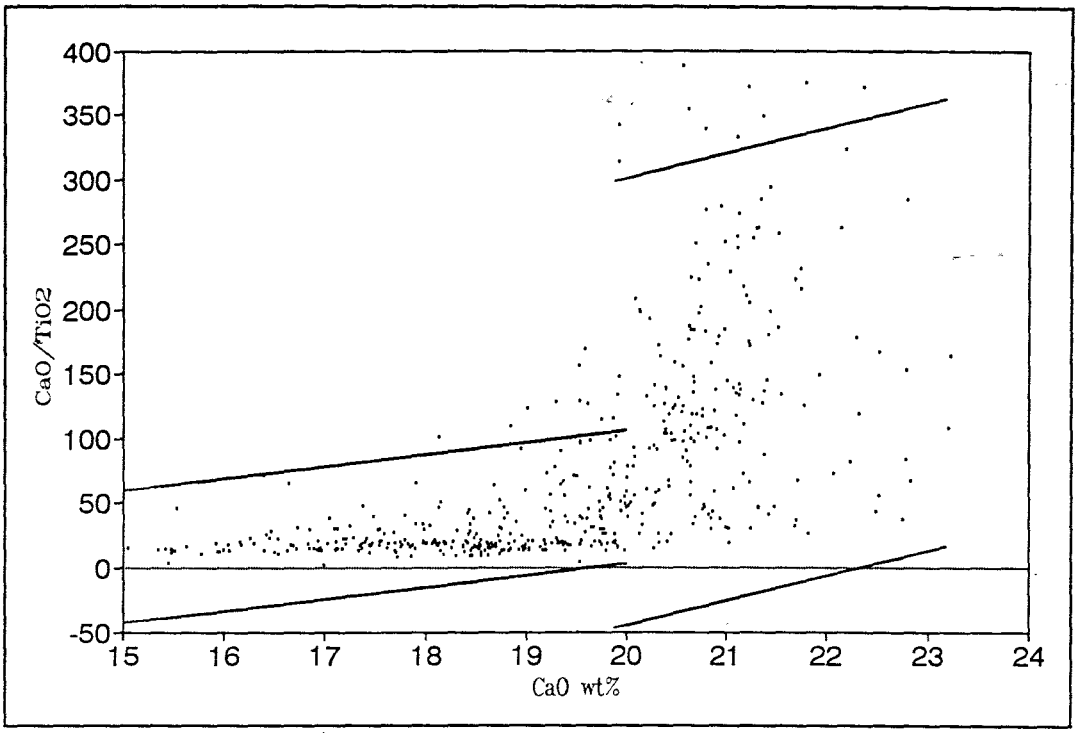

Figure 4.6 CaO/TiO_2 versus CaO for all 484 single calcium-rich pyroxene analyses. Parallel lines indicate two standard deviations either side of the mean of each population.

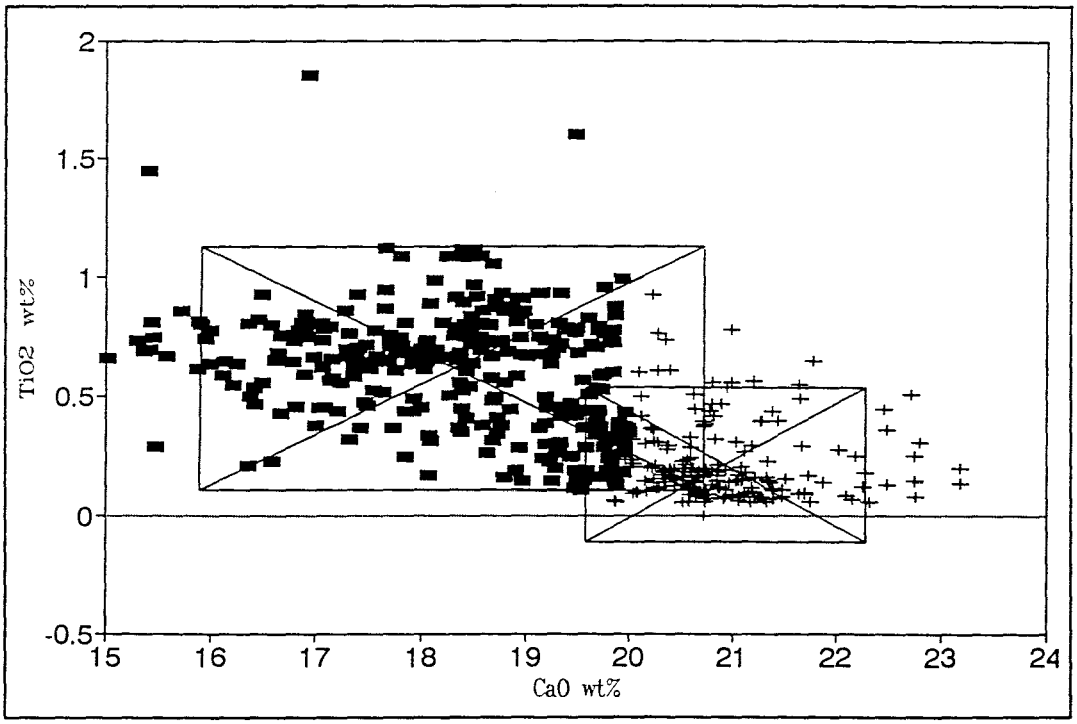

Figure 4.7 484 single New Amalfi Sheet calcium-rich pyroxene analyses divided into brown and bleached populations. Boxes enclose 2 s.d's either side of the mean of each population. ■ = brown; + = bleached.

Two boxes which encompass two standard deviations to either side the means in TiO_2 and CaO concentration, for both pyroxene varieties, were drawn together with a plot of TiO_2 versus CaO in Figure 4.7. These boxes include 95% of all analyses belonging to each pyroxene variety, assuming that both populations exhibit a normal distribution (Ott & Mendenhall, 1985). Despite a small region of overlap between these two standard deviation boxes, the overlap does not extend to the means of either pyroxene variety. The fact that the means of the two populations do not fall within the area of overlap, indicates that the two pyroxene varieties represent two separate populations.

A more thorough statistical test was used to prove that the brown and bleached pyroxenes represent two different populations, namely the Student's t test. The formulas used to obtain a value for t were taken from Ott and Mendenhall (1985) and are shown below.

$$t = \frac{\bar{x}_1 - \bar{x}_2}{Sp\sqrt{\frac{1}{n_1} + \frac{1}{n_2}}}$$

where

$$sp = \sqrt{\frac{(n_1 - 1)\, s_1^2 + (n_2 - 1)\, s_2^2}{n_1 + n_2 - 2}}$$

$\bar{x}_1$ = *mean of all brown pyroxene analyses*
$\bar{x}_2$ = *mean of all bleached pyroxene analyses*
s = *sample standard deviation*
n = *number of measurements*

The fact that the value of t, calculated from the above equation, of -26.915 is much less than the value of t, at the 99% confidence level and infinite degrees of freedom, of -2.576, indicates that the brown and bleached pyroxenes represent two separate populations at the 99% confidence level.

Averages of all brown and bleached pyroxene analyses for each sample were determined and are shown in Table 4.2. The average sum of cations per 6 oxygens was 4.009 for the brown calcium-rich pyroxenes and 4.011 for the bleached calcium-rich pyroxenes. The average charge deficit, calculated from the formula given by

Cameron and Papike (1981), was -0.0088 for the brown calcium-rich pyroxenes and -0.0157 for the bleached pyroxenes. These average charge deficit totals indicate the presence of a minor amount of Fe^{3+}, not accounted for in the cation calculation, which is slightly more abundant in the bleached pyroxenes. Average intra-sample coefficients of variation were calculated for the cations and are shown in Table 4.3. The high values of these coefficients of variation, especially with regard to the minor elements, are probably the result of the gradational and sometimes erratic nature of the transition from brown to bleached pyroxene.

Table 4.3 Average charge deficits and average intra-sample coefficients of variation for New Amalfi Sheet pyroxenes.

CHARGE BALANCE ($^{VI}Al+Fe^{3+}+Cr+2Ti-^{IV}Al-Na$)				
	Bleached CPX	Brown CPX	OPX	Pigeonite
	-0.0157	-0.0088	0.0163	0.0049
COEFFICIENTS OF VARIATION (100*std/mean)				
Cations	Bleached CPX	Brown CPX	OPX	Pigeonite
Si	0.5787	0.7300	0.2967	0.6704
Ti	52.9915	33.9116	19.1672	12.0331
Al	39.2991	28.1295	21.7382	14.2237
Cr	59.0708	58.2095	53.1547	59.4535
Fe^{2+}	10.1082	13.1172	7.1235	5.7800
Mn	17.4374	16.3248	8.7061	14.9491
Ni	78.7599	82.1105	70.6910	94.2305
Mg	16.6620	13.7896	5.6480	4.5384
Ca	2.5673	4.9861	10.9614	20.5550
Na	25.8264	21.7289	35.6000	17.9423

The average compositions for brown and bleached pyroxenes in each sample have been plotted with the averages for calcium-poor pyroxene analyses, on the pyroxene quadrilateral in Figure 4.8.

From this it can be seen that the brown calcium-rich pyroxenes define a continuous fractionation trend from dolerites to granophyres, with compositions ranging from augite to ferrohedenbergite. The bleached pyroxenes exhibit the same range in Fe/Mg composition but plot slightly closer to the Diopside-Hedenbergite join by virtue of their higher CaO content. Tie-lines joining average brown and bleached pyroxene compositions from the same sample often cross one another and show no constant orientation. This indicates that the partitioning of Fe and Mg between the two pyroxene varieties did not take place under equilibrium conditions.

4.2.1.2 The origin of the bleached calcium-rich pyroxenes.

Nwe (1976) showed that host augites from the Skaergaard intrusion, that were analyzed separately from the associated calcium-poor pyroxene exsolution lamellae, were enriched in calcium compared to the bulk composition of the augite prior to the exsolution. It may be considered possible that it is this subsolidus enrichment in calcium in host augites (because of exsolution) that has given rise to the enrichment in calcium in some of the calcium-rich pyroxenes from the New Amalfi Sheet. However the data of Coleman (1978) show that not only are host augites from the Skaergaard intrusion enriched in calcium, but that they are also enriched in titanium, compared to the bulk composition of the augites prior to exsolution. Since the bleached calcium-rich pyroxenes from the New Amalfi Sheet are enriched in calcium but depleted in titanium, compared to magmatic brown calcium-rich pyroxenes, it is unlikely that the calcium enrichment could be the result of exsolution.

In the introduction a number of reasons were cited from the literature for the occurrence of a more calcium-rich pale-green ferroaugite-to-ferrohedenbergite series, coexisting with a primary brown augite-to-ferrohedenbergite series. These included:

- Secondary alteration of the primary brown augite in the case of the Palisades Sill (Walker et al. (1973)).
- Post-cumulus crystallization in the case of the Dufek

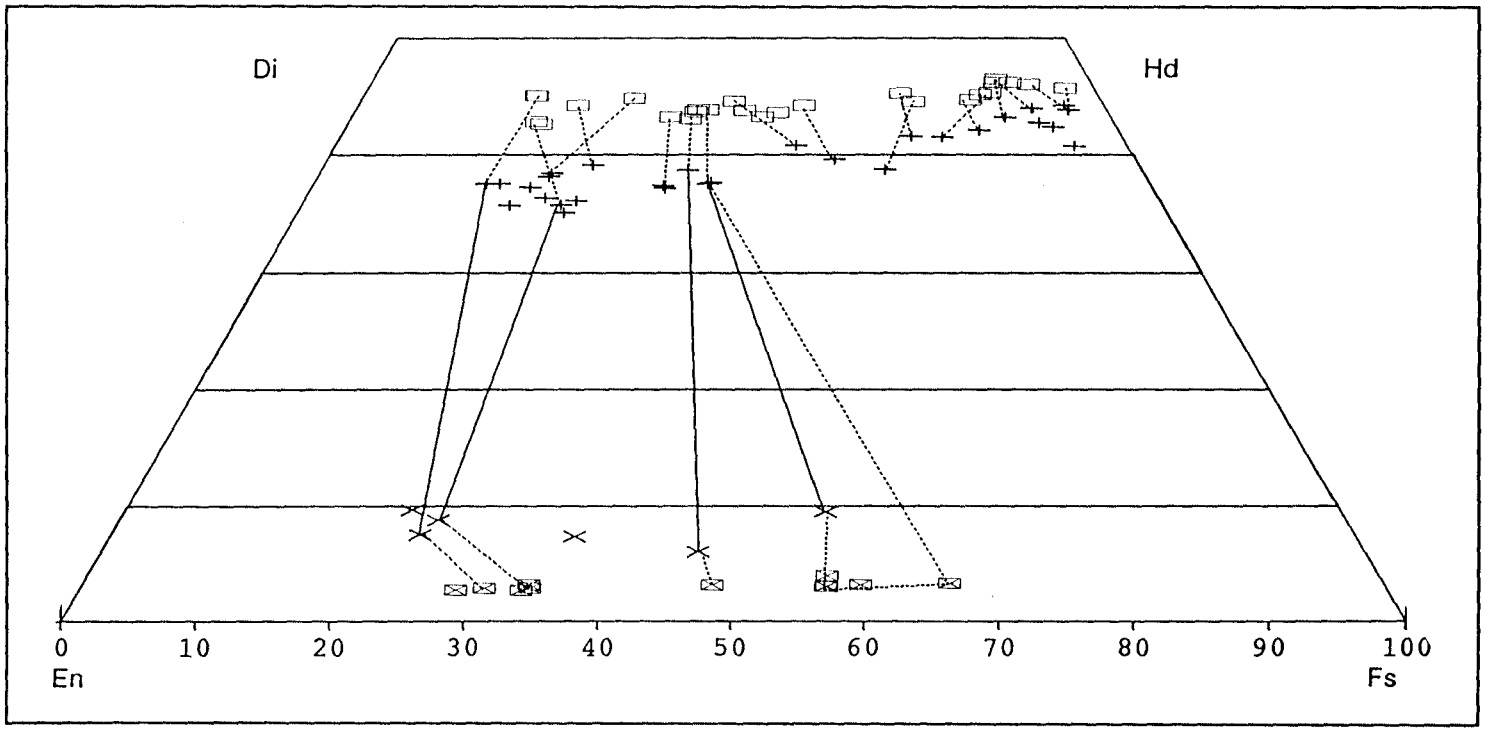

Figure 4.8 Average bleached CPX, brown CPX, pigeonite and orthopyroxene analyses for each sample. — solidus tie-lines; -- subsolidus tie-lines; ☐ = bleached CPX; + = brown CPX; x = pigeonite; ☒ = OPX.

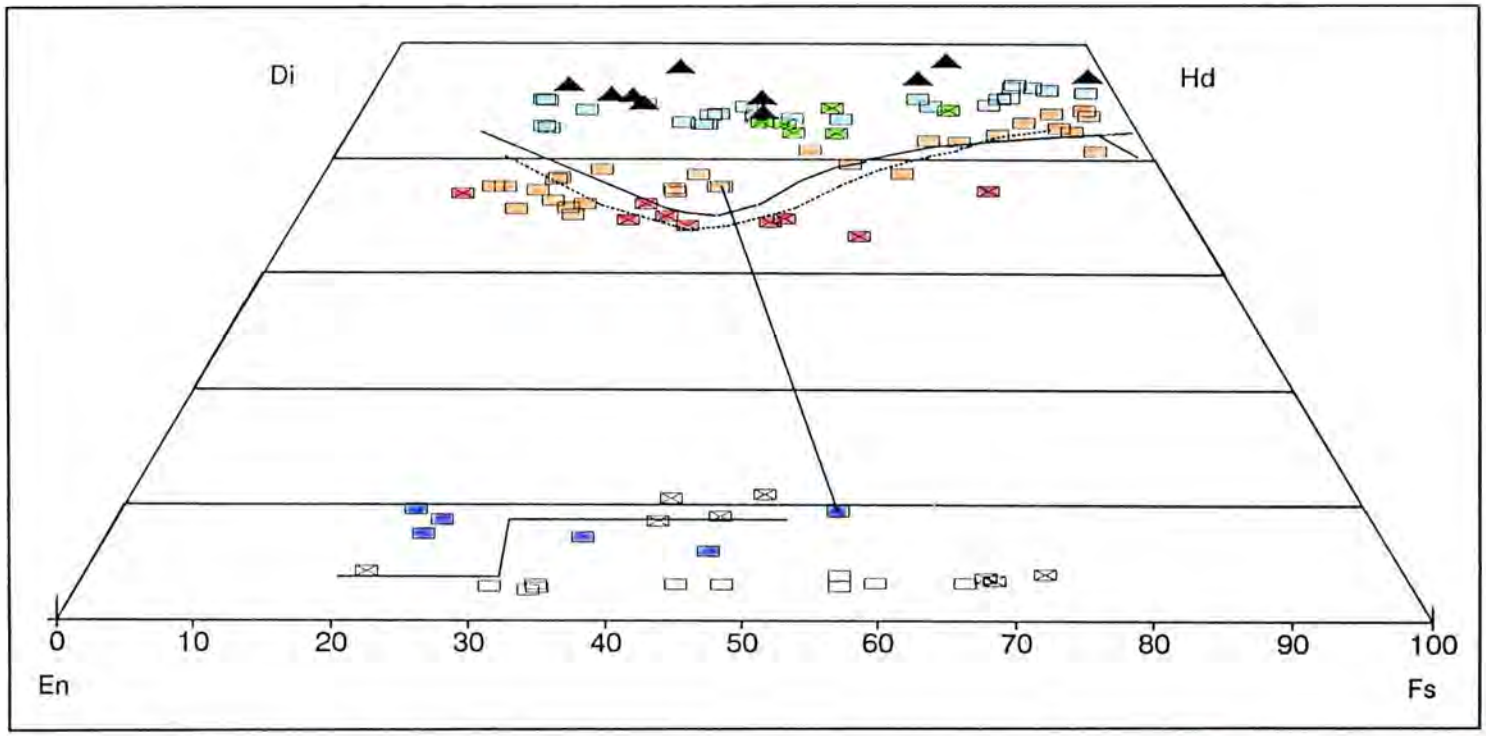

Figure 4.9 Average pyroxene analyses for the New Amalfi Sheet (□ = bleached, ■ = brown, ■ = pigeonite, ■ = OPX); Palisades Sill (⊠ = pale green CPX, ⊠ = mauve brown CPX, ⊠ = pigeonite and OPX) (Walker et al., 1973); Skaergaard Intrusion (—) (Wager and Brown, 1968); Birds River Intrusion (--) (Eales and Booth, 1974) and Skaergaard hydrothermal pyroxenes (▲) (Manning and Bird, 1986).

Intrusion (Himmelberg & Ford (1976)).

- Inversion of β-Wollastonite in the case of the Skaergaard Intrusion (Brown & Vincent (1963)).

The texture of the bleached calcium-rich pyroxenes of the New Amalfi Sheet, where they are seen partially to replace original brown augite grains, strongly supports the concept that they are the product of the alteration of the original brown augite. Inclusions of opaque oxide and hornblende within the bleached calcium-rich pyroxenes of the New Amalfi Sheet are also seen within the pale-green ferroaugites of the Palisades Sill, and may also represent the by-products of the alteration process, as suggested in the case of the Palisades Sill by Walker et al. (1973). Other similarities between the occurrence of pale-green ferroaugite at the Palisades Sill and bleached calcium-rich pyroxene at the New Amalfi Sheet include:

- Enrichment in CaO and depletion in TiO_2 of the bleached/pale-green series compared to the original brown augite series.
- Random arrangement of the tie lines connecting coexisting pairs of bleached/pale-green and original brown calcium-rich pyroxenes, indicating that the distribution of Fe and Mg between these two pyroxene series was not governed by a constant distribution coefficient K_D, which would have been the case if both pyroxene series had crystallized from a melt.
- Only the pyroxene and not the coexisting plagioclase was affected by the hydrothermal alteration.

Walker et al. (op. cit.) state that the reactions took place during the latter stages of crystallization and subsolidus cooling and were achieved largely by diffusion. Smith (1970) described a similar occurrence of normally tan coloured augites within diabases from the Sierra Ancha sill complex which had been partially 'bleached colourless' and which were seen to contain small inclusions of opaque oxide and amphibole. The bleached augite was noted to be more calcic than the original tan augite and Smith (op. cit.) considered the bleached augite to be the

result of the deuteric alteration of the original tan augite which came into contact with water-rich fluid at temperatures below that of the solidus.

Manning and Bird (1986) described the occurrence of secondary calcic pyroxenes, which formed from the reaction of magmatic augites with high-temperature aqueous solutions, within veins of the Skaergaard intrusion. These hydrothermal calcic pyroxenes are similar in composition to the bleached calcium-rich pyroxenes from the New Amalfi Sheet. This can be seen from Figure 4.9 where a number of averaged analyses from Manning and Bird (1986) have been plotted together with averaged pyroxene analyses from the New Amalfi Sheet. The hydrothermal pyroxenes, described by Manning and Bird (1986), are depleted in Fe and Mg and enriched in Ca and Si, compared to the igneous augites of the layered series of the Skaergaard Intrusion. They were also described by Manning and Bird (op. cit.) as being colourless to light green in colour, and intergrown with minute grains of magnetite, ilmenite and hornblende. An oxygen isotope study of the Skaergaard intrusion by Taylor and Forester (1979) shows that the hydrothermal fluids responsible for the alteration were of meteoric origin.

The hydrothermal pyroxenes of Manning and Bird (1986) are very similar to the pale-green pyroxenes described by Walker et al. (1973), and the bleached augite described by Smith (1970), except that they formed from the interaction of magmatic augites with hydrothermal fluids of meteoric origin, and not deuteric fluids as in the case of Smith (1970). Because of the similarity between the bleached calcium-rich pyroxenes from the New Amalfi Sheet to those described above, it seems likely that the bleached pyroxenes from the New Amalfi Sheet also formed from the interaction of magmatic calcium-rich pyroxenes with hydrothermal fluids at temperatures below that of the solidus of the magmatic pyroxenes. It is, however, not possible to say whether the hydrothermal fluids were of deuteric or meteoric origin as this can only be determined from oxygen-isotope study studies of the intrusion.

Average compositions of bleached calcium-rich pyroxenes have been recalculated using the equations of Lindsley (1983) and plotted on the pyroxene quadrilateral containing the isotherms of the pyroxene solvus at 1 atmosphere pressure (Figure 4.10). The temperatures calculated for bleached pyroxenes by this method yield the minimum temperatures of the hydrothermal fluids with which the pyroxenes equilibrated, according to Manning and Bird (1986) who used the same method to estimate the temperatures of formation of the Skaergaard hydrothermal pyroxenes. From Figure 4.10 it can be seen that the temperatures at which the bleached pyroxenes equilibrated range from 950°C in the dolerites to 500°C in the granophyres. The lowest temperature of equilibration of the New Amalfi Sheet bleached pyroxenes is the same as that determined for the Skaergaard hydrothermal pyroxenes by Manning and Bird (1986), but the highest temperature is 200° higher than the maximum temperature of 750°C calculated by Manning and Bird for the Skaergaard hydrothermal pyroxenes.

4.2.1.3 The mineral chemistry of the brown calcium-rich pyroxenes from the New Amalfi Sheet.

Pyroxenes have long been used by petrologists as petrogenetic indicators because of their abundance and prolonged period of crystallization in basaltic liquids. Bence and Papike (1972) showed that variation in the concentrations of Ti and Al within lunar pyroxenes were sensitive indicators of the position of plagioclase within the paragenetic sequence. Pyroxenes with high Ti/Al ratios of around the limiting value of 1/2 were indicative of early plagioclase nucleation prior to pyroxene nucleation. Other pyroxenes showed a shift from initially low Ti/Al ratios of around 1/4 towards the 1/2 limiting value and this sudden change in Ti/Al ratio coincided with the late entry of plagioclase in the paragenetic sequence, after the nucleation of pyroxene. The entry of plagioclase into the paragenetic sequence was also shown by Bence and Papike (op cit) to be marked by a change in the Al/Si ratio of pyroxenes crystallizing at the time, from increasing to decreasing values.

Later experimental work of Grove and Bence (1977) showed that the

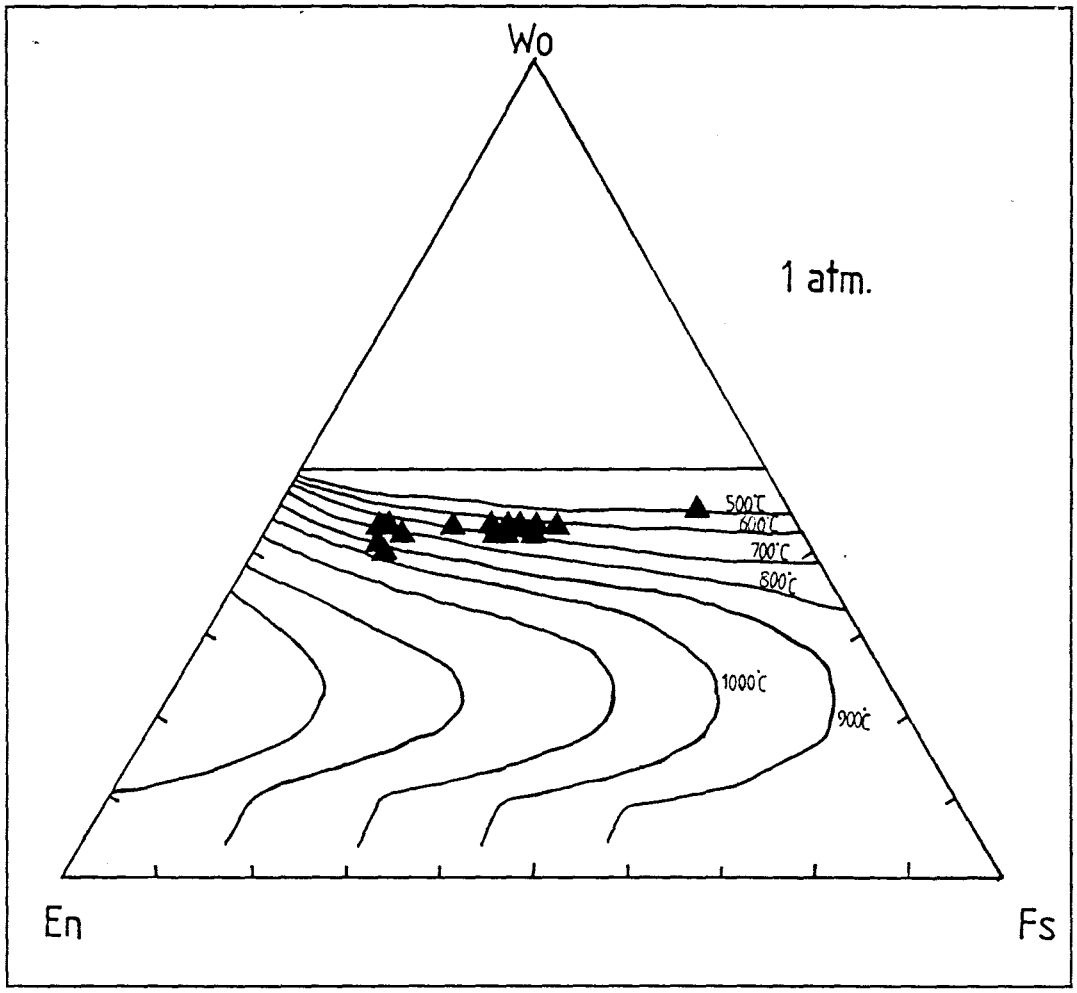

Figure 4.10 Average New Amalfi Sheet bleached pyroxene analyses projected onto the 1 atmosphere isotherms of Lindsley (1983).

partitioning of major elements (Ca, Fe & Mg) between liquid and pyroxene was independent of the cooling rate. Therefore the change in the concentration of these elements in pyroxene is a reflection of the efficiency of the fractional crystallization process, the relative diffusion of the elements in the liquid, and the timing of the entry of major phases in the crystallization sequence, because of the effect this has on the liquid line of descent, and thus on the composition of the pyroxene crystallizing from the liquid. Grove and Bence (op. cit.) also found that the partitioning of minor elements such as Ti, Al and Cr between liquid and pyroxene is strongly dependent on cooling rate and that these elements are more abundant in pyroxenes that have experienced higher rates of cooling.

Shearer et al. (1989) investigated the effects of cooling rate and the position of plagioclase in the paragenetic sequence on the partitioning of REE and trace elements between liquid and pyroxene. It was found that the suppression of plagioclase crystallization has no effect on the distribution of REE and Sr in pyroxenes, because of the large differences in distribution coefficients between these elements and plagioclase and pyroxene. It was found that REE elements are more abundant in calcium-rich pyroxenes than in calcium-poor pyroxenes, since the pyroxene M2 site is 'propped open' by the presence of Ca, thus allowing for easier entry of the REE in calcium-rich pyroxenes. The progressive enrichment in the residual melt of the REE because of fractional crystallization was, however, found to be a more important factor in controlling progressive REE enrichment in augite, than the suppression of plagioclase crystallization or the size of the M2 site. Eales et al. (1993) linked Ti and Al variation in Bushveld Complex orthopyroxenes to the entry of plagioclase as a cumulus phase within the complex.

In this section the chemical variation, with progressive differentiation of the brown calcium-rich pyroxenes of the New Amalfi Sheet, is presented and the petrogenetic significance of these variations is discussed. Despite the large average intra-sample coefficients of variation, plots of average compositions of the brown calcium-rich pyroxenes for each sample produce

continuous trends through the entire sequence from dolerites to granophyres, as was shown in Figure 4.8. The data from Figure 4.8 has been plotted in Figure 4.9 together with data from the Skaergaard Intrusion, the Palisades Sill and the Birds River Complex for comparison. It can be seen from Figure 4.9 that the range in composition of the brown calcium-rich pyroxenes from the New Amalfi Sheet is similar to that of the Skaergaard Intrusion, the Birds River Complex and the Palisades Sill, except that the New Amalfi Sheet brown pyroxenes do not exhibit a pronounced calcium minimum half-way through the fractionation sequence, as in the case of the Skaergaard Intrusion and Birds River Complex. This is probably because the New Amalfi Sheet brown pyroxene analyses represent average compositions which may be slightly enriched in CaO through the inclusion of some pyroxenes of transitional composition in the averages.

Figure 4.11 shows a plot of Al versus magnesium number (atomic $Mg/(Mg+Fe^{2+})$), hereafter referred to as Mg#. The Mg# is a sensitive indicator of degree of differentiation since rocks and ferromagnesian minerals in tholeiitic systems undergo systematic enrichment in Fe and depletion in Mg, as differentiation proceeds. The Mg# is also an indication of temperature as more evolved rocks crystallize at lower temperatures. From Figure 4.11 it can be seen that Al in the brown pyroxene decreases linearly with progressive differentiation. Maeda et al. (1991) established a trend of decreasing Al with decreasing temperature in orthopyroxenes from metaluminous rocks, and decreasing temperature seems to be one of the factors controlling the decrease in Al in the brown pyroxenes from the New Amalfi Sheet. The other factor which controls the concentration of Al in pyroxenes is the presence of plagioclase in the crystallizing assemblage, as Eales et al. (1993) found a broad trend of increasing Al in Bushveld orthopyroxenes prior to cumulus plagioclase nucleation, and declining Al after plagioclase nucleation. Thus the decrease in Al in the New Amalfi brown pyroxenes seems to indicate that plagioclase was already on the liquidus prior to emplacement and in situ differentiation of the sheet. This idea is corroborated by the fact that chilled contact dolerites exhibit a glomeroporphyritic texture with plagioclase

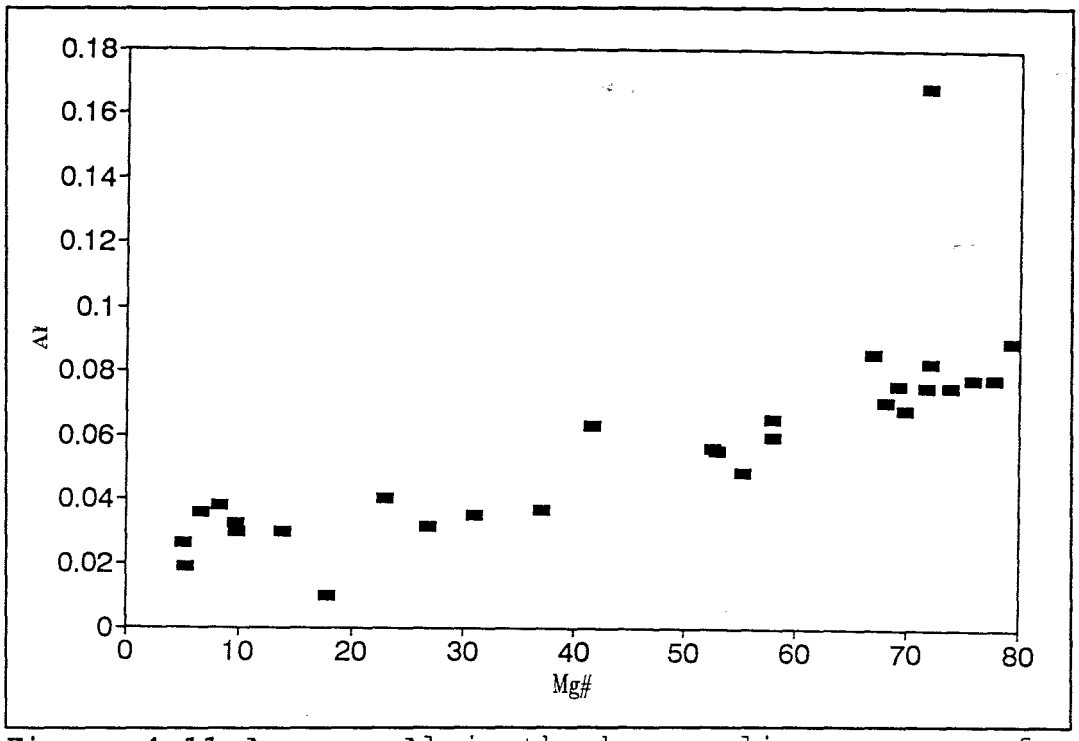

Figure 4.11 Average Al in the brown clinopyroxenes for each sample, calculated to 6 oxygens, plotted against Mg#.

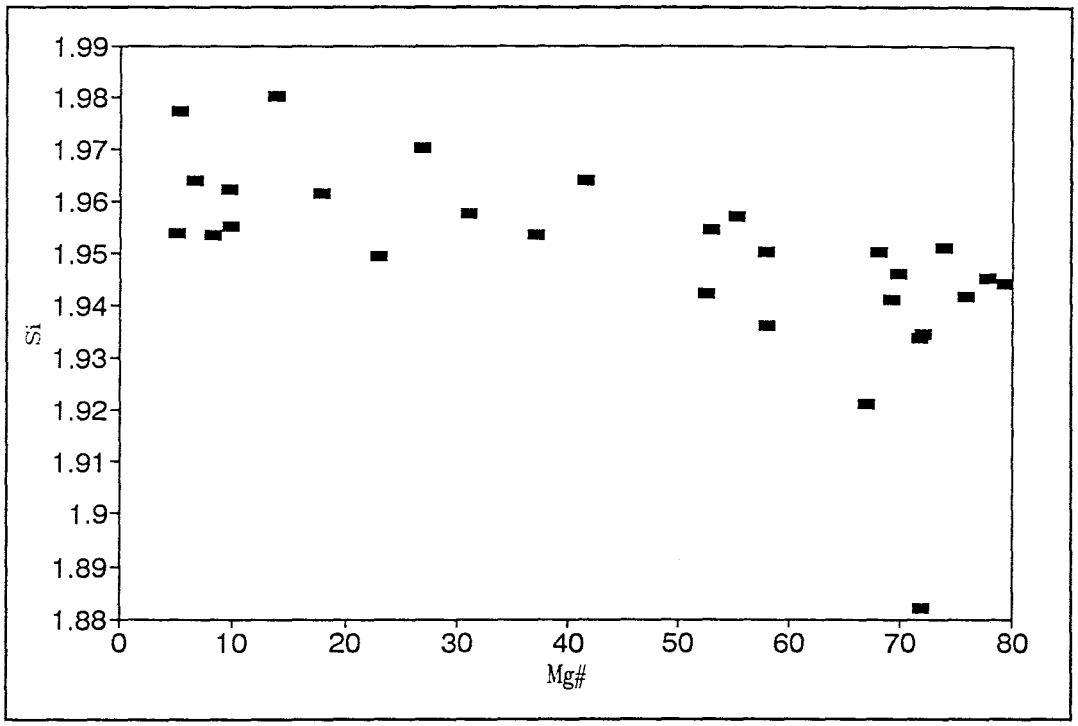

Figure 4.12 Average Si, calculated to 6 oxygens, versus Mg# for New Amalfi Sheet brown clinopyroxenes.

as a phenocrystal phase.

Figure 4.12 shows Si cations increasing with differentiation in the brown pyroxenes. This seems to reflect the increasing silica content of the New Amalfi Sheet residual melt with progressive differentiation. Figure 4.13 shows that Al content decreases with respect to Si, with Al/Si ratios decreasing from dolerites to granophyres. This once again indicates that plagioclase was already on the liquidus in the dolerites of the New Amalfi Sheet as Bence and Papike (1972) showed that Al/Si ratios decline in pyroxenes after the entry of plagioclase in the paragenetic sequence. The amount of Al drops to such low levels in the latter stages of differentiation that there is not enough Si and Al to fill the tetrahedral site, as seen in those points that plot below the line in Figure 4.13. Normally these points would be regarded as inferior analyses; but in this case, these samples seem to reflect the effect of the gradational nature of the pyroxene alteration, which has caused the averages for some of the brown pyroxenes to have lower Al than would normally be the case. In support of this idea is the fact that the bleached pyroxenes clearly have lower Al contents than the brown pyroxenes, as is shown in Figure 4.14.

In Figure 4.15, Ti has been plotted against Al for the brown pyroxenes. This type of plot has been used successfully by Bence and Papike (1972) and Eales et al. (1993) to show the point of entry of plagioclase in the paragenetic sequence. As mentioned above, Ti/Al ratios in pyroxenes increase rapidly from low values of around 1/4 to the limiting value of 1/2 after the entry of plagioclase in the paragenetic sequence. The trend seen in Figure 4.15 of increasing Ti/Al ratios, from 1/6 to over 1/2 from dolerites to granophyres in the New Amalfi Sheet, therefore represents the trend seen after plagioclase nucleation, once again indicating that plagioclase was already on the liquidus when these pyroxenes were crystallizing. Since Ti and Al enter pyroxene by means of a coupled substitution of the form $R^{2+}TiAl_2O_6$, the maximum value of Ti/Al is 1/2. The fact that brown pyroxenes from the granophyres have Ti/Al ratios over 1/2 once again indicates Al loss because of alteration in these pyroxenes.

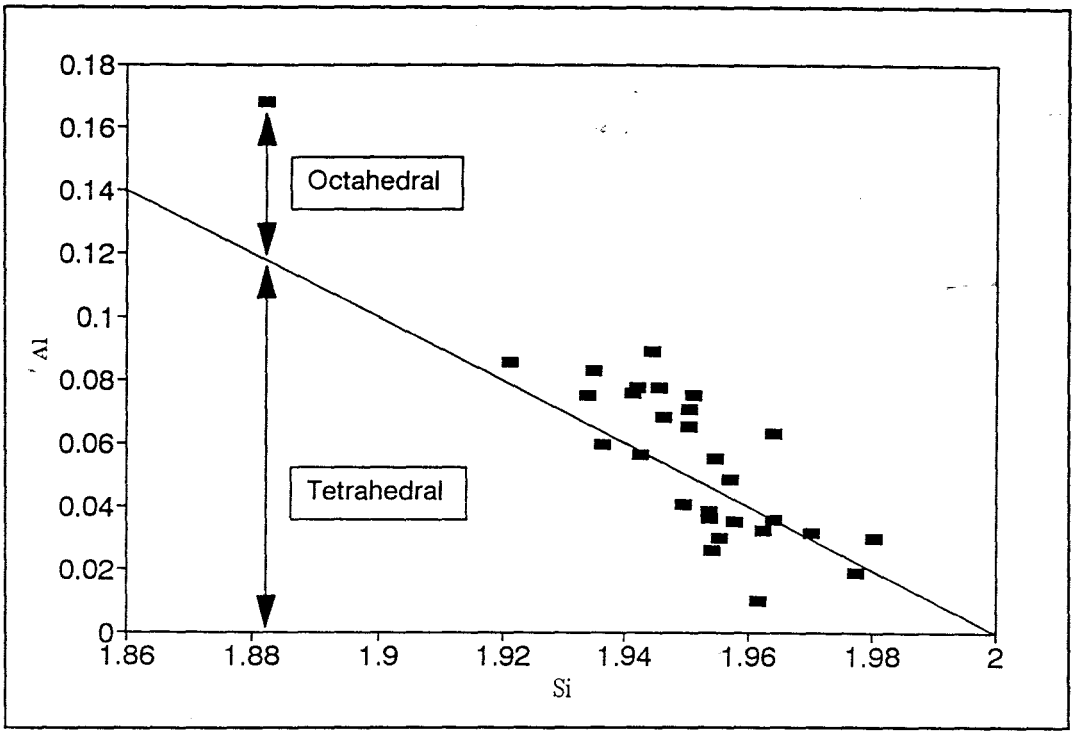

Figure 4.13 Average Al versus Si for New Amalfi Sheet brown pyroxenes.

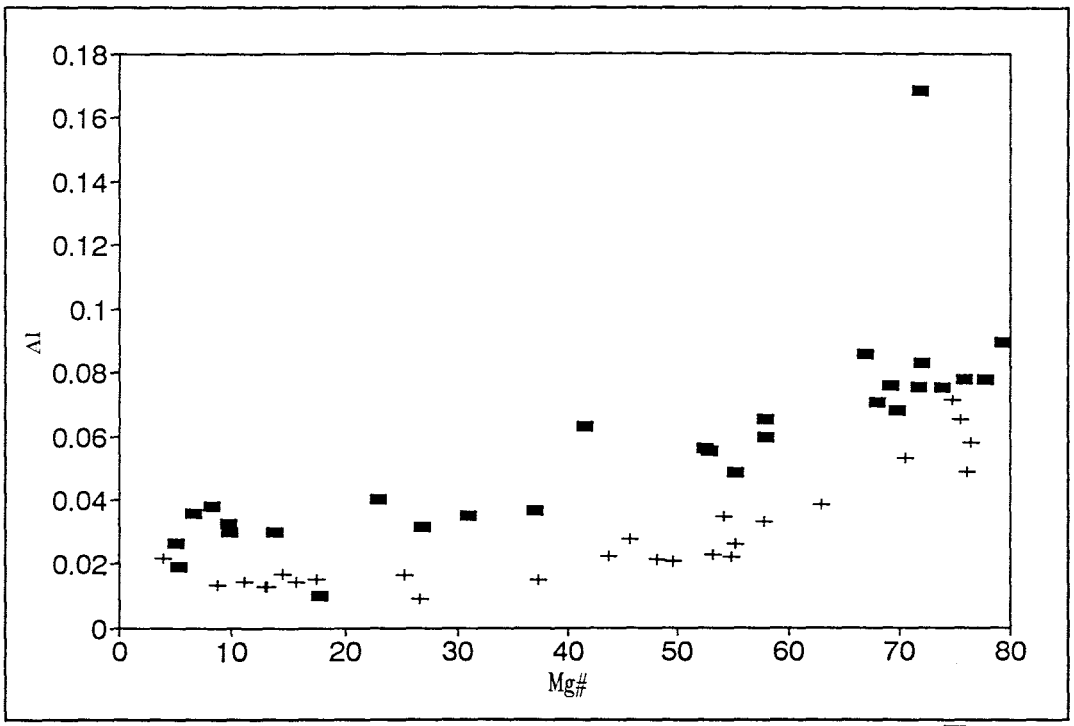

Figure 4.14 Average Al versus Mg# for brown (■) and bleached (+) clinopyroxenes.

Figure 4.16 shows that the Cr content of the brown pyroxenes declines rapidly with differentiation. This is a function of the high distribution coefficient that exists for the partitioning of Cr between the liquid and calcium-rich pyroxene. Figure 4.17 shows that there is a linear increase in Mn in brown pyroxenes with differentiation. This is very similar to the trend reported for Bushveld orthopyroxenes by Eales et al. (1993) and shows that Mn behaves in a similar way to Fe, with both increasing in pyroxenes with progressive differentiation.

4.2.2 Calcium-Poor Pyroxenes.

4.2.2.1 The calcium-poor pyroxenes and the limit of the two-pyroxene field.

From Figure 4.8 it can be seen that the most magnesian calcium-poor pyroxene analyzed from the New Amalfi Sheet is a pigeonite. This indicates that the orthopyroxene-pigeonite inversion curve had already been crossed when the lowest dolerites within the New Amalfi Sheet began to crystallize. The pigeonites can be seen to show progressive iron enrichment with differentiation through the quartz gabbros before they disappear half-way through the quartz monzodiorites. Tie-lines are shown linking the compositions of coexisting pigeonite and orthopyroxene pairs. The orthopyroxenes represent inverted pigeonites except in the case of the most iron-rich orthopyroxene shown which has the composition of ferrohypersthene. The ferrohypersthene is not considered to be the inversion product of the coexisting pigeonite, the reasons for which are discussed in the next section.

The tie-line linking the last pigeonite to form with its coexisting brown augite apparently represents the limit of the two-pyroxene field within the New Amalfi Sheet. The two-pyroxene field is that portion of the pyroxene quadrilateral in which a calcium-rich and calcium-poor pyroxene crystallized together from the liquid. The limit of the two-pyroxene field normally coincides in tholeiitic systems with an inflection in the augite trend from calcium depletion to calcium enrichment as is seen in

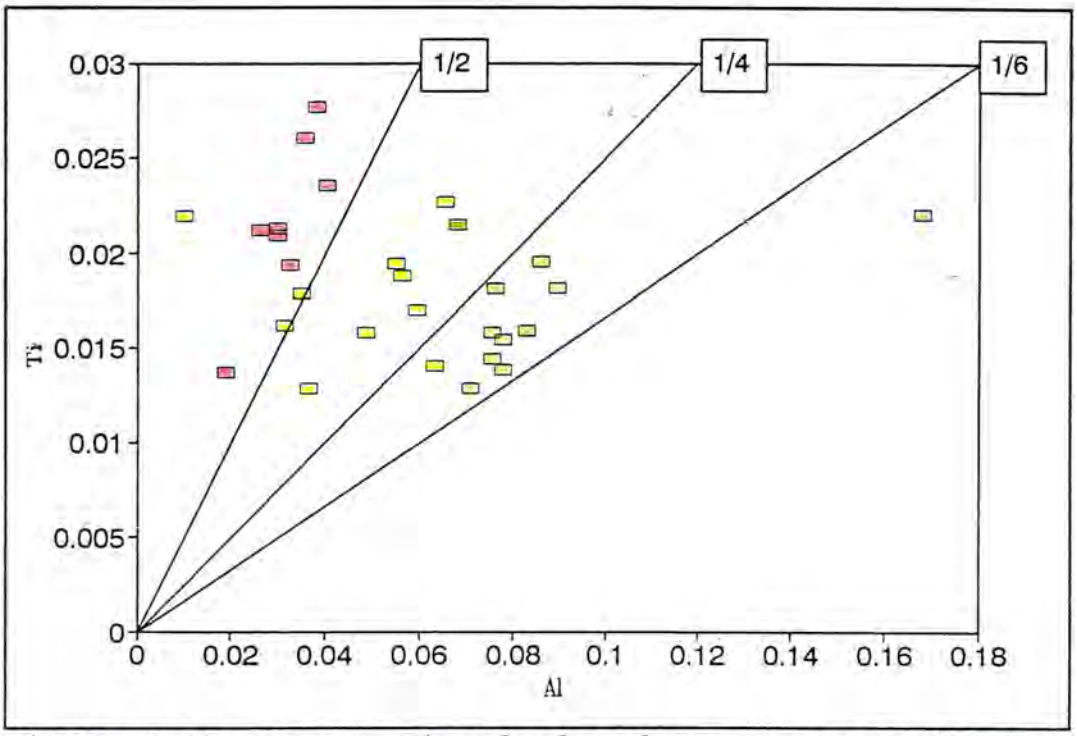

Figure 4.15 Average Ti calculated to 6 oxygens for New Amalfi Sheet brown clinopyroxenes plotted against average Al. ■ = dolerites; ■ = gabbros and diorites; ■ = granophyres

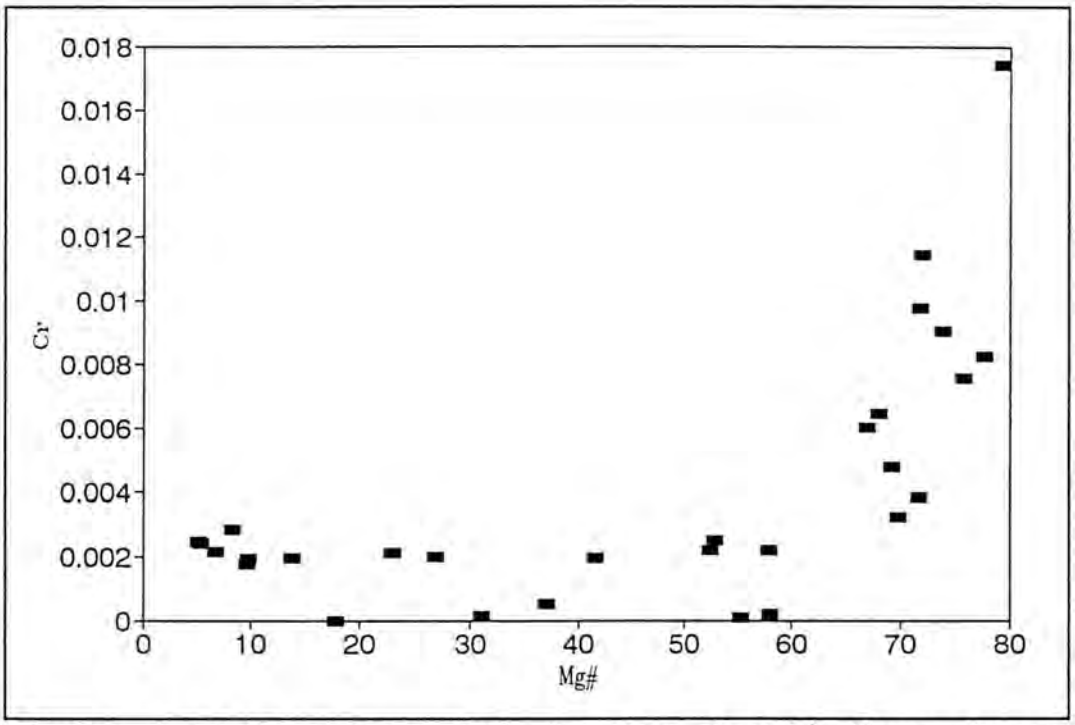

Figure 4.16 Cr versus Mg# for New Amalfi Sheet brown pyroxenes.

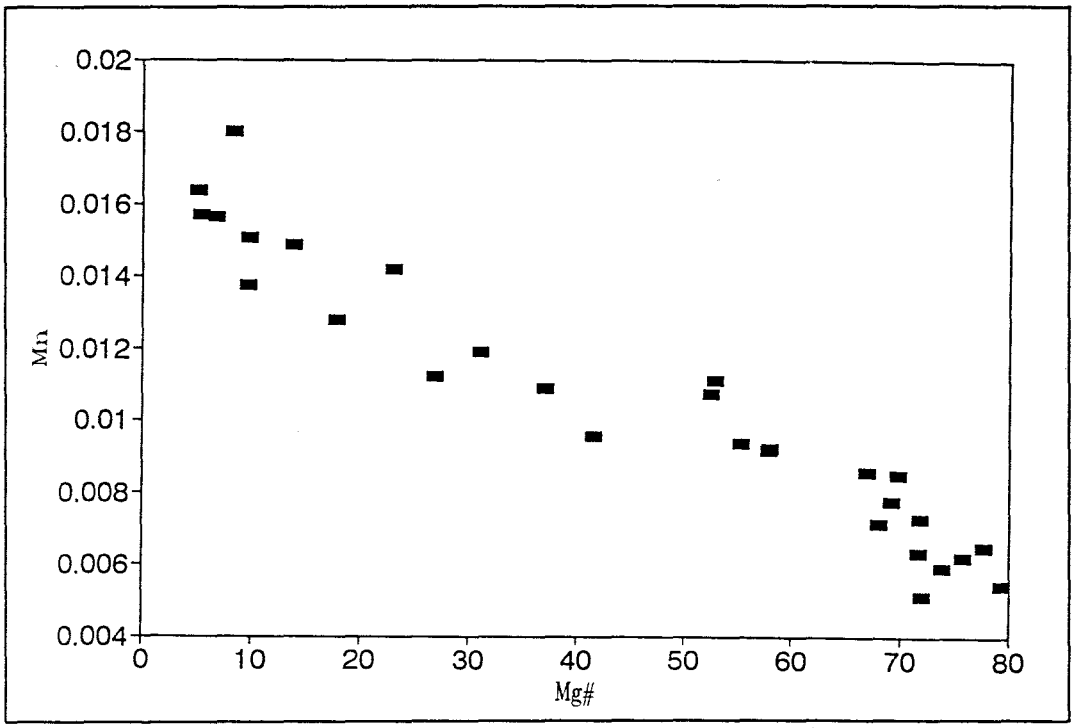

Figure 4.17 Mn versus Mg# for New Amalfi Sheet brown pyroxenes.

the case of the Skaergaard and Bushveld intrusions (Deer et al., 1978). From Figure 4.9 it can be seen that the two-pyroxene limit of the New Amalfi Sheet coincides with the inflections in the Skaergaard and Birds River augite trends, thus indicating that the limits of the two-pyroxene fields in these two intrusions occur at approximately the same position as that of the New Amalfi Sheet.

Lindsley and Munoz (1969) stated that the termination of the two-pyroxene field is due to its impinging on the 'forbidden zone'. The forbidden zone was defined as a field of fayalite and quartz found within the pyroxene quadrilateral at low pressures (2Kb or less) and within which no pyroxene was stable. The forbidden zone is found within that portion of the pyroxene quadrilateral normally occupied by iron-rich calcium-poor pyroxene at high pressure and the position of the forbidden zone boundary along the enstatite-ferrosilite join is a function of pressure and temperature. At low pressures iron-rich calcium-poor pyroxene becomes unstable and breaks down according to reaction (1).

2*(calcium-poor pyroxene) = 2*fayalite + quartz .....(1)

However in the case of the Skaergaard and Bushveld intrusions, the two-pyroxene field is terminated before the 'forbidden zone' is reached and quartz is not present as a primary phase so that reaction (1) cannot be responsible for the disappearance of calcium-poor pyroxene. Instead, the disappearance of calcium-poor pyroxene must be related to the silica activity of the melt according to reaction (2).

$Fe_2Si_2O_{6\ (\text{in pyroxene})} = Fe_2SiO_{4\ (\text{in olivine})} + SiO_{2\ (\text{in melt})}$ .....(2)

Under equilibrium conditions the above reaction can be expressed in terms of the activity of the various components according to equation (3).

$$K = \frac{a_{Fe_2SiO_4} \times a_{SiO_2}}{a_{Fe_2Si_2O_6}} \quad .....(3)$$

As can be seen from the above equation, an increase in $aSiO_2$ must cause a decrease in aFe_2SiO_4 or an increase in $aFe_2Si_2O_6$. When $aSiO_2$ is at a maximum of 1, the liquid is saturated with respect to SiO_2 and quartz will be seen as a primary phase. The stability field of calcium-poor pyroxene is then at its maximum and will thus extend to the boundary of the forbidden zone. However if $aSiO_2$ is less than one, reaction (2) will take place earlier in the differentiation sequence and the two-pyroxene field will not reach its maximum limit, namely the boundary of the forbidden zone.

It can therefore be seen that in general the presence of primary quartz coexisting with calcium-poor pyroxene prior to its disappearance indicates that the reaction (1) must have taken place and thus that the forbidden zone was reached within a particular intrusion. Campbell and Nolan (1974) consider the Palisades Sill to be an example of such an intrusion where the enrichment in SiO_2 with differentiation was sufficiently strong to cause the formation of primary quartz prior to the disappearance of calcium-poor pyroxene, and therefore stabilized the calcium-poor pyroxene until the forbidden zone was reached. In the case of the New Amalfi Sheet primary quartz is seen only within the granodiorites while pigeonite disappears shortly before this stage, in the quartz monzodiorites. Therefore it can be said that in the case of the New Amalfi Sheet the two-pyroxene field was terminated shortly before the system reached the forbidden zone and this is because SiO_2 enrichment was not high enough to stabilize the calcium-poor pyroxene until the forbidden zone was reached. The disappearance of pigeonite and therefore the termination of the two-pyroxene field within the New Amalfi Sheet was a result of reaction (2) a contention supported by the fact that the reappearance of fayalitic olivine coincides with the disappearance of pigeonite within the quartz monzodiorites.

4.2.2.2 The origin of the ferrohypersthene.

In the Palisades Sill ferrohypersthene is seen by Walker et al. (1973) as a primary phase taking the place of pigeonite in the late stages of differentiation and it is therefore seen to extend

the two-pyroxene field to low enstatite values where it terminates at the boundary of the forbidden zone, as was discussed above. The origin of ferrohypersthene within the New Amalfi Sheet is crucial to the understanding of the differentiation process, as ferrohypersthene is seen together with primary quartz in the granodiorites and this would indicate that the forbidden zone had been reached in the case of the New Amalfi Sheet as well, if the ferrohypersthene were of primary origin.

Heubner and Turnock (1980) have shown from melting experiments on natural pyroxenes that pigeonite is the liquidus phase at Fe/(Fe+Mg) values greater than 0.45 in natural systems. Orthopyroxene is stable only at lower temperatures, below that of the orthopyroxene-pigeonite inversion curve, and is therefore normally seen only as a subsolidus inversion product of pigeonite in iron-rich rocks.

Poldervaart and Hess (1951) state that the late crystallization of ferriferous orthopyroxene after that of pigeonite can normally be ascribed to growth from late-stage residual liquids at temperatures below that of the orthopyroxene-pigeonite inversion curve. This is similar to the explanation given by Himmelberg and Ford (1976) for the origin of the ferrohypersthene found within the Dufek Intrusion, namely, that it crystallized from a late-stage intercumulus liquid. Small irregularly-shaped crystals of ferrohypersthene which formed after ferropigeonite have been described from the Beaver Bay intrusion in Minnesota by Nakamura and Konda (1974). These authors also ascribe the origin of the ferrohypersthene to crystallization from intercumulus liquid which, once trapped by surrounding cumulus crystals, followed a different differentiation path to that of the main body of residual liquid, possibly because of different fO_2 conditions within the intercumulus liquid. Mangan et al. (1993) described ferrohypersthene from the York Haven Diabase Sheet in Pennsylvania, and considered it to be a product of the hydrothermal alteration of magmatic clinopyroxene.

On the basis of the work of Heubner and Turnock (1980) the

ferrohypersthene seen within the New Amalfi Sheet is unlikely to be a primary phase that crystallized directly from the fractionating liquid, since pigeonite is the stable phase at liquidus temperatures. The ferrohypersthene is unlikely to represent inverted pigeonite, because it shows no exsolution and is found together with undoubted inverted pigeonite within the quartz gabbros and the quartz monzodiorites. The inverted pigeonite shows the characteristic patchy inversion of iron-rich pigeonite and also exhibits exsolution. It would be difficult to explain why one group of inverted pigeonites, found together in the same rock as another group of inverted pigeonites, should display features such as exsolution and patchy inversion, and the other group not.

The only other two possible explanations as to the origin of the ferrohypersthene would seem to be those that have been used before in the literature, namely crystallization from late-stage intercumulus liquids at temperatures below that of the orthopyroxene-pigeonite inversion curve, or secondary alteration of pyroxene by hydrothermal fluids. The textures exhibited by the ferrohypersthenes do not help in resolving this problem, as the ferrohypersthene occurs both as an interstitial phase (Plate 3.2.5) and within composite pyroxene grains (Plate 3.2.6). The former texture would tend to support the intercumulus origin and the second the hydrothermal alteration origin. Since the hydrothermal alteration products of the calcium-rich pyroxene have already been identified and discussed in detail, it is unlikely that the same process would produce a different alteration product of the calcium-rich pyroxene. The ferrohypersthene may represent the hydrothermal alteration product of the calcium-poor pyroxene in some cases but this does not explain why the ferrohypersthene is still present at low levels within the granodiorites, after the disappearance of pigeonite in the quartz monzodiorites. Thus the ferrohypersthene is most probably of late stage intercumulus origin.

4.2.2.3 The mineral chemistry of the calcium-poor pyroxenes of the New Amalfi Sheet.

Averages of pigeonite and orthopyroxene analyses from each sample are shown in Table 4.4, and average coefficients of variation for the cations are shown in Table 4.3. The average sum of cations is 3.993 for the orthopyroxenes and 3.980 for the pigeonites. The average charge deficit of the orthopyroxenes is 0.0162, slightly higher than that of the pigeonites at 0.0049.

The mineral chemistry of the calcium-poor pyroxenes follows that of the calcium-rich pyroxenes in most cases, with Al decreasing and Si and Mn increasing in the orthopyroxenes with progressive differentiation. The same reasons put forward for the variation of these elements within the calcium-rich pyroxenes are put forward for their variation in the calcium-poor pyroxenes.

The main difference between the chemistry of the calcium-rich and calcium-poor pyroxenes lies in the variation with differentiation of Ti within the calcium-poor pyroxenes. A plot of Ti versus Al concentration within the calcium-poor pyroxenes is shown in Figure 4.18. It can be seen that both Ti and Al decrease in concentration within the calcium-poor pyroxenes with progressive differentiation from dolerites to quartz monzodiorites. This is different to what has been reported by Eales et al. (1993) for Bushveld orthopyroxenes which show decreasing Al and increasing Ti with progressive differentiation after the nucleation of plagioclase.

The crucial factor causing the different behaviour of the calcium-poor pyroxenes of the New Amalfi Sheet, with respect to Ti partitioning, appears to be the presence of primary calcium-rich pyroxene crystallizing together with the calcium-poor pyroxene, in the case of the New Amalfi Sheet. A plot of Ti versus Mg# for both calcium-poor and calcium-rich pyroxenes from the New Amalfi Sheet, in Figure 4.19, clearly shows that while Ti increases slightly with differentiation in the calcium-rich pyroxenes, it decreases with differentiation in the calcium-poor pyroxenes. This would also seem to rule out the possibility that Ti depletion in the calcium-poor pyroxenes was caused by the partitioning of the Ti into oxide phases, as a corresponding Ti depletion would then also be expected in the calcium-rich

Table 4.4

AVERAGE COMPOSITIONS OF PIGEONITES

Sample	NA72	NA99	NA100	NA124&124	NA93	NA90
Wt.%						
SiO2	54.34	54.90	54.38	52.88	51.57	51.87
TiO2	0.25	0.33	0.33	0.37	0.30	0.26
Al2O3	1.02	0.85	0.87	0.75	0.57	0.73
Cr2O3	0.09	0.17	0.08	0.07	0.00	0.06
FeO	13.99	14.75	15.23	21.74	27.42	29.67
MnO	0.32	0.25	0.32	0.28	0.49	0.45
NiO	0.09	0.03	0.02	0.06	0.01	0.04
MgO	25.43	25.01	24.37	20.38	17.07	12.53
CaO	4.94	3.78	4.43	3.57	2.90	4.34
Na2O	0.03	0.06	0.05	0.05	0.03	0.03
Total	100.51	100.12	100.07	100.14	100.36	100.00
Cations (based on 6 oxygens) :						
Si	1.9613	1.9851	1.9771	1.9775	1.9767	1.9838
Ti	0.0068	0.0089	0.0091	0.0105	0.0085	0.0074
Al	0.0433	0.0362	0.0373	0.0332	0.0258	0.0328
Cr	0.0026	0.0049	0.0024	0.0022	0.0001	0.0019
Fe2+	0.4223	0.4464	0.4630	0.6800	0.8793	0.9491
Mn	0.0097	0.0077	0.0098	0.0088	0.0160	0.0147
Ni	0.0027	0.0009	0.0006	0.0017	0.0002	0.0014
Mg	1.3681	1.3475	1.3204	1.1359	0.9747	0.7146
Ca	0.1911	0.1461	0.1726	0.1429	0.1193	0.1781
Na	0.0023	0.0040	0.0036	0.0033	0.0025	0.0025
Total	4.0102	3.987633	3.9958	3.996	4.0031	3.886116
Charge	-0.020	0.025	0.008	0.008	-0.006	0.015
Mg#	76.4	75.1	74.0	62.6	52.6	42.2
n	1	3	2	1	25	2

AVERAGE COMPOSITIONS OF ORTHOPYROXENES

Sample	NA99	NA132	NA97	NA124&125	NA100	NA93	NA95
Wt.%							
SiO2	53.91	53.83	53.32	53.55	52.14	51.45	50.93
TiO2	0.40	0.25	0.38	0.30	0.26	0.28	0.24
Al2O3	0.70	0.62	0.72	0.66	0.56	0.55	0.33
Cr2O3	0.10	0.08	0.08	0.08	0.09	0.01	0.07
FeO	19.15	20.66	20.84	21.29	25.97	28.73	32.95
MnO	0.35	0.34	0.37	0.28	0.44	0.52	0.51
NiO	0.06	0.02	0.02	0.08	0.04	0.02	0.03
MgO	23.91	22.71	22.32	22.64	18.13	17.12	13.79
CaO	1.46	1.29	1.53	1.42	1.48	1.49	1.39
Na2O	0.03	0.01	0.04	0.02	0.03	0.01	0.03
Total	100.08	99.80	99.61	100.33	99.13	100.18	100.26
Cations (based on 6 oxygens) :							
Si	1.9800	1.9933	1.9837	1.9809	1.9992	1.9800	1.9979
Ti	0.0109	0.0071	0.0106	0.0083	0.0073	0.0082	0.0072
Al	0.0301	0.0269	0.0314	0.0289	0.0248	0.0247	0.0150
Cr	0.0029	0.0022	0.0024	0.0022	0.0028	0.0002	0.0022
Fe2+	0.5884	0.6416	0.6501	0.6590	0.8398	0.9253	1.0825
Mn	0.0110	0.0106	0.0117	0.0088	0.0144	0.0171	0.0169
Ni	0.0019	0.0006	0.0006	0.0024	0.0012	0.0006	0.0008
Mg	1.3087	1.2511	1.2359	1.2475	1.0279	0.9813	0.8047
Ca	0.0576	0.0511	0.0610	0.0562	0.0610	0.0615	0.0583
Na	0.0020	0.0010	0.0031	0.0017	0.0025	0.0011	0.0021
Totals	3.9936	3.9856	3.9904	3.9960	3.9810	3.9999	3.9875
Charge	0.013	0.029	0.019	0.008	0.038	0.000	0.025
Mg#	69.0	66.1	65.6	65.4	54.9	51.5	42.6
n	4	4	8	5	3	61	10

Sample	NA91	NA90
Wt.%		
SiO2	50.47	50.50
TiO2	0.24	0.22
Al2O3	0.48	0.34
Cr2O3	0.07	0.06
FeO	32.62	35.36
MnO	0.60	0.54
NiO	0.02	0.03
MgO	13.53	11.76
CaO	1.80	1.42
Na2O	0.06	0.03
Total	99.87	100.26
Cations (based on 6 oxygens)		
Si	1.9901	2.0050
Ti	0.0071	0.0064
Al	0.0221	0.0160
Cr	0.0020	0.0020
Fe2+	1.0758	1.1750
Mn	0.0200	0.0182
Ni	0.0007	0.0008
Mg	0.7948	0.6946
Ca	0.0761	0.0605
Na	0.0044	0.0022
Totals	3.9930	3.9807
Charge	0.014	0.039
Mg#	42.5	37.14
n	6	14

pyroxenes.

Heubner (1980) states that divalent trace-element cations such as Mn, Co and Zn favour calcium-poor pyroxene whereas cations that have other valencies, such as Ti, favour calcium-rich pyroxene. The values of $D_{Ti}^{Aug/opx}$ from the literature, range between 3.3 and 0.97, with all values except the lowest one being greater than one (Heubner, 1980). This indicates that when both calcium-poor and calcium-rich pyroxene are crystallizing, Ti will favour the calcium-rich pyroxene and this may explain why Ti decreases with differentiation in the calcium-poor pyroxenes of the New Amalfi Sheet.

4.3 OLIVINES.

4.3.1 Introduction.

Magnesium-rich olivine occurs mainly within the olivine dolerites, of which the basal sample (NA99) contains 14% modal olivine. This high proportion of olivine possibly accumulated by means of gravity-induced settling. The pigeonite dolerites contain noticeably less olivine and this may be because field evidence suggests that these dolerites are found near to the steeply dipping side of the intrusion and not at its base. This would have resulted in the pigeonite dolerites cooling more quickly than most of the olivine dolerites, leaving less time to accumulate olivine. Also, it is less likely that olivine would have accumulated within the exposed pigeonite dolerites by means of gravity settling, along the steeply dipping sides of the intrusion.

Olivine is absent within the quartz gabbros but reappears again in the form of iron-rich olivine mid-way through the quartz monzodiorites. This hiatus in olivine crystallization, often referred to in the literature as the 'olivine gap', is a common feature of many differentiated tholeiitic intrusions such as the Palisades Sill and the Skaergaard Intrusion. Iron-rich olivine is seen for the last time within the fayalite-hedenbergite granophyres.

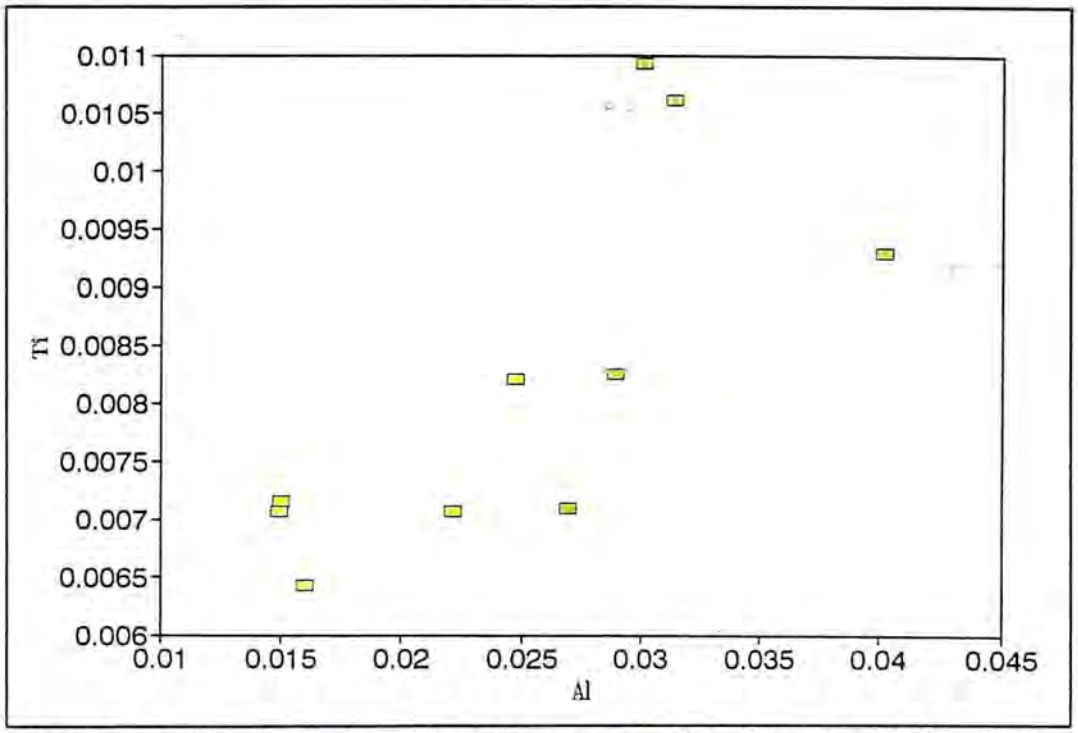

Figure 4.18 Average Ti versus Al for New Amalfi Sheet orthopyroxenes. ■ = dolerites; □ = gabbros.

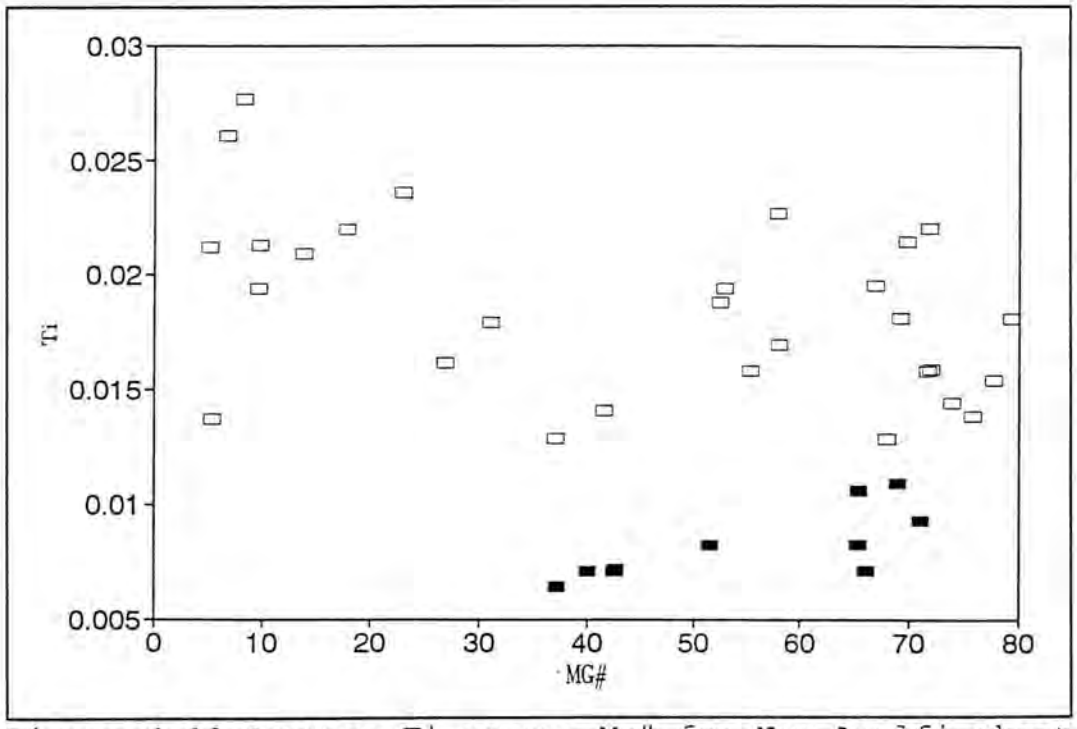

Figure 4.19 Average Ti versus Mg# for New Amalfi sheet brown pyroxenes (□) and orthopyroxenes (■).

The range in olivine compositions within the New Amalfi Sheet is from Fo_{73} to Fo_{50} prior to the olivine gap, and from Fo_{10} to Fo_2 after the olivine gap. The size of the olivine gap within the New Amalfi Sheet compares well with that of the Palisades Sill which occurs between Fo_{55} and Fo_{13} (Walker et al, 1973). The olivine gap within the Skaergaard Intrusion is, however, much smaller, occurring between Fo_{52} and Fo_{36} (Wager and Brown, 1968). This appears to be the result of silica enrichment with differentiation, within the Skaergaard intrusion being not as great as within the New Amalfi Sheet and the Palisades Sill. It can be seen from Figure 4.20, reproduced from Campbell and Nolan (1974), that the olivine gap within a particular intrusion can be increased by either increasing the level of increase in silica activity with differentiation, or by increasing the pressure. As both the New Amalfi Sheet and the Palisades Sill were intruded at shallow depths, the first option is considered more likely.

4.3.2 Mineral chemistry of the New Amalfi Sheet olivines.

Average analyses from samples containing olivine in the New Amalfi Sheet are shown in Table 4.5. A small degree of compositional zoning was noted within the magnesium-rich olivines. The iron-rich olivines show no zoning - a feature also noted by Walker et al. (1973) in the case of the iron-rich olivines of the Palisades Sill. Figure 4.21 shows a plot of Ni in olivine versus forsterite content of the olivine for the New Amalfi Sheet. It can be seen that Ni declines rapidly in olivine with decreasing forsterite content and this is a function of the high D_{Ni}^{Ol} (Hart and Davis, 1978).

Ni concentration in olivines, for a number of Karoo intrusions and for the Drumbo basalt member of Mitchell (1980), is shown plotted against the MgO content of the olivine in Figure 4.22. The data define a generally exponential curve which is once again a function of the high partition coefficient for Ni between olivine and melt. Two samples from the Insizwa lobe as well as all of the samples from the Tonti lobe of the Insizwa Complex, fall below the general trend of the data and this is thought to be due to a depletion in Ni in these olivines as a result of the

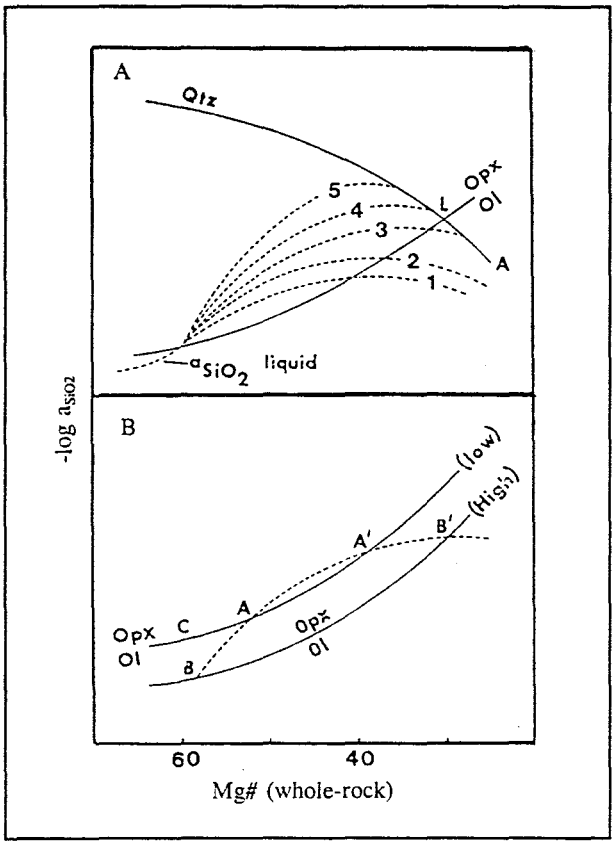

Figure 4.20 (a) The olivine gap can be increased by increasing the rate of increase of a_{SiO2} with differentiation. Curves 1 to 5 represent fractionation curves with progressively higher rates of increase in a_{SiO2} in each case.

Figure 4.20 (b) The olivine gap can also be increased by increasing the overall pressure of the system. The dotted line represents the fractionation curve for a given rate of increase in a_{SiO2} and the solid lines give the phase boundary between OPX and olivine at low and high pressure.

Table 4.5

AVERAGE COMPOSITION OF OLIVINES ANALYZED FOR EACH SAMPLE

Sample	NA99	NA100	NA101	NA130	NA131	NA132	NA97
Wt.%							
SiO2	37.33	37.00	35.30	34.95	34.88	34.69	36.98
FeO	26.96	29.71	37.12	41.18	40.14	40.88	31.68
MnO	0.42	0.46	0.52	0.55	0.57	0.61	0.48
NiO	0.18	0.13	0.11	0.13	0.10	0.11	0.16
MgO	34.67	32.79	26.68	23.13	24.14	23.36	31.17
CaO	0.06	0.09	0.07	0.02	0.05	0.04	0.04
Total	99.63	100.18	99.81	99.96	99.88	99.70	100.52
Cations (based on 4 oxygens) :							
Si	0.9991	0.9980	0.9943	1.0027	0.9971	0.9981	1.0029
Fe2+	0.6046	0.6730	0.8743	0.9885	0.9599	0.9836	0.7229
Mn	0.0096	0.0106	0.0125	0.0134	0.0138	0.0149	0.0112
Ni	0.0039	0.0029	0.0026	0.0029	0.0024	0.0027	0.0034
Mg	1.3819	1.3151	1.1200	0.9892	1.0282	1.0016	1.2554
Ca	0.0018	0.0025	0.0020	0.0007	0.0016	0.0012	0.0013
Fo	69.56	66.14	56.16	50.02	51.72	50.45	63.46
Fa	30.44	33.86	43.84	49.98	48.28	49.55	36.54
Ni ppm	1410.35	1047.05	890.35	982.72	806.27	899.72	1228.44
n	34	9	13	9	9	6	9

Sample	NA125	NA153	NA89	NA192
Wt.%				
SiO2	35.19	30.02	29.52	30.46
FeO	39.73	66.27	68.04	63.59
MnO	0.58	1.29	1.35	1.11
NiO	0.12	0.08	0.05	0.03
MgO	24.28	2.49	0.89	3.91
CaO	0.05	0.24	0.25	0.31
Total	99.95	100.38	100.10	99.42
Cations (based on 4 oxygens) :				
Si	1.0024	0.9959	0.9945	1.0051
Fe2+	0.9466	1.8385	1.9173	1.7547
Mn	0.0140	0.0362	0.0385	0.0311
Ni	0.0026	0.0022	0.0014	0.0009
Mg	1.0305	0.1230	0.0449	0.1924
Ca	0.0014	0.0084	0.0089	0.0109
Fo	52.12	6.27	2.29	9.89
Fa	47.88	93.73	97.71	90.12
Ni ppm	905.61	646.59	406.64	263.24
n	12	14	12	2

preferential partitioning of the Ni into an immiscible sulphide melt which formed at the same time as these olivines were crystallizing (Lightfoot et al., 1984).

The olivines from the New Amalfi Sheet plot slightly above the general trend of the data and this may be because of decreased Fo content within the New Amalfi Sheet olivines as a result of subsolidus re-equilibration with trapped intercumulus liquid, the so called 'trapped liquid shift effect', described for Insizwa Complex olivines by Cawthorn et al. (1992). Another explanation could be that D_{Ni}^{Ol}, which increases with decreasing MgO content of the melt (as shown by Hart and Davis, 1978), could have been higher in the case of the New Amalfi Sheet, because of a possibly lower MgO content of the initial New Amalfi Sheet melt. This would have caused more Ni to be partitioned into New Amalfi Sheet olivines.

4.4 FELDSPARS.

4.4.1 Introduction.

In the New Amalfi Sheet, plagioclase feldspar forms a continuous fractionation sequence from dolerites to fayalite-hedenbergite granophyres. Compositions range from bytownite to anorthoclase, which is found in the rims of some highly zoned plagioclase grains in fayalite-hedenbergite sample NA89 (Figure 4.23). The point at which potassium feldspar (hereafter referred to as K-feldspar) joins the fractionation sequence is difficult to determine, as it is found within the granophyric intergrowth which is present as an interstitial phase even within the lowermost dolerites. However the coarseness of the K-feldspar intergrown with quartz, in the granophyric intergrowth, increases with differentiation. It was therefore possible to obtain acceptable analyses of K-feldspar with the use of a defocused 10μ beam, within fayalite-hedenbergite granophyre sample NA89. These K-feldspar analyses, which show increasing anorthite content with fractionation, have also been plotted on Figure 4.23.

The feldspars, in the sequence from dolerites to fayalite

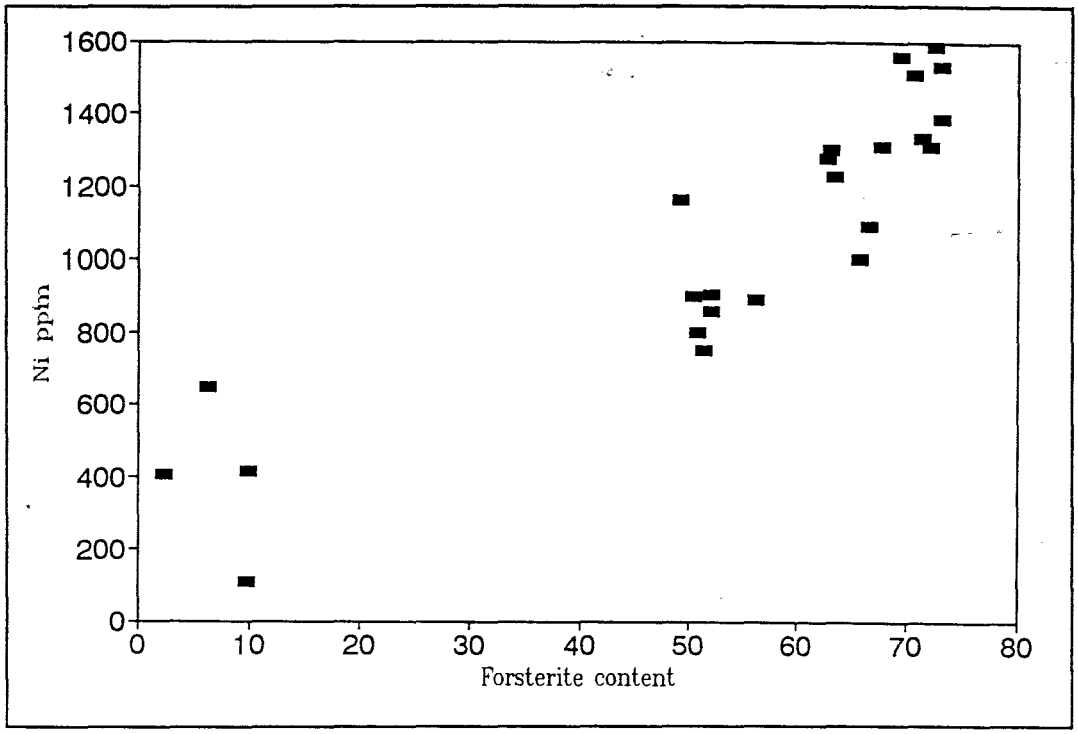

Figure 4.21 Ni versus Forsterite content of New Amalfi Sheet olivines.

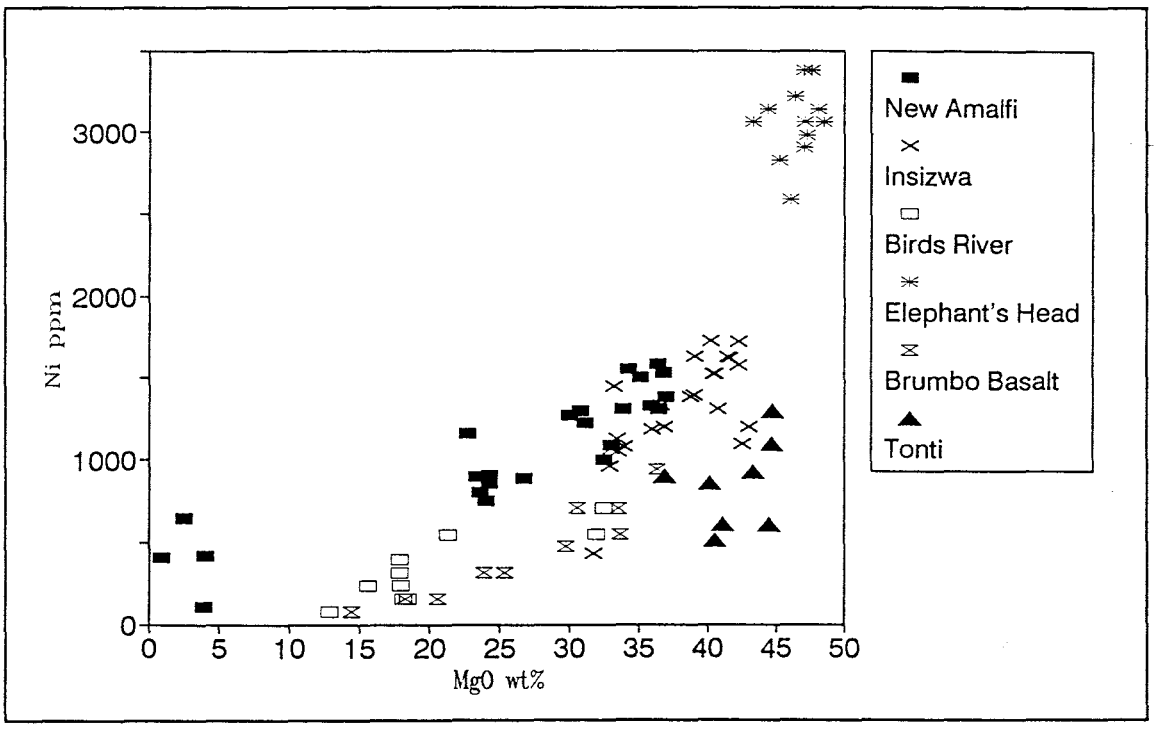

Figure 4.22 Ni versus MgO content of Karoo olivines. Data for Insizwa from Lightfoot et al. (1984); for Tonti from Cawthorn et al. (1992); for the Drumbo basalt from Mitchell, (1980) and for Birds River and Elephant's Head Dyke from H.V. Eales (pers. comm.).

hedenbergite-granophyres, therefore show an almost complete fractionation sequence with plagioclase and K-feldspar fractionating towards a common end composition which is very nearly reached in fayalite-hedenbergite granophyre sample NA89. The range in compositions of feldspars within the interval from dolerites to fayalite-hedenbergite granophyres outline the intersection of the solidus and solvus in the ternary $CaAl_2Si_2O_8$-$NaAlSi_3O_8$-$KAlSi_3O_8$ system. This has been previously described by Carmichael et al. (1974) for feldspars from alkaline lavas. Within the topmost granophyres of the New Amalfi Sheet, however, there is a sudden change in the composition of the feldspars from those compositions falling on the fractionation trend described above, to the almost pure end members albite and orthoclase (Figure 4.23).

Bowen and Tuttle (1950) showed that there is complete solid solution within the system $NaAlSi_3O_8$-$KAlSi_3O_8$-H_2O at high temperatures. They also found that when the solidus was depressed to low temperatures under the influence of high water-vapour pressure, two feldspars formed instead of one. This indicates the presence of only partial solid solution between $NaAlSi_3O_8$ and $KAlSi_3O_8$ at low temperatures, since the solidus is depressed by an increase in water vapour pressure to the extent that it is positioned directly on top of the solvus, thereby causing direct crystallization of two feldspars.

The sudden change in the composition of the feldspars within the topmost granophyres of the New Amalfi Sheet, to that of nearly pure albite and orthoclase, can therefore be explained by the depression of the feldspar solidus under the influence of an increase in water vapour pressure, within the late stage residual melt. An increase in water vapour pressure within the topmost granophyres could have been caused by the ingestion of water-laden country rock sediments. The occurrence of xenoliths of country rock sediment within the topmost granophyres provides support for this idea.

Another possible explanation for the occurrence of the two end member feldspar compositions within the topmost granophyres is

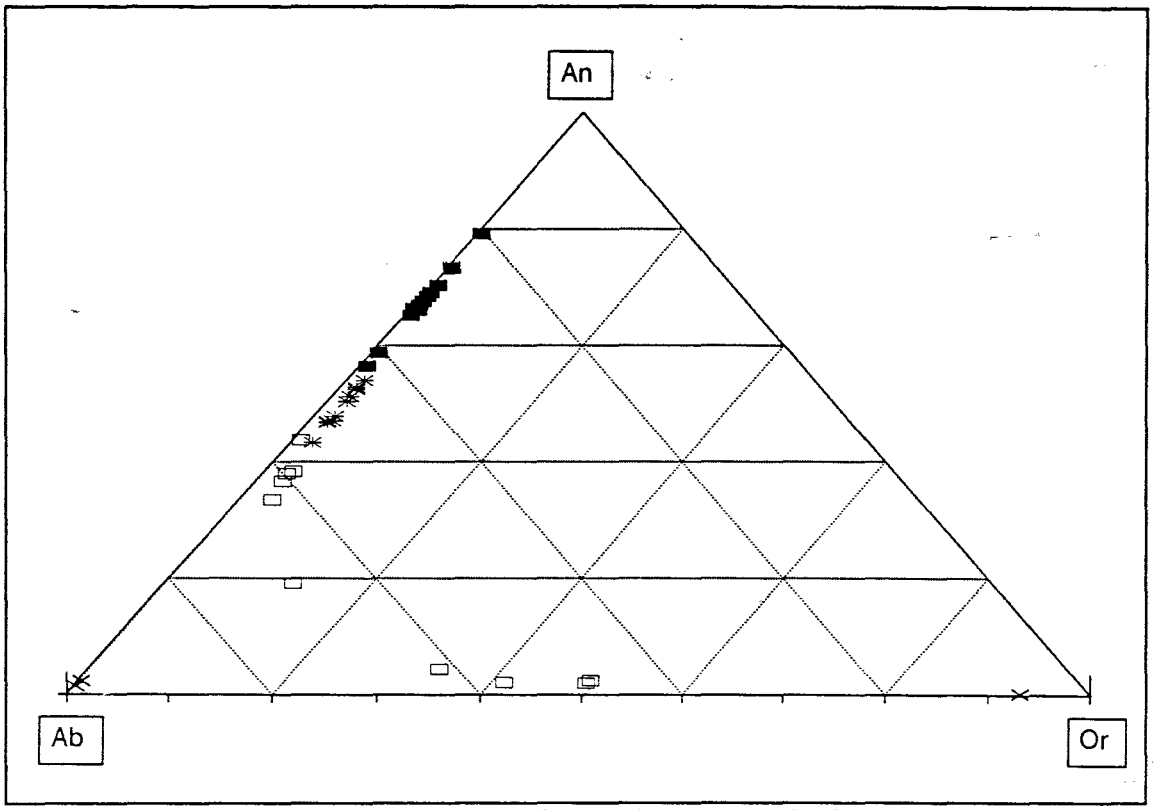

Figure 4.23 Average composition of New Amalfi Sheet feldspars for each sample. ■ = dolerites; * = gabbros and monzodiorites □ = granodiorites and fayalite-hedenbergite granophyres; x = granophyres.

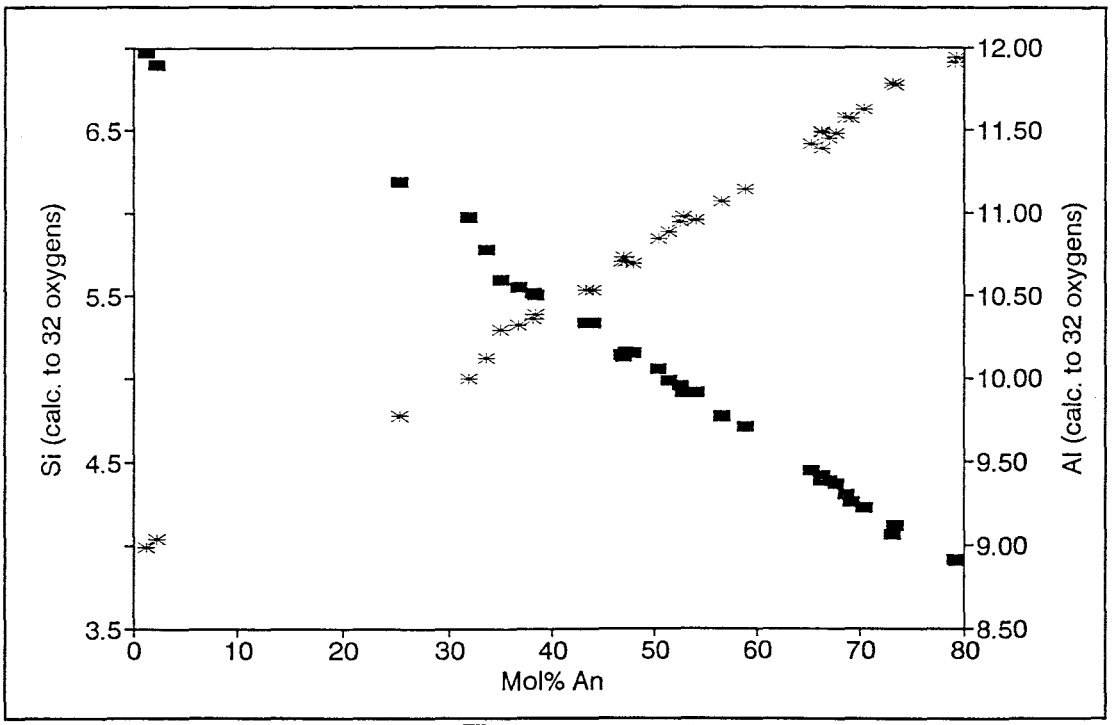

Figure 4.24 Average Si (■) and Al (*) for New Amalfi Sheet plagioclase feldspars plotted against Anorthite content.

that of simple subsolidus unmixing because of slow cooling. Perthitic K-feldspar is present within the granophyric intergrowth found within the topmost granophyres. However, the fact that the two end-member compositions were obtained with the use of a defocused 10μ electron beam indicates that these compositions probably represent bulk compositions and therefore give the composition of the feldspar at the time of crystallization as explained above.

4.4.2 The mineral chemistry of the New Amalfi Sheet feldspars and comparison with other Karoo feldspars.

Average plagioclase analyses for each sample have been calculated and are shown in Table 4.6. Plagioclase feldspars from the New Amalfi Sheet exhibit a continuous and almost completely linear increase in Si and decrease in Al with decreasing An content as shown in Figure 4.24. This is a function of the complete solid solution between the two end members of the plagioclase series, namely $CaAl_2Si_2O_8$-$NaAlSi_3O_8$.

Mitchell (1980) obtained electron microprobe data on plagioclases from a number of basalt units at the base of the Karoo lava pile, in the Molteno-Jamestown district. Mitchell was able to distinguish between a number of basalt units on the basis of the orthoclase content of the plagioclases and stated that the orthoclase content of the plagioclase was directly related to the K_2O content of the rocks from which they crystallized. In Figure 4.25 the orthoclase content of the New Amalfi Sheet plagioclases has been plotted against An content, together with analyses of plagioclases from the Vaalkop basalt unit of Mitchell (1980). It can be seen that the Vaalkop plagioclases are definitely richer in orthoclase than New Amalfi Sheet plagioclases with similar An contents. This may indicate that the liquid from which the Vaalkop plagioclases crystallized was richer in K_2O than the New Amalfi Sheet liquid. However, Evans and Moore (1968) showed that the most anorthitic plagioclases from the Makapuhi lava lake were those from coarser-grained rocks that had cooled more slowly. In the light of these findings it is impossible to make predictions on the relative K_2O contents of liquids using plagioclase

Table 4.6

AVERAGE PLAGIOCLASE FELDSPAR COMPOSITIONS

Sample	NA79	NA80	NA81	NA129	NA133	NA136
Wt.%						
SiO2	48.48	49.77	53.98	52.00	53.57	48.07
Al2O3	32.02	31.34	28.41	29.95	28.72	31.60
FeO	0.49	0.46	0.52	0.57	0.53	0.41
CaO	16.66	15.25	12.17	13.82	12.56	16.66
Na2O	2.36	3.00	5.07	3.99	4.75	2.38
K2O	0.07	0.09	0.14	0.11	0.13	0.06
Total	100.08	99.91	100.30	100.44	100.26	99.17
Cations (based on 32 oxygens) :						
Si	8.9080	9.1188	9.7754	9.4444	9.7115	8.9143
Al	6.9341	6.7695	6.0670	6.4127	6.1376	6.9085
Fe2+	0.0749	0.0699	0.0795	0.0863	0.0796	0.0629
Ca	3.2794	2.9955	2.3628	2.6904	2.4399	3.3113
Na	0.8410	1.0641	1.7802	1.4049	1.6710	0.8554
K	0.0162	0.0212	0.0325	0.0261	0.0311	0.0137
Ab/Or	98.12	98.04	98.20	98.17	98.17	98.44
An	79.27	73.42	56.60	65.28	58.91	79.22
Ab	20.33	26.07	42.62	34.09	40.34	20.47
Or	0.39	0.52	0.78	0.63	0.75	0.33
n	7	6	7	8	8	2

Sample	NA98	NA97	NA100	NA130	NA131	NA132	NA101
Wt.%							
SiO2	51.78	51.49	51.33	49.46	51.17	50.60	50.76
Al2O3	30.28	30.20	29.92	31.38	30.67	30.44	30.90
FeO	0.37	0.37	0.45	0.42	0.37	0.38	0.41
CaO	14.01	14.44	14.25	15.65	14.50	14.86	15.08
Na2O	3.85	3.74	3.81	3.10	3.59	3.58	3.41
K2O	0.11	0.09	0.10	0.09	0.09	0.09	0.10
Total	100.40	100.34	99.87	100.11	100.39	99.95	100.67
Cations (based on 32 oxygens) :							
Si	9.4033	9.3684	9.3877	9.0647	9.3055	9.2631	9.2263
Al	6.4809	6.4794	6.4497	6.7794	6.5756	6.5699	6.6226
Fe2+	0.0560	0.0564	0.0695	0.0649	0.0563	0.0586	0.0628
Ca	2.7261	2.8175	2.7930	3.0742	2.8255	2.9155	2.9375
Na	1.3548	1.3198	1.3516	1.1035	1.2660	1.2685	1.2026
K	0.0251	0.0209	0.0234	0.0214	0.0215	0.0214	0.0238
Ab/Or	98.18	98.44	98.30	98.10	98.34	98.34	98.07
An	66.38	67.75	67.02	73.24	68.69	69.31	70.53
Ab	33.01	31.75	32.42	26.25	30.79	30.18	28.90
Or	0.61	0.50	0.56	0.51	0.52	0.51	0.57
n	8	12	6	6	8	13	6

Table 4.6 (cont.)

Sample	NA125	NA96	NA95	NA94	NA93	NA92	NA91
Wt.%							
SiO2	51.62	54.93	55.41	54.46	55.30	55.27	55.60
Al2O3	30.24	27.98	27.33	27.83	28.03	27.63	26.68
FeO	0.33	0.55	0.48	0.54	0.51	0.47	0.51
CaO	14.08	11.40	10.52	11.06	11.07	10.99	10.04
Na2O	3.88	5.15	5.49	5.27	5.32	5.53	6.03
K2O	0.14	0.31	0.34	0.28	0.31	0.31	0.34
Total	100.29	100.32	99.57	99.44	100.54	100.20	99.20
Cations (based on 32 oxygens) :							
Si	9.3857	9.9197	10.0548	9.9179	9.9530	9.9852	10.1302
Al	6.4879	5.9562	5.8445	5.9739	5.9465	5.8841	5.7305
Fe2+	0.0507	0.0829	0.0736	0.0817	0.0774	0.0715	0.0783
Ca	2.7479	2.2065	2.0451	2.1584	2.1340	2.1271	1.9610
Na	1.3641	1.8033	1.9310	1.8614	1.8555	1.9389	2.1296
K	0.0321	0.0708	0.0789	0.0651	0.0702	0.0711	0.0794
Ab/Or	97.69	96.22	96.08	96.62	96.36	96.46	96.41
An	66.25	54.09	50.43	52.84	52.56	51.41	47.02
Ab	32.97	44.18	47.62	45.57	45.71	46.87	51.08
Or	0.78	1.74	1.95	1.59	1.73	1.72	1.90
n	12	12	11	8	9	9	8

Sample	NA90	NA176	NA190	NA160	NA153	NA89	NA89rim
Wt.%							
SiO2	56.43	55.96	57.67	55.96	58.21	60.12	63.01
Al2O3	26.87	26.61	26.17	26.70	25.34	24.23	22.81
FeO	0.48	0.62	0.43	0.42	0.54	0.48	0.39
CaO	10.15	10.21	9.38	10.17	8.18	7.07	5.12
Na2O	6.01	5.89	6.53	6.16	6.92	7.30	7.86
K2O	0.39	0.38	0.39	0.33	0.52	0.57	0.64
Total	100.33	99.66	100.57	99.74	99.70	99.77	99.83
Cations (based on 32 oxygens) :							
Si	10.1606	10.1533	10.3320	10.1422	10.4962	10.7767	11.1882
Al	5.7037	5.6902	5.5279	5.7044	5.3851	5.1210	4.7760
Fe2+	0.0725	0.0946	0.0649	0.0631	0.0815	0.0727	0.0583
Ca	1.9577	1.9845	1.8008	1.9750	1.5796	1.3593	0.9763
Na	2.0976	2.0708	2.2675	2.1650	2.4190	2.5361	2.7053
K	0.0885	0.0871	0.0892	0.0768	0.1185	0.1299	0.1449
Ab/Or	95.95	95.96	96.21	96.57	95.33	95.11	94.90
An	47.24	47.91	43.31	46.83	38.39	33.60	25.39
Ab	50.62	49.99	54.54	51.35	58.73	63.15	70.80
Or	2.14	2.10	2.15	1.82	2.88	3.24	3.81
n	9	7	9	6	7	11	3

Table 4.6 (cont.)

Sample	NA164	NA192	NA191	NA179	NA87	NA86	NA134
Wt.%							
SiO2	58.95	58.64	57.28	61.61	58.51	67.96	68.77
Al2O3	25.23	25.36	25.99	23.80	24.82	19.60	19.48
FeO	0.37	0.43	0.43	0.40	0.54	0.05	0.08
CaO	8.06	8.30	9.38	6.36	7.48	0.50	0.27
Na2O	7.35	7.17	6.52	7.09	7.43	11.99	11.90
K2O	0.49	0.41	0.13	0.55	0.43	0.07	0.05
Total	100.43	100.31	99.73	99.81	99.21	100.15	100.56
Cations (based on 32 oxygens) :							
Si	10.5455	10.5079	10.3361	10.9676	10.5871	11.8959	11.9653
Al	5.3196	5.3563	5.5286	5.0010	5.2935	4.0438	3.9955
Fe2+	0.0553	0.0639	0.0644	0.0605	0.0820	0.0070	0.0124
Ca	1.5440	1.5933	1.8136	1.2182	1.4504	0.0937	0.0502
Na	2.5495	2.4904	2.2829	2.4442	2.6083	4.0693	4.0158
K	0.1108	0.0945	0.0308	0.1249	0.0981	0.0145	0.0113
Ab/Or	95.84	96.35	98.67	95.17	96.38	99.64	99.72
An	36.73	38.13	43.93	31.88	34.89	2.25	1.24
Ab	60.64	59.61	55.33	64.82	62.75	97.40	98.48
Or	2.63	2.26	0.75	3.29	2.36	0.35	0.28
n	7	7	8	9	1	8	3

AVERAGE POTASSIUM FELDSPAR COMPOSITIONS

Sample	NA89	NA89rim	NA179	NA86
Wt.%				
SiO2	66.70	66.54	66.20	64.72
Al2O3	18.40	18.94	18.08	18.37
FeO	0.20	0.22	0.06	0.08
CaO	0.42	0.62	0.04	0.01
Na2O	5.35	6.49	0.30	0.75
K2O	8.37	6.27	15.51	15.43
Total	99.43	99.08	100.18	99.36
Cations (based on 32 oxygens) :				
Si	12.0537	11.9823	12.1299	12.0017
Al	3.9198	4.0201	3.9047	4.0152
Fe2+	0.0297	0.0331	0.0096	0.0125
Ca	0.0816	0.1190	0.0075	0.0012
Na	1.8741	2.2651	0.1064	0.2695
K	1.9296	1.4415	3.6260	3.6508
Ab/Or	49.27	61.20	2.87	6.89
An	2.10	3.13	0.20	0.03
Ab	48.24	59.25	2.86	6.89
Or	49.67	37.62	96.94	93.08
n	2	2	2	4

compositions from rocks that underwent different rates of cooling.

The An content of the average plagioclase analyses for each sample from the New Amalfi Sheet have been plotted against the Mg# of the corresponding average brown calcium-rich pyroxene analysis in Figure 4.26. It can be seen that there is a direct relationship between the fractionation of both the plagioclase and the pyroxene, indicating that both phases were efficiently isolated from the liquid in order to cause the fractionation. This relationship breaks down in the late stages of differentiation where the composition of the plagioclase shifts suddenly to almost pure albite without a similar shift in the composition of the corresponding pyroxene. This appears to be another manifestation of the sudden increase in water vapour pressure in the late stages of differentiation, which suppressed the feldspar solidus, so that it sat directly on top of the feldspar solvus, thereby causing the two end members albite and K-feldspar to crystallize. This, of course, did not affect the composition of the pyroxenes crystallizing at the same time.

4.5 OXIDE PHASES.

4.5.1 Spinel.

4.5.1.1 Introduction.

Eales and Snowden (1979) stated that the spinels within cumulus picrites at the base of the Elephant's Head Dike, which acted as the conduit through which magma entered the New Amalfi Sheet, were of two generations. There was stated to be, firstly, an older generation of small spinel inclusions within olivine and secondly, a later exsolved spinel phase which exhibited a plate-like dendritic habit, also found within the olivines. Zoned spinel grains were found within rocks from the chilled margin of the dike. These spinels showed a sharp contact between Cr-rich cores and Fe-rich margins, and this was taken to indicate the existence of an hiatus between the crystallization of high-Cr spinel cores and low-Cr, high-Ti and -Fe spinel margins. Eales

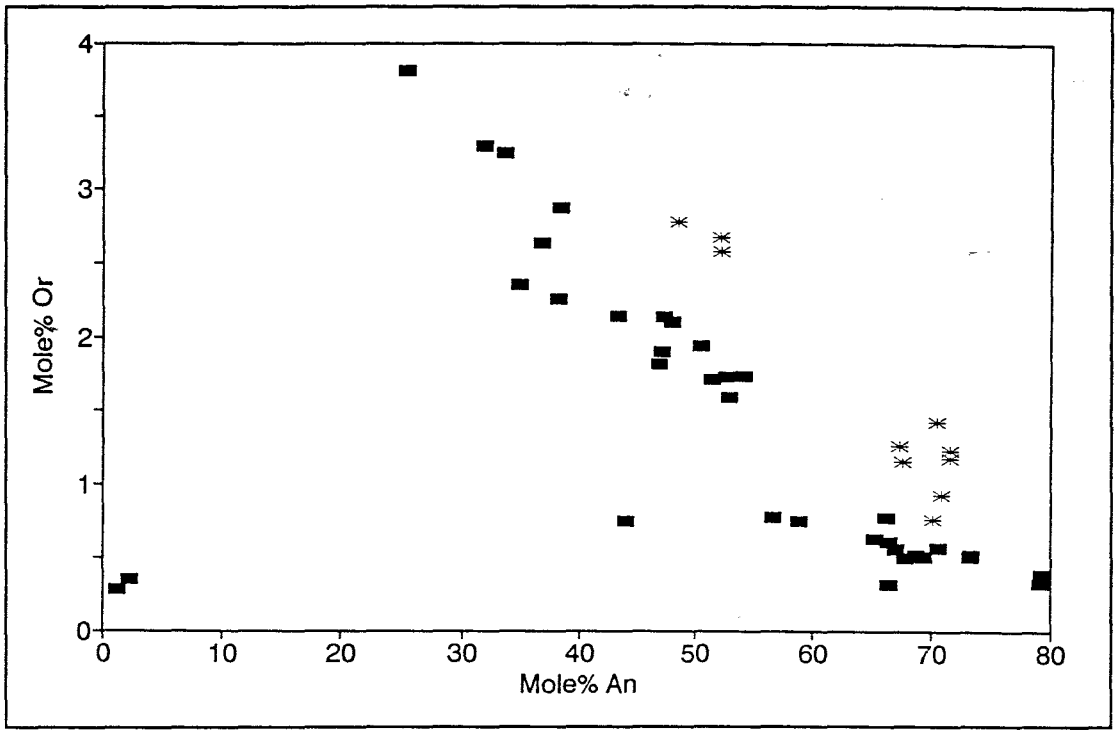

Figure 4.25 Average orthoclase versus anorthite content for New Amalfi Sheet plagioclase (■) compared to the plagioclase from the Vaalkop basalt (*) from Mitchell (1980).

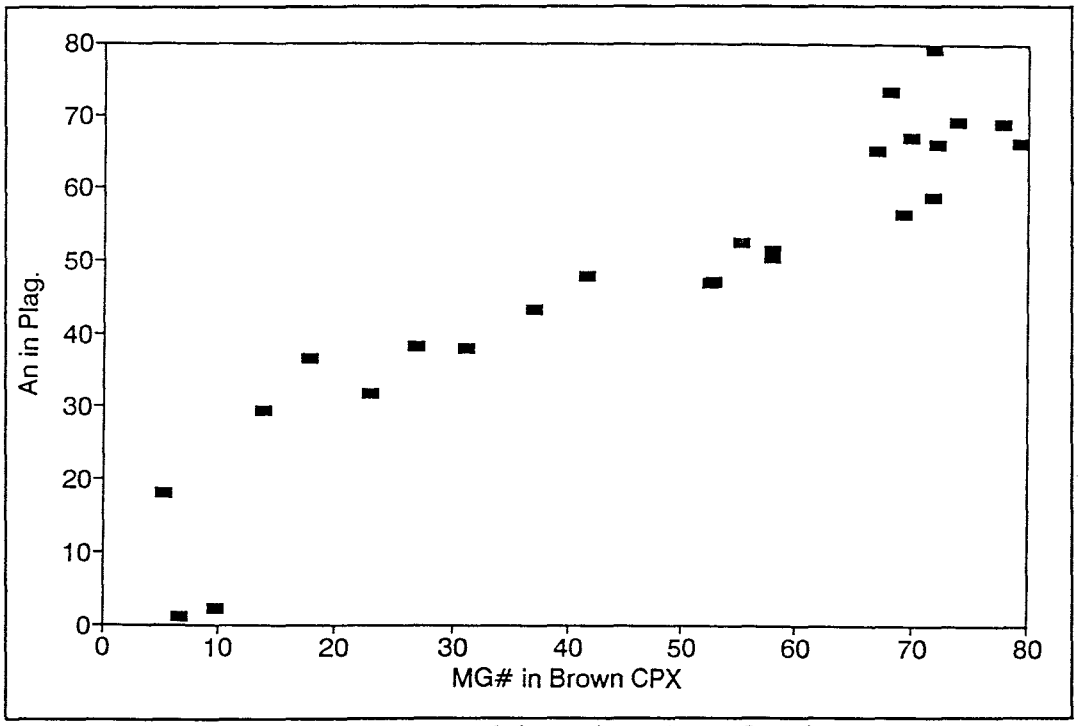

Figure 4.26 Average anorthite in the plagioclase versus the average Mg# of the clinopyroxene in each sample for which both phases were analyzed.

and Snowden (op. cit.) showed that there was no hiatus but a continuous variation in composition from aluminian chromite to chromian Ti-magnetite in the spinels from the picrites of the Elephant's Head Dike. This was seen to be because the picrites cooled more slowly, allowing time for diffusion and homogenization of any zonal structure within the spinels.

Eales et al. (1980) state that the changes in composition with height in the spinels of the Elephant's Head Dike are due to fractionation. A systematic change in the composition of spinels with height, as a result of fractionation, is not seen in larger Karoo intrusions such as the Insizwa Complex. This is due to the added complexity of host silicate phases affecting the composition of the spinels in the larger intrusions. The larger intrusions cooled more slowly, allowing time for diffusion between host silicate phases and spinels to affect the composition of the spinels, thereby obscuring the compositional changes which were already present because of fractionation.

Eales et al. (op. cit.) defined three stages of spinel crystallization in Karoo rocks which are related to the nature of the co-precipitating phases, which affect the liquid line of descent and in turn, the composition of the spinel crystallizing from the melt. These three stages listed below are:

a) An initial stage in which spinels exhibit a modest increase in Al and similar decrease in Cr without any change in Fe3+. This stage is related to the initial crystallization of chromite prior to and concurrently with olivine crystallization.
b) A second stage in which spinels show a progressive decrease in Al and increase in Fe3+ without any significant change in Cr. This stage is related to the beginning of plagioclase nucleation, together with chrome spinel and olivine.
c) A final stage in which spinels exhibit rapid depletion in Cr. This is related to the beginning of pyroxene crystallization which rapidly takes up all remaining Cr in the melt.

Eales et al. (op. cit.) state further that the three stages of nucleation of chromiferous spinel are complete by 30% fractionation of a typical Karoo magma and that there is an hiatus in spinel nucleation until 67% fractionation at which stage Ti-magnetites typically nucleate. Hill and Roeder (1974) postulated that the hiatus in spinel nucleation is due to a reaction relationship that exists between spinel, clinopyroxene and liquid at low fO_2 conditions. Hill and Roeder (op. cit.) state that at higher fO_2 there should be no hiatus in spinel nucleation. Hill and Roeder (op. cit.) also showed that spinel is stabilized at low fO_2 conditions by an increased Cr content of the melt. A decrease in the Cr content of the melt pushes the spinel liquidus to lower temperatures and higher fO_2.

Eales et al. (op. cit.) found no evidence for a reaction relationship between spinel and pyroxene in Karoo rocks. They therefore prefer to ascribe the hiatus in spinel nucleation in Karoo rocks to the depletion in Cr in the melt after their stage c). This causes the spinel liquidus to be depressed to lower temperatures as shown by Hill and Roeder (op. cit.), thereby causing an hiatus in spinel nucleation until the magma temperature drops to the temperature required for a new phase of spinel (Ti-magnetite) nucleation to begin.

4.5.1.2 Mineral chemistry of the New Amalfi Sheet spinels.

Average electron microprobe analyses of spinels from the New Amalfi Sheet, with Fe_2O_3 calculated according to the method of Droop (1987) and recalculated to 100 wt%, are shown in Table 4.7. The compositional variation within the chrome-bearing spinels of the New Amalfi Sheet, as shown in Figure 4.27, is almost identical to the trend exhibited by the Elephant's Head Dike spinels, with both intrusions showing a continuous range in compositions from aluminian chromite to Ti-magnetite. All analyses enclosed by the thick dashed line in Figure 4.27 represent single analyses of small spinel inclusions found within olivine in the basal olivine dolerite sample NA99. The most chrome-rich spinel from the New Amalfi Sheet was analysed from the groundmass of a fine-grained pigeonite dolerite (NA79), taken

close to the edge of the intrusion. All other spinels, analysed from the entire range of rock types found within the New Amalfi Sheet, plot in the Ti-magnetite corner in Figure 4.27. There exists therefore a time gap between the most Fe-rich spinel found as an inclusion in olivine, and the Ti-magnetites which occur as late-stage anhedral interstitial phases. This time gap corresponds to the hiatus in spinel nucleation in Karoo rocks reported by Eales et al. (op. cit.).

In Figure 4.28 the field of spinel compositions in the New Amalfi Sheet is shown by the heavy dashed line, together with the average compositions of Karoo spinels taken from Eales et al. (1980) and average Elephant's Head spinel compositions taken from Eales (1979). The light dashed line encloses the compositional range of average Karoo and Elephant's Head spinel compositions and the letters A, B and C denote the three stages of chromian spinel evolution as defined by Eales et al. (op. cit.). It can be seen that New Amalfi Sheet spinels span all three stages of chromian spinel evolution, thus indicating that the paragenetic sequence during the initial stages fractionation of the New Amalfi Sheet was : spinel -> spinel + olivine -> spinel + olivine + plagioclase -> spinel + olivine + plagioclase + pyroxene.

The range in composition of the Ti-magnetites of the New Amalfi Sheet is shown in Figure 4.29. It can be seen that all Ti-magnetite analyses plot on a remarkably straight line which extends from the composition of pure magnetite to that of pure ulvöspinel. The Ti-magnetites therefore plot along a mixing line between magnetite and ulvöspinel. This feature was also noted for Karoo Ti-magnetites by Reynolds (1983) who stated that it was due to differing degrees of oxidation exsolution of magnetite-ulvöspinel solid solution as described by Buddington and Lindsley (1964). The degree of oxidation is not related to height or degree of differentiation in the New Amalfi Sheet and probably reflects differing local fO_2 conditions during subsolidus cooling.

4.5.2 Ilmenite.

Table 4.7

AVERAGE COMPOSITION OF SPINELS ANALYZED FOR EACH SAMPLE

Sample	NA79	NA99incl.	NA99	NA98	NA97	NA125	NA93
Wt.%							
TiO2	0.89	3.52	9.31	6.16	8.07	7.90	13.25
Al2O3	16.23	7.72	1.10	0.60	1.07	2.47	1.43
Cr2O3	40.89	24.09	1.50	0.43	0.65	0.17	0.18
Fe2O3	8.88	30.00	48.23	55.95	51.72	51.13	41.62
FeO	28.65	31.50	39.44	36.20	37.46	37.15	43.01
MnO	0.22	0.39	0.23	0.45	0.48	0.21	0.33
NiO	0.10	0.19	0.09	0.12	0.09	0.07	0.00
MgO	4.15	2.57	0.10	0.07	0.46	0.90	0.17
Total	100.00	100.00	100.00	99.98	100.00	100.00	100.00
Cations (based on 4 oxygens) :							
Ti	0.0230	0.0958	0.2706	0.1788	0.2357	0.2360	0.3817
Al	0.6589	0.3388	0.0495	0.0274	0.0493	0.1155	0.0646
Cr	1.1135	0.7046	0.0455	0.0131	0.0202	0.0053	0.0054
Fe3+	0.2303	0.8258	1.3874	1.6242	1.5168	1.5278	1.1997
Fe2+	0.8253	0.9676	1.2665	1.1678	1.2197	1.2338	1.3777
Mn	0.0062	0.0123	0.0074	0.0146	0.0158	0.0070	0.0108
Ni	0.0028	0.0055	0.0026	0.0038	0.0027	0.0023	0.0000
Mg	0.2131	0.1408	0.0060	0.0038	0.0265	0.0532	0.0098
n	1	11	2	3	3	1	1

Sample	NA90	NA176	NA153	NA89	NA86	NA81	NA133
Wt.%							
TiO2	14.44	5.21	11.40	12.44	11.59	8.54	11.16
Al2O3	1.18	0.87	0.93	0.33	0.24	0.78	0.93
Cr2O3	0.28	0.24	0.02	0.01	0.00	0.15	0.08
Fe2O3	39.33	57.39	45.24	44.86	46.33	51.42	46.39
FeO	44.18	35.61	41.12	42.38	41.37	38.78	41.13
MnO	0.33	0.26	0.34	0.41	0.47	0.29	0.39
NiO	0.01	0.02	0.00	0.00	0.00	0.03	0.05
MgO	0.06	0.02	0.03	0.00	0.01	0.01	0.04
Total	99.82	99.63	99.08	100.45	100.00	100.00	100.16
Cations (based on 4 oxygens) :							
Ti	0.4264	0.1516	0.3277	0.3616	0.3264	0.2485	0.3166
Al	0.0548	0.0395	0.0421	0.0153	0.0106	0.0357	0.0415
Cr	0.0087	0.0074	0.0006	0.0003	0.0000	0.0046	0.0025
Fe3+	1.1619	1.6703	1.3018	1.3117	1.3055	1.4973	1.3176
Fe2+	1.4505	1.1517	1.3149	1.3733	1.2954	1.2547	1.2980
Mn	0.0112	0.0085	0.0111	0.0136	0.0149	0.0095	0.0125
Ni	0.0004	0.0007	0.0000	0.0000	0.0000	0.0010	0.0014
Mg	0.0035	0.0010	0.0017	0.0000	0.0004	0.0006	0.0022
n	4	3	1	2	2	1	4

Sample	NA134
Wt.%	
TiO2	8.50
Al2O3	0.47
Cr2O3	0.00
Fe2O3	52.21
FeO	38.86
MnO	0.26
NiO	0.00
MgO	0.00
Total	100.31
Cations (based on 4 oxygens)	
Ti	0.2469
Al	0.0215
Cr	0.0001
Fe3+	1.4975
Fe2+	1.2449
Mn	0.0084
Ni	0.0001
Mg	0.0000
n	7

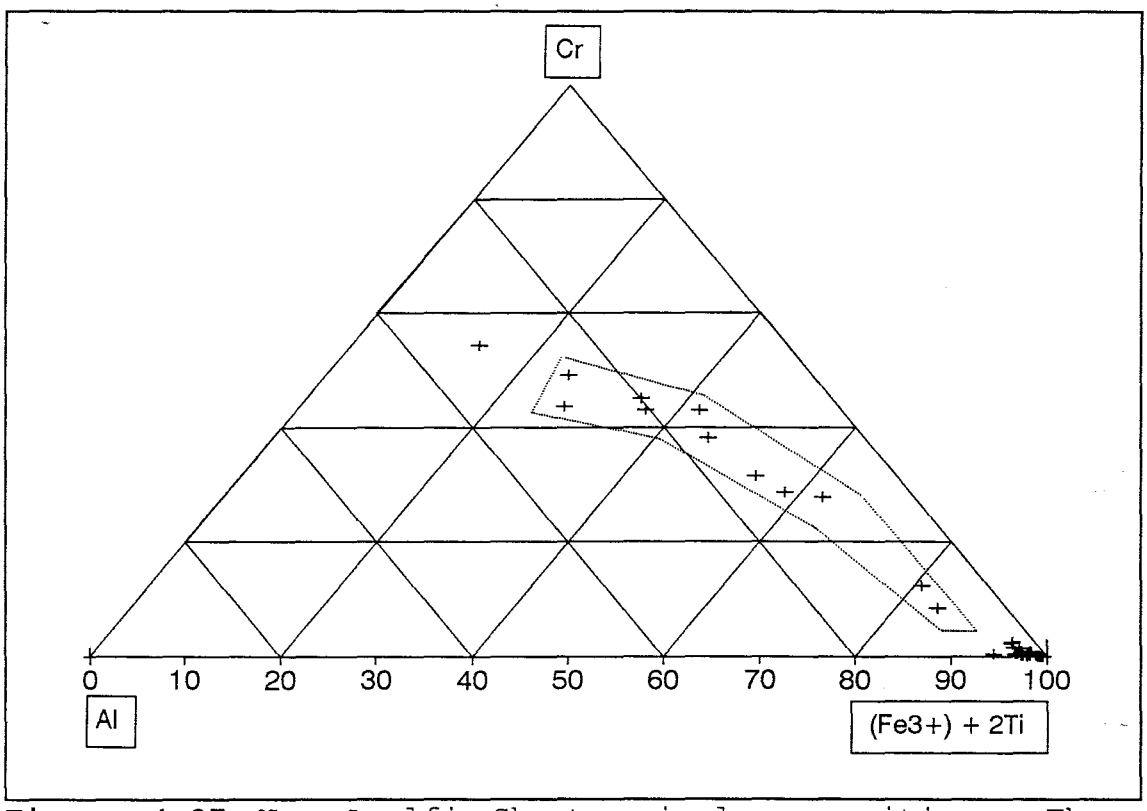

Figure 4.27 New Amalfi Sheet spinel compositions. Those enclosed by the heavy dashed line are the compositions of spinel inclusions found in olivine in the basal olivine dolerite NA99.

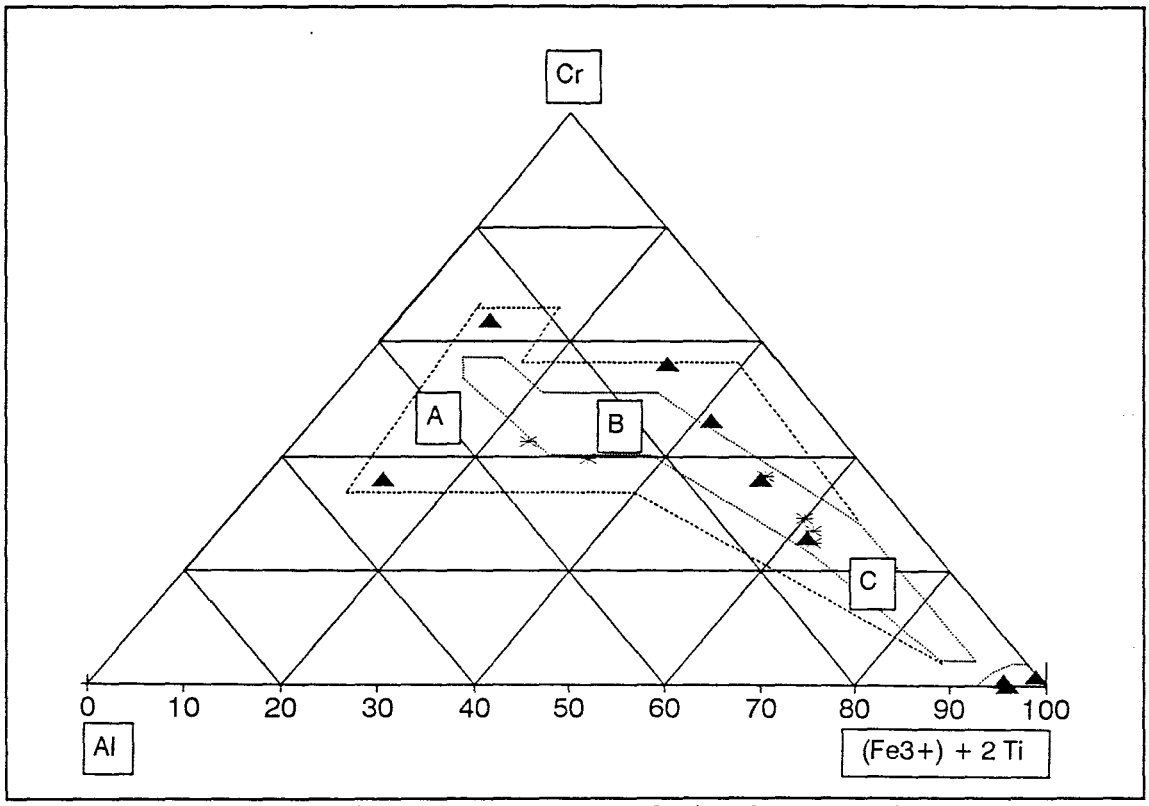

Figure 4.28 The field of New Amalfi Sheet spinel analyses shown by the heavy dashed line compared to selected spinel analyses from the Elephant's Head Dyke (*), Eales (1979); and Karoo in general (▲), Eales et al. (1980).

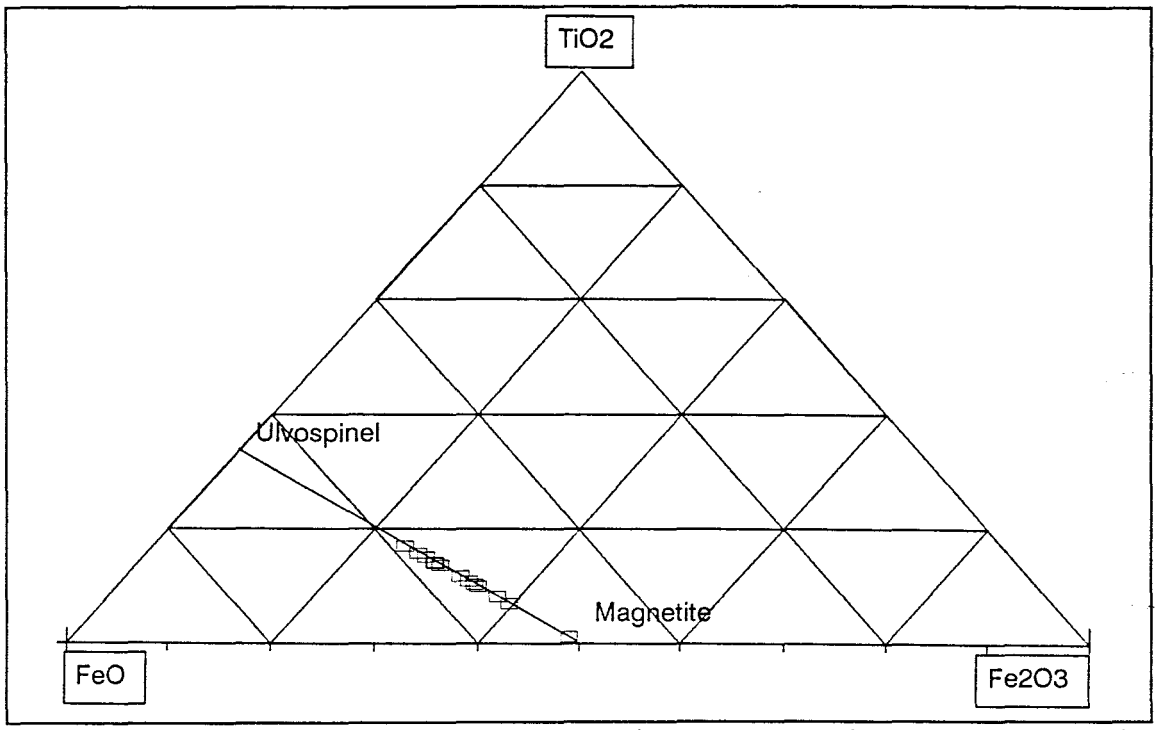

Figure 4.29 New Amalfi Sheet titanomagnetites plotted in terms of mole% FeO, Fe_2O_3 and TiO_2.

4.5.2.1 Mineral chemistry of ilmenites in the New Amalfi Sheet.

Average ilmenite analyses for a selected group of samples from the New Amalfi Sheet, with Fe_2O_3 calculated according to the method of Droop (1987) and recalculated to 100 Wt%, are shown in Table 4.8. Reynolds (1983) states that the composition of most Karoo ilmenites falls close to the $FeTiO_3$ end member. It was also shown by Reynolds (op. cit.) that there is a limited amount of variation in terms of the MgO and MnO concentrations of Karoo ilmenites with the highest MnO and lowest MgO concentrations found in ilmenite grains which occur in late-stage micropegmatite. Reynolds (op. cit.) suggests that this represents a weakly defined fractional crystallization trend in the Karoo ilmenites. However Reynolds (op. cit.), also noted that the MnO content of vermiform ilmenites, produced by deuteric alteration of composite oxide grains, is always higher than that of the primary ilmenite found within the same sample. Therefore it is possible that the increase in MnO content of late stage ilmenites within the Karoo may be the result of the same process which formed the vermiform ilmenite, namely deuteric alteration, and not the result of fractional crystallization.

In Figure 4.30 single ilmenite analyses from the New Amalfi Sheet have been plotted together with average Karoo ilmenite compositions. It can be seen that both data sets show progressive depletion in $MgTiO_3$ and enrichment in $MnTiO_3$. The average MgO concentrations of New Amalfi Sheet ilmenites have been plotted against average MnO concentrations in Figure 4.31. MgO concentration in New Amalfi Sheet ilmenites can be seen to be initially rapidly depleted in dolerites to quartz gabbros, with no corresponding change in MnO content. From the quartz monzodiorites onwards, there is a sudden large increase in MnO content of the ilmenite, with no corresponding change in MgO content. A similar pattern is seen in Figure 4.32 where it can be seen that TiO_2 in the ilmenite increases steeply with essentially no change in MnO content, from dolerites to quartz gabbros, after which TiO_2 remains essentially constant and MnO

Table 4.8

AVERAGE COMPOSITION OF ILMENITES ANALYZED FOR EACH SAMPLE

Sample	NA99	NA98	NA97	NA125	NA95	NA93	NA90
Wt.%							
TiO2	49.15	49.89	48.65	50.74	50.70	49.97	49.69
Al2O3	0.04	0.02	0.02	0.05	0.03	0.01	0.03
Cr2O3	0.10	0.09	0.00	0.05	0.03	0.03	0.01
Fe2O3	7.55	6.06	8.12	4.30	4.16	4.78	5.43
FeO	41.72	42.72	42.49	43.62	44.01	44.28	44.02
MnO	0.54	0.50	0.44	0.28	0.44	0.45	0.38
NiO	0.04	0.01	0.03	0.01	0.00	0.00	0.00
MgO	1.06	0.91	0.44	0.96	0.64	0.11	0.16
Total	100.20	100.21	100.19	100.00	100.00	99.62	99.71
Cations (based on 3 oxygens) :							
Ti	0.9246	0.9416	0.9099	0.9619	0.9439	0.9540	0.9476
Al	0.0012	0.0007	0.0005	0.0014	0.0009	0.0004	0.0008
Cr	0.0020	0.0017	0.0000	0.0009	0.0005	0.0006	0.0001
Fe3+	0.1418	0.1144	0.1519	0.0811	0.0776	0.0912	0.1037
Fe2+	0.8730	0.8966	0.8836	0.9199	0.9113	0.9402	0.9336
Mn	0.0115	0.0106	0.0092	0.0059	0.0092	0.0098	0.0082
Ni	0.0008	0.0003	0.0005	0.0001	0.0000	0.0000	0.0000
Mg	0.0394	0.0341	0.0165	0.0360	0.0234	0.0040	0.0059
Mg#	4.32	3.66	1.84	3.76	2.51	0.42	0.63
n	6	7	2	4	2	2	5

Sample	NA176	NA153	NA89	NA86	NA81	NA133
Wt.%						
TiO2	51.36	50.95	50.38	50.29	50.63	50.30
Al2O3	0.01	0.04	0.01	0.01	0.02	0.02
Cr2O3	0.00	0.00	0.00	0.00	0.00	0.00
Fe2O3	2.44	3.17	4.51	4.02	4.93	4.75
FeO	44.61	44.93	44.60	43.98	44.59	44.64
MnO	1.50	0.80	0.68	1.22	0.60	0.48
NiO	0.00	0.00	0.01	0.00	0.00	0.01
MgO	0.03	0.05	0.01	0.00	0.19	0.05
Total	99.96	99.94	100.20	99.51	100.97	100.26
Cations (based on 3 oxygens) :						
Ti	0.9742	0.9790	0.9448	0.9536	0.9532	0.9491
Al	0.0003	0.0014	0.0002	0.0002	0.0006	0.0004
Cr	0.0000	0.0000	0.0000	0.0000	0.0001	0.0000
Fe3+	0.0462	0.0612	0.0846	0.0761	0.0929	0.0897
Fe2+	0.9410	0.9600	0.9300	0.9275	0.9335	0.9365
Mn	0.0321	0.0172	0.0143	0.0259	0.0128	0.0102
Ni	0.0000	0.0001	0.0002	0.0000	0.0000	0.0003
Mg	0.0012	0.0018	0.0003	0.0001	0.0069	0.0020
Mg#	0.13	0.18	0.03	0.02	0.73	0.22
n	5	2	6	2	1	2

increases sharply.

In the light of the observations of Reynolds (op. cit.), that the highest MnO content of Karoo ilmenites occurs in the deuteric vermiform ilmenite, the sudden increase in MnO seen in the average ilmenite compositions from the most differentiated rocks of the New Amalfi Sheet may reflect a secondary deuteric alteration effect, and not fractional crystallization. This idea is supported by the petrography which shows an increase in the proportion of vermiform ilmenite in the fayalite-hedenbergite granophyres and granophyres. This increase in the proportion of vermiform ilmenite is probably what has caused the increase in MnO content, within the average ilmenite analyses for samples from the most differentiated rocks from the New Amalfi Sheet. Therefore the variation of MgO, TiO_2 and MnO within the ilmenites of the New Amalfi Sheet reflect a two-stage process, whereby MgO is initially rapidly depleted, and TiO_2 is initially rapidly enriched, in New Amalfi Sheet ilmenites, because of fractional crystallization. In the most differentiated rocks, this is then overprinted by the effects of the subsolidus deuteric alteration, which formed the vermiform ilmenite, causing the average ilmenite compositions of the rocks most affected by the deuteric alteration to show an enrichment in MnO.

In Figure 4.33 it can be seen that there is a progressive depletion in Fe_2O_3 in the ilmenites of the New Amalfi Sheet, from dolerites to granophyres. This is different to what is seen in the case of the magnetites of the New Amalfi Sheet, which show no consistent variation in Fe_2O_3 with differentiation, since oxidation of magnetite-ulvöspinel solid solution took place during sub-solidus cooling. Buddington and Lindsley (1964) showed that ilmenite-hematite solid solution decreases with decreasing temperature. The depletion in Fe_2O_3 in New Amalfi Sheet ilmenites from dolerites to granophyres may therefore reflect decreasing temperatures of equilibration of the ilmenite.

The ilmenites of the New Amalfi Sheet have therefore recorded changes in chemistry brought about initially by fractional crystallization, and subsequently by subsolidus alteration which

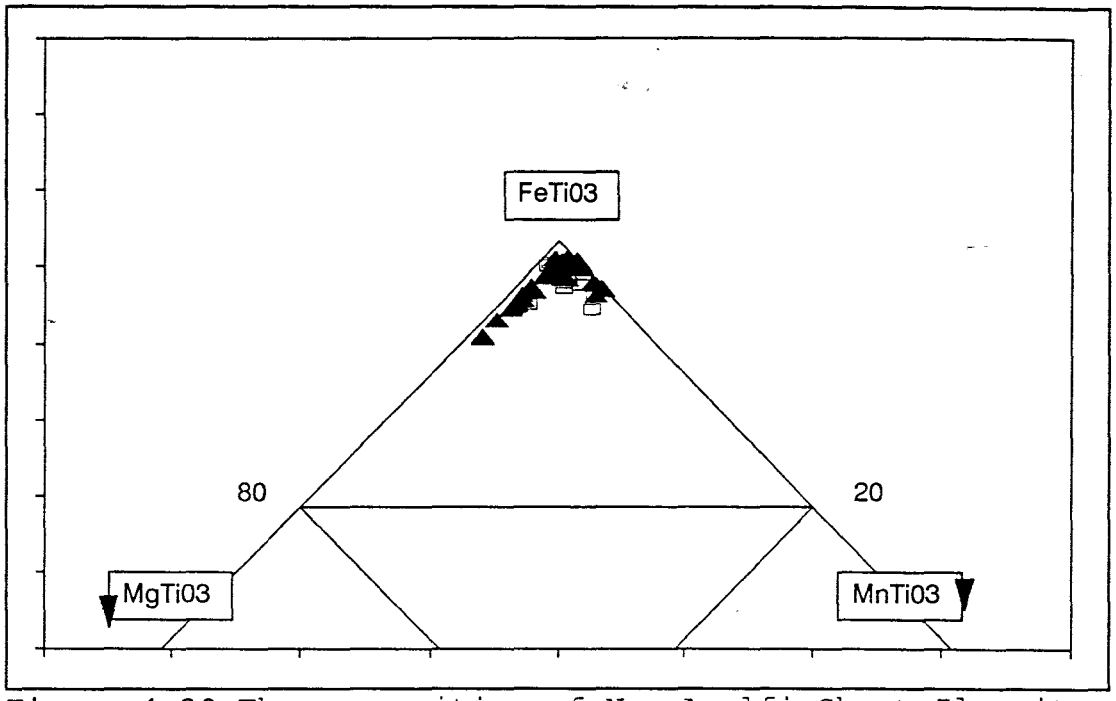

Figure 4.30 The composition of New Amalfi Sheet Ilmenites (▲) compared to selected Karoo ilmenite (□) compositions from Reynolds (1983).

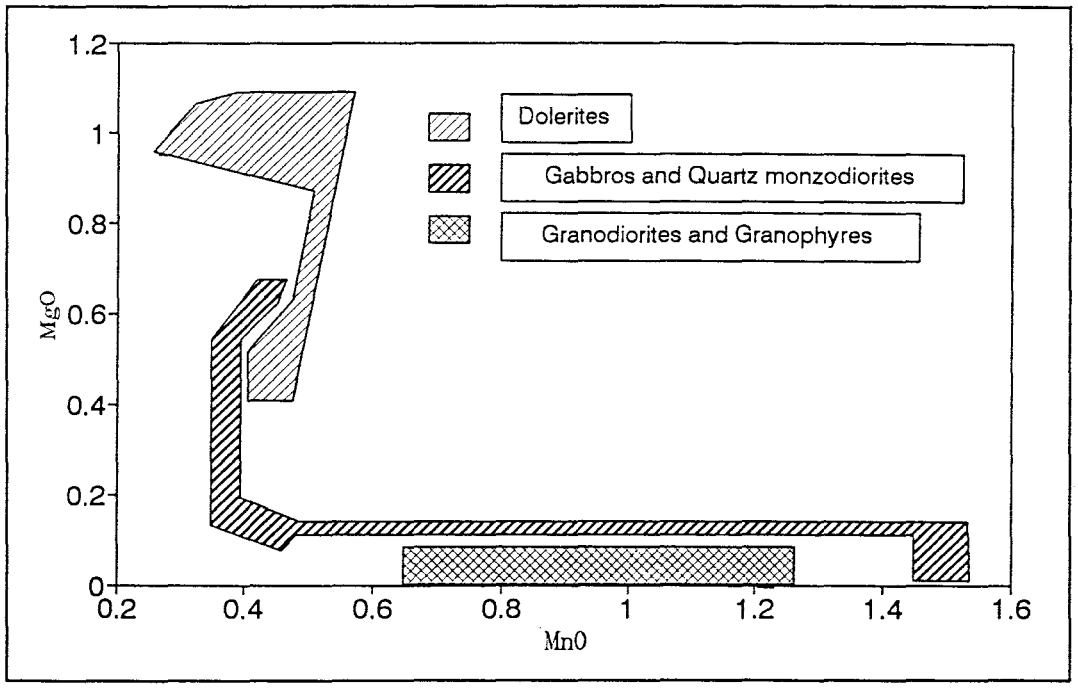

Figure 4.31 The fields of average MgO versus MnO for New Amalfi Sheet ilmenites.

produced the vermiform ilmenite. This alteration event may be the same as the hydrothermal alteration which produced the bleached pyroxene. If this is so, then the hydrothermal alteration of the bleached pyroxene was caused by deuteric fluids, as Reynolds (op. cit.) considers deuteric alteration to be responsible for the formation of vermiform ilmenite in Karoo rocks.

The fact that the ilmenites of the New Amalfi Sheet have preserved their liquidus and early subsolidus chemistry indicates that interaction with host silicate phases, which would tend to obscure this chemistry, was minimal. Lightfoot et al. (1987) have shown that there is a direct relationship between the modal content of olivine in picrites of the Insizwa Complex and the MgO content of the ilmenites. This, they state, indicates substantial subsolidus interaction between ilmenites and host silicate phases. However Cawthorn et al. (1988) state that no direct relationship was found between ilmenite and host silicate composition, in picrites sampled elsewhere in the Insizwa Complex. Therefore it is not yet proven whether or not sub-solidus re-equilibration of ilmenites with host silicate phases occurred within the Insizwa Complex. The evidence presented above suggests that it did not occur within the much smaller, and therefore faster-cooling, New Amalfi Sheet.

4.6 SUMMARY.

a) Two varieties of calcium-rich pyroxene are found within the New Amalfi Sheet. The first variety is brown in colour and represents the original magmatic calcium-rich pyroxene. The second variety formed from the partial hydrothermal alteration of the first variety, during which it was partially 'bleached' to a dirty white colour. The bleached variety is easily recognized by electron microprobe analysis because it contains a higher CaO content and a lower TiO_2 content than the original brown variety.

b) Pyroxene thermometry shows that the temperature of the hydrothermal alteration ranges from 950°C in the dolerites to 500°C in the granophyres.

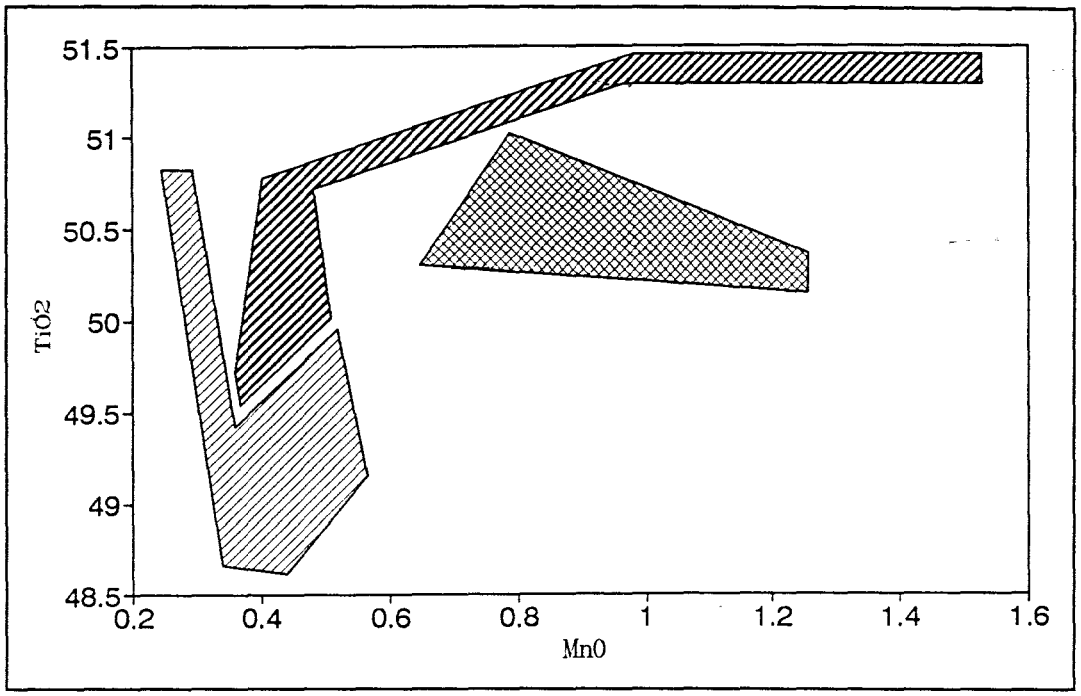

Figure 4.32 The fields of average TiO_2 versus MnO for New Amalfi Sheet ilmenites.

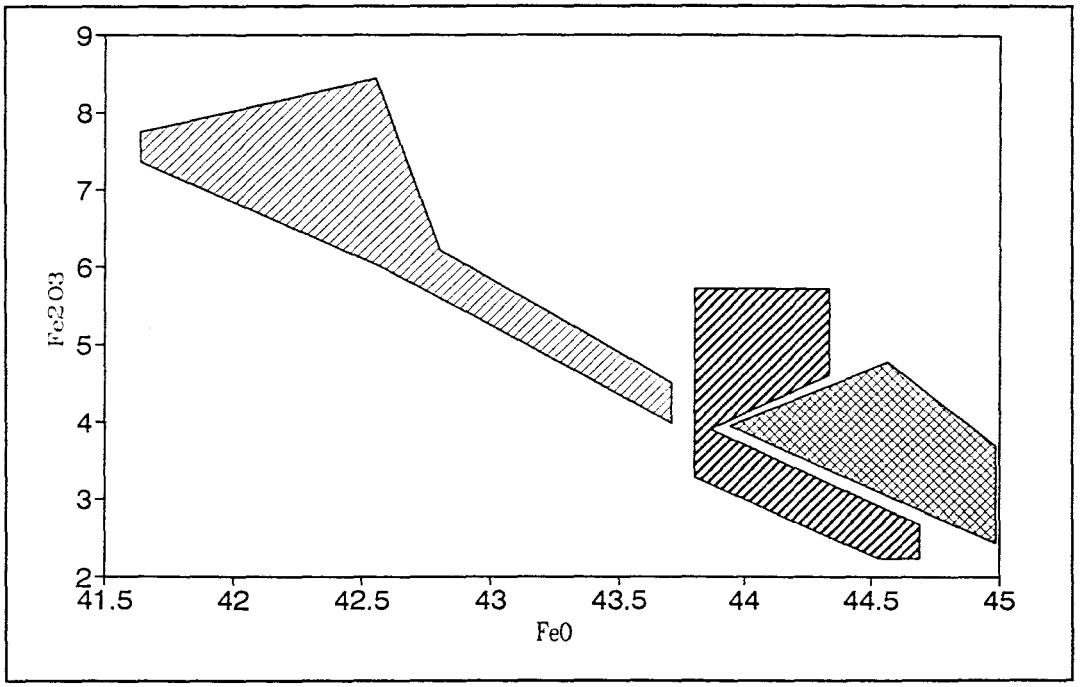

Figure 4.33 The fields of average Fe_2O_3 versus FeO for New Amalfi Sheet ilmenites.

c) The mineral chemistry of the brown calcium-rich pyroxene shows that plagioclase was already on the liquidus at the time when the pyroxenes which were analysed, began to crystallize.

d) Pigeonite was already on the liquidus at the time that the first dolerites crystallized.

e) The disappearance of pigeonite, which marks the termination of the two-pyroxene field within the New Amalfi Sheet, coincides with the reappearance of olivine. The absence of cumulus quartz at this time indicates that the physical limit of calcium-poor pyroxene stability, the boundary of the forbidden zone, was not reached within the New Amalfi Sheet.

f) The position of the two-pyroxene limit for the New Amalfi Sheet is similar to that of the Skaergaard and Birds River intrusions.

g) The ferrohypersthene found within the New Amalfi Sheet seems to have formed as a result of direct crystallization from late-stage intercumulus liquid.

h) The chemistry of the New Amalfi Sheet calcium-poor pyroxenes shows that both Ti and Al are depleted with progressive differentiation. This is different to what is observed in other intrusions such as the Bushveld Complex, and is probably due to the presence of cumulus calcium-rich pyroxene crystallizing together with calcium-poor pyroxene, in the case of the New Amalfi Sheet. Since $D_{Ti}^{Aug/opx}$ is greater than 1, the calcium-rich pyroxene competes successfully with the calcium-poor pyroxene for the available Ti in the melt.

i) The olivine gap within the New Amalfi Sheet is similar in size to that of the Palisades Sill but larger than that of the Skaergaard Intrusion. This seems to be the result of a higher degree of silica enrichment with differentiation in

the case of the New Amalfi Sheet and Palisades Sill.

j) Olivines from the New Amalfi Sheet plot slightly above the general Karoo trend in a graph of Ni versus Fo content. This may be due to a higher D_{Ni}^{Ol} for the New Amalfi Sheet liquid, due to a possible initially higher MgO content, or the trapped liquid shift effect.

k) The shift in plagioclase and K-feldspar compositions from the almost complete fractionation trend to the two end members, albite and orthoclase, is the result of the suppression of the feldspar solidus because of an increase in water vapour pressure within the late-stage residual melt. The increase in water vapour pressure was probably the result of the ingestion of water-laden country rock sediments.

l) The differentiation trend of the Cr-bearing spinels of the New Amalfi Sheet spans all three stages of spinel crystallization within the Karoo, as defined by Eales et al. (1980). This indicates that the paragenetic sequence for the early stages of fractionation of the New Amalfi Sheet liquid was: chromite -> chromite + olivine -> chromite + olivine + plagioclase -> chromite +v olivine + plagioclase + pyroxene.

m) The magnetites of the New Amalfi Sheet plot along a mixing line between ulvöspinel and magnetite. This is the result of differing degrees of subsolidus oxidation of magnetite-ulvöspinel solid solution.

n) Ilmenites from the New Amalfi Sheet display a trend of rapidly decreasing MgO and increasing TiO_2 which is thought to be due to fractional crystallization. A second trend of rapidly increasing MnO in ilmenites, from the most differentiated rocks, is thought to reflect a later event of subsolidus deuteric alteration.

o) Decreasing Fe_2O_3 with progressive differentiation in New

Amalfi Sheet ilmenites is thought to reflect decreasing temperatures of equilibration.

p) Continuous trends in pyroxene, olivine, feldspar, spinel and ilmenite compositions, indicate that the granophyres are probably genetically related to the undoubtedly igneous rocks of the sheet.

5 WHOLE-ROCK GEOCHEMISTRY

5.1 MAJOR ELEMENT GEOCHEMISTRY

5.1.1 Introduction

Walker and Poldervaart (1949) state that the fractionation of Karoo magma results in a dominating iron-enrichment trend which is only surpassed in the very last stages of crystallization by silica, sodium and potassium enrichment. They state that the iron-enrichment trend exhibited by Karoo magmas is the result of the dominant fractionation of ferromagnesian phases over that of plagioclase feldspars. Only in the latter stages of differentiation did plagioclase fractionation overtake that of the ferromagnesian minerals, thereby causing the transition from iron-enrichment to silica, sodium and potassium enrichment in the Karoo magma.

Eales and Booth (1974) showed that the gabbro-ferrogabbro-ferrotholeiite fractionation trend, seen in the case of the Birds River Complex, also follows an iron-enrichment trend which is followed by silica and alkali enrichment in the closing stages of differentiation. They consider the iron-enrichment trend to be the result of fractionation under conditions of slightly decreasing partial pressure of oxygen. The change to sharply decreasing iron and strong silica and alkali enrichment, in the most evolved ferrotholeiites, was ascribed to a change to fractionation under conditions of increasing partial pressure of oxygen, possibly brought about by the dissociation of CO_2 from country rock sediments as well as the high Fe^{3+}/Fe^{2+} ratio found within these sediments.

Eales and Booth (op. cit.) also showed that continuous trends could be seen when major element whole-rock data from the Birds River Complex, the Mount Arthur Complex and the New Amalfi Sheet were plotted together on the same diagram. Eales (1990) showed that MgO is a very useful index of fractionation for use with Karoo rocks, since a straight-line relationship with a correlation coefficient of -0.978 exists when MgO whole-rock data

Table 5.1

WHOLE-ROCK ANALYSES RECALCULATED TO 100 wt%

PIGEONITE DOLERITES

Sample	NA140	NA79	NA80	NA81	NA85	NA72	NA129
SiO2		51.85	51.85	53.12	50.43	51.94	51.55
TiO2		0.88	0.90	1.25	1.05	0.85	0.91
Al2O3		15.60	15.11	14.20	15.77	15.78	14.39
Fe2O3		11.18	11.21	11.73	12.26	10.38	11.07
MnO		0.18	0.16	0.19	0.20	0.16	0.17
MgO		7.24	7.29	6.12	6.39	7.90	9.07
CaO		10.60	10.41	9.85	10.72	10.59	10.21
Na2O		1.86	2.35	2.55	2.30	1.79	1.93
K2O		0.52	0.61	0.81	0.73	0.47	0.54
P2O5		0.10	0.10	0.18	0.15	0.14	0.15
		100.00	100.00	100.00	100.00	100.00	100.00
Mg#		56.20	56.29	50.83	50.77	60.11	61.85
TRACE ELEMENTS (ppm)							
Sr	208.7	127.2	133.4	202.3	192.1	211.1	182.6
Rb	14.1	15.6	17.1	18.5	21.0	13.7	16.6
Y	29.9	27.0	26.0	28.5	28.0	20.8	24.4
Zr	95.9	81.3	85.9	102.5	93.6	65.5	77.0
Nb	7.6	2.2	2.0	9.6	4.7	5.7	6.9
Co		49.9	47.7	40.4	45.6	45.3	51.2
Cr		368.5	357.9	140.8	135.5	300.6	436.2
V		248.4	251.0	299.6	269.9	240.1	234.7
Zn		87.4	86.8	98.8	93.9	86.0	86.4
Cu		100.2	105.7	108.0	133.5	86.7	92.3
Ni		102.1	95.2	52.4	65.0	120.5	170.6
Th	0.0	0.0	1.5	0.0	1.8	0.0	2.0
Pb	2.9	3.0	3.7	3.5	3.2	2.4	3.1
Ce	28.4	21.9	25.3	25.0	26.9	21.5	25.9
Nd	14.2	11.3	12.0	13.1	17.0	11.7	12.1
La	9.7	8.3	9.7	10.7	11.0	7.1	7.9
Ba	244.8	151.4	174.5	224.5	237.1	218.6	163.1
Sc	35.6	33.3	32.2	38.4	34.8	32.7	31.7

OLIVINE DOLERITES

Sample	NA136	NA125	NA124	NA97	NA98	NA99	NA184
SiO2	51.34	51.29	51.06	49.98	51.27	49.13	53.17
TiO2	1.07	0.89	0.88	0.86	0.83	0.79	1.13
Al2O3	14.81	15.94	16.41	16.39	15.49	13.29	14.13
Fe2O3	12.51	10.21	9.91	10.35	10.38	11.62	12.08
MnO	0.19	0.16	0.16	0.18	0.17	0.17	0.19
MgO	6.39	7.62	7.56	8.54	8.09	13.13	6.32
CaO	10.73	10.95	11.05	10.68	10.87	9.06	10.07
Na2O	2.20	2.28	2.31	2.36	2.30	2.16	2.13
K2O	0.58	0.53	0.53	0.54	0.49	0.52	0.62
P2O5	0.16	0.13	0.13	0.13	0.12	0.13	0.17
	100.00	100.00	100.00	100.00	100.00	100.00	100.00
Mg#	50.29	59.64	60.16	62.02	60.69	69.10	50.89
TRACE ELEMENTS (ppm)							
Sr	175.6	204.2	205.4	216.5	196.1	176.3	222.1
Rb	14.4	13.7	11.7	10.6	11.0	12.0	19.2
Y	26.9	21.5	21.1	21.1	20.1	20.2	27.4
Zr	95.7	69.5	65.4	63.8	59.0	63.0	85.2
Nb	4.9	4.8	6.0	5.9	5.0	5.4	8.0
Co	44.5	44.7	41.3	47.2	46.2	64.3	44.0
Cr	131.5	376.5	437.4	370.9	370.7	906.2	32.5
V	272.0	218.9	224.2	214.1	220.3	204.4	293.3
Zn	95.8	76.2	76.2	79.7	76.8	83.2	95.4
Cu	124.8	86.6	85.4	85.8	86.1	80.2	97.6
Ni	69.3	130.1	110.9	146.9	115.5	340.1	48.0
Th	0.0	0.0	0.0	0.0	0.0	0.0	0.0
Pb	2.3	2.6	2.1	0.0	2.2	2.2	2.5
Ce	27.4	19.5	14.6	18.5	19.1	15.9	23.0
Nd	15.5	10.6	8.6	9.3	9.4	8.6	11.5
La	11.4	7.5	9.2	5.8	7.8	6.9	10.8
Ba	206.7	161.3	156.8	157.7	142.0	152.1	208.8
Sc	33.7	29.7	31.7	29.2	32.3	28.0	39.5

Table 5.1 (cont.)

	QUARTZ GABBROS					
Sample	NA185	NA92	NA93	NA95	NA96	NA186	NA187
SiO2	52.48	52.53	53.36	53.67	53.50	53.40	53.59
TiO2	0.83	1.35	1.37	1.29	1.28	1.20	1.21
Al2O3	14.98	14.59	13.85	14.36	13.52	13.83	13.77
Fe2O3	9.96	13.53	13.23	12.60	13.18	12.66	13.01
MnO	0.18	0.21	0.20	0.20	0.20	0.20	0.21
MgO	7.86	4.69	5.26	4.92	5.53	5.93	5.53
CaO	11.20	9.43	9.15	9.11	9.16	9.65	9.26
Na2O	2.13	2.67	2.54	2.76	2.59	2.26	2.35
K2O	0.29	0.80	0.84	0.92	0.86	0.70	0.88
P2O5	0.10	0.20	0.19	0.18	0.18	0.18	0.19
	100.00	100.00	100.00	100.00	100.00	100.00	100.00
Mg#	60.98	40.68	44.03	43.58	45.35	48.13	45.69
TRACE ELEMENTS (ppm)							
Sr	233.8	230.0	215.7	226.7	213.7	212.4	213.8
Rb	5.2	17.4	18.8	22.1	21.0	15.6	21.4
Y	18.8	30.1	32.8	30.1	31.5	28.3	29.5
Zr	56.9	94.3	102.6	93.9	97.8	89.0	96.5
Nb	2.8	9.1	9.8	8.1	9.7	7.2	10.2
Co	43.6	42.0	42.5	42.9	45.3	45.9	45.2
Cr	41.3	9.4	11.9	9.4	12.0	18.1	13.1
V	301.5	315.8	307.3	300.8	321.6	313.3	317.2
Zn	82.5	105.9	105.4	99.9	106.1	101.7	101.7
Cu	87.5	184.3	199.7	307.3	187.0	224.8	275.8
Ni	73.5	30.6	39.4	40.0	42.3	50.0	43.7
Th	0.0	0.0	0.0	0.0	1.6	0.0	1.6
Pb	1.7	3.8	4.6	3.8	3.8	1.8	2.4
Ce	18.1	28.0	31.7	28.2	29.7	26.3	31.6
Nd	9.0	13.5	14.7	15.1	13.8	13.0	17.0
La	5.5	10.5	10.3	13.1	11.5	9.3	10.5
Ba	152.8	257.3	267.1	245.6	238.1	221.9	247.6
Sc	40.3	39.9	39.5	39.2	43.9	42.3	42.9

	QUARTZ MONZODIORITES						
Sample	NA188	NA189	NA160	NA176	NA190	NA191	NA169
SiO2	50.98	50.92	51.53	52.90	53.53	52.70	55.30
TiO2	2.78	2.87	2.88	2.69	2.81	3.31	2.63
Al2O3	11.78	11.81	11.46	11.87	11.62	11.43	11.04
Fe2O3	18.70	18.68	18.99	18.20	17.81	18.64	17.87
MnO	0.22	0.23	0.23	0.23	0.24	0.23	0.22
MgO	4.15	3.88	3.53	3.09	3.06	2.67	2.16
CaO	8.06	8.16	7.59	7.61	7.23	7.07	6.12
Na2O	2.07	2.26	2.37	2.09	2.29	2.40	2.47
K2O	1.01	0.94	1.13	0.98	1.11	1.28	1.77
P2O5	0.25	0.25	0.30	0.34	0.30	0.27	0.44
	100.00	100.00	100.00	100.00	100.00	100.00	100.00
Mg#	30.52	29.15	26.90	25.17	25.41	22.12	19.30
TRACE ELEMENTS (ppm)							
Sr	183.5	188.4	189.6	212.6	196.6	198.3	175.9
Rb	23.9	23.8	29.7	28.4	30.8	33.6	44.4
Y	38.9	38.6	44.2	51.6	45.1	46.5	61.8
Zr	132.7	136.6	156.3	173.5	167.8	178.0	231.0
Nb	12.9	12.5	14.6	18.2	15.6	16.6	22.9
Co	60.5	57.4	54.7	51.0	49.2	48.9	43.7
Cr	5.1	6.6	8.3	8.2	10.2	12.9	13.7
V	1079.3	848.0	742.9	556.7	344.9	280.4	167.6
Zn	146.6	145.2	150.1	151.5	159.3	165.2	174.9
Cu	323.0	303.8	279.2	248.7	243.0	244.1	172.0
Ni	36.5	27.9	27.8	17.1	10.8	8.5	7.1
Th	2.0	2.1	3.8	2.7	4.7	4.5	4.5
Pb	3.9	5.2	5.9	6.0	6.1	5.9	8.6
Ce	39.7	34.8	42.5	47.8	47.7	52.9	59.4
Nd	18.9	18.0	24.1	25.0	23.4	24.9	33.0
La	12.7	13.0	18.7	18.4	19.6	20.3	26.4
Ba	310.0	324.0	401.8	352.4	374.6	418.3	504.6
Sc	47.3	46.5	42.0	41.0	39.3	39.3	32.8

Table 5.1 (cont.)

			GRANODIORITES				
Sample	NA90	NA91	NA192	NA161	NA153	NA193	NA179
SiO2	49.24	49.76	58.47	56.79	57.94	60.00	63.33
TiO2	3.08	2.62	1.92	1.93	1.75	1.59	1.25
Al2O3	11.90	12.30	11.58	11.06	11.22	11.60	11.10
Fe2O3	19.31	18.20	15.01	17.32	16.93	14.79	13.72
MnO	0.22	0.23	0.20	0.22	0.22	0.20	0.20
MgO	4.23	4.44	1.44	1.33	1.18	1.03	0.83
CaO	8.49	8.76	5.92	5.82	5.34	5.03	4.44
Na2O	2.43	2.57	2.74	2.82	2.69	2.78	2.42
K2O	0.89	0.91	2.02	1.96	2.09	2.34	2.37
P2O5	0.21	0.22	0.70	0.76	0.63	0.64	0.36
	100.00	100.00	100.00	100.00	100.00	100.00	100.00
Mg#	30.25	32.60	15.96	13.23	12.10	12.07	10.70
TRACE ELEMENTS (ppm)							
Sr	196.8	192.4	189.6	179.5	185.3	181.4	191.9
Rb	20.7	22.2	49.5	48.8	54.7	60.8	65.0
Y	35.9	32.8	74.0	80.3	79.4	81.8	84.4
Zr	112.0	111.8	271.3	253.2	262.6	302.5	339.4
Nb	10.6	8.1	25.0	25.9	26.9	28.6	29.9
Co	61.2	59.6	27.2	43.9	22.7	19.4	15.8
Cr	3.5	3.5	13.0	20.3	12.0	13.1	12.2
V	1077.0	1041.4	10.3	5.9	0.0	2.4	0.0
Zn	138.1	129.7	160.4	208.8	180.4	167.2	172.7
Cu	387.6	351.7	62.5	68.0	61.8	53.5	45.2
Ni	31.6	38.3	0.0	3.8	4.2	3.9	5.0
Th	1.8	0.0	5.7	6.3	5.9	6.7	7.9
Pb	4.8	4.4	6.0	9.8	11.6	9.4	9.2
Ce	36.7	37.1	78.3	82.3	76.5	77.9	86.1
Nd	18.6	20.4	42.4	45.4	43.6	45.4	48.4
La	10.9	14.2	30.8	31.6	32.8	37.5	39.5
Ba	309.4	300.2	566.0	550.9	605.7	645.0	896.8
Sc	47.7	45.9	32.7	27.5	24.9	22.4	19.7

			FAYALITE-HEDENBERGITE GRANOPHYRES				
Sample	NA162	NA164	NA159	NA155	NA158	NA165	NA166
SiO2	61.01	60.25	63.13	64.43	65.62	63.80	66.13
TiO2	1.37	1.39	1.16	1.08	0.99	1.09	0.95
Al2O3	11.38	11.39	11.73	11.80	11.79	11.71	11.77
Fe2O3	14.67	15.24	12.74	11.73	10.91	12.26	10.52
MnO	0.20	0.23	0.19	0.16	0.15	0.17	0.15
MgO	0.81	0.80	0.62	0.63	0.47	0.62	0.43
CaO	4.72	4.89	4.20	3.90	3.55	4.12	3.44
Na2O	3.00	3.10	3.36	3.32	3.47	3.29	3.47
K2O	2.42	2.31	2.59	2.70	2.84	2.68	2.94
P2O5	0.41	0.41	0.29	0.26	0.21	0.25	0.20
	100.00	100.00	100.00	100.00	100.00	100.00	100.00
Mg#	9.85	9.38	8.74	9.64	7.90	9.13	7.53
TRACE ELEMENTS (ppm)							
Sr	171.1	180.7	172.3	185.1	155.6	174.6	164.4
Rb	65.8	60.3	67.1	71.6	71.5	68.4	77.7
Y	78.7	79.8	90.3	89.3	103.5	86.3	85.6
Zr	298.7	298.2	331.8	348.4	340.1	325.4	353.3
Nb	31.2	31.3	34.0	33.6	34.9	35.2	35.2
Co	15.0	14.3	10.8	9.1	9.8	10.3	9.0
Cr	16.4	16.1	12.6	12.2	14.3	16.9	10.8
V	0.0	0.0	0.0	0.0	0.0	0.0	0.0
Zn	202.7	169.0	165.3	166.3	198.3	169.1	150.5
Cu	47.5	48.2	40.0	35.4	31.8	40.4	33.2
Ni	4.0	7.2	4.2	5.7	4.9	5.1	0.0
Th	6.4	6.1	6.9	8.2	7.7	7.9	7.8
Pb	15.8	9.7	10.2	12.1	12.1	12.2	12.6
Ce	79.9	82.0	84.4	91.4	95.0	85.3	90.5
Nd	43.2	45.1	46.7	51.0	51.6	47.5	48.4
La	36.3	33.4	39.9	38.9	45.3	37.1	41.3
Ba	652.4	647.7	710.8	719.6	749.8	739.2	838.0
Sc	22.0	21.6	17.7	17.0	13.9	16.9	13.2

Table 5.1 (cont.)

	FAYALITE-HEDENBERGITE GRANOPHYRES						
Sample	NA167	NA171	NA172	NA170	NA89	NA168	NA83
SiO2	64.95	62.91	63.14	66.08	64.62	72.52	71.45
TiO2	1.02	1.21	1.16	0.93	1.07	0.53	0.62
Al2O3	11.92	11.67	11.66	11.59	11.91	11.42	11.51
Fe2O3	11.58	13.00	12.97	10.95	11.67	6.29	7.31
MnO	0.16	0.18	0.19	0.17	0.16	0.09	0.10
MgO	0.55	0.61	0.59	0.44	0.41	0.24	0.25
CaO	3.78	4.16	4.17	3.45	3.76	1.44	1.54
Na2O	3.09	3.36	3.21	3.21	3.35	3.65	3.66
K2O	2.70	2.59	2.60	3.00	2.81	3.78	3.49
P2O5	0.25	0.31	0.31	0.17	0.24	0.05	0.07
	100.00	100.00	100.00	100.00	100.00	100.00	100.00
Mg#	8.62	8.51	8.22	7.44	6.55	6.92	6.37
TRACE ELEMENTS (ppm)							
Sr	161.9	171.9	178.7	170.7	163.2	108.0	91.9
Rb	71.1	67.2	62.7	76.4	69.2	95.1	89.1
Y	89.6	89.6	83.7	89.9	89.6	107.3	143.3
Zr	327.5	332.0	337.8	370.1	339.4	372.0	488.3
Nb	33.2	33.7	33.3	36.8	36.0	37.8	35.0
Co	9.8	13.2	9.1	7.4	9.1	3.4	4.0
Cr	12.2	11.9	16.1	11.9	9.9	8.3	5.6
V	0.0	0.0	0.0	0.0	0.0	0.0	0.0
Zn	165.2	176.2	168.6	158.3	162.2	115.3	130.1
Cu	36.7	38.2	36.4	36.5	35.0	16.1	17.0
Ni	3.7	3.8	5.0	3.4	0.0	4.3	5.3
Th	7.3	7.7	7.4	9.3	8.0	11.2	11.0
Pb	12.5	10.0	10.7	13.6	12.8	13.8	15.2
Ce	88.9	92.4	85.0	95.5	90.4	103.4	111.9
Nd	48.4	48.6	48.2	50.5	48.9	60.7	81.5
La	43.6	45.6	39.2	44.7	40.2	57.0	85.7
Ba	722.5	716.8	717.2	820.3	781.2	957.0	761.5
Sc	15.0	18.0	16.2	13.2	16.0	5.0	8.8

		GRANOPHYRES			VEIN	VEIN	XNOLTH.		SNDSTNE.
Sample	NA182	NA86	NA87	NA88	NA121	NA134	NA181	Sample	NA113
SiO2		66.83	68.51	72.01	71.29	72.12	72.58	SiO2	81.17
TiO2		0.91	0.80	0.56	0.68	0.55	0.55	TiO2	0.46
Al2O3		11.68	11.78	11.88	11.36	11.28	11.46	Al2O3	10.39
Fe2O3		10.31	9.03	6.41	7.02	6.18	5.93	Fe2O3	3.27
MnO		0.15	0.14	0.11	0.09	0.09	0.08	MnO	0.08
MgO		0.35	0.17	0.09	0.28	0.19	0.24	MgO	0.49
CaO		3.10	2.44	1.14	1.61	1.78	1.20	CaO	0.23
Na2O		3.36	3.60	3.92	4.17	4.15	4.08	Na2O	1.50
K2O		3.11	3.38	3.84	3.41	3.63	3.84	K2O	2.30
P2O5		0.18	0.14	0.05	0.08	0.04	0.05	P2O5	0.10
		100.00	100.00	100.00	100.00	100.00	100.00		100.00
Mg#		6.25	3.57	2.80	7.30	5.74	7.48	Mg#	22.90
TRACE ELEMENTS (ppm)								TRACE ELEMENTS (ppm)	
Sr	212.3	134.8	132.9	91.7	120.9	96.2	87.3	Sr	73.2
Rb	50.6	76.3	88.2	105.3	68.2	96.8	79.9	Rb	91.8
Y	77.0	95.5	102.9	142.4	87.6	107.3	87.3	Y	28.9
Zr	272.4	411.3	404.0	455.2	424.9	477.4	459.6	Zr	313.7
Nb	27.4	37.1	38.9	39.9	34.5	35.4	35.1	Nb	14.4
Co		7.4	6.5	2.5	5.6	3.5	4.4	Co	11.5
Cr		7.7	7.7	5.8	9.1	7.2	14.2	Cr	39.8
V		0.0	0.0	0.0	2.6	0.0	0.0	V	57.9
Zn		150.4	155.6	128.4	98.3	124.3	91.8	Zn	49.5
Cu		29.4	28.6	19.9	30.0	23.0	11.0	Cu	13.3
Ni		0.0	3.1	4.2	3.5	4.7	6.2	Ni	16.7
Th	6.2	9.3	9.3	11.2	10.0	11.5	10.6	Th	13.7
Pb	8.6	12.6	15.1	17.6	10.7	14.7	14.9	Pb	15.7
Ce	78.3	93.5	97.0	111.4	94.8	108.9	93.1	Ce	60.3
Nd	43.6	51.5	54.7	75.5	53.4	56.4	48.2	Nd	29.1
La	32.3	41.6	50.1	75.5	47.6	53.3	42.5	La	34.6
Ba	632.1	794.0	867.0	1105.5	772.2	805.0	985.4	Ba	740.1
Sc	21.9	13.4	10.7	5.5	7.1	4.9	4.7	Sc	9.1

from the Birds River Complex is plotted against percentage crystallization. For this reason MgO has been used as an index of fractionation in the Harker diagrams shown in the next section. Fifty-seven whole-rock analyses, covering the entire range of compositions seen within the New Amalfi Sheet, are presented in Table 5.1. Volatiles have been subtracted from the analyses, which have then been recalculated to 100 wt%. The original analyses prior to recalculation are shown in Appendix II. Analytical techniques used have been summarized in Appendix I.

5.1.2 Harker diagrams.

In Figure 5.1, MgO can be seen to decrease progressively with fractionation from 13.13 wt% in the basal olivine dolerite (which contains 14% modal olivine, probably cumulus in nature) to 0.09 wt% in the most evolved granophyre. Because of the olivine enrichment seen within the basal olivine dolerite, this sample is often displaced from the fractionation trend defined by the rest of the whole-rock samples.

Silica increases slightly with differentiation from the dolerites to the top of the quartz gabbros, from 49.13 wt% to 53.7 wt%. This is followed by a sudden decrease in SiO_2 at the beginning of the quartz monzodiorites, because of the diluting effect of cumulus opaque-oxide phases which enter the paragenesis at this stage. From this point onwards, SiO_2 increases exponentially with progressive differentiation, as seen from the hyperbolic shape of the curve, and reaches a maximum of 72 wt% in the most evolved granophyre.

Al_2O_3 decreases steadily with fractionation to a low of 11 wt%, but the rate of decrease declines towards the end stages of fractionation. TiO_2, Fe_2O_3 and MnO all follow similar trends. This involves constant to slightly decreasing concentrations up till half-way through the dolerite range, followed by a steady increase up till the end of the quartz gabbro range, which is followed by a sudden increase, because of the effect of cumulus opaque-oxides, and a slight decrease, followed finally by a

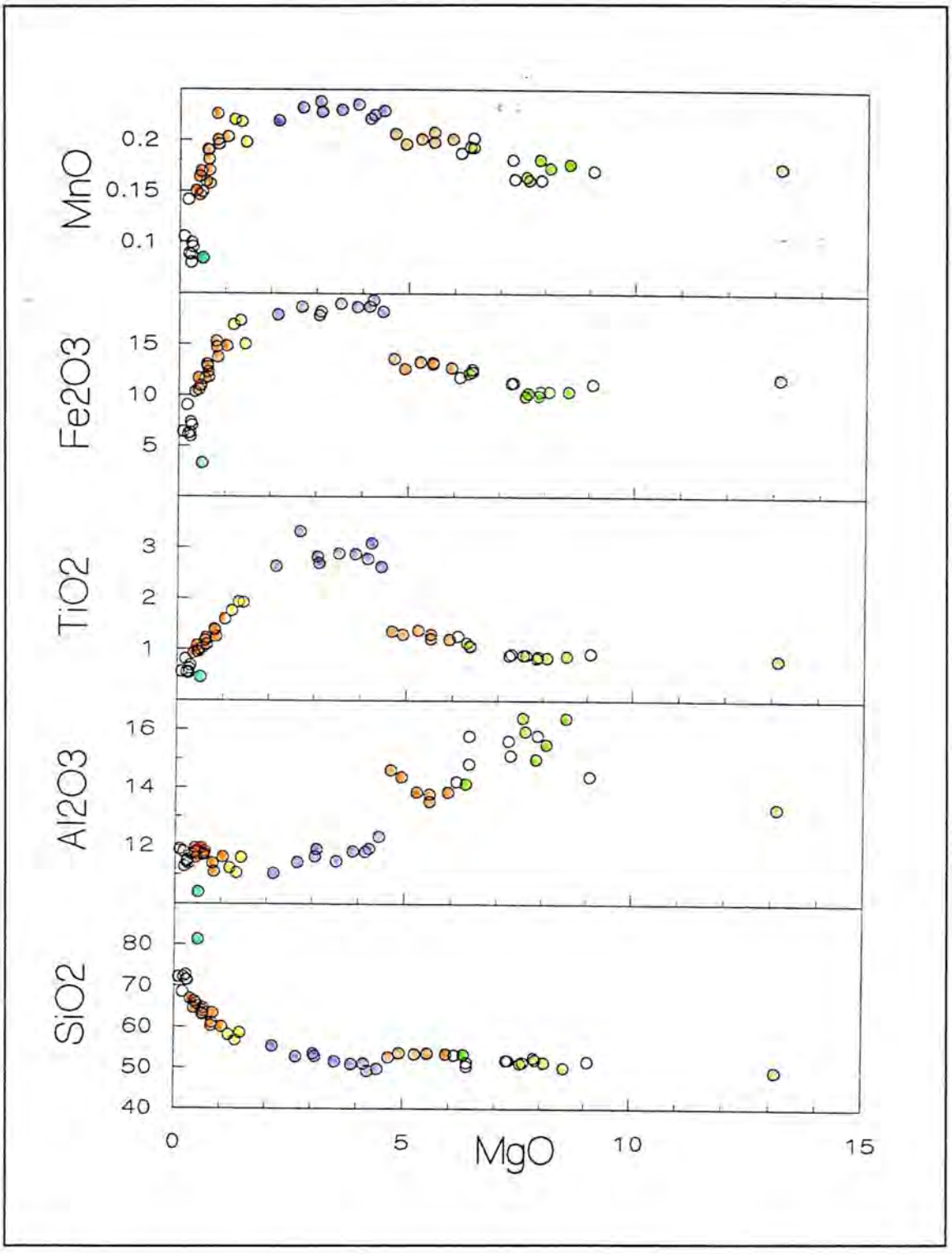

Figure 5.1 New Amalfi Sheet whole-rock analyses. ● = olivine dolerites; ○ = pigeonite dolerites; ● = quartz gabbros; ● = quartz monzodiorites; ● = granodiorites; ● = fayalite-hedenbergite granophyres; ○ = granophyres ● = sediment

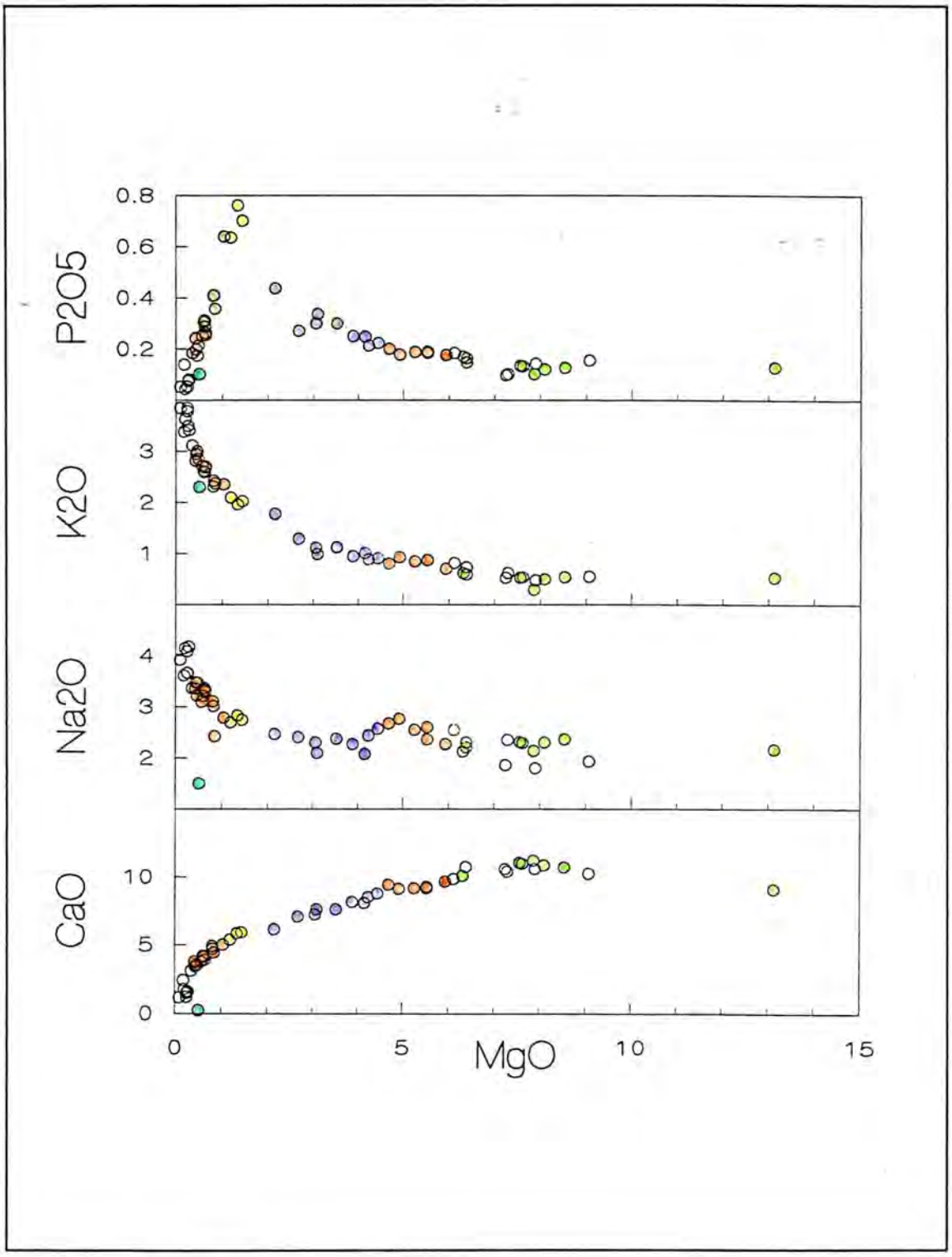

Figure 5.1 (cont.)

sharp decrease which lasts till the end of the differentiation trend.

CaO shows an exponential decrease with progressive differentiation, from 11 wt% to 1.1 wt%. Na_2O and K_2O both show exponential increases with differentiation from 1.79 wt% and 0.29 wt% respectively to maxima of 3.92 wt% and 3.84 wt% respectively. P_2O_5 increases exponentially from 0.1 wt% in the dolerites to 0.76 wt% at the top of the granodiorites, at which point it decreases rapidly to below 0.1% in the most evolved granophyres.

Figure 5.2 clearly shows the relative entry points of the opaque-oxides and apatite into the paragenetic sequence, as shown by the effect that this has on the concentrations of P_2O_5 and TiO_2 in the magma. Initially both P_2O_5 and TiO_2 behave incompatibly and both increase with differentiation. Opaque-oxides enter the paragenetic sequence first, as seen from the first inflection after which TiO_2 decreases while P_2O_5 is still increasing. Apatite then enters the paragenetic sequence as well, at the second inflection, after which both TiO_2 and P_2O_5 decrease with differentiation, reaching almost the same concentrations as those seen in the most primitive rocks.

In all the plots shown in Figures 5.1 and 5.2, a continuous fractionation trend exists between the dolerites and granophyres. This suggests that the granophyres were derived from the fractional crystallization of a mafic parent, and does not support a metasomatic origin for the New Amalfi Sheet granophyres.

5.1.3 Qualitative interpretation of mineral phases involved in the fractional crystallization process.

In Figures 5.3 (a & b) whole-rock compositions have been plotted together with average clinopyroxene, olivine, plagioclase and spinel compositions for each sample. The compositions of the average Lesotho Type magma (Marsh and Eales, 1984) and the New Amalfi Sheet initial liquid are also shown. The relevant calculations are presented in the section on trace elements.

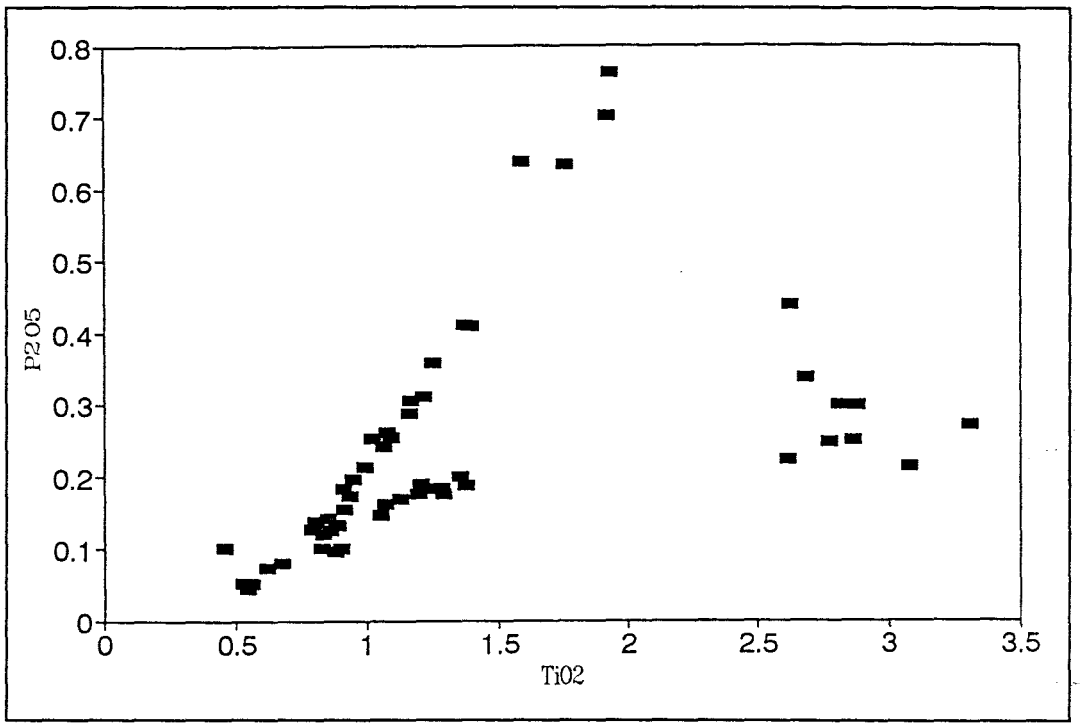

Figure 5.2 Whole-rock P_2O_5 versus TiO_2 for the New Amalfi Sheet.

From Figure 5.3 (a & b) it can be seen that a number of dolerite samples plot along a mixing line between the New Amalfi Sheet initial liquid, and the most MgO-rich olivine. This suggests that these dolerites have undergone cumulus enrichment in olivine. It can also be seen that there is a wide range in MgO concentration in the olivines in the olivine dolerites, with most of the olivines not falling on the mixing line. This suggests that many of the olivines from the olivine dolerites may have had their compositions modified during subsolidus cooling to more iron-rich compositions. This has been previously documented for rocks from the Insizwa Complex by Cawthorn et al. (1992) who explained that it is due to the interaction between olivine and entrapped cumulus liquid, termed the trapped liquid shift effect.

From the point representing the New Amalfi Sheet initial liquid, to the end of the quartz gabbro range, both SiO_2 and Fe_2O_3 increase in the residual liquid and this appears to be due to combined plagioclase and clinopyroxene fractionation. The entry of opaque-oxide minerals into the paragenetic sequence at the start of the quartz gabbro range marks the transition to decreasing Fe_2O_3 and a greater rate of increase in SiO_2.

5.1.4 Pearce Element Ratios.

Pearce element ratios provide a means for determining the absolute degree of change in various elements during chemical differentiation, based on the concept that conserved elements (elements that remain unchanged in absolute amount during differentiation) are used as common denominators within the ratios. Ratios with conserved elements in the numerators will remain constant throughout the differentiation process, but ratios with elements that are involved in the differentiation process as the numerator will vary according to their stoichiometry in the separated phases (Russel and Nicholls, 1988). This therefore provides a means of determining if a suite of rocks are related to each other by the differentiation of a common parent (i.e., are comagmatic) as well as which phases were involved in the differentiation process.

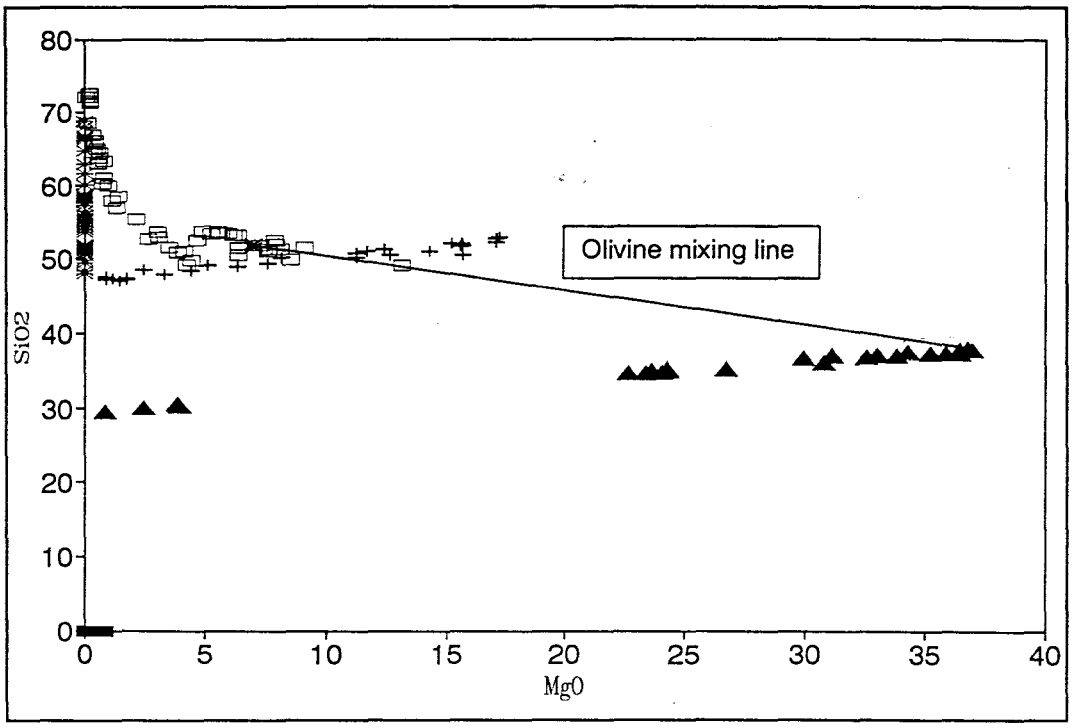

Figure 5.3 (a) New Amalfi Sheet whole-rock SiO_2 versus MgO plotted together with average mineral data. □ = whole-rock; + = calcium-rich pyroxenes; ▲ = olivines; * = plagioclase; ■ = magnetite; x = Average Lesotho type magma; x = New Amalfi Sheet initial liquid.

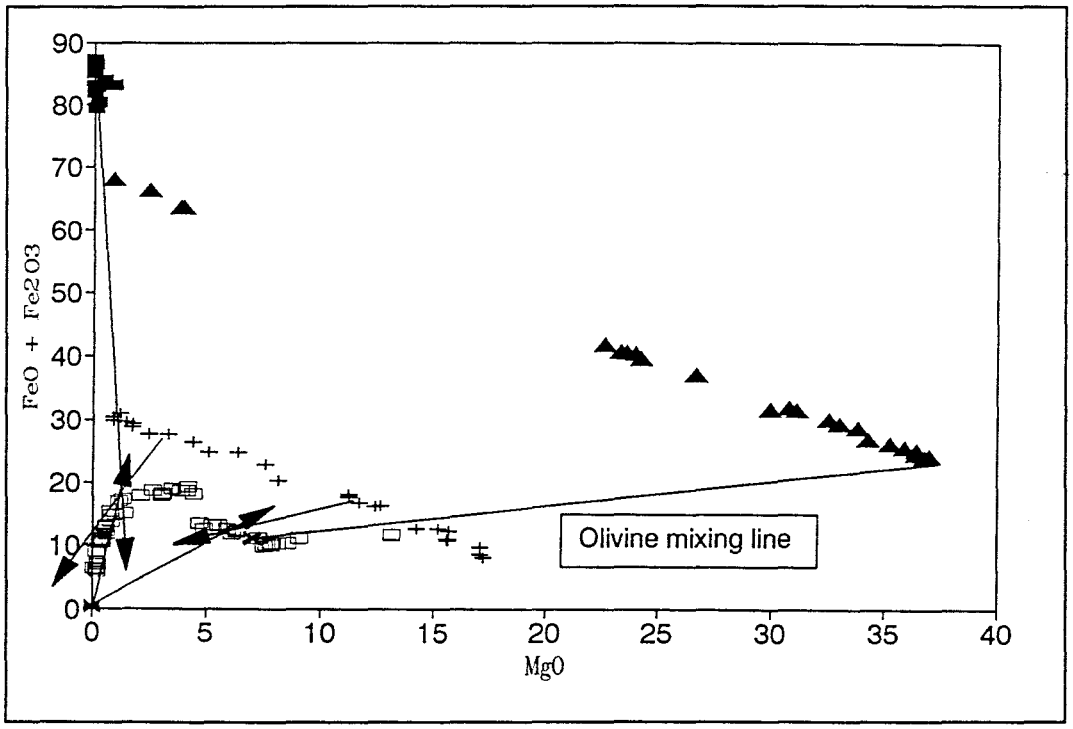

Figure 5.3 (b) New Amalfi Sheet whole-rock Fe_2O_3 versus MgO plotted together with average mineral data.

In Figure 5.4, two Pearce element ratios made up entirely of conserved elements have been plotted against each other. These ratios should not change throughout the differentiation process if the suite of rocks is comagmatic and the suite of rocks should plot as a tight cluster of points. As can be seen from Figure 5.4, this is indeed the case for most of the New Amalfi Sheet whole-rock samples, including the granophyres, and this provides strong support for the view that these rocks are comagmatic, and that the granophyres are related to the rest of the New Amalfi Sheet by differentiation from a common parent. Those few samples that plot away from the cluster have probably undergone secondary changes in some of the elements represented in the ratios plotted, because of weathering or alteration.

In Figure 5.5 the Pearce element ratios 0.5(Mg+Fe)/K and Si/K have been specially selected, so that any chemical compositions that are derived by either the addition or subtraction of olivine alone will plot along a straight line with a slope of 1 (Russel and Nicholls, op. cit.). If any other phase which contains either Fe, Mg or Si is either added or subtracted, then the slope will deviate from 1. The data in Figure 5.5 plots along a straight line with a slope of 0.216, indicating that olivine separation alone was not responsible for the differentiation. The low value of the slope suggests that olivine fractionation was of minor significance.

In Figure 5.6 the Pearce element ratios have been selected so as to eliminate the effects of olivine and Fe-Ti oxide separation. A slope of 1 would indicate plagioclase separation alone, and a vertical slope clinopyroxene separation alone. If both phases separate, the data will define a slope of between 1 and infinity, with the proportion of plagioclase to pyroxene given by the relation (CPX + PL)/PL=slope (Russel and Nicholls, op. cit.). The data for the New Amalfi Sheet defines a slope of 2.62 and hence the calculated ratio of CPX/PL=1.62 indicates that clinopyroxene fractionation dominated over that of plagioclase.

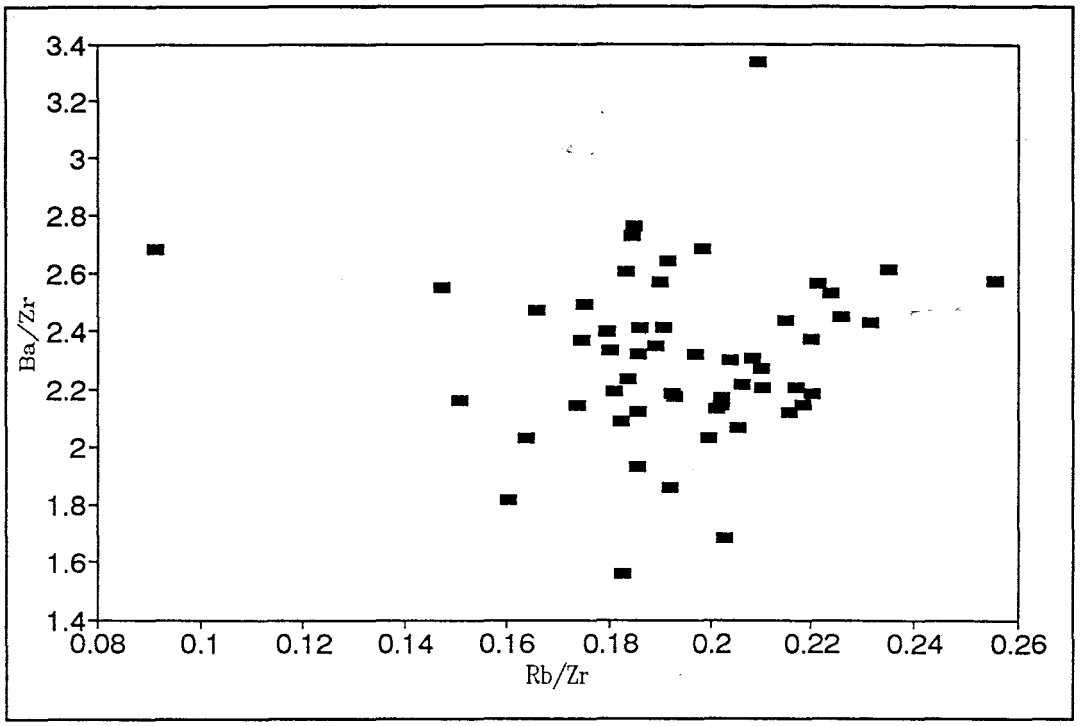

Figure 5.4 A plot of two Pearce element ratios with conserved elements in the numerator and denominator.

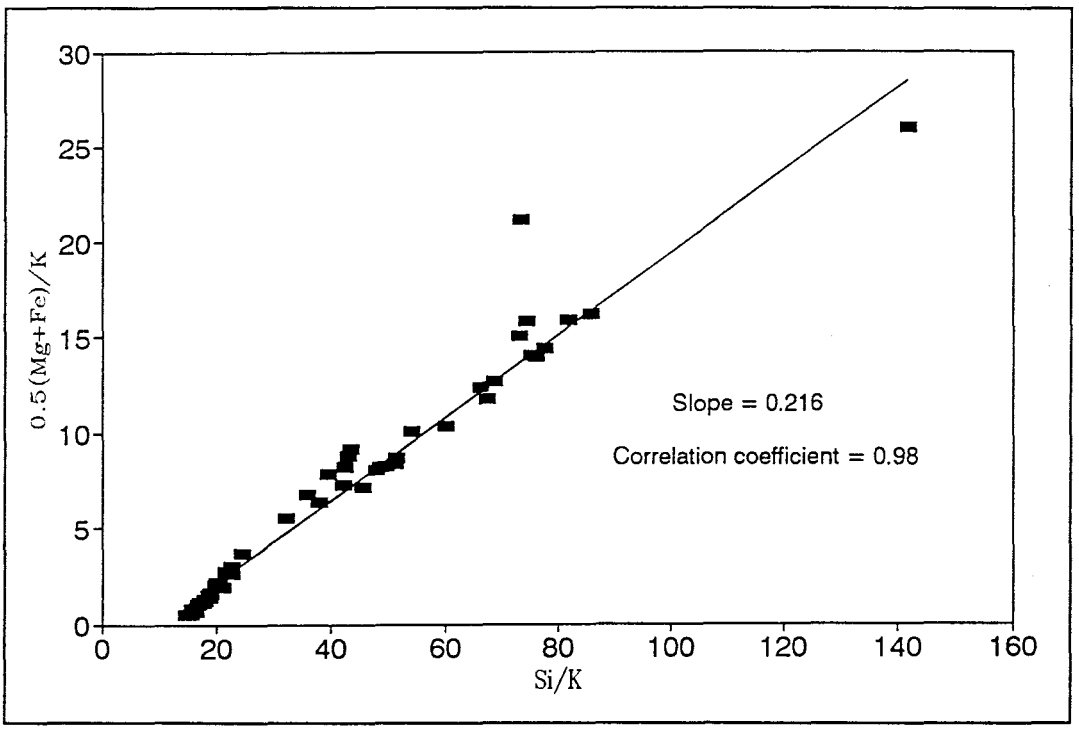

Figure 5.5 Whole-rock data plotted in terms of two Pearce element ratios.

5.1.5 AFM Plot.

The whole-rock data for the New Amalfi Sheet, captured during the course of this study, has been plotted on the ternary AFM diagram (Figure 5.7) together with Birds River data from Eales (1990) and Skaergaard data from Wager and Brown (1968) for comparison. It can be seen that the iron-enrichment exhibited by the New Amalfi Sheet is slightly greater than that of the Birds River Complex but does not reach the extreme levels exhibited by the Skaergaard Intrusion. The different levels of iron-enrichment seen in these three intrusions is probably related to different redox conditions during crystallization, as suggested by Eales and Booth (1974), but the iron-enrichment trend itself seems to be caused by plagioclase, pyroxene and/or olivine fractionation as has been shown above. It has also been shown above that the transition to decreasing iron and rapidly increasing silica and alkalis is marked by the appearance of cumulus opaque-oxide phases.

5.2 TRACE ELEMENT GEOCHEMISTRY.

5.2.1 Incompatible trace element geochemistry.

In Figure 5.8, the variation, with progressive differentiation, of the incompatible elements Ti, P, K, Rb, Y, Nb, Th, Pb, La, Ce, Ba and Zr, is shown. Zr is used on the abscissa for the same reasons put forward by Marsh and Eales (1984), namely that it is precisely determined by means of XRF methods, it is relatively unaffected by alteration, and it exhibits near-perfect incompatible behaviour during most of the differentiation stage of tholeiitic magmas.

The fractionation interval over which incompatible behaviour is maintained by both elements in each plot in Figure 5.8, is marked by a straight line relationship, which, when extrapolated, passes through the origin. Regression lines have been calculated for each plot and the slope, intercept and correlation coefficients are shown in Table 5.2.

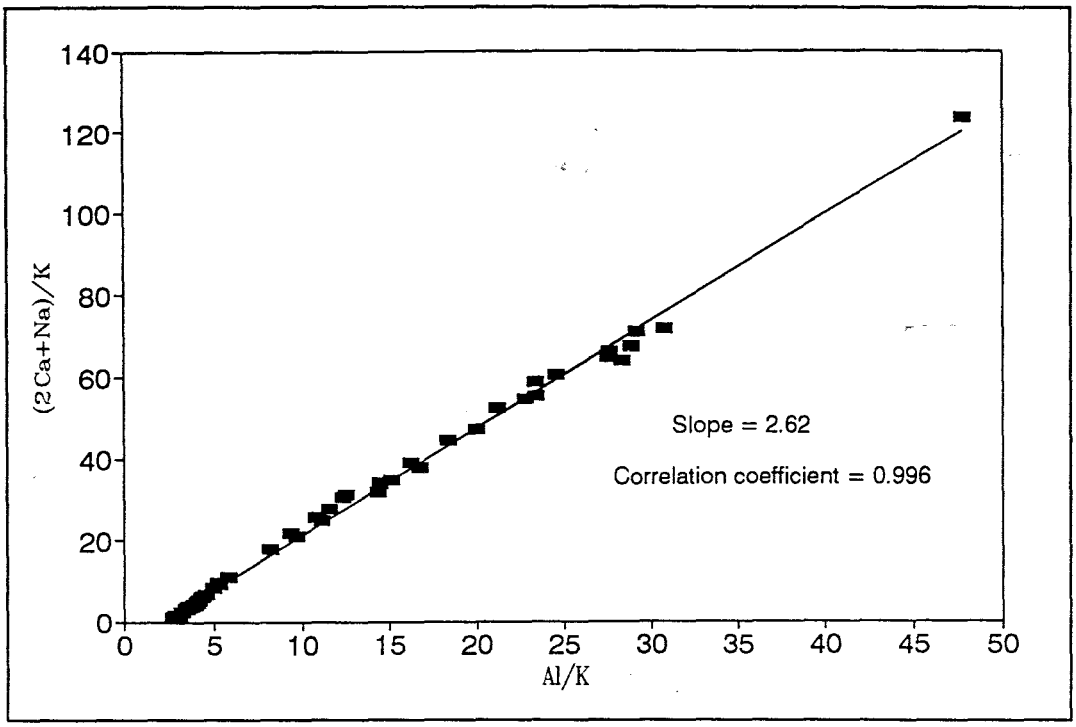

Figure 5.6 Whole-rock data plotted in terms of two Pearce element ratios.

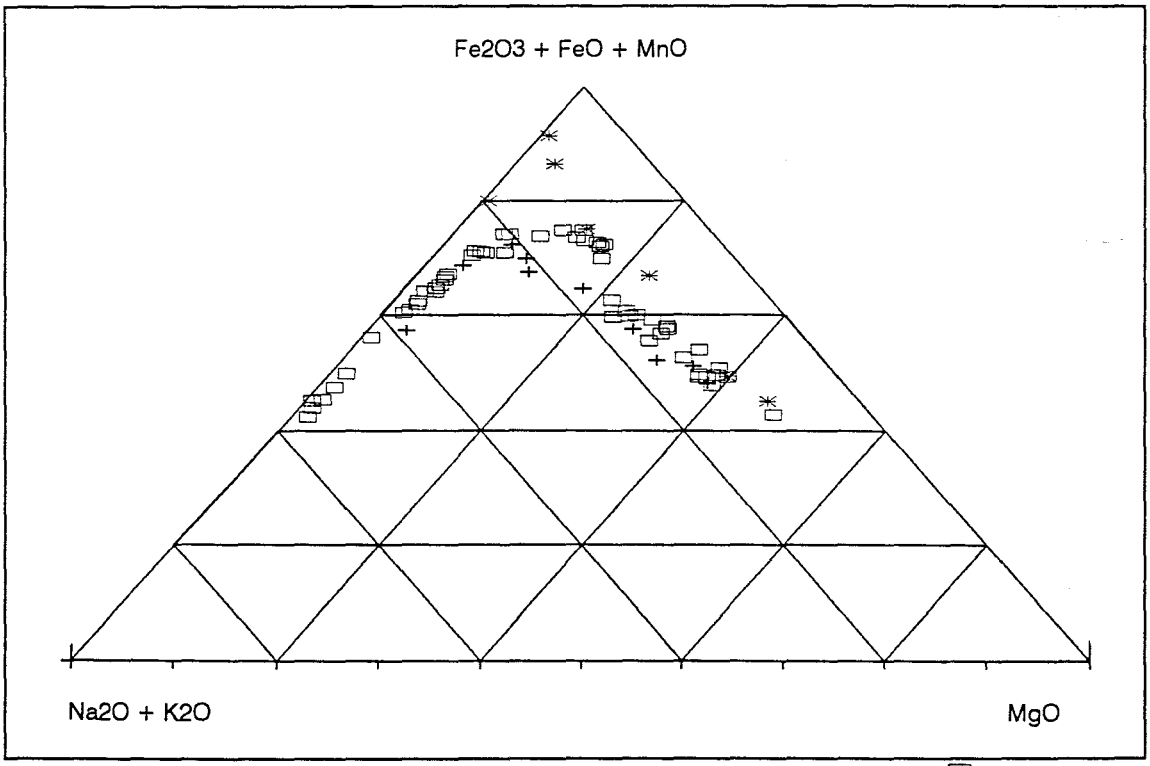

Figure 5.7 New Amalfi Sheet whole-rock analyses (□) plotted on the AFM diagram together with Birds River data (+) (Eales, 1990) and Skaergaard data (*) (Wager and Brown, 1968) for comparison.

The incompatible behaviour of an element is typically disrupted when a mineral that readily accepts the element into its lattice begins to nucleate. It can be seen from Figure 5.8 that incompatible behaviour breaks down in the case of Ti at the top of the quartz gabbros, and this coincides with the entry of cumulus magnetite and ilmenite to the paragenetic sequence. Ti is an essential structural element within the ilmenite lattice and Ti has a distribution coefficient of 7.5 between magnetite and melt (Pearce and Norry, 1979). Therefore, the nucleation of these two minerals is responsible for the breakdown in the incompatible behaviour of Ti.

The elements P, Y and Pb show a break-down of incompatible behaviour at the beginning of the granodiorite range and this is due to the nucleation of cumulus apatite within the granodiorites. Once again, the depletion in P can be explained by its being an essential structural element within apatite. Y^{3+} is closest in size to Ca^{2+} and Y can therefore be expected to enter into early Ca sites such as those provided by augite and plagioclase (Taylor, 1965). The fact that Y is concentrated into the later-forming Ca sites of apatite instead, is probably due to the more covalent character of the Y=O bond compared to the Ca-O bond (Taylor, 1965). Taylor (op. cit.) states that Pb^{2+} is intermediate in size between Ca^{2+} and K^{+} and can therefore be expected to substitute for either element. However, the Ca site in apatite is considered to be a particularly suitable site for Pb since the Ca occurs in nine-fold co-ordination with oxygen (Taylor, op. cit.).

The elements K, Ba, Rb, Ce, La, Nd and Nb all show a breakdown in incompatible behaviour at the top of the fayalite-hedenbergite granophyres. K is an essential component of K-feldspar and Ba has a distribution coefficient between K-feldspar, and melt of 6.12 (Philpotts and Schnetzler, 1970). Both elements will therefore be taken up by the K-feldspar found within the abundant granophyric intergrowth in the granophyres. Taylor (1965) states that Rb is very similar in size and chemical character to K and can therefore be expected to take up K sites readily.

Table 5.2 Regression Data

X	Y	X coeff.	intercept	correlation coeff.
log Ni	log Zr	-0.485	2.841	0.904
log MgO	log Zr	-0.902	2.654	0.898
Zr	TiO_2	0.0013	0	0.771
Zr	K_2O	0.008	0	0.984
Zr	P_2O_5	0.002	0	0.921
Zr	Rb	0.201	0	0.984
Zr	Y	0.294	0	0.974
Zr	Nb	0.098	0	0.971
Zr	Th	0.023	0	0.971
Zr	Pb	0.036	0	0.923
Zr	Ce	0.271	0	0.981
Zr	Nd	0.147	0	0.983
Zr	La	0.119	0	0.982
Zr	Ba	2.249	0	0.979
log Zr	log SiO_2	0.056	1.611	0.230
Zr	Al_2O_3	-0.058	19.560	0.703
log Zr	log Fe_2O_3	0.494	0.120	0.824
log Zr	log MnO	0.626	-1.939	0.787
log Zr	log CaO	-0.270	1.524	0.534

Taylor (1965) states that the bulk of the rare earth elements found in granites are found in monazite. It is possible that this mineral was mistaken for zircon, which is optically very similar to monazite, during the petrological examination of the granophyres. This would explain the depletion of the rare earth elements Ce, La and Nd within the granophyres. It is not clear into which phase Nb has partitioned within the granophyres, as this element would normally be expected to show incompatible behaviour throughout the differentiation of tholeiitic melts, as seen in the case of the Birds River Complex (Eales, 1990). Possibly the abundant stilpnomelane found within the drusy

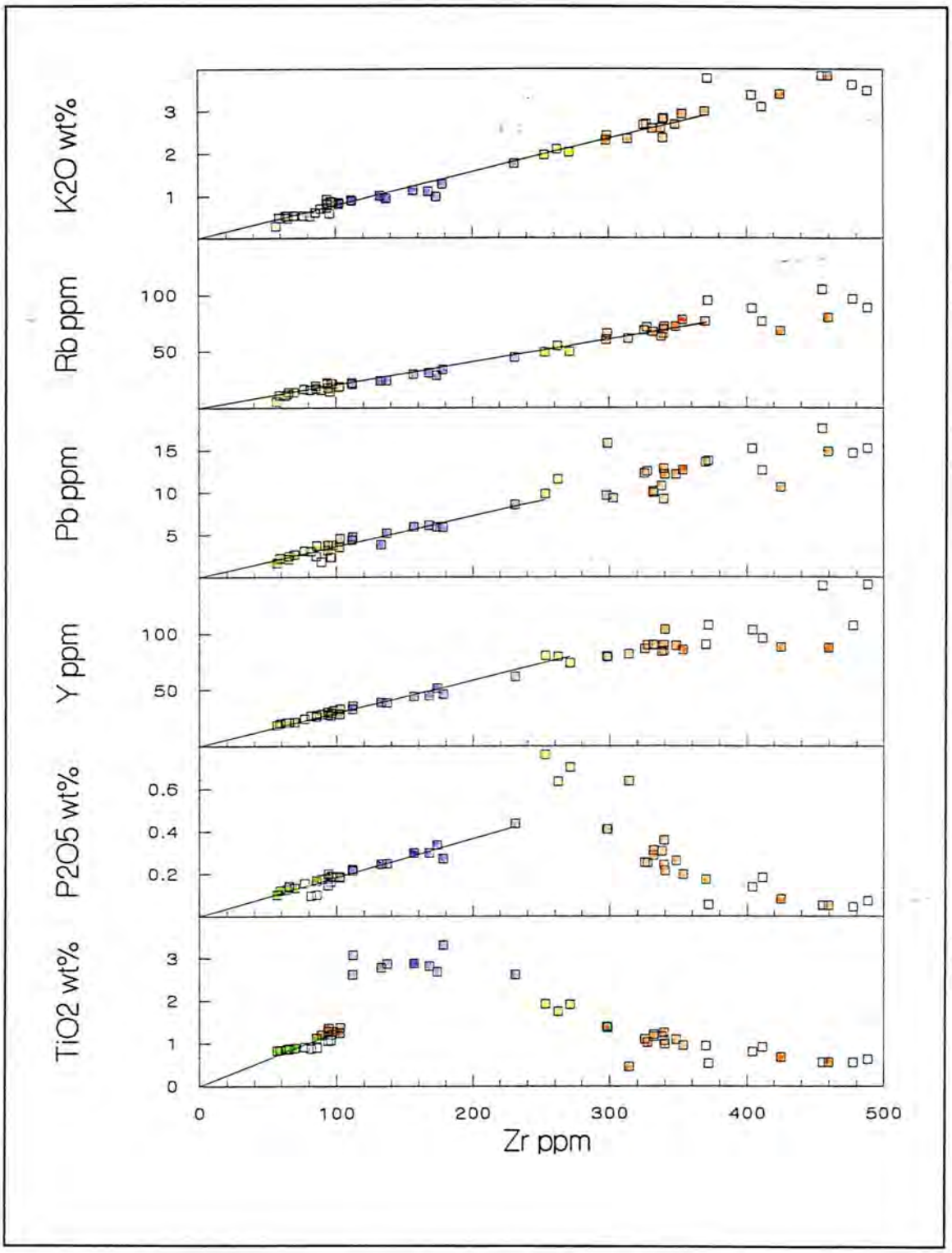

Figure 5.8 New Amalfi Sheet trace elements plotted against Zr. ■ = olivine dolerites; □ = pigeonite dolerites; ■ = quartz gabbros; ■ = quartz monzodiorites; ■ = granodiorites; ■ = fayalite-hedenbergite granophyres; □ = granophyres.

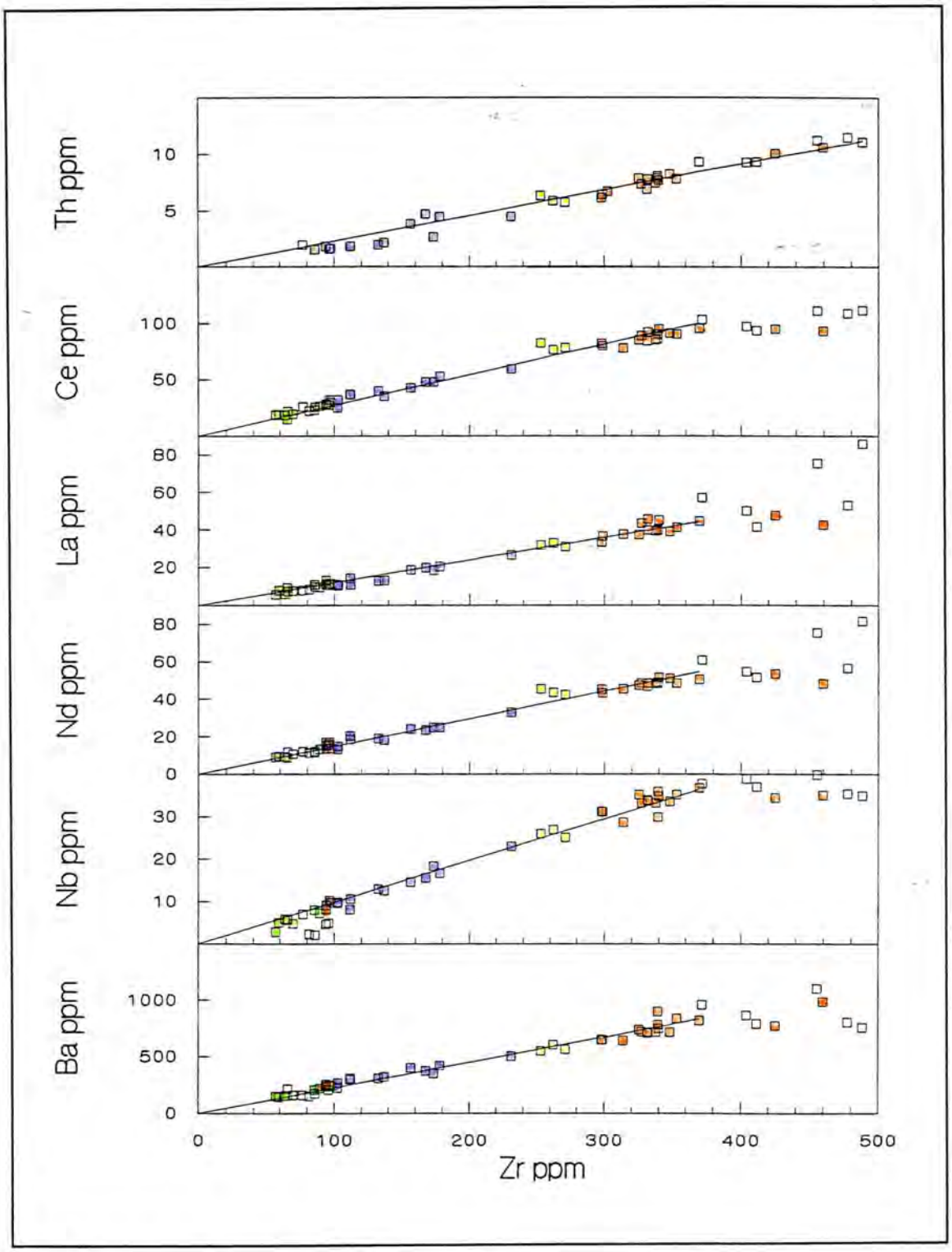

Figure 5.8 (cont.)

cavities in the granophyres has taken up much of the Nb, as it forms part of the mica group of minerals; Pearce and Norry (1979) state that the presence of, amongst other minerals, biotite, in rock suites from Andean-type margins may explain the deviation from linearity of Nb-Zr plots for these rocks.

Lastly, the Th-Zr plot shows no deviation from linearity throughout the sequence from dolerites to granophyres, and this indicates, firstly, that both these elements have behaved incompatibly throughout the fractional crystallization process. Secondly, the fact that the granophyres plot along a straight line trend which passes through undoubtedly igneous rocks as well, indicates that they must be related to the dolerites by fractional crystallization. If monazite and not zircon is present in the granophyres, it may seem strange that Th was not taken up by this mineral, but Deer et al. (1966) state that Th-free monazite is known.

5.2.2 Estimation of the composition of the New Amalfi Sheet initial liquid.

The method used to estimate the New Amalfi Sheet initial liquid composition is similar to that used by Eales (1990) to estimate the trace element composition of the Birds River initial liquid. This method is used since chilled-margin analyses may not be truly representative of the initial liquid composition, because of the possible effects of flow differentiation, interaction with country rock, and alteration. Samples that are the most primitive in terms of having the lowest concentrations of incompatible elements, may also not be representative of the initial liquid, since they may have undergone dilution arising out of cumulus enrichment in early-formed phases.

The method used here makes use of the linear relationship that exists between Zr on the abscissa and other incompatible elements, in the initial stages of fractionation. If an independent estimate of the Zr content of the initial liquid can be obtained, then the corresponding initial values of the other incompatible elements can also be derived by solving the straight

line equation. Allegre et al. (1977) showed that fractional crystallization may be modelled in terms of the Rayleigh equation, which takes the form:

$$C_l^i = C_0^i F^{(D-1)}$$

where C_l^i = the concentration of any trace element i in the residual liquid.

C_0^i = the concentration of any trace element i in the initial liquid.

F = the fraction of residual liquid remaining.

D = the bulk distribution coefficient,

then, in the case of a highly incompatible element (the concentration of which will be denoted as C^*) D is very small and the Rayleigh equation can be written as $F = C_0^*/C_l^*$. This can be substituted into the Rayleigh equation for a compatible element (for which D is large), the concentration of which will be denoted by C^c, which yields the following relationship:

$$C_l^c = C_0^c (C_0^*/C_l^*)^{(D-1)}$$

Taking logs of both sides of the equation yields:

$$\log C_l^c = \log C_0^c + (D-1)\log C_0^* - (D-1)\log C_l^*$$

Therefore if D is constant, a plot of $\log C_l^c$ against $\log C_l^*$ should produce a straight line. Allegre et al. (op cit.) state that fairly large errors in the estimation of C^c can be tolerated and yet still produce a more accurate estimation of the corresponding C^*, from the solution of the straight line equation, since large changes in C^c occur during the initial stages of fractionation while the corresponding change in C^* is small.

A plot of this form is shown in Figure 5.9 (a), where log Zr has been plotted against log Ni for the New Amalfi Sheet. This yields a straight-line relationship with a correlation coefficient of -0.904. Three independent estimates of the Ni content of the initial liquid were drawn from three discrete data sets which are the same as those used by Eales (1990), namely:

a) The average of whole-rock analyses of 22 Eastern Cape Province chilled margin dolerites (from Marsh and Eales, 1984, p37).

b) The average of whole-rock analyses of 59 dolerites from the Central area of the Karoo Igneous Province.

c) The average of whole-rock analyses of 27 of the more primitive Lesotho Group basalts (i.e. those basalts with between 6-8% MgO) from Marsh and Eales (1984).

Substitution into the straight-line equation of the three estimates of initial Ni obtained from the above sources, gives three estimates of the New Amalfi Sheet initial Zr concentration. In Figure 5.9 (b) an inverse linear relationship with a correlation coefficient of -0.898 has been obtained by plotting log Zr against log MgO for the New Amalfi Sheet. Although MgO is a major element and therefore does not behave according to the Rayleigh equation, it shows an exponential depletion in the residual liquid when plotted against Zr, and therefore a log-log plot of these two elements produces a straight line. Three further estimates of the Zr concentration of the New Amalfi Sheet initial liquid were thus obtained by substituting estimates of the initial MgO concentration from the three data sets, given above, into the straight-line equation for Figure 5.9 (b). Lastly, another three estimates of the New Amalfi Sheet initial Zr concentration were obtained by substituting estimates for the initial incompatible element concentrations, from each of the three data sets, into the straight-line equations for the incompatible elements versus Zr, shown in Table 5.2, and taking the averages of the initial Zr estimates obtained for each of the three data sets. The three independent estimates of the initial levels of Ni, MgO and the incompatible elements are shown in Table 5.3, together with the nine estimates of the New Amalfi Sheet initial Zr concentration obtained from them.

The average of the nine estimates gives an initial Zr concentration for the New Amalfi Sheet of 78 ± 2.8ppm. This is similar to the Zr concentration of the most primitive Lesotho basalts (75ppm; Marsh and Eales, 1984) and similar to that of chilled dolerite sample NA79 from the New Amalfi Sheet, Table

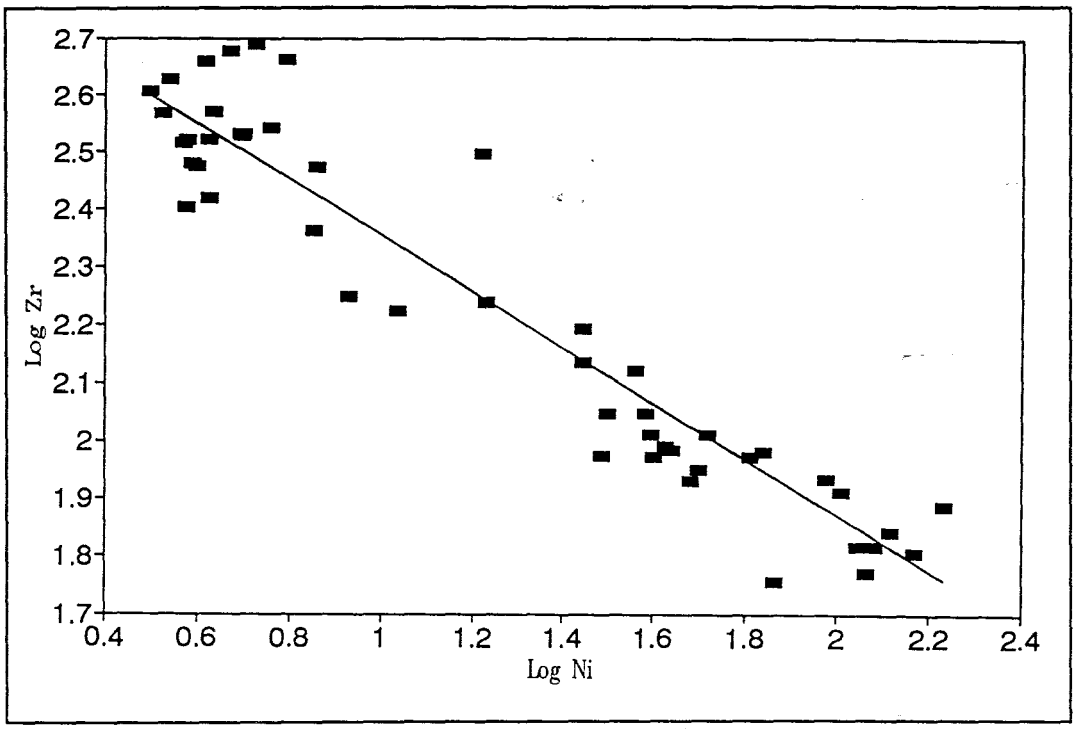

Figure 5.9 (a) Log Zr versus Log Ni for the New Amalfi Sheet.

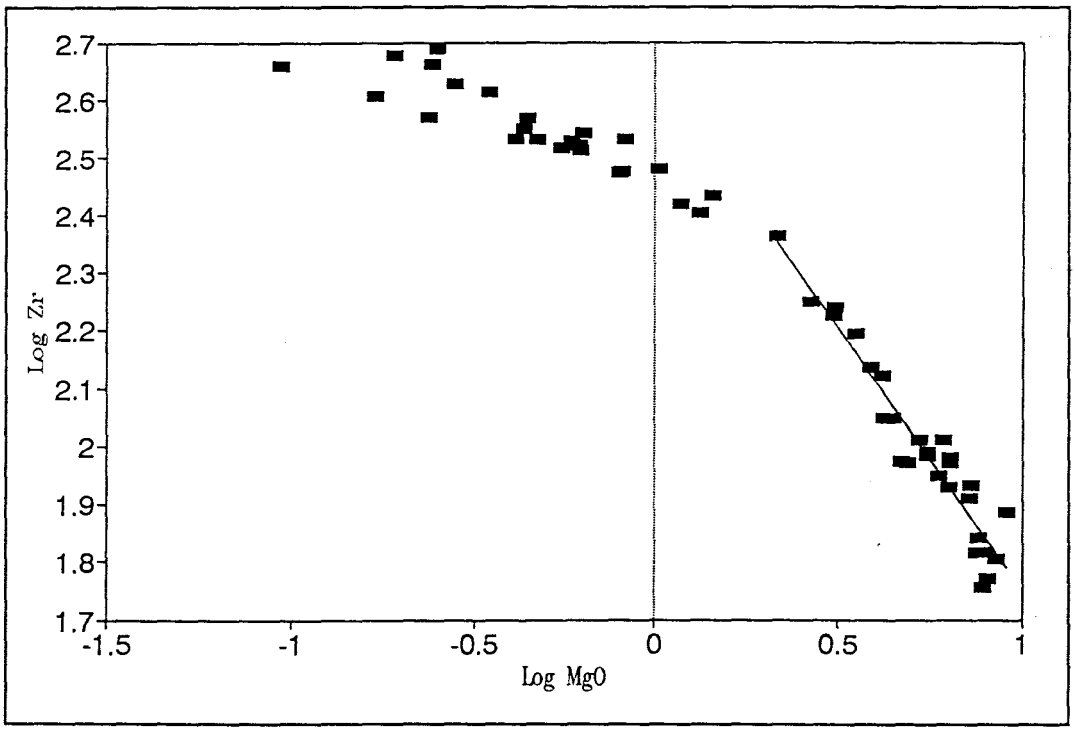

Figure 5.9 (b) Log Zr versus Log MgO for the New Amalfi Sheet.

Table 5.3 Three independent data sets for estimating the New Amalfi Sheet initial liquid Zr concentration and 9 estimates (a-i) of initial Zr.

	Eastern Cape Dolerites	Zr	Central Province Dolerite	Zr	Lesotho Basalts	Zr
TiO_2	1	79.0	0.98	77.4	0.93	73.4
K_2O	0.56	71.5	0.58	74.1	0.73	93.2
P_2O_5	0.17	93.0	0.16	87.5	0.16	87.5
Rb	12.5	62.0	12.1	60.1	10.2	50.6
Y	26	88.6	14.2	82.5	23.3	79.4
Nb	6.3	64.0				
Ce	25	92.3				
Nd	14	95.1				
Ba	213	94.7	193	86.2	164	72.9
Avg.		82.2_a		78.0_b		76.2_c
MgO	6.86	79.3_d	6.92	78.7_e	7.38	74.3_f
Ni	87	79.4_g	84.7	80.5_h	101	73.9_i

5.4. It is however lower than the estimate obtained by Eales (1990) for the Birds River Complex (84.2 ± 3 ppm).

The concentrations of the incompatible elements, Ni and MgO in the New Amalfi Sheet initial liquid were then obtained by substituting the initial Zr concentration for the New Amalfi Sheet, of 78ppm, into the relevant straight-line equations given in Table 5.2. Log-log plots have been used to derive straight-line relationships between SiO_2, Fe_2O_3, MnO and CaO and Zr. Al_2O_3 vs. Zr yields a suitably straight line for the earliest stages of fractionation without the use of a log-log plot. The regression data for these plots is also given in Table 5.2. Substitution of the initial Zr concentration into these straight line equations yields the concentrations of these major elements in the initial liquid. The initial concentration of the remaining major element, Na_2O was obtained by subtracting the total of the other major elements from 100.

Table 5.4 New Amalfi Sheet initial liquid compared to the average Lesotho basalt from Marsh and Eales (1984) and three New Amalfi Sheet chilled dolerites.

	NAS initial liquid	Av. Lesotho Basalt	NA79	NA80	NA136
SiO_2	51.99	51.50	51.85	51.85	51.34
TiO_2	0.99	0.95	0.88	0.90	1.07
Al_2O_3	15.06	15.69	15.60	15.11	14.81
Fe_2O_3	11.35	10.96	11.18	1.21	12.51
MnO	0.18	0.16	0.18	0.16	0.19
MgO	6.99	7.01	7.24	7.29	6.39
CaO	10.30	10.69	10.60	10.41	10.73
Na_2O	2.39	2.17	1.86	2.35	2.20
K_2O	0.61	0.70	0.52	0.61	0.58
P_2O_5	0.14	0.16	0.10	0.10	0.16
Rb	15.72	12	15.62	17.14	14.43
Y	22.89	24	27.04	26.00	26.89
Zr	78.00	94	81.34	85.86	95.72
Nb	7.67	4.9	2.24	2.02	4.93
Ni	90.32	94	102.12	95.23	69.25
Th	1.78		0.00	1.55	0.00
Pb	2.81		3.02	3.69	2.31
Ce	21.13		21.89	25.30	27.39
Nd	11.48		11.30	11.98	15.54
La	9.32		8.32	9.70	11.38
Ba	175.46	177	151.41	174.49	206.66

A complete estimate of the major element, incompatible element and Ni content of the New Amalfi Sheet initial liquid is shown in Table 5.4. It compares favourably with the whole-rock analyses of three New Amalfi Sheet chilled dolerites, and to the average whole rock-analysis of 49 Lesotho basalts obtained from Table II of Marsh and Eales (1984). This is considered to provide strong proof that the New Amalfi Sheet initial liquid

falls within the Lesotho magma type as defined by Marsh and Eales (1984).

5.2.3 Estimation of F for each whole-rock sample.

The Rayleigh equation has been used to model the fractional crystallization process. As shown above, the Rayleigh equation can be approximated by $F = C_0^*/C_l^*$ when one is dealing with incompatible elements for which D is small. C_0^* can be obtained from the initial liquid calculated above and C_l^* from the whole-rock analysis for each sample. In Table 5.5, F has been calculated for each incompatible element in each sample and then averaged for each sample. F values were not calculated in cases where a particular incompatible element no longer behaves incompatibly or where concentrations of C_l^* were considered to be so low as to give rise to possible analytical error. The average of the coefficients of variation of the averaged F values calculated for each sample is 7.4, which indicates that the results are remarkably consistent despite the many potential sources of error.

The low average coefficient of variation indicates that the variation of the incompatible element concentrations in sequence from the dolerites to the granophyres is consistent with a process of fractional crystallization, modelled by the Rayleigh equation. This provides further support for the view that the granophyres are differentiates of the New Amalfi Sheet initial liquid. The most evolved granophyre represents 15.8% of the initial liquid (84.1% crystallization) and this is similar to the most evolved rock in the Birds River Complex, which represents 16% of the initial liquid (84% fractional crystallization; Eales, 1990). From Table 5.5 it can be seen that all of the olivine dolerites and two of the pigeonite dolerites have negative F values. This indicates that these rocks represent liquids that have undergone some cumulus enrichment.

5.2.4 Trace element concentrations plotted against percentage crystallization.

The percentage crystallization of the initial liquid that each

Table 5.5

CALCULATION OF AVERAGE F FOR EACH SAMPLE

Sample	NA79	NA80	NA81	NA85	NA86	NA87	NA88
Rb	1.0067	0.9173	0.8481	0.7503			
Y	0.8465	0.8805	0.8022	0.8188			
Zr	0.9589	0.9085	0.7612	0.8329			
Nb			0.8006				
Th					0.1911	0.1919	0.1586
Pb	0.9304	0.7622	0.8033	0.8867			
Ce	0.9653	0.8350	0.8461	0.7842			
Nd	1.0157	0.9579	0.8771	0.6743			
La			0.8721	0.8493			
Ba	1.1588	1.0056	0.7815	0.7401			
TiO2	1.1274	1.0974	0.7909	0.9391			
K2O	1.1639	0.9950	0.7541	0.8377			
P2O5			0.7652	0.9587			
Average F	1.0193	0.9288	0.8085	0.8247	0.1911	0.1919	0.1586
sd	0.1099	0.0994	0.0426	0.0853			
cv	10.78	10.70	5.27	10.34			

Sample	NA160	NA176	NA190	NA191	NA169	NA192	NA161
Rb	0.5296	0.5529	0.5100	0.4672	0.3537	0.3177	0.3221
Y	0.5174	0.4435	0.5073	0.4922	0.3705	0.3092	0.2849
Zr	0.4991	0.4494	0.4648	0.4381	0.3376	0.2875	0.3081
Nb	0.5265	0.4210	0.4928	0.4613	0.3343	0.3065	0.2956
Th			0.3765	0.3960	0.3969	0.3108	0.2816
Pb	0.4739	0.4705	0.4593	0.4774	0.3286		0.2865
Ce	0.4966	0.4418	0.4432	0.3997	0.3559	0.2700	0.2568
Nd	0.4763	0.4598	0.4901	0.4605	0.3481	0.2707	0.2528
La	0.4998	0.5100	0.4767	0.4612	0.3551	0.3042	0.2960
Ba	0.4367	0.4979	0.4684	0.4194	0.3477	0.3100	0.3185
TiO2							
K2O	0.5412	0.6198	0.5514	0.4755	0.3450	0.3020	0.3116
P2O5	0.4697	0.4166	0.4697	0.5186	0.3197		
Average F	0.4970	0.4803	0.4759	0.4556	0.3494	0.2989	0.2922
sd	0.0311	0.0615	0.0424	0.0365	0.0202	0.0169	0.0229
cv	6.25	12.80	8.91	8.02	5.79	5.66	7.84

Sample	NA89	NA90	NA91	NA92	NA93	NA95	NA96
Rb	0.2271	0.7596	0.7092	0.9041	0.8361	0.7127	0.7480
Y		0.6383	0.6972	0.7607	0.6975	0.7603	0.7255
Zr	0.2298	0.6966	0.6978	0.8273	0.7602	0.8308	0.7976
Nb	0.2130	0.7249		0.8422	0.7807	0.9520	0.7878
Th	0.2218						
Pb		0.5885	0.6435	0.7478	0.6156	0.7408	0.7460
Ce	0.2338	0.5761	0.5701	0.7553	0.6664	0.7484	0.7119
Nd	0.2347	0.6180	0.5637	0.8523	0.7793	0.7596	0.8340
La	0.2330		0.6602			0.7161	0.8151
Ba	0.2246	0.5671	0.5844	0.6820	0.6569	0.7144	0.7368
TiO2				0.7326	0.7209	0.7698	0.7720
K2O	0.2171	0.6863	0.6732	0.7595	0.7226	0.6616	0.7075
P2O5		0.6574	0.6277	0.7034	0.7445	0.7954	0.7607
Average F	0.2261	0.6513	0.6427	0.7788	0.7255	0.7635	0.7619
sd	0.0077	0.0653	0.0546	0.0685	0.0639	0.0736	0.0404
cv	3.39	10.03	8.49	8.79	8.81	9.63	5.30

Sample	NA153	NA193	NA179	NA162	NA164	NA159	NA155
Rb	0.2872	0.2583	0.2417	0.2390	0.2605	0.2344	0.2197
Y	0.2883						
Zr	0.2970	0.2578	0.2298	0.2611	0.2616	0.2351	0.2239
Nb	0.2847	0.2680	0.2563	0.2460	0.2452	0.2259	0.2282
Th	0.3027	0.2655	0.2264	0.2766	0.2898	0.2583	0.2164
Pb	0.2428						
Ce	0.2761	0.2712	0.2453	0.2644	0.2578	0.2504	0.2313
Nd	0.2631	0.2527	0.2371	0.2657	0.2545	0.2458	0.2251
La	0.2850	0.2494	0.2369	0.2576	0.2804	0.2344	0.2405
Ba	0.2897	0.2720	0.1956	0.2690	0.2709	0.2468	0.2438
TiO2							
K2O	0.2914	0.2602	0.2573	0.2521	0.2645	0.2353	0.2263
P2O5							
Average F	0.2825	0.2617	0.2363	0.2590	0.2650	0.2407	0.2284
sd	0.0167	0.0080	0.0185	0.0117	0.0136	0.0102	0.0090
cv	5.93	3.06	7.84	4.54	5.12	4.22	3.95

Average coefficient of variation (cv) 7.40

Table 5.5 (cont.)

Sample	NA125	NA124	NA97	NA98	NA99	NA72	NA129
Rb	1.1482	1.3395	1.4832	1.4349	1.3092	1.1451	0.9461
Y	1.0649	1.0842	1.0855	1.1403	1.1320	1.0992	0.9379
Zr	1.1221	1.1929	1.2219	1.3231	1.2378	1.1904	1.0128
Nb		1.2886	1.2903	1.5217	1.4275		1.1063
Th							
Pb	1.0677						0.9099
Ce	1.0838	1.4490	1.1435	1.1091	1.3331	0.9837	0.8174
Nd	1.0843	1.3287	1.2372	1.2247	1.3379	0.9846	0.9508
La							
Ba	1.0877	1.1192	1.1128	1.2358	1.1540		1.0760
TiO2	1.1148	1.1238	1.1483	1.1889	1.2533		1.0820
K2O	1.1443	1.1598	1.1400	1.2428	1.1621		1.1255
P2O5	1.0605	1.0449	1.1198	1.1671	1.1025	0.9857	0.9033
Average F	1.0978	1.2131	1.1982	1.2588	1.2449	1.0648	0.9880
sd	0.0324	0.1315	0.1187	0.1316	0.1066	0.0924	0.0991
cv	2.95	10.84	9.91	10.46	8.56	8.68	10.03

Sample	NA158	NA165	NA166	NA167	NA168	NA171	NA172
Rb	0.2198	0.2298	0.2022	0.2211		0.2340	0.2506
Y							
Zr	0.2293	0.2397	0.2208	0.2382		0.2349	0.2309
Nb	0.2198	0.2178	0.2176	0.2308		0.2278	0.2306
Th	0.2323	0.2262	0.2273	0.2426	0.1592	0.2297	0.2392
Pb							
Ce	0.2225	0.2478	0.2335	0.2377		0.2288	0.2485
Nd	0.2227	0.2418	0.2371	0.2372		0.2363	0.2383
La	0.2068	0.2520	0.2267	0.2149		0.2054	0.2388
Ba	0.2340	0.2374	0.2094	0.2428		0.2448	0.2446
TiO2							
K2O	0.2147	0.2275	0.2074	0.2255		0.2356	0.2343
P2O5							
Average F	0.2224	0.2356	0.2202	0.2323	0.1592	0.2308	0.2395
sd	0.0086	0.0111	0.0121	0.0099		0.0108	0.0072
cv	3.88	4.70	5.48	4.25		4.68	3.00

Sample	NA136	NA184	NA185	NA186	NA187	NA188	NA189
Rb		0.8171		1.0085	0.7360	0.6576	0.6594
Y	0.8513	0.8368	1.2195	0.8085	0.7753	0.5886	0.5937
Zr	0.8149	0.9159	1.3708	0.8762	0.8083	0.5877	0.5708
Nb		0.9593		1.0597	0.7530	0.5932	0.6120
Th							
Pb		1.1246				0.7288	0.5393
Ce	0.7714	0.9168	1.1656	0.8031	0.6694	0.5324	0.6067
Nd	0.7389	1.0023	1.2743	0.8834	0.6734	0.6062	0.6373
La	0.8225	0.8639			0.8918	0.7348	0.7188
Ba	0.8490	0.8404	1.1484	0.7905	0.7085	0.5661	0.5416
TiO2	0.9237	0.8800	1.1956	0.8284	0.8203		
K2O		0.9887		0.8777	0.6964	0.6051	0.6462
P2O5	0.8643	0.8333		0.8000	0.7408	0.5668	0.5623
Average F	0.8295	0.9149	1.2290	0.8736	0.7521	0.6152	0.6080
sd	0.0571	0.0908	0.0823	0.0922	0.0680	0.0654	0.0548
cv	6.88	9.93	6.70	10.55	9.05	10.63	9.02

Sample	NA170	NA83	NA121	NA134	NA181	NA182	NA140
Rb	0.2058					0.3109	
Y						0.2972	0.7666
Zr	0.2107					0.2863	0.8133
Nb	0.2083					0.2796	1.0066
Th	0.1912	0.1611	0.1773	0.1552	0.1678	0.2871	
Pb							0.9757
Ce	0.2214					0.2699	0.7440
Nd	0.2272					0.2632	0.8107
La	0.2096					0.2900	0.9659
Ba	0.2139					0.2776	0.7167
TiO2							
K2O	0.2033						
P2O5							
Average F	0.2102	0.1611	0.1773	0.1552	0.1678	0.2847	0.8500
sd	0.0104					0.0143	0.1150
cv	4.93					5.02	13.53

sample represents has been calculated from the average F values for each sample. In Figure 5.10, various trace elements have been plotted against percent crystallization for each sample. It can be seen that Ni and Cr have their highest concentrations in samples that have been enriched in cumulus phases, and that they are both depleted in residual liquids. Ni is depleted until it is essentially below detection limit at 54% crystallization, and Cr reaches this point at 22% crystallization. The rapid depletion in Cr occurs probably because it is taken up by early-forming chromite and pyroxene. It has been shown in the previous chapter that olivine readily depletes the melt in Ni because of the high D^{Ol}_{Ni}. Beyond the dolerite range, Ni depletion flattens out and this is probably due to the cessation of olivine crystallization, with the Ni now probably largely being taken up by clinopyroxene which has a lower distribution coefficient.

At the beginning of the quartz monzodiorite range (35% crystallization) the elements Ti, Cu, Co, V and Sc, which were earlier enriched in the residual melts, begin to be depleted in the residual melt. This coincides with the appearance of cumulus magnetite and ilmenite as well as chalcopyrite globules. Ti, Co, V and Sc all have high coefficients for partitioning between magnetite and ilmenite, and melt (Irving, 1978) and this explains why these elements begin to be depleted at this stage. Taylor (1965) states that Cu will increase in concentration in residual melts until Cu-rich sulphide phases appear. This appears to the case for the New Amalfi Sheet where the start of Cu depletion coincides with a sudden increase in the proportion of chalcopyrite in the rocks. A similar feature is seen in the case of the Skaergaard Intrusion, and Wager and Brown (1968) state that "(sulphide) immiscibility relationships played a dominant part in controlling the amount of copper in the rocks".

P_2O_5 increases rapidly in the melt until the beginning of the granodiorite range (70% crystallization) at which point abundant apatite enters the assemblage and P_2O_5 is rapidly depleted. Zn also begins to be depleted at this stage but it is not known whether this indicates that Zn is also being taken up by apatite, as this has not been reported in the literature. Taylor (1965)

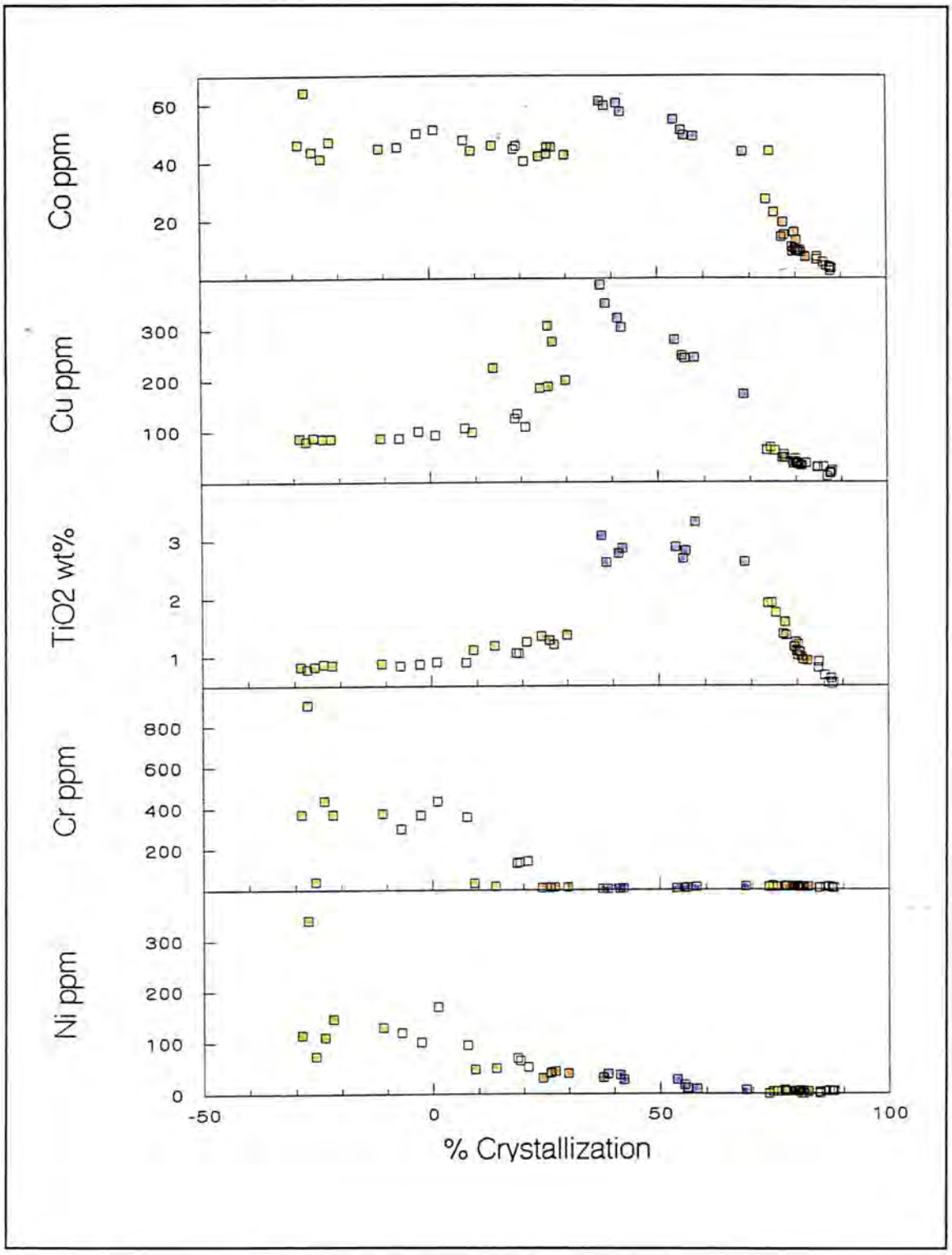

Figure 5.10 Selected trace elements plotted against percent crystallization. ■ = olivine dolerites; □ = pigeonite dolerites; ■ = quartz gabbros; ■ = quartz monzodiorites; ■ = granodiorites; ■ = fayalite-hedenbergite granophyres; □ = granophyres.

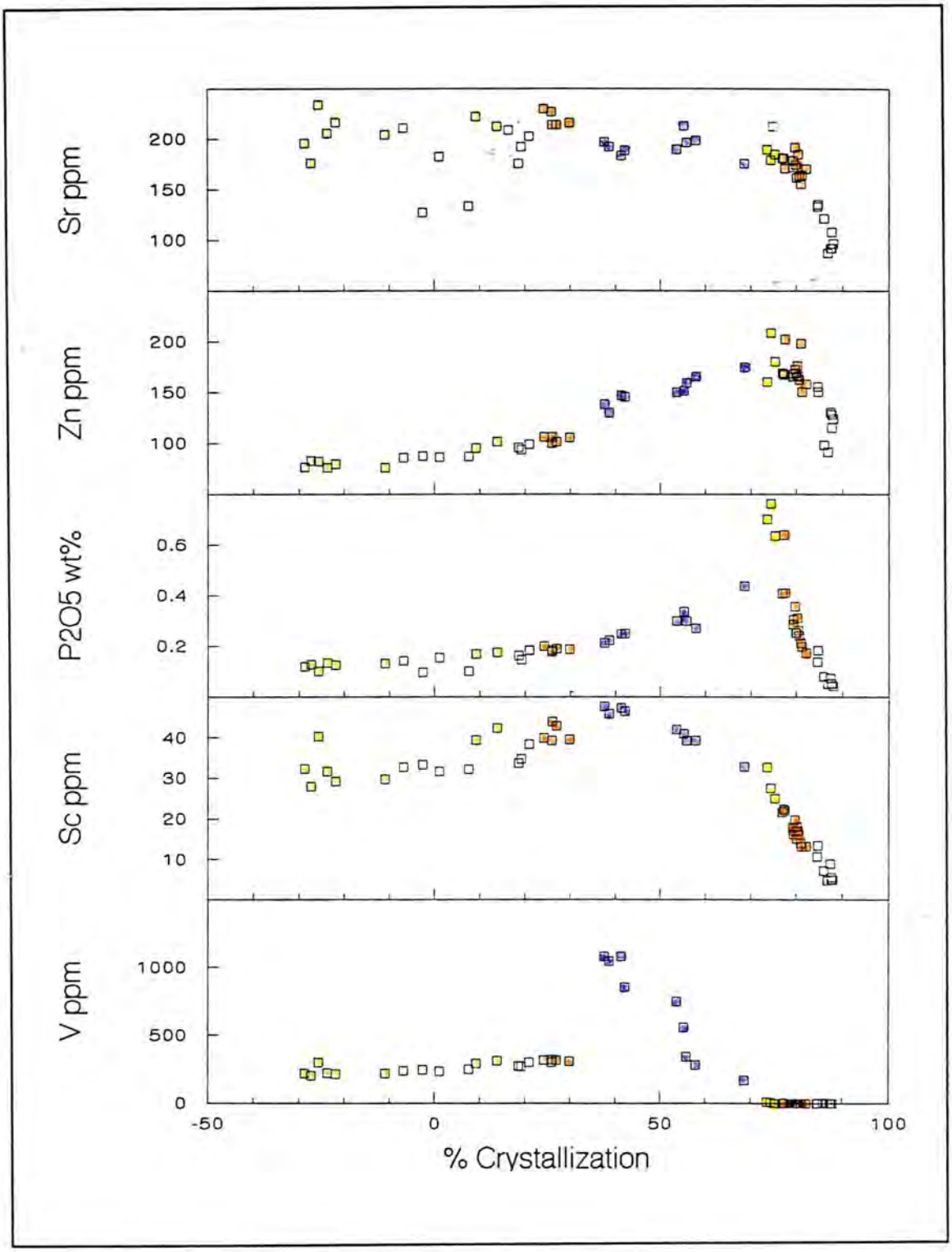

Figure 5.10 (cont.)

states that Zn should take up the same positions as Fe^{2+}, which has very nearly the same ion size. However the Zn-O bond is more covalent than the Fe-O bond and thus Zn will enter Fe^{2+} sites at a later stage. Therefore, the entry of Zn into magnetite may have been delayed and the depletion of Zn at the same time as the entry of apatite is merely a coincidence.

It can be seen from Figure 5.10 that Sr concentration is highly variable, probably because of alteration effects, and that Sr concentration decreases marginally in the residual liquid until evolution of the fayalite-hedenbergite granophyres (73% crystallization) at which point there is a sudden rapid decrease in the Sr concentration of the magma. Taylor (1965) states that Sr^{2+} is intermediate in size between Ca^{2+} and K^{+} and that Sr therefore enters Ca positions in plagioclase and K positions in K-feldspar, although D_{Sr}^{Kspar} ($\pm$ 10, Irving, 1978) is much larger than D_{Sr}^{Plag} (1-3, Irving, 1978). Sr is probably largely taken up by plagioclase prior to 73% crystallization and the low rate of Sr depletion during this period indicates that the proportion of plagioclase crystallizing was slightly above 50%, using an average distribution coefficient of 2, thereby giving a bulk distribution coefficient slightly above 1.

The sudden and rapid depletion of Sr after 73% crystallization indicates a sudden increase in the bulk distribution coefficient, and this must be due to the crystallization of significant amounts of K-feldspar at this stage. This may be correlated with the appearance of much coarser grained perthitic K-feldspar in the granophyric intergrowth of the fayalite-hedenbergite granophyres.

5.3 MODELLING THE DIFFERENTIATION OF THE NEW AMALFI SHEET BY MEANS OF LEAST SQUARES MIXING.

A computer program, similar to that used by Eales (1990) has been used to model the various stages of the differentiation of the New Amalfi Sheet. A particular differentiation step is modelled by entering the compositions of the parent liquid and the residual liquid as well as the composition of the mineral phases

that are suspected to have fractionated to produce the residual liquid. The computer program combines (mixes) the compositions of the residual liquid and the extracted phases in various proportions in order to obtain a calculated parent liquid composition which most closely resembles that of the actual input parent liquid composition. The mix with the lowest sum of the squares of the residuals, is arithmetically, the best solution. The degree to which this approaches reality is dependent on how closely the input data conform to reality. The progressive differentiation of the New Amalfi Sheet has been modelled using the calculated New Amalfi Sheet initial liquid composition as the parent liquid, and a representative whole-rock sample from each rock unit, from the quartz gabbros to the granophyres, as the residual liquid in each differentiation step. In addition to this, averaged microprobe data on the mineral phases was used for each sample. These whole-rock and mineral data are shown in Appendix III. For the purposes of the modelling, the total iron content of the whole-rock analyses was converted to FeO. The olivine compositions were calculated, for each sample that contains olivine, from the equation given by Roeder and Emslie (1970), instead of using the measured olivine compositions which are suspected to have been modified by the trapped liquid shift effect. The results of the modelling are shown below.

Mix 1.) Differentiation of the parent liquid (NAINI) to quartz gabbro (NA93).

NAINI = NA93(0.6867) + INIOL(0.0511) + 79PL(0.1093) + 93PL(0.0693) + 99CPX(0.0366) + 93CPX(0.0440) + APAT(0.0003)

	NAINI(obs)	NAINI(calc)	Diff.
SiO_2	51.99	51.99	0.00
TiO_2	0.99	0.98	-0.01
Al_2O_3	15.06	15.06	0.00
FeO	10.21	10.21	0.00
MgO	6.99	6.99	0.00
CaO	10.30	10.30	0.00
Na_2O	2.39	2.38	-0.01
K_2O	0.61	0.61	0.00
P_2O_5	0.14	0.14	0.00

$\sum$ (residuals)^2 = 0.0002
F = 0.6867 (trace elements : 0.7255)
Total crystal extract for
differentiation step (%) = 31.33 (trace elements : 27.45)
Total plagioclase (%) = 18.02
Total CPX (%) = 8.13
Total olivine (%) = 5.15
Total apatite (%) = 0.03

The first differentiation step from the initial liquid to the quartz gabbros involves 31.33% crystallization with plagioclase being the dominant separating phase, followed by clinopyroxene and then olivine. This contrasts with the situation at Birds River, where pyroxene was the dominant fractionating phase in the early stages of differentiation (Eales, 1990). The F value calculated from the mix for NA93 (0.6867) is slightly lower than that calculated from trace elements (0.7255) but, the residuals for this mix are arithmetically very good.

Mix 2.) Differentiation of quartz gabbro (NA93) to quartz monzodiorite (NA176).

NA93 = NA176(0.6506) + 93PL(0.0798) + 176PL(0.1587) + 93CPX(0.6451) + 176CPX(-0.5485) + 90MAG(0.0265) + 176ILM(-0.0158)

	NA93(obs)	NA93(calc)	Diff.
SiO_2	53.36	53.36	0.00
TiO_2	1.37	1.37	0.00
Al_2O_3	13.85	13.85	0.00
FeO	11.91	11.91	0.00
MgO	5.26	5.26	0.00
CaO	9.15	9.14	-0.01
Na_2O	2.54	2.53	-0.01
K_2O	0.84	0.72	-0.12
P_2O_5	0.19	0.22	0.03

$\sum$ (residuals)^2 = 0.01
F = 0.4468 (trace elements : 0.4803)
Total crystal extract for

differentiation step (%) = 23.99 (trace elements : 24.52)
Total plagioclase (%) = 16.55
Total CPX (%) = 6.70
Total magnetite (%) = 1.84
Total ilmenite (%) = -1.10

The second differentiation step from quartz gabbro to the quartz monzodiorite shows that plagioclase separation was still dominant. Magnetite began to separate in significant amounts, as well as a small amount of cumulus ilmenite. This conforms with the petrography which revealed the appearance of a significant amount of opaque-oxides in the quartz monzodiorites. Residuals for this mix are again good and the degree of crystal extraction (24%) is similar to that calculated from trace element data (24.5%).

Mix 3.) Differentiation of quartz monzodiorite (NA176) to granodiorite (NA153).

NA176 = NA153(0.5666) + 93PL(0.1898) + 176CPX(0.1421) + 153OL(0.0928) + 90MAG(-0.0249) + 176ILM(0.0380) + 86KF(-0.0081)

	NA176(obs)	NA176(calc)	Diff.
SiO_2	52.90	52.88	-0.02
TiO_2	2.69	2.69	0.00
Al_2O_3	11.87	11.80	-0.07
FeO	16.38	16.38	0.00
MgO	3.09	3.13	0.04
CaO	7.61	7.63	0.02
Na_2O	2.09	2.61	0.52
K_2O	0.98	1.12	0.14

$\sum$ (residuals)^2 = 0.30
F = 0.2558 (trace elements : 0.2825)
Total crystal extract for
differentiation step (%) = 19.36 (trace elements : 19.77)
Total plagioclase (%) = 8.55
Total CPX (%) = 6.40
Total olivine (%) = 4.18

Total ilmenite (%) = 1.71
Total magnetite (%) = -1.12
Total K-feldspar (%) = -0.36
+ apatite

For the differentiation step from the quartz monzodiorites to the granodiorites the residuals are statistically poor and this may be because of the effect of cumulus magnetite in the quartz monzodiorites, as well as because a large number of phases were separating at this stage (the computer program allows for only 6 phases to be modelled). For this reason, P was left out of the mix and one can assume that a certain amount of apatite also separated. Plagioclase separation is still dominant and olivine shows a reappearance which also conforms with what is seen in the rocks. It can also be seen that cumulus K-feldspar appears, and this probably correlates with that seen in the granophyric intergrowth.

Mix 4.) Differentiation of granodiorite (NA153) to fayalite-hedenbergite granophyre (NA89).

NA153 = NA89(0.8847) + 153PL(0.6504) + 89PL(-0.6264) + 176CPX(0.0648) + 176OL(0.0094) + 90MAG(0.0533) + 89KF(-0.0448)

	NA153(obs)	NA153(calc)	Diff.
SiO_2	57.94	57.94	0.00
TiO_2	1.75	1.76	0.01
Al_2O_3	11.22	11.22	0.00
FeO	15.22	15.22	0.00
MgO	1.18	1.18	0.00
CaO	5.34	5.34	0.00
Na_2O	2.69	2.69	0.00
K_2O	2.09	2.09	0.00

$\sum$ (residuals)^2 = 0.0001
F = 0.2240 (trace elements : 0.2261)
Total crystal extract for
differentiation step (%) = 2.92 (trace elements : 5.64)
Total plagioclase (%) = 0.65

Total CPX (%) = 1.77
Total olivine (%) = 0.26
Total magnetite (%) = 1.46
Total K-feldspar (%) = -1.22
+ apatite

In the differentiation step from the granodiorites to the fayalite-hedenbergite granophyres, clinopyroxene is now the dominant separating phase, with magnetite second, and plagioclase and olivine subordinate. Residuals are again good and the F value is similar to that calculated from trace element data although the crystal extracts for this step are slightly different.

Mix 5.) Differentiation of fayalite-hedenbergite granophyre (NA89) to granophyre (NA88).

NA89 = NA88(0.7974) + 89PL(0.1948) + 86PL(-0.0830) + 89KF(-0.0430) + 153CPX(0.0828) + 153OL(-0.0008) + 90MAG(0.0472)

	NA89(obs.)	NA89(calc.)	Diff.
SiO_2	64.62	64.62	0.00
TiO_2	1.07	1.19	0.12
Al_2O_3	11.91	11.91	0.00
FeO	10.50	10.48	-0.02
MgO	0.41	0.49	0.08
CaO	3.76	3.76	0.00
Na_2O	3.35	3.34	-0.01
K_2O	2.81	2.80	-0.01

$\sum$ (residuals)^2 = 0.02
F = 0.1786 (trace elements : 0.1586)
Total crystal extract for
differentiation step (%) = 4.54 (trace elements : 6.75)
Total plagioclase (%) = 2.56
Total CPX (%) = 1.90
Total olivine (%) = 0.02
Total magnetite (%) = 1.08
Total K-feldspar (%) = -0.98
+ apatite

Overall Results:

Total crystal extract for all differentiation steps:	82.14%
Value determined from trace element data:	84.14%
Total plagioclase extracted:	46.33%
Total clinopyroxene " :	24.9%
Total olivine " :	9.57%
Total magnetite " :	3.26%
Total ilmenite " :	0.61%
Total K-feldspar " :	-2.56%
Total apatite " :	0.03%

For the last step, from the fayalite-hedenbergite granophyres to the granophyres, plagioclase is again the dominant phase removed and clinopyroxene and magnetite subordinate. Residuals for this mix are good. The final F value of 0.1786 indicates a total of 82.14% crystallization, which compares well to that obtained from the trace element data (0.1586). The latter indicates a total of 84.14% crystallization. This represents good agreement between major and trace element modelling and strongly supports the contention that the granophyres are differentiates of the New Amalfi Sheet initial liquid.

From the final compilation it can be seen that plagioclase is, overall, the dominant fractionating phase, with clinopyroxene second. This is in agreement with the Birds River data where the overall proportion of the separated phases plagioclase : augite : pigeonite : olivine : magnetite after 70% crystallization was 50 : 39 : 3 : 7 : 1. It is in poor agreement with the results obtained from the Pearce element ratios, which indicated that clinopyroxene should be the dominant phase.

5.4 SUMMARY.

a) Continuous trends in major and trace element variation diagrams and successful modelling of the differentiation from the dolerites to the granophyres using major and trace elements indicate that the granophyres are differentiates of the New Amalfi Sheet initial liquid.

b) The iron-enrichment trend exhibited by the New Amalfi Sheet is slightly more pronounced than that at the Birds River Complex but not as extreme as in the case of the Skaergaard intrusion. The transition from iron-enrichment to decreasing iron and sharply increasing silica and alkali enrichment at New Amalfi is marked by the entry of cumulus opaque-oxides in the paragenesis.

c) The incompatible behaviour of Ti breaks down with the appearance of cumulus magnetite and ilmenite at the beginning of the quartz monzodiorite range. That of P, Y and Pb breaks down with the appearance of cumulus apatite in the granodiorites, and that of K, Ba, Rb, Ce, La, Nd and Nb with the separation of K-feldspar, monazite and stilpnomelane in the granophyres. Th and Zr remain incompatible throughout.

d) The Zr concentration of the New Amalfi Sheet initial liquid is estimated to be 78 ± 2.8ppm, and this is similar to that of the most primitive Lesotho basalts.

e) The calculated New Amalfi Sheet initial liquid is very similar to the average Lesotho basalt of Marsh and Eales (1984) and this indicates that the initial liquid belongs to the Lesotho magma type.

f) Cr is rapidly depleted in residual liquids by chromite and pyroxene separation and Ni is initially rapidly depleted by olivine in the dolerites, followed by less rapid depletion by pyroxene in the gabbros. Co, V and Sc are depleted by magnetite and ilmenite, and Cu is scavenged at the same time by immiscible sulphide globules in the quartz monzodiorites. Zn is depleted (probably by magnetite) in the granodiorites and Sr, which decreases gradually until the evolution of the fayalite-hedenbergite granophyres, is rapidly depleted after this by the separation of K-feldspar.

g) Modelling of differentiation by least squares mixing

indicates that the differentiation up to granophyre NA88 involved 82.14% crystallization. This estimate compares favourably with that calculated for this sample from trace element data (84.14%). Plagioclase was, overall, the most abundant phase to separate at 46.33%, followed by clinopyroxene (24.9%), olivine (9.57%), magnetite (3.26%) cumulus K-feldspar (2.56%) and minor ilmenite and apatite.

6 Rb-Sr ISOTOPE STUDY OF THE NEW AMALFI SHEET.

6.1 INTRODUCTION.

The Rb-Sr isotope system has been shown to be a useful petrogenetic tool when one is faced with the problem of distinguishing between rocks of crustal or mantle origin. Faure and Powell (1972) stated that " because the Rb/Sr ratio of the continental crust is about 10 times greater than that of the upper mantle, strontium in the continental crust has become enriched in ^{87}Sr. Therefore, rocks formed by melting, metasomatism, or assimilation of typical crustal materials will be labelled by having higher initial $^{87}Sr/^{86}Sr$ ratios than the ratios of uncontaminated rocks derived from the mantle". A Rb-Sr isotope study would clearly be useful in providing further evidence as to the possible metasomatic or magmatic origin of the New Amalfi granophyres.

It is hoped that this study will also provide further insight into the timing of volcanism in the Karoo Central area. Fitch and Miller (1984) gave a best-estimate age for the Central area basalts, from their conventional K-Ar and $^{40}Ar/^{39}Ar$ data, of 193 ± 5 m.y.. However, they stated that many of the Karoo dolerites within the Central area have apparent K-Ar ages that are younger than that of the basalts. This may be because the K-Ar method of dating tends to give young ages because of its susceptibility to the effects of alteration. Fitch and Miller (op. cit.) plotted all available K-Ar and Rb-Sr age data for the Karoo on a histogram which showed that there were a number of statistically valid peaks in Karoo igneous activity at 204 ± 5 m.y, 193 ± 5 m.y, 186 ± 3 m.y., 178 ± 5 m.y., 165 ± 5 m.y and at 150 ± 5 m.y. Thus, later Central area intrusives might conform with one of these later peaks in igneous activity, after 193 m.y..

The Birds River Complex was given an age, using the Rb-Sr method of dating based on ten whole-rock samples, of 196.8 ± 11.2 m.y. and an initial $^{87}Sr/^{86}Sr$ ratio (hereafter referred to as R_0) of .70503 ± 10 (Allsopp et al., 1984). Problems related to local contamination and alteration necessitated the removal of four

data points in order to obtain an isochron. Richardson (1984) obtained an internal isochron age of 182 ± 2 m.y and an R_0 of .70621 ± 2, using the Rb-Sr method on the freshest available samples taken from within the Tandjiesberg dolerite sill, within the Karoo Central area. Other whole-rock samples taken from the sill plotted significantly above the internal isochron and this was attributed to the effects of mild hydrothermal alteration. The internal isochron age is considered to be reliable (Dr J.S Marsh, pers. comm.). Seven samples taken from the top to the bottom of the Lesotho lava pile all have ages which fall within 182 ± 2 m.y., using the Ar^{39}/Ar^{40} method of dating (Hooper et. al., 1993). A Rb-Sr age of 178 ± 3 m.y. given by mica separates from the Insizwa Complex, a Karoo Central area intrusive near to the New Amalfi Sheet, was obtained recently by Dr F.J. Kruger (pers. comm.).

The mafic rocks belonging to the Karoo Central area show a range in R_0 from .7046 to .7094, with the bulk of the them falling between .7046 and .7070 (Bristow et al., 1984). These authors argue against large-scale crustal contamination and prefer source-region heterogeneity as an explanation for the high and variable R_0 values of Karoo mafic rocks in general. Marsh et al., (1992) state that in a few cases there is some isotopic evidence to support crustal contamination in the Karoo suite but the major basalt types, including the Lesotho-type to which most of the Central area intrusives belong (Marsh & Eales, 1984), have isotopic signatures which conform to recognized enriched mantle reservoirs. This is however a contentious issue as some petrologists believe that the high R_0 values exhibited by continental flood basalts (CFB's) are the result of interaction of MORB-type magmas with continental crust, as has been proposed for the Deccan Traps by Mahoney et al. (1982).

It is not the purpose of this chapter to discuss the source of CFB's. The conflicting points of view are only briefly mentioned here so that when the term 'mantle-derived' is used later on to describe rocks belonging to the New Amalfi Sheet, it be seen as only one possible point of view. The term is used here to describe rocks that have suffered no assimilation of crustal

material subsequent to their being emplaced, from whatever source, at present levels within the crust.

The usage of the terms 'metasomatism' and 'hydrothermal alteration' has already been discussed, but is briefly repeated here as it is vital that the difference between them be understood, as both are used extensively in this chapter. The term 'metasomatism' applies specifically to the process by which Poldervaart (1944) postulated that country rock sandstone was transformed into metasomatic granophyre, at New Amalfi, under the action of fluids rich in Fe, Mg and Ca, emanating from the differentiated tholeiites below. The term 'hydrothermal alteration' by contrast refers to a process whereby some of the minerals in a rock have under the action of circulating hydrothermal fluids undergone partial recrystallisation to form an assemblage of minerals that are stable at temperatures below those at which the rock initially crystallised. Slight changes in the bulk chemistry of the rock may occur but this applies mainly to the redistribution of relatively small amounts of elements that are mobile in aqueous fluids, such as potassium. This is the major difference between hydrothermal alteration and metasomatism which results in a significant change to the bulk chemistry of the rock as well as the complete transformation of the rock from a sediment to a rock that is igneous in appearance.

The Rb-Sr isotope system is known to be vulnerable to alteration effects, which can cause a change in either the $^{87}Sr/^{86}Sr$ or $^{87}Rb/^{86}Sr$ ratios of affected samples. This may cause an increase in the calculated R_0 values for these samples. As mentioned above, rocks formed by assimilation of crustal material or by metasomatism of existing crustal material will also have higher R_0 values than pristine mantle-derived rocks. It may therefore be difficult to distinguish between these three processes, on the basis of R_0, in cases where each may have been active.

The effects of hydrothermal alteration of the New Amalfi Sheet rocks have already been described and for this reason it was

decided to analyze both plagioclase separates and whole rock samples. Petrographic examination showed that much of the plagioclase was still fresh. This indicated that initial ratios could be readily obtained from plagioclase analyses without significant error being incurred from back-dating to an incorrect age. This is because plagioclase contains very little Rb and therefore has a very low $^{87}Rb/^{86}Sr$ ratio.

6.2 SAMPLING AND ANALYTICAL TECHNIQUES.

A representative suite of ten samples was chosen for the isotopic study. The main criteria for sample selection were (a) a regular Mg# spacing between samples, and (b) the freshness of the plagioclase in each sample. These ten samples were all used for whole-rock Rb-Sr determination. They included a sample of country-rock sandstone (sample 113wr) and a sample of a small (20cm diam.) country-rock xenolith (sample 181wr) which, as has been previously mentioned, was found within the top-most exposure of granophyre found at the top of a rounded hill on the north-eastern side of the sheet. Granophyre sample 182wr was collected from this same top-most granophyre exposure. Plagioclase separates were extracted from all samples except 181wr and 113wr.

The analytical procedure followed is described in Appendix I. After hand-picking, all plagioclase samples contained some grains that showed slight milky discolouration around the edges. A very small but perfectly fresh plagioclase separate sample was therefore taken from rock 89 [89pl(sp)], in addition to the normal plagioclase separate, to determine what effects the slight alteration of the plagioclase might have on the data. This small sample weighed 0.0006g whereas the other plagioclase separates weighed between 0.01g and 0.02g.

6.3 RESULTS.

All results are shown in Table 6.1. All errors are quoted at the 95% confidence level and a decay constant of 1.42×10^{-11} hr^{-1} has been used in the calculation of R_0. It can be seen from Table 6.1 that plagioclase separate Sample 184pl has an anomalously low Sr

TABLE 6.1 wr = whole rock; pl = plagioclase separate; (sp) = special completely fresh plagioclase separate; decay constant = 1.42000E-11

Sampl No.	Lithology	Rb ppm	Sr ppm	$^{87}Rb/^{86}Sr$	$^{87}Sr/^{86}Sr$	R_0 180 Ma	95% conf.	Part of isochron
113wr	sandstone	86.700	69.750	3.601656	0.722787	0.713569	0.000592	N
181wr	xenolith	80.580	88.650	2.631281	0.713162	0.706428	0.000423	N
182wr	granophyre	51.190	220.20	0.672635	0.708289	0.706568	0.000155	N
89wr	granophyre	68.700	160.60	1.237776	0.708741	0.705573	0.000216	Y
164wr	granophyre	59.890	183.40	0.944830	0.707980	0.705562	0.000181	Y
176wr	quartz monzo-diorite	27.480	208.90	0.380570	0.706988	0.706014	0.000138	Y
90wr	quartz monzo-diorite	20.820	193.30	0.311590	0.706460	0.705663	0.000136	Y
184wr	quartz gabbro	17.150	215.90	0.229793	0.706270	0.705682	0.000136	Y
124wr	olivine dolerite	11.430	206.80	0.159885	0.705926	0.705517	0.000136	Y
99wr	olivine dolerite	11.740	174.90	0.194189	0.706773	0.706276	0.000136	N
182pl	granophyre	18.75	598.10	0.090691	0.706512	0.706280	0.000138	N
89pl	granophyre	2.8670	442.7	0.018733	0.705539	0.705491	0.000140	Y
89pl(sp)	granophyre	0.9478	288.86	0.009491	0.705763	0.705739	0.000141	Y
164pl	granophyre	8.4040	507.60	0.047892	0.705604	0.705481	0.000139	Y
176pl	quartz monzo-diorite	3.8020	414.40	0.026539	0.705627	0.705559	0.000140	Y
90pl	quartz monzo-diorite	13.610	327.20	0.120326	0.705990	0.705682	0.000137	Y
184pl	quartz gabbro	3.7910	14.400	0.761735	0.708312	0.706363	0.000162	N
124pl	olivine dolerite	7.6070	373.20	0.058962	0.705661	0.705510	0.000139	Y
99pl	olivine dolerite	2.9980	354.00	0.024499	0.705985	0.705922	0.000140	N

concentration, which is an order of magnitude less than that of the other plagioclase separates. This result is obviously suspect, and although there is no clear explanation for this the sample was given no further attention.

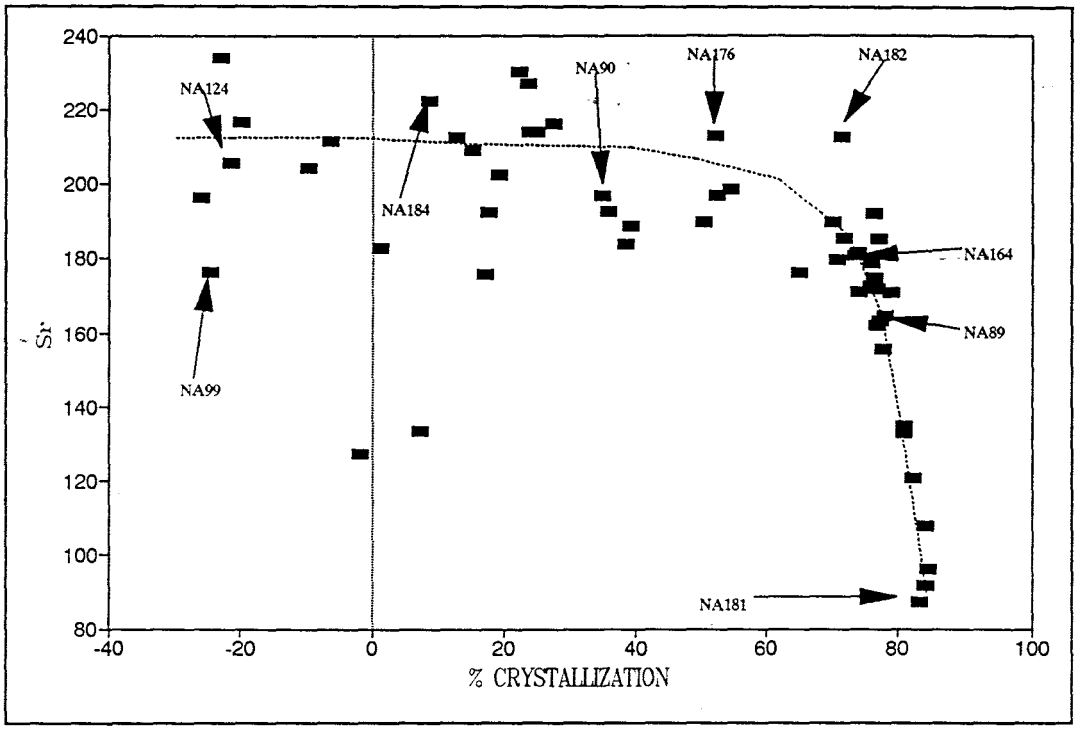

Figure 6.1 (a) Sr versus percent crystallization showing the position of samples used for isotopic analysis. The dashed line shows the general trend of the relatively unaltered samples.

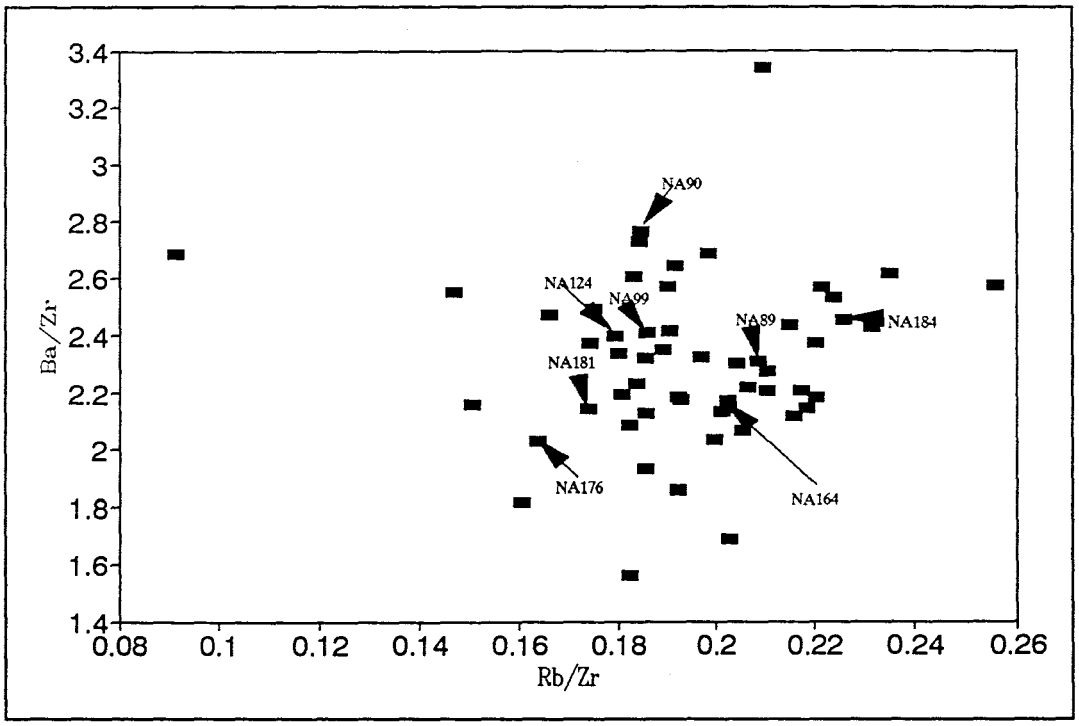

Figure 6.1 (b) A plot of two incompatible Pearce element ratios showing the position of samples used for isotopic analysis.

6.3.1 The effects of hydrothermal alteration on the concentrations and isotopic ratios of Rb and Sr in the whole-rock and plagioclase samples.

The rocks belonging to the New Amalfi Sheet have all suffered some degree of hydrothermal alteration, as indicated by at least some discolouration of the pyroxenes. It is vital to the interpretation of Rb-Sr isotopic data that the effects of this be established.

6.3.1.1 The mobility of Sr and Rb in the whole-rock samples.

Figure 6.1a shows a plot of whole-rock Sr against percent crystallization for the New Amalfi Sheet. Sr concentration stays more or less constant in the whole-rock samples until the end stages of differentiation, at which stage it drops off sharply. Although there is some scatter in the data points showing that Sr has been mobile in some samples, the samples chosen for isotope analysis (except samples 99wr and 182wr) plot fairly close to the dashed line which represents the average trend of the data. This indicates that Sr has not been significantly mobile in all samples selected for isotope analysis, except in samples 99wr and 182wr where the Sr does appear to have been slightly more mobile.

The use of Pearce element ratios has already been discussed in chapter 5. It has been shown that a plot of two incompatible element ratios with a common denominator will produce a cluster of points if the suite of rocks are comagmatic. These plots can also be useful in determining the relative degree of alteration that a sample has undergone. If one assumes that the New Amalfi suite of rocks is comagmatic then any sample that plots away from the cluster must have had its element ratios disturbed by some secondary process, i.e. alteration. In Figure 6.1b the incompatible element ratios Ba/Zr and Rb/Zr have been plotted against one another. It can be seen that all the samples chosen for isotope analysis plot within the cluster indicating that all three incompatible elements, the most important of which in this case being Rb, have remained relatively immobile in these

samples.

6.3.1.2 The mobility of Sr and Rb in the plagioclase separates.

In the case of the plagioclase separates, it can be seen from Table 6.1 that there are large increases in the concentrations of Rb and Sr in sample 89pl relative to sample 89pl(sp), with the proportional increase in Rb being greater than that for Sr. This causes the $^{87}Rb/^{86}Sr$ ratio to be greater in sample 89pl than in sample 89pl(sp). The $^{87}Sr/^{86}Sr$ ratio of sample 89pl is however less than that of sample 89pl(sp).

The increases in the $^{87}Rb/^{86}Sr$ ratio and the concentrations of Rb and Sr between 89pl(sp) and 89pl could be due to a sampling error incurred because sample 89pl(sp) is much smaller than 89pl and thus is non-representative. Both Rb and Sr normally increase with increasing Ab content (Smith, 1974), and this could explain the higher concentration of these elements in 89pl if 89pl(sp) represented a significantly higher proportion of grain cores. The plagioclase in rock 89 does show strong compositional zoning. This does not, however explain the decrease in $^{87}Sr/^{86}Sr$ between samples 89pl(sp) and 89pl, which must therefore be an alteration effect which has resulted in a loss of ^{87}Sr and/or ^{87}Rb in 89pl. The decrease in $^{87}Sr/^{86}Sr$ is however only small and therefore the effects of alteration in this case are not considered to be of concern in terms of its effects on R_0 calculation.

Alteration of plagioclase may also cause an increase in $^{87}Sr/^{86}Sr$ with resultant increase in the calculated R_0, as has been shown by Brooks (1968). This may have occurred in the case of samples 182pl and 99pl, both of which have $^{87}Sr/^{86}Sr$ ratios that are significantly higher than the other plagioclase separate samples. It is not possible at this stage to rule out assimilation as a mechanism by which these two samples had their $^{87}Sr/^{86}Sr$ ratios increased.

6.3.2 A Rb-Sr isochron age for the New Amalfi Sheet.

On the basis of the discussion above it was decided to exclude

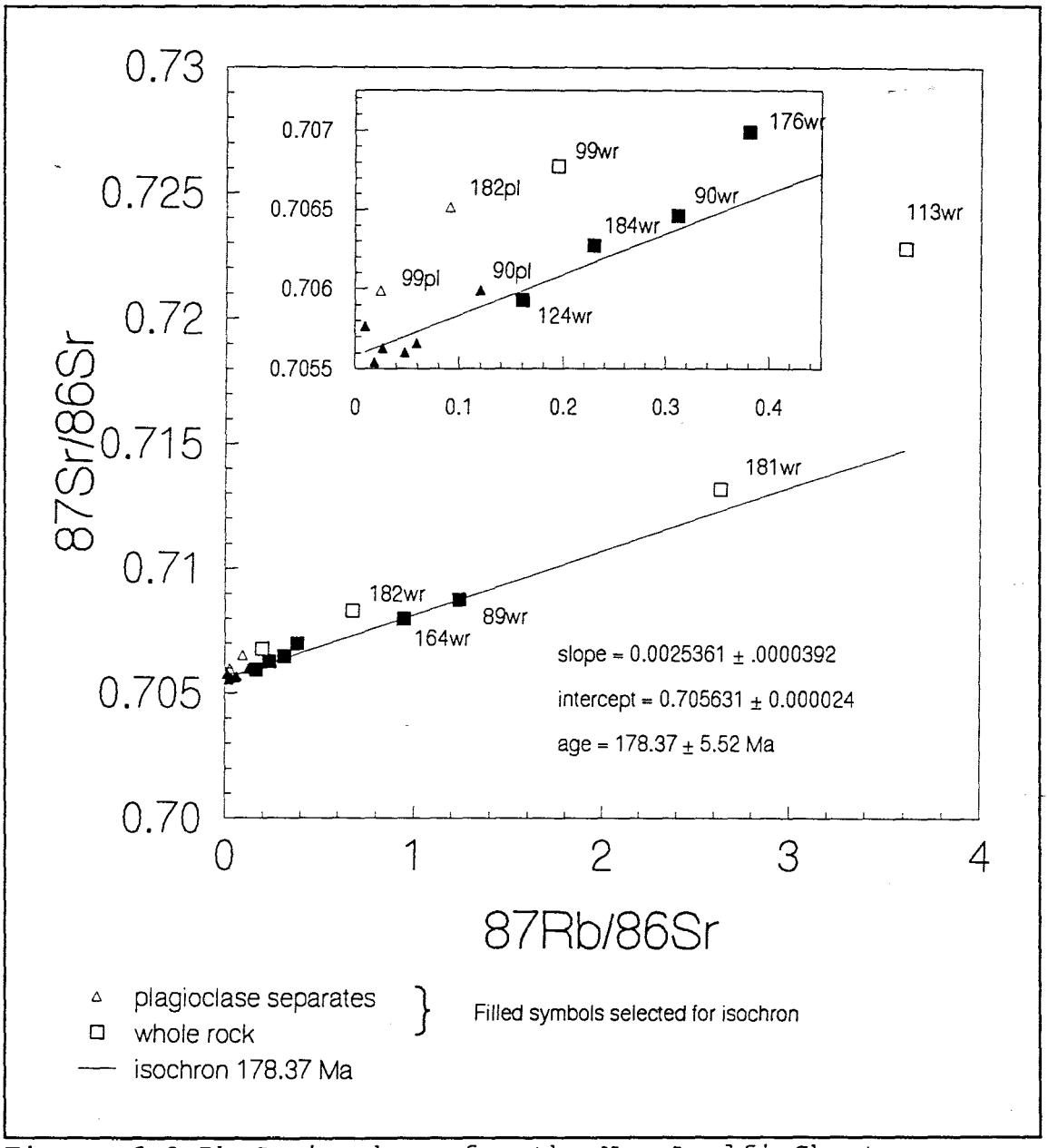

Figure 6.2 Rb-Sr isochron for the New Amalfi Sheet.

samples 99wr and 182wr from the calculation of the isochron regression line. Plagioclase samples 99pl and 182pl were also excluded on the basis of their $^{87}Sr/^{86}Sr$ ratios having been significantly increased. Samples 181wr and 113wr are excluded because of their crustal origin. The resulting isochron, obtained by fitting a regression line to the remaining 12 points, is shown in Figure 6.2. The slope of the isochron gives an age of 178.37 ± 5.52 Ma and an intercept of 0.705631 ± .000024. This intercept reflects the R_0 of the New Amalfi Sheet as a whole. This age for the New Amalfi Sheet is in excellent agreement with that of 178 ± 5 Ma given by Fitch and Miller (1984) for the first peak of intrusive activity following the extrusion of Lesotho Formation basalts at 193 Ma. It is also in agreement, within acceptable error, with the age of 182 ± 2 Ma given by Richardson (1984) for the Tandjiesberg dolerite sill, as well as with the recent ages of 182 ± 2 of Hooper et al. (1993) for the Lesotho basalts and the 178 ± 3 Ma age of Dr F.J Kruger (pers. comm.) for the Insizwa Complex .

The age for the New Amalfi Sheet does not agree with the age of 196.8 ± 11.2 Ma given by Allsopp et al.(1984) for the Birds River Complex. The latter corresponds rather with that of Fitch and Miller (op. cit.) for the main phase of extrusion of basalts in the Central area at 193 ± 5 Ma. This age for the Central area basalts must now come into question, in the light of the recent age given by Hooper et al., (1993) for the same rocks, as it would seem now that the initial eruption of Central area basalts was at 180 Ma, which corresponds to the age obtained for the New Amalfi Sheet.

6.3.3 Isotopic equilibration of the sedimentary xenolith.

An important feature of Figure 6.2 is that the sedimentary xenolith (181wr) plots very close to the isochron. If one assumes that the xenolith originally had an R_0 similar to that of country-rock sandstone sample 113wr, then it appears that the R_0 of the xenolith has been reset during partial ingestion. However the Sr concentration of the xenolith remains very different to that of its host, granophyre 182wr.

Isotopic equilibration of xenoliths has also been noted by Pin (1991), who reported that there was no difference in R_0 between host granitoids and xenoliths, regardless of whether they were of mafic igneous, sedimentary or metamorphic origin. Only the largest of these xenoliths had slightly different R_0 values to those of the granitoids. Sieger et al. (1992) state that the data of Pin (1991) is consistent with almost complete isotopic equilibration achieved between host rocks and xenoliths in the molten state.

Baker (1989) and Lesher (1990) have both studied the chemical and tracer diffusion of Sr between mafic and granitic melts. It has been shown that tracer diffusion, whereby isotopic equilibration takes place and which merely involves the swopping of one Sr isotope for another, is much faster (with diffusivities an order of magnitude greater) than chemical diffusion, with which chemical equilibration takes place, where actual chemical bonds must be broken in order for Sr to replace other elements within a silicate lattice. This leads to a decoupling of the Sr concentration and Sr isotopic composition of the two melts. Thus R_0 equilibration may be achieved without the equilibration of the Sr concentration at the stage when solidification occurs. This therefore leads to deviations from the expected binary mixing paths of Langmuir et al. (1978). This decoupling of Sr concentration and isotopic composition is seen in the case of the xenolith 181wr, which, despite having an R_0 which is essentially the same as that of its host 182wr, has less than half its Sr concentration.

6.3.4 The implications of R_0 variation in the rocks of the New Amalfi Sheet and their plagioclase separates.

An age of 180 Ma has been used for the calculation of R_0 values, which are shown in Table 6.1. The highest R_0 exhibited by the rocks which form part of the sheet is that of the granophyre 182wr (0.706568). The R_0 of granophyre 182wr is much closer to the R_0 of the New Amalfi Sheet (0.705579) than to that of the country-rock sandstone sample 113wr (0.713363). Thus the data seems to favour a mechanism of either a slight amount of

assimilation and/or hydrothermal alteration for producing the slightly elevated R_0 of granophyre 182wr rather than one by which country-rock sandstone was metasomatized to produce the granophyre, in which case one would except the product to retain the high R_0 of its country-rock parent. Therefore the rest of this section is devoted to interpreting the isotopic variation that is seen within the New Amalfi Sheet in terms of either a small amount of assimilation and/or hydrothermal alteration.

R_0 values for all samples except 113wr and 181wr have been plotted against $^{87}Rb/^{86}Sr$ in Figure 6.3 to produce an isochron diagram at 180 Ma. Tie-lines joining plagioclase and whole-rock pairs have been drawn in as well as the difference in R_0 between whole-rock and plagioclase pairs(ΔR_0). The ΔR_0 reflects the degree of alteration that has affected the whole-rock relative to the plagioclase separate or may reflect the fact that plagioclase was on the liquidus at the time when possible assimilation took place in which case the plagioclase would reflect the R_0 of the magma prior to assimilation.

All the samples that plot within the dotted rectangle in Figure 6.3 have similar R_0 values within the limits of their uncertainties (not shown, to avoid clutter). They also have small ΔR_0 values that are less than their uncertainties and thus ΔR_0 is not statistically significant. Therefore the samples in the rectangle are considered to be relatively unaltered (or unaffected by assimilation) and their R_0 values reflect that of the parent magma. As granophyre samples 89 and 164 both plot within the rectangle this is considered to be strong support for the argument that these rocks were formed by means of igneous differentiation.

In the case with all the samples that plot outside of the rectangle (99wr, 176wr and 182wr), their R_0 values have been significantly raised above that of the parent magma as seen from the fact that they have positive ΔR_0 values that are larger than their uncertainties. This increased R_0 could either have been caused by alteration and/or assimilation, as was explained above, and it is not possible at this stage to distinguish between these

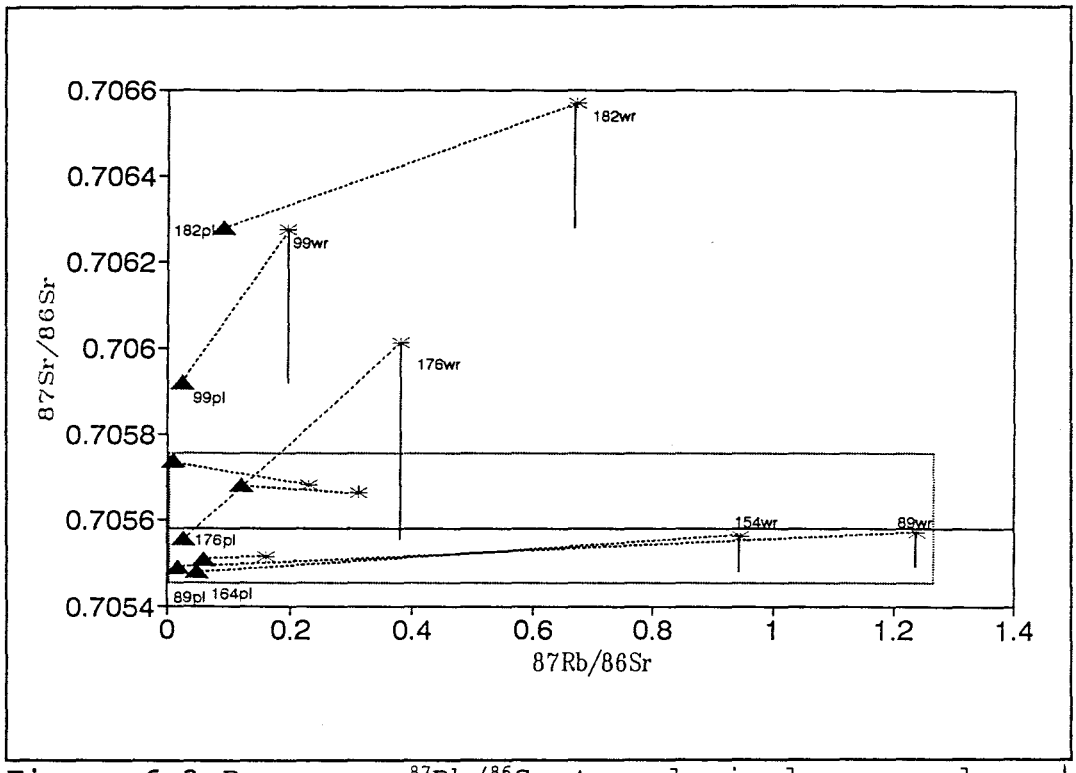

Figure 6.3 R_0 versus $^{87}Rb/^{86}S$. Δ = plagioclase samples; ★ = whole-rock samples; dashed lines join plagioclase and whole-rock pairs; vertical lines give δR_0.

two processes.

6.3.5 The origin of the granophyres in the light of Rb-Sr isotope evidence.

The main argument, so far, for the granophyres being igneous differentiates is based on the fact that their R_0 values are much lower than would have been expected had they been the metasomatized products of country-rock sandstone of which sample 113wr is an example. In fact, as has been shown above, the R_0 values of granophyre samples 89 and 164 are identical to that of the sheet as a whole, within the limits of the uncertainties, and the R_0 of granophyre sample 182 is only slightly elevated and thus better explained by either slight assimilation and/or hydrothermal alteration.

Some might argue however that the low R_0 of the granophyres is due to isotopic equilibration of a metasomatic granophyre which originally had a high R_0, as has taken place in the case of the country-rock xenolith. In this section various objections to this argument are presented.

The main argument against isotopic equilibration is based on the time limits imposed by the tracer and chemical diffusion rates between mafic and felsic magmas. Lesher (1990) states that " As molecular diffusivities are small (10^{-6} - 10^{-8} $cm.s^{-1}$) for silicate liquids, the length scales on which compositional heterogeneities can exist must also be small (metres or less) to produce homogenized products on reasonable convective time scales (10^3-10^4 yr)." Baker (1989) has calculated that in 10^3 years Sr chemical equilibration is attained within less than one meter either side of the contact between two magmas and that isotopic equilibration is achieved up to two meters either side of the contact.

At New Amalfi the granophyre has a maximum thickness of approximately 70m and the whole sheet is approximately 440m thick. Huppert and Sparks (1988) have calculated that a 500m sill takes 90 years to reach 60% crystallinity, at which point

it is essentially solid. Jaupart et al. (1993) have shown that magma cooling time calculations are all based on an incorrect measurement of the thermal conductivity of basalt magma and that calculated cooling times should in fact be 5 times greater. Even if the 90 years calculated by Huppert and Sparks (op. cit.) is multiplied by 5 this time period is still too short to produce complete isotopic equilibration in a layer of granophyre 70m thick, as can be seen from the calculations of Baker (op. cit.). In the case of the Skaergaard Intrusion, Leeman and Dasch (1978) found that country-rock gneisses and Marginal Border Group gabbros had identical R_0 values for a distance of only 15cm to either side of the contact.

The granophyres may not have been in the molten state during possible isotopic equilibration, however diffusion rates are even slower in the solid state. Cherniak and Watson (1992) have calculated on the basis of Sr diffusion rates in feldspar crystals that the cores of crystals with a diameter of 1mm would undergo Sr isotopic equilibration only if kept at temperatures of between 700°C and 800°C for several million years. They therefore conclude that R_0 values are retained in feldspar cores exposed to all but the most extreme thermal events. It is interesting to note, in the light of the data of Cherniak and Watson (op cit.), that the R_0 of the plagioclase separates at New Amalfi is either equal to or less than that of the whole-rock samples. As the plagioclase can be expected to retain the high R_0 of the supposed metasomatic granophyres for longer than the whole-rock, one would expect higher R_0 values in the plagioclase than in the whole-rock.

Therefore, on the basis of the arguments above, the R_0 of the granophyres is considered to be primary and not the result of a process of isotopic equilibration of the crustal R_0 of a metasomatic granophyre. The Rb-Sr isotopic data presented above therefore do not support a metasomatic origin for the New Amalfi Sheet granophyres. The granophyres appear to represent the end-products of fractional crystallization of a parent tholeiitic magma. The top-most granophyre (182wr) may have suffered from the effects of mild hydrothermal alteration and/or a limited amount

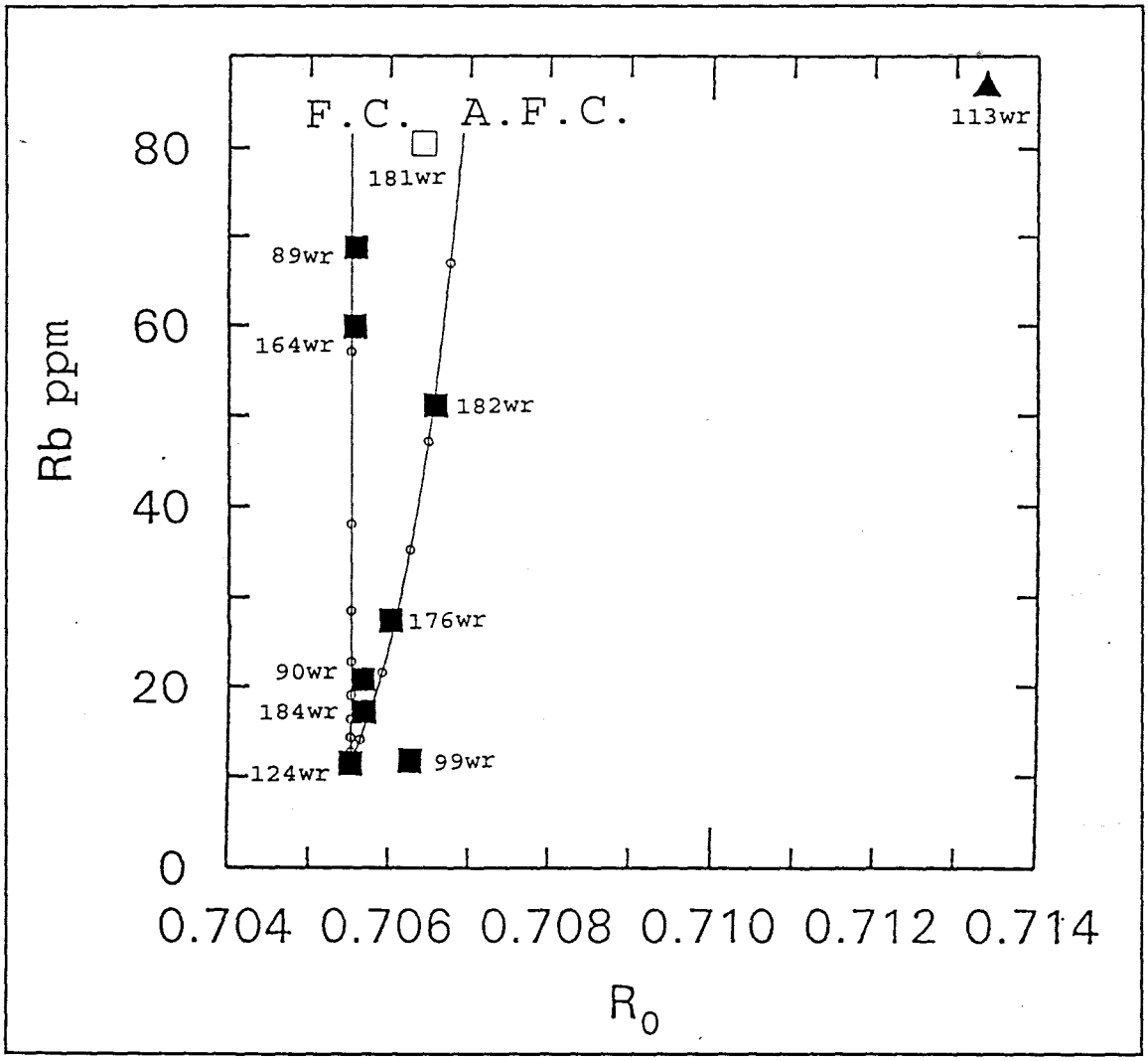

Figure 6.4 Rb versus R_0 shown together with modelled fractional crystallization and AFC curves. Small circles on curves indicate divisions of F at intervals of 0.1.

of assimilation of country-rock material. This has raised the R_0 of this granophyre slightly above that of mantle-source values.

6.3.6 AFC modelling of R_0 variation for the New Amalfi Sheet.

The range in R_0 for the whole-rock samples has been plotted against Rb in Figure 6.4. Rb has been used instead of Sr since it has not been affected by secondary alteration, as has already been shown. Assimilation fractional crystallisation (AFC) has been modelled using the equations of DePaolo (1981). The most primitive unaltered sample, 124wr, has been modelled as the parent and the sandstone 113wr used as the contaminant. Rb has been assumed to exhibit perfectly incompatible behaviour with D^{Bulk} Rb set at zero. This is considered to be a valid assumption because of the very low distribution coefficients for Rb in plagioclase and pyroxene in basaltic magmas (Philpotts and Schnetzler, 1970) and because AFC curves are insensitive to minor variations in D^{Bulk} (Marsh, 1989).

In Figure 6.4 samples 124wr, 184wr, 90wr, 164wr and 89wr can be seen to plot along a line representing fractional crystallization, thereby confirming that these rocks have not had their R_0 affected by alteration or assimilation, and thus reflect the R_0 of their parent magma.

Samples 182wr and 176wr fall onto an AFC curve with the r parameter (being the constant ratio of the rate of assimilation over the rate of fractional crystallization) equal to 0.125. This therefore indicates that assimilation and not alteration was responsible for the slight elevation in the R_0 values of samples 182wr and 176wr. However the amount of assimilation was only slight and fractional crystallisation was by far the dominant process as seen from the low r value.

Similarly it can been seen that hydrothermal alteration was the sole cause of the R_0 elevation of sample 99wr as no AFC curve with D^{Bulk}Rb less than 1 can pass through sample 99wr in Figure 6.4, no matter what value of r is used.

6.4) SUMMARY.

(a) The New Amalfi Sheet has been dated using the Rb-Sr isochron method at 178.37 ± 5.52 Ma. This is in agreement with the most recent data for the eruption of the Central area basalts.

(b) The sedimentary xenolith 181wr has had its R_0 reset during partial ingestion. However, the Sr concentration remains different to that of its host, and this is an example of the decoupling of isotopic and chemical equilibration because of differences in diffusivities for the tracer and chemical diffusion of Sr.

(c) Since the granophyres have low R_0 values, they are not considered to be the result of the metasomatism of country-rock sandstones, but rather the products of fractional crystallisation of a tholeiitic parent.

(d) Of the igneous rocks that were analyzed, samples 124, 184, 90, 164 and 89 have essentially constant R_0 values within the limits of the uncertainties and they are therefore considered to have been unaffected by hydrothermal alteration or assimilation and reflect the R_0 of their parent magma.

(e) The slight elevation in R_0 seen in rocks 182, 176 and 99 is due to the effects of assimilation fractional crystallisation (AFC) and/or hydrothermal alteration. It has been possible to distinguish which of these processes was responsible for the elevation in R_0 in each case. In the case of samples 176 and 182 AFC was solely responsible for raising R_0 however the amount of assimilation was small as seen from the small value of r. In the case of sample 99, hydrothermal alteration alone was responsible for raising R_0.

7. CONCLUSIONS.

7.1 PHYSICAL CHARACTERISTICS OF THE NEW AMALFI SHEET.

The New Amalfi intrusion has the basic shape of a steep-sided sheet that dips at 5° towards the west. The steep sides break out laterally into two flatly lying peripheral sheets. Three rock types were distinguished in the field, namely dolerite, gabbro and granophyre. The gabbro-granophyre package forms a 'sandwich horizon' within the top half of the sheet, which is completely enclosed by dolerite. The sheet has an overall vertical thickness of 440m at its thickest part. Faulting subsequent to emplacement has resulted in the formation of two small grabens with rotation along the northern-most graben fault.

7.2 INTRUSION AND DIFFERENTIATION OF THE NEW AMALFI SHEET.

The initial liquid that intruded to form the New Amalfi Sheet had a composition very similar to that of the average Lesotho type magma as defined by Marsh and Eales (1984), and the initial Zr concentration was similar to that of the most primitive Lesotho basalts. Pigeonite, clinopyroxene and plagioclase were already on the liquidus at the time the liquid was intruded. Cumulus olivine collected in the basal olivine dolerites.

The paragenetic sequence of the phases crystallizing from the liquid, as determined from petrography, is chromite → olivine → plagioclase → pigeonite and augite. Cumulus magnetite and ilmenite enter the paragenetic sequence together with immiscible sulphide droplets at the beginning of the evolution of the quartz monzodiorites after 35% crystallization. In the late-stages of crystallization, augite changes composition towards ferrohedenbergite and olivine reappears in the form of fayalite, coincident with the disappearance of pigeonite. Apatite appears as a cumulus phase for the first time, after 70% crystallization, in the granodiorites. Granophyric intergrowth, which contains coarse perthitic K-feldspar, becomes the most abundant modal entity within the fayalite-hedenbergite granophyres.

Differentiation of the intrusion was dominated by the separation of plagioclase and pyroxene, with a minor role being played by olivine and opaque oxides during certain stages of the differentiation. Both plagioclase and pyroxene appear to have been effectively separated from the residual liquid, because there is a direct relationship between the anorthite content of the plagioclase and the Mg# of the pyroxenes in each sample.

Least squares modelling of the differentiation shows that the most evolved rock within the sheet represents 17.9% of the initial liquid. This compares well with the figure obtained from trace-element modelling of the differentiation using the Rayleigh equation, which shows that this same sample represents 15.9% of the initial liquid. This degree of fractional crystallization is similar to that which occurred in the case of the Birds River Complex where the most evolved rock represents 16% of the initial liquid (Eales, 1990).

It appears that a number of blocks of country rock were stoped from the roof of the intrusion and digested by the crystallizing magma, and appear now as small xenoliths in the top-most granophyres. This is also manifest in the mineral chemistry of the feldspars, which indicate a sudden increase in water-vapour pressure during the closing stages of differentiation, probably brought about by the ingestion of water-laden sediments. The assimilation and contemporaneous fractional crystallization of the sheet has also been modelled using the equations of De Paolo (1981) and this shows that the rate of assimilation divided by the rate of fractional crystallization is only 0.125, indicating a very small amount of assimilation in the top-most granophyres.

The New Amalfi Sheet has been dated, using the Rb-Sr isochron method, at 178.37 $\pm$ 5.52 Ma. This is in agreement with the most recent dates for the timing of Central area volcanicity.

7.3 SUBSOLIDUS COOLING OF THE NEW AMALFI SHEET.

Subsolidus reaction between deuteric fluids and ilmenite-magnetite intergrowths caused the destruction of some of the

magnetite component and the formation of vermiform ilmenite overgrowths upon the existing ilmenite. These vermiform ilmenites increase in proportion with increasing height in the intrusion as can be seen from the increase in their MnO content, with height. This indicates an increase in deuteric activity with height in the intrusion.

Deuteric fluids are also considered to have been responsible for the formation of bleached hydrothermal pyroxenes which also increase in abundance with height in the intrusion. These bleached hydrothermal pyroxenes can be distinguished from the unaltered magmatic pyroxenes by virtue of the fact that they are relatively enriched in CaO and depleted in TiO_2. The increase in deuteric alteration with height may indicate that the deuteric fluids were derived from the compaction of cumulates at the base of the intrusion as suggested for the Palisades Sill by Shirley (1987). The temperature of the deuteric fluids was estimated from pyroxene thermometry to range between 950°C and 500°C.

Most of the deuteric fluids became concentrated in the granophyres, as indicated by the presence of drusy cavities with euhedral quartz and zircon, aplitic veins which contain bands of drusy cavities, and the increase in the grain size of the granophyres where cut by joint planes. All of these observations point to a high degree of fluid movement within the granophyres during subsolidus cooling. Shirley (op. cit.) also reported extensive localized aqueous alteration in zones within the Palisades Sill where aqueous magma accumulated, and this is matched by the extensive hydrothermal alteration of pyroxenes and high proportion of vermiform ilmenite seen in the granophyres of the New Amalfi Sheet.

The iron-rich orthopyroxene, ferrohypersthene, formed from the interstitial liquid during subsolidus cooling and this mineral is thus not a liquidus phase as postulated by Walker et al. (1973) in the case of the Palisades Sill. Olivine reacted with the intercumulus liquid in the dolerites, thereby causing it to re-equilibrate to more iron-rich compositions. Magnetite, apart from reacting with deuteric liquids, also underwent varying

degrees of subsolidus oxidation of magnetite-ulvöspinel intergrowth. Ilmenite appears not to have suffered any subsolidus re-equilibration and retains the chemical signatures of fractional crystallization as well as subsequent deuteric alteration.

7.4 THE ORIGIN OF THE GRANOPHYRES.

Numerous arguments have been put forward which are collectively considered to provide conclusive evidence that the New Amalfi Sheet granophyres are igneous differentiates. Firstly the presence of unbroken trends revealed by modal analysis, mineral chemistry and major- and trace-elements, from the dolerites to the granophyres provides strong support for the postulate that these rocks are genetically related. Secondly, successful major- and trace-element modelling of the differentiation sequence from the dolerites to the granophyres clearly shows that it is possible derive the granophyres by means of fractional crystallization of the New Amalfi Sheet initial liquid.

Lastly, Sr initial isotopic ratios for two of the granophyres are low and similar to that of the undoubtedly igneous rocks of the sheet, indicating that the granophyres were derived from a common mantle-derived parent. One other granophyre analysed had a slightly elevated Sr initial ratio, and this was shown to be due to a small amount of assimilation of crustal material.

REFERENCES.

Allegre, C.J., Treuil, M., Minster, J-F, Minster, B. & Albarede, F. (1977). Systematic use of trace elements in igneous process Part I : Fractional crystallization processes in volcanic suites. *Contr. Miner. Petrol.*, **60**, 57-75.

Allsopp, H.L., Bristow, J.W., Logan, C.T., Eales, H.V. & Erlank, A.J. (1984). Rb-Sr geochronology of three Karoo - related igneous complexes. *Spec. Publ. geol. Soc. S. Afr.*, **13**, 281-287.

Baker, D.R. (1989). Tracer versus trace element diffusion: Diffusional decoupling of Sr concentration from Sr isotope composition. *Geochim. cosmochim. Acta.*, **53**, 3015-3023.

Bence, A.E. & Papike, J.J. (1972). Pyroxenes as recorders of lunar basalt petrogenesis: Chemical trends due to crystal liquid interaction. *Proc. Third Lunar Sci. Conference*, 431-469.

Best, M.G. (1982). *Igneous and Metamorphic Petrology*. W.H. Freeman and Company, New York, 630 pp.

Bowen, N.L. & Tuttle, O.F. (1950). The system $NaAlSi_3O_8$-$KAlSi_3O_8$-H_2O. *J. Geol.*, **58**, 489-517.

Bristow, J.W., Allsopp, H.L., Erlank, A.J., Marsh, J.S., & Armstrong, R.A. (1984). Strontium Isotope characterization of Karoo Volcanic Rocks. *Spec. Publ. geol. Soc. S. Afr.*, **13**, 295-329.

Brooks, C. (1968). Relationship between feldspar alteration and precise post-crystallization movement of rubidium and strontium isotopes in a granite. *J. Geophys. Res.*, **73**, 4751-4757

Brown, G.M. & Vincent, E.A. (1963). Pyroxenes from the late stages of fractionation of the Skaergaard Intrusion, East

Greenland. *J. Petrology*, **4**, 175-197.

Bruynzeel, D. (1957). A petrographic study of the Waterfall Gorge profile at Insizwa. *Annals Univ. Stellenbosch*, **33**, 484-535.

Buchanan, D.L. (1979). A combined Transmission Electron Microscope and Electron Microprobe Study of Bushveld Pyroxenes from the Bethal Area. *J. Petrology*, **20**, 327-354.

Buddington, A.F. & Lindsley, D.H. (1964). Iron-titanium oxide minerals and synthetic equivalents. *J. Petrology*, **5**, 310-357.

Cameron, M. & Papike, J.J. (1981). Structural and chemical variations in pyroxenes. *Am. Miner.*, **66**, 1-50.

Campbell, I.H. & Nolan, J. (1974). Factors Effecting the Stability of Ca-Poor Pyroxene and the Origin of the Ca-Poor Minimum in Ca-Rich Pyroxenes from Tholeiitic Intrusions. *Contr. Miner. Petrol.*, **48**, 205-219.

Carmichael, S.E., Turner, F.J. & Verhoogen, J. (1974). *Igneous Petrology*, McGraw-Hill, New York, 739 pp.

Cawthorn, R.G., Maske, S., De Wet, M., Groves, D.I. & Cassidy, K.F. (1988). Contrasting magma types in the mount ayliff Intrusion (Insizwa Complex), Transkei: Evidence from ilmenite compositions. *Canadian Mineralogist*, **26**, 145-160.

Cawthorn, R.G., Bernhard, K.R. & Jones, I.M. (1992). Evidence for the trapped liquid shift effect in the Mount Ayliff Intrusion, South Africa. *Contr. Miner. Petrol.*, **111**, 194-202.

Cherniak, D.J. & Watson, E.B. (1992). A study of strontium diffusion in K-feldspar, Na-K feldspar and anorthite using Rutherford Backscattering Spectroscopy. *Earth Planet. Sc. Lett.*, **113**, 411-425.

Coleman, L.C. (1978). Solidus and Subsolidus Compositional Relationships of Some Coexisting Skaergaard Pyroxenes. *Contr. Miner. Petrol.*, **66**, 221-227.

Cox, K.G., Bell, J.D. & Pankhurst, R.J. (1979). *The Interpretation of Igneous Rocks*. George Allen & Unwin Ltd., London, 450 pp.

Deer, W.A., Howie, R.A. & Zussman, J. (1966). *An introduction to the rock forming minerals*, Longman, Hong Kong, 528pp.

Deer, W.A., Howie, R.A. & Zussman, J. (1978). *Rock Forming Minerals; Vol 2A; Single Chain Silicates*, Longman, London, 668pp.

Depaolo, D.J. (1981). Trace element and isotopic effects of combined wallrock assimilation and fractional crystallisation. *Earth Planet. Sc. Lett.*, **53**, 189-202.

Droop, G.T.R. (1987). A general equation for estimating Fe^{3+} concentrations in ferromagnesian silicatesand oxides from microprobe analyses, using stoichiometric criteria. *Min. Mag.*, **51**, 431-435.

Eales, H.V. (1979a). Anomalous Karroo spinels along the chromite-titanomagnetite join. *S. Afr. J. Sci.*, **75**, 24-29.

Eales, H.V., (1979b). Contrasted trace-element variations in two Karroo cumulus complexes. *Chemical Geology*, **29**, 39-48.

Eales, H.V. (1990). The Birds River Intrusion - a quantitative model for Karoo CentralProvince basalt fractionation. *S. Afr. J. Geol.*, **93**, 717-728.

Eales, H.V. & Booth, P.W.K. (1974). The Birds River Gabbro Complex, Dordrecht District. *Trans. geol. Soc S. Afr.*, **77**, 1-15.

Eales, H.V. & Robey, J van A. (1976). Differentiation of

tholeiitic Karroo Magma at Birds River, South Africa. *Contr. Miner. Petrol.*, **56**, 101-117.

Eales, H.V. & Marsh, J.S. (1979). High-Mg tholeiitic rocks and their significance in the Karroo Central Province. *S. Afr. J. Sci.*, **75**, 400-404.

Eales, H.V. & Snowden, D.V. (1979). Chromiferous Spinels of the Elephant's Head Dike. *Mineral. Deposita*, **14**, 227-242.

Eales, H.V., Reynolds, I.M. & Gouws, D.A. (1980). The spinel-group minerals of the central Karoo tholeiitic province. *Trans. geol. Soc. S. Afr.*, **83**, 243-253.

Eales, H.V., Marsh, J.S. & Cox, K.G. (1984). The Karoo Igneous Province: An Introduction. *Spec. Publ. geol. Soc. S. Afr.*, **13**, 1-26.

Eales, H.V., Teigler, B. & Maier, W.D. (1993). Cryptic Variations of Minor Elements Al, Cr, Ti and Mn in Lower and Critical Zone Orthopyroxenes of the Western Bushveld Complex. *Mineralog. Mag.*, **57**, 257-264.

Evans, B.W. & Moore, J.G. (1968). Mineralogy as a Function of Depth in the Prehistoric Makapuhi Tholeiitic Lava Lake. *Contr. Miner. Petrol.*, **17**, 85-115.

Faure, G. & Powell, J.L. (1972). *Strontium Isotope Geology*. Springer-Verlag, Heidelberg, 188 pp.

Fitch, F.J. & Miller, J.A. (1984). Dating Karoo igneous rocks by the conventional K-Ar and $^{40}Ar/^{39}Ar$ age spectrum methods. *Spec. Publ. geol. Soc. S. Afr.*, **13**, 247-266.

Ford, A.B. (1970). Development of the layered series and capping granophyre of the Dufek Intrusion of Antarctica. *Spec. Publ. geol. Soc. S. Afr.*, **1**, 492-510.

Grove, T.L. & Bence, A.E. (1977). Experimental study of

pyroxene-liquid interaction in quartz-normative basalt. *Proc Eighth Lunar Sci. Conference*, 1549-1579.

Haggerty, S.E. (1976). Oxidation of opaque mineral phases in basalts. In: Rumble, D. (ed) *Reviews in Mineralogy Vol 3 Oxide Minerals*, Min. Soc. Amer., Hg1-Hg99.

Hamilton, E.I. (1963). The isotopic composition of strontium in the Skaergaard intrusion, East Greenland, *J. Petrology*, **4**, 383-391.

Hart, J.S. & Davis, K.E. (1978). Nickel Partitioning Between Olivine and Silicate Melt. *Earth planet.Sc.Lett.*, **40**, 203-219.

Heubner, J.S. (1980). Pyroxene Phase Equilibria at Low Pressure. In: Prewitt C.T. (ed) *Reviews in Mineralogy Vol 7 Pyroxenes*, Min. Soc. Amer., 213-2588.

Heubner, J.S. & Turnock, A.C. (1980). The melting relations at 1 bar of pyroxenes largely of Ca-, Mg- and Fe - bearing componants. *Am. Miner.*, **65**, 225-271.

Hill, R. & Roeder, P. (1974). The crystallization of Spinel from basaltic liquid as a function of oxygen fugacity. *J.Geol*, **82**, 709-729.

Himmelberg, G.R. & Ford, A.B. (1976). Pyroxenes of the Dufek Intrusion, Anatarctica. *J. Petrology*, **17**, 219-243.

Hooper, P.R., Duncan, R.A., Marsh, J.S. & Duncan, A.R. (1993) The Basalts of Lesotho, Karoo Province, Southern Africa (abstr.). *EOS*, **74**, 553.

Huppert, H.E. & Sparks, R.S.J. (1988). The fluid dynamics of crustal melting by injection of basaltic sills. *Trans. R. Soc. Edinburgh*, **79**, 237-243.

Husch, J.M. (1990). Palisades sill: Origin of the olivine zone

by separate magmatic injection rather than gravity settling. *Geology*, **18**, 699-702.

Irving, A.J. (1978). Areview of experimental studies of crystal/liquid trace element partitioning. *Geochim. cosmochim. Acta*, **42**, 743-770.

Kenyon, A.K. (1976). *Reaction phenomena between Karroo dolerite and Cave Sandstone xenoliths in the Birds River complex*. M.Sc. thesis (unpubl.), Rhodes University, Grahamstown.

Korzhinsky, D.S. (1970). *Theory of Metasomatic Zoning*, Clarendon Press, Oxford, 162 pp.

Jaupart, C., Davaille, A. & Snyder, D. (1993) On the cooling of magma bodies. *EOS*, **74**.

Langmuir, C.H., Vocke, R.D.Jr., Hanson, G.N. & Hart, S.R. (1978). A general mixing equation with applications to Icelandic basalts. *Earth Planet. Sc. Lett.*, **37**, 380-392.

Leeman, W.P. & Dasch, E.J. (1978). Strontium, lead and oxygen isotopic investigation of the Skaergaard Intrusion, East Greenland. *Earth planet. Sc. Lett.*, **41**, 47-59.

Le Maitre, R.W. (1989). *A classification of igneous rocks and glossary of terms: Recommendations of the International Union of Geological Sciences Subcommission on the Systematics of Igneous Rocks*. Blackwell Scientific Publications, Oxford, 193 pp.

Lesher, C.E. (1990). Decoupling of chemical and isotopic exchange during magma mixing. *Nature*, **344**, 235-237.

Lightfoot, P.C., Naldrett, A.J. & Hawkesworth, C.J. (1984). The Geology and Geochemistry of the Waterfall Gorge Section of the Insizwa Complex with Particular Reference to the Origin of the Nickel Sulfide Deposits. *Econ. Geol.*, **79**, 1857-1879.

Lightfoot, P.C., Naldrett, A.J. & Hawkesworth, C.J. (1987). Re-Evaluation of chemical variation in the Insizwa Complex, Transkei. *Canadian Mineralogist*, **25**, 79-90.

Lindgren, W. (1928). *Mineral Deposits*. McGraw-Hill, New York, 1049 pp.

Lindsley, D.H. (1983). Pyroxene Thermometry. *Am. Miner.*, **68**, 477-493.

Lindsley, D.H. & Munoz, J.L. (1969). Subsolidus Relations Along the Join Hedenbergite-Ferrosilite. *Am.J.Sc.*, **Schairer Vol 267-A**,295-324.

Maeda, J., Shimura, T., Arita, K., Osanai, Y., Murata, M., Bamba, M. & Suetake, S. (1991). Chemical features of orthopyroxene in peraluminous igneous rocks. *Am. Miner.*, **76**, 1674-1682.

Mahoney, J., MacDougall, J.D., Lugmair, G.W., Murali, A.M.,Sankar, Das. M., & Goplan, K. (1982). Origin of the Deccan Trap flows at Mahabaleshwar inferred from Nd and Sr isotopic and chemical evidence. *Earth Planet. Sc. Lett.*, **60**, 47-60.

Mangan, M.T., Marsh, B.D., Froelich, A.J. & Gottfried, D. (1993). Emplacement and Differentiation of the York Haven Diabase Sheet, Pennsylvania. *J. Petrology*, **34**, 1271-1302.

Manning, C.E. & Bird, D.K. (1986). Hydrothermal clinopyroxenes of the Skaergaard intrusion. *Contr. Miner. Petrol.*, **92**, 437-447.

Marsh, J.S. (1989). Geochemical constraints on coupled assimilation and fractional crystallization involving upper crustal compositions and continental tholeiitic magma. *Earth Planet. Sc. Lett.*, **92**, 70-80.

Marsh, J.S. & Eales, H.V. (1984). Chemistry and petrogenesis of

igneous rocks of the Karoo Central Area, Southern Africa. *Spec. Publ. geol. Soc. S. Afr.*, **13**, 27-67.

Marsh, J.S., Sweeney, R.J. & Armstong, R.A. (1992). New Pb, Sr, and Nd isotope data from the Karoo Province. (abstract) Geocongress '92 Geol. Soc. S. Afr. Bloemfontein, 262-264.

Maske, S. (1966). The petrography of the Ingeli mountain range. *Annals Univ. Stellenbosch*, **41**, 1-109.

McBirney, A.R. (1975). Differentiation of the Skaergaard Intrusion. *Nature*, **253**, 691-694.

McDougall, I. (1962). Differentiation of the Tasmanian Dolerites: Red Hill dolerite-granphyre association. *Geol. Soc. Am. Bull.*, **73**, 279-316.

Mitchell, A.A. (1980). *The extrusive and Basaltic rocks of the Molteno-Jamestown area*. Unpubl. Masters Thesis, Rhodes University, 195pp.

Nakamura, Y. & Konda, T. (1974). Compositional relations of pyroxenes in a ferrogabbro from Beaver Bay intrusion, Minnesota. *Lithos*,**7**, 7-14.

Norrish, K. & Hutton, J.T. (1969). An accurate X-ray spectrographic method for the analysis of a wide range of geological samples. *Geochim. cosmochim. Acta.*, **33**, 431-453.

Nwe, Y.Y. (1976). Electron-Probe Studies of the Earlier Pyroxenes and Olivines from the Skaergaard Intrusion, East Greenland. *Contr. Miner. Petrol.*, **55**, 105-126.

Nwe, Y.Y. & Copely, P.A. (1975). Chemistry, subsolidus relations and electron petrography of pyroxenes from the late ferrodiorites of the Skaergaard Intrusion, East Griqualand. *Contr. Miner. Petrol.*, **53**, 37-54.

Ott, L. & Mendenhall, W. (1985). *Understanding Statistics*.

Duxbury Press, Boston, 493pp.

Pearce, J.A. & Norry, M.J. (1979). Petrogenetic implications of Ti, Zr, Y, and Nb variations in volcanic rocks. *Contr. miner. Petrol.*, **69**, 33-47.

Philpotts, J.A. & Schnetzler, C.C. (1970). Phenocryst-matrix partition coefficients for K, Rb, Sr and Ba, with applications to anorthosite and basalt genesis. *Geochim. cosmochim. Acta.*, **34**, 307-322.

Pin, C. (1991). Sr-Nd isotopic study of igneous and metasedimentary enclaves in some Hercynian granitoids from the Massif Central, France. In: Didier, J. & Barbarin, B. (eds.) *Developments in Petrology 13: Enclaves and Granite Petrology*. Elsevier, Amsterdam, 333-344.

Poldervaart, A. (1944). The petrology of the Elephants Head Dyke and New Amalfi Sheet (Matatiele). *Roy. Soc. S. Africa*, **30**, 85-119.

Poldervaart, A. & Hess, H.H. (1951) Pyroxenes in the Crystallization of Basic Magma. *J. Geol.*, **59**, 472-489.

Reynolds, I.M. (1983). The iron-titanium oxide mineralogy of Karoo dolerite in the eastern cape and southern orange free state. *Trans. geol. Soc. S. Afr.*, **86**, 211-220.

Richardson, S.H. (1984). Sr, Nd and O isotope variation in an extensive Karoo dolerite sheet, Southern Namibia. *Spec. Publ. geol. Soc. S. Afr.*, **13**, 289-293.

Robey, J. van A. (1976). *Aspects of the geochemistry of the Karroo dolerites and basalts of the north-eastern Cape Province South Africa*. M.Sc. thesis (unpubl.), Rhodes University, 118 pp.

Roeder, P.L. & Emslie, R.F. (1970). Olivine-liquid equilibrium. *Contr. miner. Petrol.*, **29**, 275-289.

Russel, J.K. & Nicholls, J. (1988) Analysis of petrologic hypothesis with Pearce element ratios. *Contr. miner. Petrol.*, **99**, 25-35.

Scholtz, D.L. (1936). The magmatic nickeliferous ore deposits of -East Griqualand and Pondoland. *Trans. Geol. Soc. S. Afr.*, **39**, 81-210.

Shearer, C.K., Papike, J.J., Simon, S.B. & Shimuza, N. (1989). An ion microprobe study of the intra-crystalline behaviour of REE and selected trace elements in pyroxene from mare basalts with different cooling and crystallization histories. *Geochim. cosmochim. Acta.*, **53**, 1041-1054.

Shirley, D.N. (1987). Differentiation and compaction in the Palisades Sill, New Jersey. *J.Pet.*, **28**, 835-867.

Smith, J.V. (1974). *Feldspar Minerals*, **2**, Springer-Verlag, Germany, 690 pp.

Smith, D. (1970). Mineralogy and Petrology of the Diabasic Rocks in a Differentiated Olivine Diabase Sill Complex, Sierra Ancha, Arizona. *Contr. Miner. Petrol.*, **27**, 95-113.

Taylor, S.R. (1965). Application of trace element data to problems in petrology. *Phys. Chem. Earth*, **6**, 133-214.

Taylor, H.P. & Forester, R.W. (1979). An Oxygen and Hydrogen Isotope Study of the Skaergaard Intrusionand its Country Rocks: a Description of a 55 M.y. Old Fossil Hydrothermal System. *J. Petrology*, **20**, 355-419.

Wager, L.R. & Brown, G.M. (1968). *Layered Igneous Rocks*. Oliver & Boyd, London, 588 pp.

Walker, F. & Poldervaart, A. (1941). The metasomatism of Karroo sediments by dolerite. *Trans. Roy. S. Africa*, **44**, 127-148.

Walker, F. & Poldervaart, A. (1949). Karroo dolerites of the

Union of South Africa. *Geol. Soc. Am. Bull.*, **60**, 591-706.

Walker, K.R. (1969). The Palisades Sill, New Jersey: A Reinvestigation. *Spec. Paper Geol. Soc. Am.*, **111**, pp 177.

Walker, K.R., Ware, N.G. & Lovering, J.F. (1973). Compositional variations in the pyroxenes of the differentiated Palisades Sill, New Jersey. *Geol. Soc. Am. Bull.*, **84**, 89-110.

Wasserburg, G.J., Albee, A.L. & Lanphere, M.A. (1964). Migration of radiogenic strontium during metamorphism. *J. Geophys. Res.*, **69**, 4395-4401.

Williams, C.M. (1991). *The petrography and geochemistry of the New Amalfi Sheet (Matatiele)*. Hons. thesis (unpubl.), Rhodes University, 53 pp.

Van der Laan, S.R. & Wyllie, P.J. (1992). Experimental interaction of granitic and basaltic magmas and implications for mafic enclaves. *J. Petrology*, **35**, 491-517.

APPENDIX I

i) Analytical procedure for electron microprobe analysis.

Sample thin sections were first polished down to a 1/4μ finish and then coated with a carbon film. Electron microprobe analysis of the major phases in each sample was effected with the use of the Rhodes University Joel CXA-733 Superprobe, operating at 15KV and with a beam current of 25nA. A Duncumb-Reed atomic number correction scheme was used. Standards used for calibration were Jadeite (Rhodes), Orapa ilmenite, Wollastonite (JVPL) and Orthoclase (JVPL). All phases except the pyroxenes were analysed with a defocused 10 micron beam. The counting times were set at 30 seconds for peak and 10 seconds for background positions.

ii) Analytical procedure for whole rock analysis.

All whole rock samples were initially crushed to chip size and the least weathered chips were then selected and ground to fine powders. Whole rock analyses were obtained with the use of the Rhodes University Phillips PW 1480 X-ray spectrometer. Fusion disks, prepared according to the method of Norrish and Hutton (1969), were used for the analysis of all major elements except sodium. Sodium and trace elements were analysed from powder briquettes. A standard set of analytical conditions were used and working curves were determined from internationally recognized standards.

iii) Analytical procedure for Rb-Sr isotope analysis.

Sample preparation prior to the wet chemistry stage for the whole rock samples involved the grinding of the freshest available chips down to a fine powder in order to ensure sample homogeneity. For the plagioclase separates, samples were crushed and sieved and the 500μ - 250μ size fraction was selected for magnetic separation. After magnetic separation the fraction consisted of plagioclase and quartz which was then washed with dilute HCl in order to remove brown stains that were present on many grains. The final stage involved hand picking of the freshest plagioclase grains. The isotope dilution technique was

used to determine Rb and Sr concentrations. Spiked samples were dissolved in HF and then converted to a chloride with 6N HCl. Chemical separation of Rb and Sr was achieved with the use of ion exchange columns. Samples were loaded on to double rhenium filaments in the case of Rb and single rhenium filaments in the case of Sr. Two mass spectrometers at the Bernard Price Institute of Geophysical Research (Witwatersrand University) were used to obtain isotopic ratios. No correction for blanks was necessary.

APPENDIX II : ORIGINAL WHOLE-ROCK ANALYSES BEFORE RECALCULATION

	NA79	NA80	NA81	NA85	NA86	NA87	NA88
SiO2	51.33	51.62	53.45	49.97	65.89	67.50	71.13
TiO2	0.87	0.90	1.26	1.04	0.90	0.79	0.55
Al2O3	15.45	15.04	14.29	15.63	11.52	11.61	11.73
Fe2O3	11.07	11.16	11.80	12.15	10.17	8.90	6.33
MnO	0.18	0.16	0.19	0.20	0.15	0.14	0.10
MgO	7.17	7.26	6.16	6.33	0.34	0.17	0.09
CaO	10.49	10.36	9.91	10.62	3.06	2.40	1.13
Na2O	1.86	2.35	2.55	2.30	3.36	3.60	3.92
K2O	0.52	0.61	0.81	0.72	3.07	3.33	3.80
P2O5	0.10	0.10	0.18	0.14	0.18	0.14	0.05
LOI	0.99	0.17	0.28	1.46	0.98	1.04	0.81
H2O-	0.64	0.26	0.03	0.53	0.43	0.52	0.35
Total	100.65	99.99	100.92	101.10	100.03	100.14	100.00

TRACE ELEMENTS (ppm)

Sr	125.9	132.8	203.5	190.4	132.9	131.0	90.6
Rb	15.5	17.1	18.7	20.8	75.2	86.9	104.1
Y	26.8	25.9	28.7	27.7	94.1	101.4	140.7
Zr	80.5	85.5	103.1	92.8	405.4	398.0	449.7
Nb	2.2	2.0	9.6	4.7	36.6	38.4	39.5
Co	52.2	48.0	43.9	49.1	13.2	13.2	9.5
Cr	403.6	378.0	149.3	143.5	15.6	5.5	2.5
V	266.7	259.5	314.8	283.5	0.0	0.0	0.0
Zn	86.5	86.4	99.4	93	148.3	153.3	126.8
Cu	99.2	105.2	108.7	132.3	29	28.2	19.7
Ni	101.1	94.8	52.7	64.4		3.1	4.1
Th		1.54		1.79	9.18	9.14	11.09
Pb	2.99	3.67	3.52	3.14	12.43	14.92	17.36

APPENDIX II : ORIGINAL WHOLE-ROCK ANALYSES BEFORE RECALCULATION

	NA89	NA90	NA91	NA92	NA93	NA95	NA96
SiO2	63.69	49.70	49.45	52.14	52.96	53.63	52.97
TiO2	1.05	3.11	2.60	1.34	1.36	1.28	1.27
Al2O3	11.74	12.01	12.23	14.48	13.74	14.34	13.38
Fe2O3	11.50	19.49	18.08	13.43	13.13	12.59	13.05
MnO	0.16	0.23	0.23	0.20	0.20	0.20	0.20
MgO	0.41	4.27	4.42	4.65	5.22	4.91	5.47
CaO	3.71	8.57	8.70	9.36	9.09	9.11	9.07
Na2O	3.35	2.43	2.57	2.67	2.54	2.76	2.59
K2O	2.77	0.90	0.90	0.80	0.84	0.92	0.85
P2O5	0.24	0.21	0.22	0.20	0.19	0.18	0.18
LOI	0.84	0.10	0.19	0.39	0.52	0.35	0.37
H2O-	0.43	0.51	0.38	0.45	0.35	0.33	0.34
Total	99.88	101.53	99.97	100.12	100.13	100.60	99.75

TRACE ELEMENTS (ppm)

Sr	160.9	198.7	191.2	228.3	214.1	226.5	211.7
Rb	68.2	20.9	22.0	17.3	18.7	22.0	20.8
Y	88.3	36.2	32.6	29.9	32.6	30.1	31.2
Zr	334.5	113.0	111.1	93.6	101.8	93.8	96.8
Nb	35.5	10.7	8.0	9.0	9.8	8.1	9.6
Co	16.1	66.4	63.8	46.2	48.0	45.9	47.0
Cr	4.8	0.0	0.0	4.9	7.8	18.9	3.9
V	0.0	1122.2	1079.2	331.0	324.3	326.7	337.6
Zn	159.9	139.4	128.9	105.1	104.6	99.8	105.1
Cu	34.5	391.3	349.6	182.9	198.2	307	185.2
Ni		31.9	38.1	30.4	39.1	40	41.9
Th	7.91	1.83					1.61
Pb	12.6	4.82	4.34	3.73	4.53	3.79	3.73

APPENDIX II : ORIGINAL WHOLE-ROCK ANALYSES BEFORE RECALCULATION

	NA125	NA124	NA97	NA98	NA99	NA113	NA72
SiO2	51.06	51.30	49.60	52.17	49.47	78.89	51.45
TiO2	0.88	0.88	0.86	0.85	0.80	0.44	0.84
Al2O3	15.86	16.49	16.27	15.76	13.38	10.10	15.63
Fe2O3	10.17	9.96	10.28	10.56	11.70	3.18	10.28
MnO	0.16	0.16	0.17	0.18	0.17	0.08	0.16
MgO	7.59	7.59	8.47	8.23	13.22	0.48	7.82
CaO	10.90	11.10	10.61	11.06	9.12	0.22	10.49
Na2O	2.28	2.31	2.36	2.30	2.16	1.50	1.79
K2O	0.53	0.53	0.53	0.50	0.53	2.24	0.47
P2O5	0.13	0.13	0.12	0.12	0.13	0.10	0.14
LOI	0.41	0.26	0.37	0.23	0.41	2.48	1.15
H2O-	0.22	0.15	0.21	0.22	0.14	0.33	0.28
Total	100.19	100.86	99.85	102.18	101.23	100.05	100.51

TRACE ELEMENTS (ppm)

Sr	203.3	206.4	214.9	199.5	177.5	71.2	209.12
Rb	13.6	11.8	10.5	11.2	12.1	89.3	13.6
Y	21.4	21.2	20.9	20.4	20.4	28.1	20.63
Zr	69.2	65.7	63.4	60.0	63.5	304.9	64.91
Nb	4.8	6.0	5.9	5.1	5.4	14.0	5.64
Co	46.5	44.1	50.6	53.6	59.5	14.0	44.9
Cr	400.8	479.7	395.9	408.6	909.4	40.0	297.8
V	228.5	238.1	223.2	240.5	203.6	60.8	237.9
Zn	75.9	76.6	79.1	78.2	83.8	48.1	85.2
Cu	86.2	85.8	85.2	87.6	80.8	12.9	85.9
Ni	129.5	111.4	145.8	117.6	342.4	16.2	119.4
Th						13.28	
Pb	2.62	2.09		2.24	2.22	15.29	2.42

APPENDIX II : ORIGINAL WHOLE-ROCK ANALYSES BEFORE RECALCULATION

	NA129	NA136	NA184	NA185	NA186	NA187	NA188
SiO2	51.75	51.75	53.20	52.31	53.34	53.82	50.90
TiO2	0.92	1.08	1.13	0.83	1.19	1.21	2.77
Al2O3	14.44	14.93	14.14	14.93	13.82	13.83	11.77
Fe2O3	11.11	12.61	12.09	9.92	12.65	13.07	18.68
MnO	0.17	0.19	0.19	0.18	0.20	0.21	0.22
MgO	9.10	6.44	6.32	7.83	5.93	5.55	4.14
CaO	10.25	10.81	10.07	11.16	9.63	9.30	8.05
Na2O	1.93	2.20	2.13	2.13	2.26	2.35	2.07
K2O	0.54	0.59	0.62	0.29	0.69	0.88	1.01
P2O5	0.16	0.16	0.17	0.10	0.17	0.19	0.25
LOI	0.07	-0.23	0.48	0.62	0.70	0.23	0.25
H2O-	0.65	0.92	0.31	0.32	0.34	0.24	0.35
Total	101.10	101.47	100.83	100.63	100.93	100.88	100.46

TRACE ELEMENTS (ppm)

Sr	183.27	176.94	222.18	233.08	212.17	214.67	183.28
Rb	16.68	14.54	19.25	5.18	15.57	21.45	23.87
Y	24.5	27.1	27.37	18.71	28.28	29.65	38.83
Zr	77.31	96.48	85.21	56.72	88.92	96.91	132.52
Nb	6.96	4.97	8	2.83	7.23	10.23	12.91
Co	51.4	44.9	44	43.5	45.8	45.4	60.4
Cr	437.9	132.5	32.5	41.2	18.1	13.2	5.1
V	235.6	274.2	293.5	300.5	312.9	318.6	1077.7
Zn	86.7	96.6	95.5	82.2	101.6	102.1	146.4
Cu	92.7	125.8	97.7	87.2	224.5	277	322.5
Ni	171.3	69.8	48	73.3	49.9	43.9	36.4
Th	1.98					1.62	1.96
Pb	3.1	2.33	2.5	1.65	1.81	2.37	3.85

APPENDIX II : ORIGINAL WHOLE-ROCK ANALYSES BEFORE RECALCULATION

	NA189	NA160	NA176	NA190	NA191	NA169	NA192
SiO2	51.11	51.18	52.44	53.10	53.00	55.49	57.59
TiO2	2.88	2.86	2.66	2.79	3.33	2.63	1.89
Al2O3	11.85	11.38	11.76	11.53	11.49	11.08	11.40
Fe2O3	18.75	18.86	18.04	17.67	18.75	17.93	14.79
MnO	0.24	0.23	0.23	0.24	0.23	0.22	0.20
MgO	3.90	3.50	3.07	3.04	2.69	2.17	1.42
CaO	8.19	7.54	7.54	7.17	7.11	6.14	5.83
Na2O	2.27	2.37	2.09	2.30	2.40	2.47	2.74
K2O	0.95	1.12	0.98	1.10	1.29	1.77	1.99
P2O5	0.25	0.30	0.33	0.30	0.27	0.44	0.69
LOI	0.05	0.55	0.57	0.52	0.51	0.82	0.88
H2O-	0.28	0.52	0.43	0.51	0.39	0.59	0.55
Total	100.69	100.42	100.14	100.26	101.46	101.74	99.96

TRACE ELEMENTS (ppm)

Sr	189.15	188.36	210.74	195.03	199.47	176.52	186.78
Rb	23.93	29.48	28.18	30.58	33.84	44.6	48.74
Y	38.7	43.94	51.16	44.76	46.77	61.99	72.92
Zr	137.15	155.23	172.02	166.47	179.04	231.8	267.19
Nb	12.58	14.47	18.06	15.44	16.72	23.02	24.65
Co	57.6	54.3	50.6	48.8	49.2	43.8	26.8
Cr	6.6	8.2	8.1	10.1	13	13.7	12.8
V	851.2	737.9	551.8	342.2	282	168.2	10.1
Zn	145.7	149.1	150.2	158	166.1	175.5	158
Cu	304.9	277.3	246.5	241.1	245.5	172.6	61.6
Ni	28	27.6	16.9	10.7	8.5	7.1	
Th	2.14	3.81	2.65	4.69	4.52	4.5	5.64
Pb	5.23	5.89	5.92	6.07	5.92	8.58	5.88

APPENDIX II : ORIGINAL WHOLE-ROCK ANALYSES BEFORE RECALCULATION

	NA161	NA153	NA193	NA179	NA162	NA164	NA159
SiO2	57.32	57.64	58.79	62.34	61.61	61.12	64.21
TiO2	1.95	1.74	1.56	1.23	1.38	1.41	1.18
Al2O3	11.17	11.16	11.37	10.93	11.50	11.55	11.93
Fe2O3	17.48	16.84	14.49	13.50	14.82	15.46	12.95
MnO	0.22	0.22	0.20	0.19	0.20	0.23	0.19
MgO	1.35	1.17	1.00	0.82	0.82	0.81	0.63
CaO	5.88	5.31	4.93	4.37	4.77	4.96	4.28
Na2O	2.82	2.69	2.78	2.42	3.01	3.10	3.36
K2O	1.98	2.08	2.30	2.33	2.44	2.34	2.64
P2O5	0.77	0.63	0.63	0.35	0.41	0.41	0.29
LOI	0.64	0.67	1.04	1.17	0.63	0.38	0.51
H2O-	0.57	0.46	0.51	0.50	0.34	0.41	0.35
Total	102.13	100.61	99.59	100.15	101.93	102.19	102.52

TRACE ELEMENTS (ppm)

Sr	181.18	184.32	177.69	188.88	172.82	183.33	175.28
Rb	49.27	54.44	59.62	64.01	66.42	61.21	68.2
Y	81.11	78.97	80.14	83.09	79.49	80.97	91.82
Zr	255.57	261.19	296.41	334.1	301.68	302.47	337.48
Nb	26.19	26.8	28.04	29.46	31.49	31.73	34.54
Co	44.3	22.6	19	15.6	15.1	14.5	11
Cr	20.5	11.9	12.8	12	16.6	16.3	12.8
V	6	0	2.4	0	0	0	0
Zn	210.8	179.4	163.8	170	204.7	171.4	168.1
Cu	68.6	61.5	52.4	44.5	48	48.9	40.7
Ni	3.8	4.2	3.8	4.9	4	7.3	4.3
Th	6.38	5.85	6.57	7.74	6.5	6.23	7.01
Pb	9.9	11.51	9.17	9.05	15.96	9.81	10.34

APPENDIX II : ORIGINAL WHOLE-ROCK ANALYSES BEFORE RECALCULATION

	NA155	NA158	NA165	NA166	NA167	NA168	NA171
SiO2	64.14	66.62	63.42	65.86	64.54	72.45	63.24
TiO2	1.08	1.01	1.09	0.95	1.01	0.53	1.22
Al2O3	11.75	11.97	11.63	11.72	11.84	11.41	11.73
Fe2O3	11.68	11.07	12.19	10.48	11.51	6.28	13.07
MnO	0.16	0.15	0.17	0.15	0.16	0.09	0.18
MgO	0.63	0.48	0.62	0.43	0.55	0.24	0.61
CaO	3.88	3.60	4.09	3.42	3.75	1.44	4.18
Na2O	3.32	3.47	3.29	3.48	3.09	3.65	3.36
K2O	2.68	2.88	2.67	2.93	2.69	3.78	2.60
P2O5	0.26	0.22	0.25	0.20	0.25	0.05	0.31
LOI	0.74	0.55	0.63	0.63	1.06	0.68	0.31
H2O-	0.48	0.39	0.48	0.40	0.51	0.38	0.27
Total	100.79	102.41	100.53	100.63	100.96	100.97	101.10

TRACE ELEMENTS (ppm)

Sr	184.23	157.94	173.57	163.77	160.93	107.85	172.85
Rb	71.24	72.61	67.98	77.42	70.64	95.02	67.54
Y	88.94	105.11	85.8	85.22	89.04	107.21	90.03
Zr	346.78	345.3	323.47	351.83	325.41	371.62	333.77
Nb	33.46	35.43	35.01	35.1	33.02	37.76	33.85
Co	9.1	9.9	10.2	9	9.7	3.4	13.3
Cr	12.1	14.5	16.8	10.8	12.1	8.3	12
V	0	0	0	0	0	0	0
Zn	165.5	201.3	168.1	149.9	164.2	115.2	177.1
Cu	35.2	32.3	40.2	33.1	36.5	16.1	38.4
Ni	5.7	5	5.1		3.7	4.3	3.8
Th	8.19	7.78	7.82	7.8	7.29	11.17	7.79
Pb	12.07	12.3	12.15	12.55	12.43	13.75	10.03

APPENDIX II : ORIGINAL WHOLE-ROCK ANALYSES BEFORE RECALCULATION

	NA172	NA170	NA83	NA121	NA134	NA181
SiO2	63.54	64.81	71.48	71.93	72.57	73.97
TiO2	1.17	0.92	0.62	0.69	0.55	0.56
Al2O3	11.74	11.37	11.51	11.47	11.35	11.68
Fe2O3	13.05	10.74	7.31	7.08	6.22	6.04
MnO	0.19	0.17	0.10	0.10	0.09	0.08
MgO	0.59	0.44	0.25	0.28	0.19	0.25
CaO	4.20	3.39	1.54	1.62	1.79	1.22
Na2O	3.31	3.21	3.66	4.17	4.15	4.08
K2O	2.62	2.94	3.49	3.44	3.65	3.91
P2O5	0.31	0.17	0.07	0.08	0.04	0.05
LOI	0.92	1.08	0.30	0.17	0.04	0.61
H2O-	0.67	0.51	1.00	0.54	0.67	0.35
Total	102.31	99.73	101.34	101.56	101.31	102.80

TRACE ELEMENTS (ppm)

Sr	179.89	167.45	91.9	121.96	96.76	89.01
Rb	63.14	74.93	89.15	68.79	97.37	81.42
Y	84.23	88.16	143.36	88.34	108	88.99
Zr	339.95	363.01	488.47	428.7	480.36	468.47
Nb	33.47	36.11	35	34.77	35.63	35.76
Co	9.2	7.3	4	5.6	3.5	4.5
Cr	16.2	11.7	5.6	9.2	7.2	14.5
V	0	0	0	2.6	0	0
Zn	169.7	155.3	130.1	99.2	125.1	93.6
Cu	36.6	35.8	17	30.3	23.1	11.2
Ni	5	3.3	5.3	3.5	4.7	6.3
Th	7.49	9.13	11.05	10.13	11.54	10.81
Pb	10.81	13.29	15.22	10.76	14.78	15.16

APPENDIX III : VECTORS AND MINERALS USED IN MIXING CALCULATIONS.

Oxide (wt%)	SiO_2	TiO_2	Al_2O_3	FeO	MnO	MgO	CaO	Na_2O	K_2O	P_2O_5
NAINI	51.99	0.99	15.06	10.21	0.18	6.99	10.30	2.39	0.61	0.14
NA93	53.36	1.37	13.85	11.91	0.20	5.26	9.15	2.54	0.84	0.19
NA176	52.90	2.69	11.87	16.38	0.23	3.09	7.61	2.09	0.98	0.34
NA153	57.94	1.75	11.22	15.22	0.22	1.18	5.34	2.69	2.09	0.63
NA89	64.62	1.07	11.91	10.50	0.16	0.41	3.76	3.35	2.81	0.24
NA88	72.01	0.56	11.89	5.77	0.11	0.09	1.14	3.92	3.84	0.05
INIOL	39.24			18.48		42.28				
176OL	36.31			34.09		29.60				
153OL	32.67			53.52		13.81				
79PL	48.48		32.02	0.49			16.66	2.36	0.07	
93PL	55.30		28.03	0.51			11.07	5.32	0.31	
176PL	55.96		26.61	0.62			10.21	5.89	0.38	
153PL	58.21		25.34	0.54			8.18	6.92	0.52	
89PL	60.12		24.23	0.48			7.07	7.30	0.57	
86PL	67.96		19.60	0.05			0.5	11.99	0.07	
89KF	66.78		18.32	0.21			0.47	5.34	8.44	
86KF	64.72		18.37	0.08			0.01	0.75	15.43	
99CPX	53.89	0.37	1.47	6.88	0.2	18.77	17.43	0.13		
93CPX	50.95	0.63	1.21	16.97	0.32	12.08	17.61	0.21		
176CPX	49.62	0.64	2.09	20.42	0.29	8.29	17.64	0.59		
153CPX	48.71	0.73	0.83	25.16	0.34	5.15	18.53	0.24		
90MAG		14.44	1.18	79.57	0.33	0.06				
176ILM		51.79	0.01	46.80	1.50	0.03				
APAT				0.32	0.02	0.05	55.08	0.04	0.01	42.40